2026 OPAL

Optics, Photonics and Lasers

Proceedings of the 9th International Conference on Optics, Photonics and Lasers (OPAL' 2026)

Edited by Sergey Y. Yurish

IFSA

2026 OPAL

Optics, Photonics and Lasers

Proceedings of the 9th International Conference on Optics, Photonics and Lasers (OPAL' 2026)

20-22 May 2026,

Ibiza (Balearic Islands), Spain

Edited by Sergey Y. Yurish

IFSA Publishing

Sergey Y. Yurish, *Editor*
Optics, Photonics and Lasers
OPAL' 2026 Conference Proceedings

E-mail (for orders and customer service enquires): ifsa.books@sensorsportal.com

Visit our Home Page on http://www.sensorsportal.com

ISBN: 978-84-09-86144-6
BN-20260512-XX
BIC: TTB

Contents

Foreword

It is my great pleasure to introduce the Proceedings of the *9th International Conference on Optics, Photonics and Lasers (OPAL' 2026)*, held on 20–22 May 2026 in Ibiza, Balearic Islands, Spain.

OPAL has always been conceived as an international forum where fundamental advances in optics and photonics meet practical engineering, emerging applications, and future-oriented technological visions. The 2026 edition continues this tradition by bringing together researchers, engineers, academics, industry specialists, and young scientists working across a broad and rapidly evolving field. The contributions collected in these proceedings reflect both the maturity of optical science and its remarkable ability to generate new directions in communication, sensing, imaging, quantum technologies, laser engineering, materials processing, biomedical instrumentation, and space-related applications. Each paper has been rigorously peer-reviewed and selected for its originality, scientific merit, and potential impact.

The papers included in this volume demonstrate the wide scientific scope of OPAL' 2026. They range from high-repetition-rate and high-average-power femtosecond laser systems, nonlinear frequency conversion, chirped pulse amplification, and self-compression techniques, to silicon nonlinear optics, integrated photonic devices, and wavelength-selective structures for modern data transmission and sensing. Considerable attention is also given to optical and photonic sensing, including fiber Bragg gratings, plasmonic and SERS-based sensors, distributed fiber-optic sensing, THz polarimetry, and advanced methods for simultaneous measurement of physical parameters in complex environments.

Another important part of the programme is devoted to holography, light-field microscopy, 3D visualization, optical triggering systems, camera–projector calibration, and fringe projection profilometry. These works clearly show how optics and photonics continue to provide enabling tools for high-resolution imaging, computational visualization, high-speed optical systems, and precise measurement technologies. The proceedings also include contributions in quantum optics and quantum information, such as single-photon and multiphoton sources, non-Gaussianity, and entanglement-based quantum key distribution, confirming the increasing role of photonics in the development of secure and quantum-enabled technologies.

At the same time, OPAL' 2026 looks beyond established applications. Contributions addressing laser propulsion and the exploration of Proxima Centauri b, passive daytime radiative cooling metamaterials, femtosecond-laser-based replication of microstructures, and light–matter interaction at the limits of classical models remind us that optics and photonics are not only tools for incremental improvement, but also engines of scientific imagination and long-term technological progress.

I would like to express my sincere gratitude to all authors for their valuable scientific contributions and for sharing their latest results with the OPAL community. I also warmly thank the members of the International Programme Committee, reviewers, session chairs, invited speakers, and all colleagues who contributed their time and expertise to the preparation of the conference and these proceedings. Their efforts are essential for maintaining the scientific quality, international character, and professional atmosphere of OPAL.

Special thanks are due to the organizing team and IFSA Publishing for their continuous support in preparing this volume and ensuring the successful realization of the conference. I am also grateful to all participants for their active involvement, discussions, and exchange of ideas, which are the true foundation of any successful scientific meeting.

I hope that these proceedings will serve not only as a record of OPAL' 2026, but also as a useful reference and source of inspiration for further research, cooperation, and innovation in optics, photonics, and laser technologies.

Prof., Dr. Sergey Y. Yurish
OPAL' 2026 Chairman

(001)

A Versatile High Repetition Rate and High Average Power Laser Source Based on Rod-Type Yb-Doped Fiber Amplifier and Efficient Nonlinear Frequency Conversion

Julius Vengelis [1], J. Pimpė [1,2], S. Armalytė [1], J. Banys [1], V. Jarutis [1] and A. Dubietis [1]
[1] Vilnius University Laser Research Center, Saulėtekio Ave. 10, Vilnius, LT-10223, Lithuania
[2] Light Conversion Ltd., Keramikų str. 2B, Vilnius, LT-10223, Lithuania
Tel.: +370 6 2377017
E-mail: julius.vengelis@ff.vu.lt

Summary: We present high repetition rate (76 MHz) and high average power (72 W) femtosecond laser amplification system based on Yb-doped rod-type large mode area photonic crystal fiber that uses pre-chirp managed amplification (PCMA) and fiber chirped pulse amplification (FCPA) techniques. A combined experimental and numerical study reveals the physical origin of incompressible chirp regions in hybrid Yb-fiber amplifiers, providing practical guidelines for achieving high quality pulse compression in high average power regime. The designed laser amplifier system delivers transform-limited 114 fs pulses with excellent beam quality and long-term stability, establishing a robust driver for subsequent frequency conversion based on generation of laser harmonics and optical parametric amplification. Building on this foundation, we demonstrate efficient generation of second (41 W at 515 nm), third (17 W at 343 nm) and fourth (>4 W at 257 nm) harmonics, as well as second harmonic pumped and bulk supercontinuum seeded optical parametric amplifier producing up to 11 W of broadly tunable femtosecond output from the visible to SWIR. Altogether these results establish a versatile high repetition rate and high average power femtosecond laser platform for advanced spectroscopy, nonlinear microscopy, ultrafast nonlinear optics and photonics applications.

Keywords: Rod-type fiber amplifier, High average power femtosecond pulses, High repetition rate femtosecond pulses, Optical parametric amplifier, Bulk supercontinuum, Harmonic modules.

1. Introduction

High average power and high repetition rate ultrafast UV laser systems find numerous applications in diverse fields: time resolved spectroscopy [1], laser material processing [2] and photonics [3], to mention a few. Fiber-based architectures are especially attractive due to excellent heat removal, compactness and alignment robustness. However, direct laser pulse amplification in fiber-based systems can lead to laser-induced damage and complex pulse distortions due to interaction between material dispersion, gain and nonlinear effects. Therefore, during amplification it is essential to properly control nonlinear effects. In particular, even when average power scales up, the amplified pulse may become difficult to compress close to the transform-limited duration if the spectral phase develops strong modulations.

A straightforward route to extend emission wavelengths of the state-of-the-art ultrafast near-infrared (NIR) lasers into the visible, ultraviolet (UV) and deep ultraviolet (DUV) spectral regions, relies on frequency up-conversion processes, such as second (SH), third (TH), and fourth (FH) harmonics generation in nonlinear crystals with second-order nonlinearity, where borate crystals: BBO, LBO, BIBO and CLBO serve as main nonlinear materials for this purpose [4]. Furthermore, frequency down-conversion processes such as optical parametric generation (OPG) and optical parametric amplification (OPA) provide a way to achieve continuously tunable output radiation. Efficient frequency conversion in the femtosecond regime requires proper account for spatial and temporal walk-off, as well as for two-photon absorption, which is particularly strong in the DUV spectral range. Moreover, at high pulse repetition rates, due to relatively poor thermal conductivity of nonlinear crystals, absorption of laser radiation gives rise to thermal effects, resulting in temperature gradient-induced phase mismatch, which limits conversion efficiency, and thermal lensing as well as heat-induced birefringence, which deteriorate the output beam profile. It has to be noted that under such operating conditions, even small intrinsic linear absorption of fundamental and SH radiation produces a non-negligible heating effect [5]. Eventually, evolution of dynamic defects under intense UV exposure and quality of anti-reflection coatings have impact on laser-induced damage threshold of the nonlinear crystal and the overall long-term performance characteristics [6]. The advent of Yb-doped rod-type amplifiers [7] significantly advanced the development of high repetition rate and high average power femtosecond laser systems, which hold a great, but yet very poorly explored potential for the generation of femtosecond NIR, visible, UV and DUV pulses with multi-watt average powers.

In this work we present a versatile ultrafast platform based on a hybrid pre-chirp managed amplification (PCMA) fiber chirped-pulse amplification (FCPA) setup in a polarization-maintaining rod-type Yb-doped large-mode-area

photonic crystal fiber. Building on this femtosecond laser system, we further demonstrate efficient nonlinear frequency up-conversion including CLBO for improved DUV scaling. Finally, we demonstrate a second harmonic pumped, bulk supercontinuum seeded two-stage LBO OPA delivering up to 11 W total average power and broad tuning from the visible to the SWIR (675 nm - 2.2 μm) at 76 MHz.

2. Methods and Setup

The seed source for the PCMA-FCPA laser system was a commercial Kerr lens mode-locked 6 W, 76 MHz Yb:KGW oscillator (FLINT, Light Conversion) that emitted slightly chirped pulses of 112 fs duration (compressible down to 98 fs) with a central wavelength of 1028 nm and 15.5 nm spectral bandwidth (FWHM). The oscillator pulses were temporally stretched in a four-pass stretcher based on a transmission diffraction grating G1 (800 lines/mm, the first-order diffraction efficiency of 97%, Wasatch Photonics). The group delay dispersion (GDD) was varied from 0.024 to 2.47 ps^2, which yielded the stretched seed pulse duration adjustable in the range of 600 fs – 60 ps. The laser amplification was performed in an 80.4 cm length Yb-doped polarization-maintaining double-clad rod-type LMA PCF (aeroGAIN-ROD-PM85, NKT Photonics) with core and cladding diameters of 85 μm and 260 μm ± 15 μm, respectively. Both fiber ends were protected by anti-reflection coated end caps, and thermal management was ensured with water cooled casing. The amplifier pump source was a continuous wave laser diode (e24i, nLIGHT), which provided a total output power of 140 W and a central wavelength at 976 nm. LMA PCF featured an exceptional power handling with a 3300 μm^2 area and mode field diameter of 65 μm ± 5 μm and high pump absorption of >15 dB over the entire fiber length. The amplified output beam was then directed to a double-pass compressor. The pulse compressor consisted of a pair of transmission diffraction gratings, whose characteristics were identical to those of the transmission grating used in the pulse stretcher, ensuring accurate compensation of group delay dispersion up to the third-order.

To generate the second harmonic (SH) signal, a 2 mm thick BBO crystal cut for type-I phase matching ($\phi = 90°$, $\theta = 23°$) was used. Both crystal faces were AR-coated for 1030 nm and 515 nm wavelengths to minimize reflection losses. To improve the SH beam quality, a walk-off compensation scheme was employed by replacing the monolithic 2 mm BBO crystal with two 1 mm thick BBO crystals, oriented with opposite c-axes. The extraordinary-polarized SH beam generated in the first crystal experiences spatial walk-off from the fundamental beam, which is compensated in the second crystal due to the reversed walk-off direction, thereby preserving excellent beam quality.

For third-harmonic (TH) generation, a sum-frequency mixing process was implemented in a 1.1 mm thick BBO crystal cut for type-I phase matching ($\phi = 90°$, $\theta = 32°$). The crystal input face was AR-coated for fundamental (1030 nm) and SH (515 nm) wavelengths, while the output face was AR-coated for the TH (343 nm) radiation. Fourth harmonic (FH) generation was investigated in two nonlinear borate crystals: β-BaB_2O_4 (BBO) and $CsLiB_6O_{10}$ (CLBO). The BBO crystal was 0.7 mm thick and cut for type-I phase matching ($\phi = 90°$, $\theta = 50°$), while the CLBO crystal was 2 mm thick with a type-I cut of $\phi = 90°$ and $\theta = 65°$. Both crystals had input faces AR-coated for the SH wavelength (515 nm) and output faces AR-coated for the FH wavelength (257 nm).

An 85:15 beamsplitter at the PCMA-FCPA laser system output was used to organize the seed generation and OPA pump channels. A smaller fraction of the laser output (~10 W) was used for the seed generation: bulk supercontinuum generated in 10 mm thick potassium gadolinium tungstate (KGW) crystal. A short-pass filter F with high transmission in the 600–900 nm wavelength range was used to filter out long-wavelength components of the supercontinuum and suppress the intense spectral part around the pump wavelength. The major fraction of the laser output was used to produce SH which served as pump for the OPA. Our OPA consisted of two stages. At the first OPA stage seed and pump beams were focused with a lens into 3.7 mm thick, AR-coated LBO crystal cut for type I phase matching ($\phi = 13°$, $\theta = 90°$). With the estimated pump beam diameter of 60 μm (at the $1/e^2$ intensity level) and pump pulse peak intensity of ~200 GW/cm^2, the first OPA stage produced a signal wave with an average power of 100 mW – 2 W, depending on the wavelength. The remaining portion of the SH radiation (22 W) after first OPA stage was used as a pump for the second OPA stage which employed an identical LBO crystal. The dichroic mirror DM3 in the signal propagation path was used to remove the idler wave. With an estimated pump pulse peak intensity of ~150 – 200 GW/cm^2, OPA2 was driven into saturation within most of the tuning range. In both OPA stages LBO crystals were mounted on water-cooled copper-based optical mounts. The positively chirped signal pulses were compressed using a prism compressor consisting of two N-SF11 prisms, while the negatively chirped idler pulses were compressed during the propagation in zinc selenide (ZnSe) plates.

3. Key Results

The built PCMA-FCPA system operates at 76 MHz and delivers nearly transform-limited 114 fs pulses with 72 W average power (82 W before compression), excellent beam quality ($M^2 < 1.1$) and power stability (0.16% RMS power fluctuations over 70 hours). Beyond performance metrics, in a combined experimental and numerical analysis we reveal the physical origin of “incompressible” chirp regions in such hybrid amplifiers, providing practical guidelines

for selecting the seed pre-chirp to ensure high-quality pulse compression at high average power. We further demonstrated efficient nonlinear frequency up-conversion: tens of watts SH and TH generation output (41 W at 515 nm and 17.7 W at 343 nm) and >4 W FH generation around 257 nm using borate crystals, including CLBO for improved DUV scaling. The two-stage OPA delivers up to 11 W nearly transform-limited sub-70 fs signal and sub-100 fs idler pulses (measured using SH frequency-resolved optical gating, i.e., FROG, technique) across the entire tuning range. As a proof, the positively chirped signal pulses at 800 nm were compressed down to 62 fs using prism pair compressor, while the negatively chirped idler pulses at 1.45 μm were compressed to 92 fs by the propagation in normally dispersive bulk material.

It is important to note that all stages of our femtosecond laser system demonstrate very good power stability (Fig. 1) making them practical laser radiation sources for the aforementioned applications.

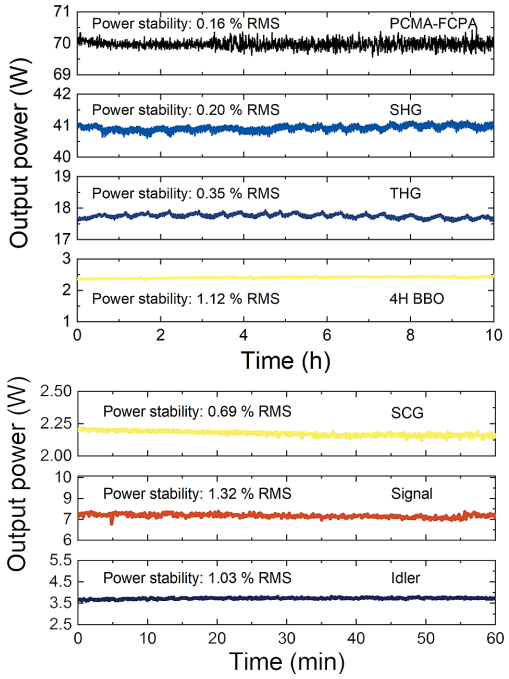

Fig. 1. Power stability of PCMA-FCPA amplifier, SH, TH and FH generation stages measured over 10 hours of continuous operation; supercontinuum generation (SCG) stage and OPA signal (at 800 nm) and idler (at 1450 nm) waves, measured over 1 hour of continuous operation. SCG average power was scaled by a factor of 100 for visualization purposes.

4. Conclusions

The reported research establishes a practical, high-performance blueprint for scaling femtosecond sources at tens of MHz repetition rates to the >70 W average power level and efficient frequency conversion stages while preserving spectral, temporal and spatial quality along with long-term stability: key characteristics for advanced applications, such as high-speed imaging, nonlinear spectroscopy, precision metrology, and laser-based nanofabrication. Beyond demonstrating record average power levels at 76 MHz repetition rate, the presented hybrid PCMA–FCPA architecture is accompanied by a clear experimentally validated understanding of pulse compressibility features: the identification of an “incompressible” pre-chirp region links performance limitations directly to spectral modulations that cannot be removed by a standard pulse compressor. This provides important insight into design of such laser systems, improving reproducibility as well as accelerating further power and bandwidth scaling.

Acknowledgements

J.V., J.P., S.A., J.B. and V.J. acknowledge funding from the Research Council of Lithuania (LMTLT), grant S-MIP-23–23.

A.D. acknowledges the “Universities’ Excellence Initiative” programme by the Ministry of Education, Science and Sports of the Republic of Lithuania under the agreement with the Research Council of Lithuania (project No.S-A-UEI-23–6).

References

[1]. T. Kobayashi, A. Yabushita, Y. Kida, Development of sub 10 fs visible-NIR, UV, and DUV pulses and their applications to ultrafast spectroscopy, *Photonics*, Vol. 3, Issue 4, 2016, 64.

[2]. M. Maiuri, M. Garavelli, G. Cerullo, Ultrafast spectroscopy: State of the art and open challenges, *Journal of the American Chemical Society*, Vol. 142, Issue 1, 2020, pp. 3-15.

[3]. J. Klein-Wiele, J. Bekesi, P. Simon, Sub-micron patterning of solid materials with ultraviolet femtosecond pulses, *Applied Physics A*, Vol. 79, Issue 4-6, 2004, pp. 775-778.

[4]. Z. Ma, Q. Hao, Y. Han, S. Pan, Ultraviolet nonlinear frequency conversion of solid-state lasers in 200-400 nm spectral region, *Laser & Photonics Reviews*, Vol. 20, 2026, e01629.

[5]. R. Riedel, J. Rothhardt, K. Beil, B. Gronloh, et al., Thermal properties of borate crystals for high power optical parametric chirped-pulse amplification, *Optics Express*, Vol. 22, Issue 15, 2014, pp. 17607-17619.

[6]. H. Turcicova, O. Novak, J. Muzik, D. Stepankova, et al., Laser induced damage threshold (LIDT) of β-barium borate (BBO) and cesium lithium borate (CLBO) – Overview, *Optics and Laser Technology*, Vol. 149, 2022, 107876.

[7]. W. Liu, D. N. Schimpf, T. Eidam, J. Limpert, et al., Pre-chirp managed nonlinear amplification in fibers delivering 100 W, 60 fs pulses, *Optics Letters*, Vol. 40, Issue 2, 2015, pp. 151-154.

(003)

Silicon Nonlinear Optics and Photonics

H. J. Eichler [1], B. Szyszka [2] and O. Lux [3]
[1] Technische Universität Berlin, Institut für Physik und Astronomie, 10623 Berlin, Germany
[2] Technische Universität Berlin, Institut für Hochfrequenz- und Halbleiter-Systemtechnologien, 10587 Berlin, Germany
[3] Deutsches Zentrum für Luft- und Raumfahrt, Institut für Physik der Atmosphäre, 82234 Oberpfaffenhofen, Germany
Tel.: + 49 30 314 27382
E-mail: bernd.szyszka@tu-berlin.de

Summary: Silicon Photonics denotes optical systems built analog to electronic transistor circuits. Photons or light beams are propagating by waveguides often etched into thin Silicon CMOS layers as photonic crystals. Their effective refractive index is controlled by nanosized holes which allows linear and curved waveguiding. Strong optical pumping leads to stimulated Raman scattering and high gain amplification or even Raman laser action. Applying electrical fields or injecting electrical currents perpendicular to photonic waveguides results in electrooptic effects allowing effective amplitude or phase modulation of light coupled into the waveguides. Light coupled out may be detected by standard photoelectric devices placed on the photonic Silicon chip. Electronic circuits for generation and detection of photonic signals can be integrated into the same chip. Thus, photonic devices are used as transmitters and receivers or combined transceivers in glass fiber communication systems. Silicon photonic chips are expected to meet the increasing data and bandwidth demands of the worldwide internet.

Longitudinally structured photonic waveguides serve as optical filters. Numerous applications like autonomous driving and medical sensing are investigated for further massive deployment.

The talk will outline basic research results obtained in the former Optical Institute of the Technische Universität Berlin.

Keywords: NLO of silicon, Raman laser, Electro-optic effect, Electron hole pairs, Silicon Photonics (SiPho), Wave guide, Filter, Modulator, Photodiode, CMOS platform, Glass fiber, Data processing and transfer, Sensing, Quantum computing.

1. Introduction

Silicon Photonics denotes optical systems built analog to electronic transistor circuits. Photonic devices for light generation, amplification, modulation, switching, deflection, processing and detection of light can be constructed on a CMOS platform [1, 2]. Thus, silicon photonic chips are expected to meet the increasing data and bandwidth demands of a worldwide internet [3]. Numerous applications like fiberoptic communications, autonomous driving and medical sensing [4] are investigated for further massive deployment. Due to the CMOS compatibility, integration of optical and electrical signal processing on one single platform enables ultra-high data rate transmission for data centers, or even on-chip communication.

2. Silicon Nonlinear Optics (NLO)

In Berlin, we started to investigate nonlinear optical effects in bulk Silicon (see Fig. 1) and then designed and characterized integrated photonic waveguide structures produced in the CMOS fab IHP in Frankfurt/Oder (Germany). The effective confinement of optical waves in Silicon nano-waveguides leads to nonlinear four-wave mixing and Stimulated Raman Scattering (SRS) based on interaction between light and lattice vibrations [5, 6]. SRS is useful for light amplification and frequency shifting, generating integrated frequency combs.

Further strong nonlinear optical effects in Silicon are due to generation of electron hole pairs changing the absorption and refraction of the material. These effects have been first investigated in bulk Silicon leading to defocusing, grating formation and picosecond pulse amplification [7]. Later, electrical carrier injection into pn-junctions was used to construct fast electrooptic modulators for optical data transmission.

3. Silicon Photonics: Optical Waveguides

Important applications of Silicon Photonic (SiPho) devices are expected for data transmission by glass fibers [8]. For this purpose, a laser beam with a standard wavelength of 1.3 µm is coupled into a Silicon wave guide which has high transmission at this wavelength [9]. A section of the waveguide works as electrooptic modulator encoding the data on the laser beam. The waveguide with the modulator section is integrated with the electronic driver circuit into a tiny Silicon chip and is denoted as transmitter [10, 11]. The modulated laser beam is coupled into the glass fiber which guides the data stream over large distances.

At the fiber endface the data stream is detected by a photoelectric device denoted as receiver. For bi-directional use of a fiber the transmitter and receiver are combined into a single photonic device, the transceiver. Optical waveguides for construction of transceivers and other Silicon Photonic devices are shown in Fig. 2.

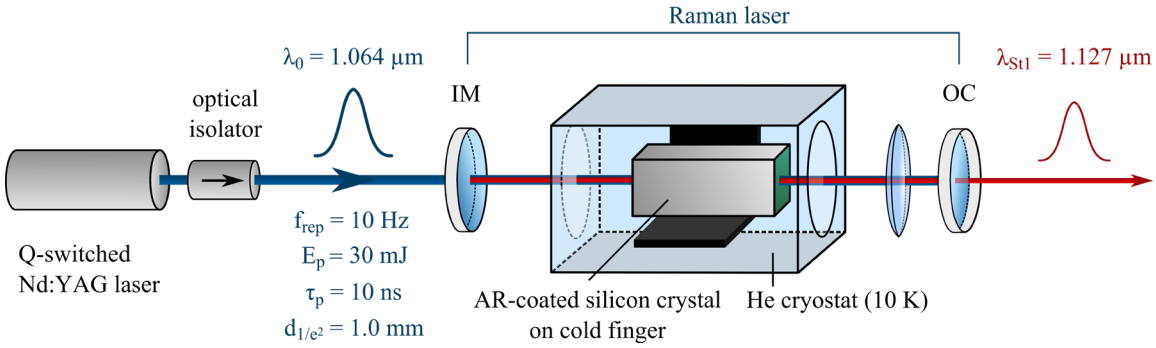

Fig. 1. Experimental setup of a bulk Silicon Raman laser for wavelength conversion from 1.064 to 1.127 µm. The cross section of the Silicon crystal is about 1cm x 1cm (Figure taken from [5]).

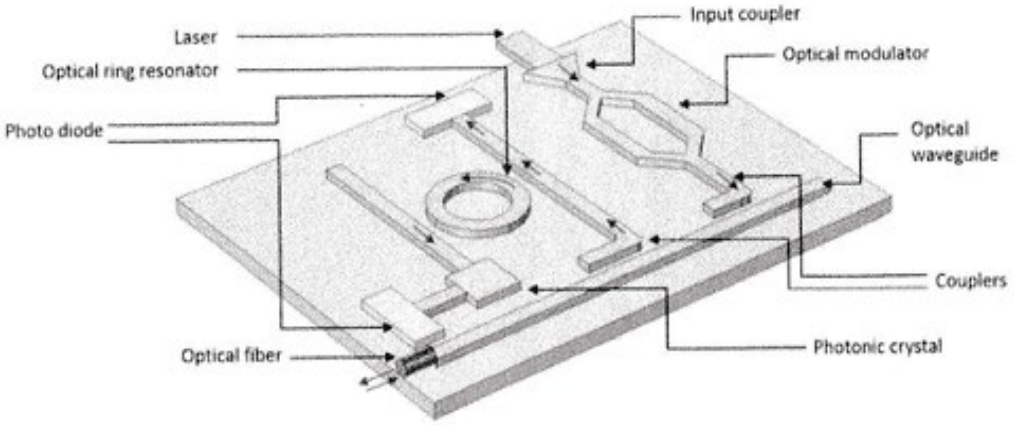

Fig. 2. Waveguides are etched into e.g., 200 nm Silicon layers on oxidized CMOS Silicon chips covered by a structured mask. Rectangular Silicon Photonic waveguides may have a cross section of 200 × 500 nm. Mostly linear waveguides are shown. Light is coupled into waveguide by focusing the divergent beam of an optical fiber onto the endface of the waveguide. A circular waveguide may serve as an Optical ring resonator. Light is fed into the ring by the evanescent wave from a linear fiber. Source: COMSOL Software.

Glass fibers for data transmission are mainly operated at 1.3 and 1.6 µm. Therefore, many SiPho developments are done at these wavelengths. Laser diodes are available but their implementation to Silicon wafers is demanding. It is desirable to have Silicon light sources instead [12, 13]. The weak electroluminescence of Silicon can be enhanced and shifted using Silicon quantum dots. Laser action has been demonstrated by optical pumping with a fs-Laser. Electrical excitation of diodes at the desired wavelength has still to be demonstrated.

4. Silicon Photonics: Wavelength Filters

The wavelength filter shown in Fig. 3 is produced by etching holes with diameter *a* into a linear waveguide. This changes the effective refractive index of the wave guide in the hole region. The structure behaves like an interference filter or Fabry Perot resonator with high transmission if the length *l* is equal to the half wavelength of the light propagating through the waveguide, see Fig. 4. The total filter length amounts to only 1 µm.

Fig. 2 shows a Mach Zehnder Interferometer which is also used for optical modulators. This Interferometer can also act as wavelength filter.

In Fig. 4, the ratio between a peak wavelength at special cavity length corresponds to the effective refractive index of the waveguide. This index is mainly given by the high refractive index of Silicon.

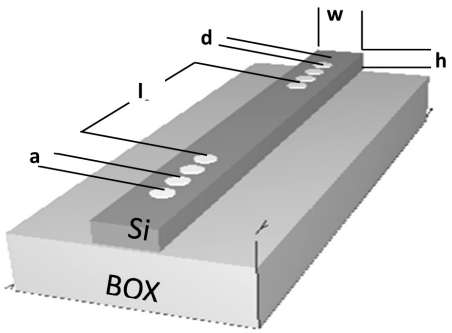

Fig. 3. Fabry Perot wavelength or light frequency filter. The Silicon wave guide was fabricated on a buried oxide or BOX layer on a Silicon chip.

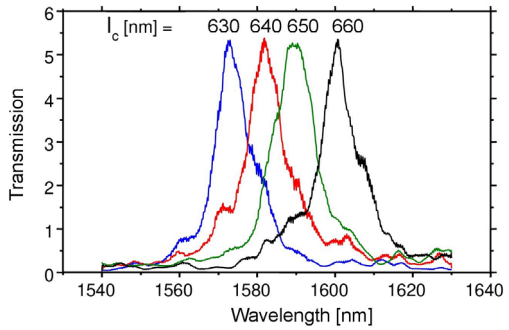

Fig. 4. Spectra (Transmission in arbitrary units) of the FP wavelength filter shown in Fig.3.

5. Silicon Photonics: Optical Modulator

A Fabry Perot Filter can be tuned by injecting electron hole pairs into the cavity region *I* of the waveguide. This changes the refraction of Silicon effectively, as has been indicated already in bulk Silicon, see Section 2 above. Thus, instead of optical carrier excitation, electrical carrier injection into pn-junctions was used to construct fast electrooptic modulators integrated into transceivers for optical data transmission and other photonic devices.

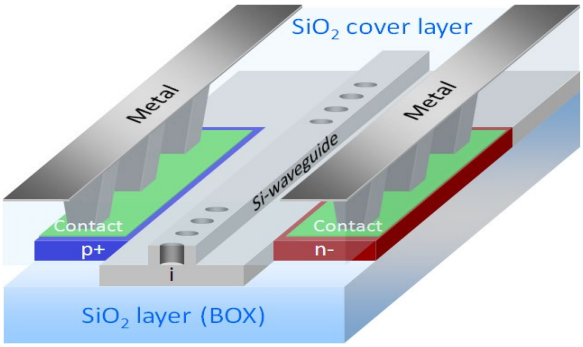

Fig. 5. Principal setup of an optical modulator. Electrons and holes are injected into a waveguide placed into a pin junction. The refractive index is modulated by applying an electrical dc or ac voltage.

6. Silicon Photonics: International Projects

Richard A. Soref is considered to pioneer Silicon Photonics in the USA. He published his first paper entitled "Single-crystal silicon: a new material for 1.3 and 1.5 µm" in *Electronics Letters 1985.* Since then, US companies dominated the further development of SiPho, e.g.:

- Cisco Systems, San Jose, California;
- Hamamatsu Photonics Japan;
- IBM Corporation USA;
- Intel Corporation, Santa Barbara, California;
- STMicroelectronics, Switzerland worldwide.

The spin-off company *Sicoya* in Berlin started in 2007 to investigate and produce transceiver devices. This company is part of the current project *Starlight* sponsored by the European Union EU which intends to develop the mass production of Si-photonic devices on 30 cm wafers.

Rather large activities on Silicon Photonics are ongoing also in Spain and England.

The international company NVIDIA invested into the pioneering Laser Companies Coherent and Lumentum (former Spectra Physics) for R&D on Silicon Photonics for large data centers.

The journals Laser Focus and ElectroOptics report regularly on these activities.

7. Conclusions

Silicon photonics (SiPho) uses light (photons) instead of just electricity (electrons) to process data for compact communication and sensing systems. It combines optical waveguides, modulators, filters and detectors on a silicon substrate and can be integrated together with electronic components. SiPho devices as transceivers in glass fiber networks help to overcome bandwidth limitations of copper wires for applications in data centers, telecommunications, sensors, and quantum computing, offering high speed and low power. Cost-effective mass production is possible by established semiconductor manufacturing platforms like Complementary Metal Oxide Semiconductor (CMOS) techniques.

Acknowledgements

Thanks are due to: Dr. Christoph Theiss from Sicoya GmbH for explaining the structure and goals of the STARLIGHT project, Prof. Jürgen Eichler from the Academy for Laser Safety in Berlin, Prof. Sigurd Schrader from Technical University of Applied Sciences Wildau for fruitful cooperation on Silicon Photonics.

References

[1]. S. Meister, H. J. Eichler, Photonic integrated circuits for optical communication, *Optik & Photonik*, Vol. 7, Issue 2, 2012, pp. 59-62.

[2]. S. Meister, A. Al-Saadi, B. A. Franke, S. Mahdi, et al., Photonic crystal microcavities in SOI waveguides produced in a CMOS environment, *Proceedings of SPIE*, Vol. 7606, 2010, 760616.

[3]. A. Al-Saadi, H. J. Eichler, S. Meister, High speed silicon electro-optic modulator with p-i-n comb diode, *Optical and Quantum Electronics*, Vol. 44, Issue 3-5, 2012, pp. 125-131.

[4]. H. J. Eichler, B. Liu, M. Kayser, S. I. Khomenko, Er:YAG-laser at 2.94 µm Q-switched by a FTIR-shutter with silicon output coupler and polarizer, *Optical Materials*, Vol. 5, Issue 4, 1996, pp. 259-265.

[5]. O. Lux, H. Rhee, V. Lisinetskii, H. J. Eichler, Stimulated Raman scattering and Raman laser operation in silicon single crystals at low temperatures,

Laser Physics Letters, Vol. 9, Issue 12, 2012, pp. 858-867.

[6]. H. Rhee, O. Lux, S. Meister, U. Woggon, et al., Operation of a Raman laser in bulk silicon, *Optics Letters*, Vol. 36, Issue 9, 2011, pp. 1644-1646.

[7]. H. J. Eichler, F. Massmann, Diffraction efficiency and decay times of free-carrier gratings in silicon, *Journal of Applied Physics*, Vol. 53, Issue 4, 1982, pp. 3237-3242.

[8]. S. Meister, H. J. Eichler, A. Al Sadi, Optical modulator, Patent US9195112B2, *United States*, 2015.

[9]. S. Mahdi, M. Grehn, A. Al-Saadi, M. Höfner, et al., Facet preparation of silicon nano-waveguides by cleaving the SOI chip, *Journal of Nonlinear Optical Physics & Materials*, Vol. 20, Issue 4, 2011, pp. 509-523.

[10]. S. Meister, H. Rhee, A. Al-Saadi, B. A. Franke, et al., Matching p-i-n-junctions and optical modes enables fast and ultra-small silicon modulators, *Optics Express*, Vol. 21, Issue 13, 2013, pp. 16210-16221.

[11]. S. Meister, H. Rhee, A. Al-Saadi, B. A. Franke, et al., High-speed Fabry-Pérot optical modulator in silicon with 3-µm diode, *Journal of Lightwave Technology*, Vol. 33, Issue 4, 2015, pp. 878-881.

[12]. D. C. Wang, C. Zhang, P. Zeng, W. J. Zhou, et al., An all-silicon laser based on silicon nanocrystals with high optical gains, *Science Bulletin*, Vol. 63, Issue 2, 2018, pp. 75-77.

[13]. S. M. A. Hosseini-Saber, R. Muydinov, N. Ahmadi, J. Ibaceta-Jaña, et al., Photoluminescence and stability of sputtered SiOx layers, *Physica Status Solidi A*, Vol. 218, Issue 20, 2021, 2100277.

[14]. F. Maier-Flaig, J. Rinck, M. Stephan, T. Bocksrocker, et al., Multicolor silicon light-emitting diodes (SiLEDs), *Nano Letters*, Vol. 13, Issue 2, 2013, pp. 475-480.

Biographies

Professor Hans Eichler completed his PhD at Technische Universität Berlin. He continued to do research on nonlinear optics and published together with expert coauthors the books Laser Induced Dynamic Gratings and Lasers, Basics Advances Applications, Vol. 50 and 220 of Springer Series in Optical Sciences. He started investigations on nonlinear optics of bulk Silicon at 1980 in Bell Labs USA and continued to develop integrated CMOS structures with students and coworkers in Berlin. Until 2013 he served as CTO and CEO of the research company Laser Medicine and Technology Berlin LMTB GmbH.

Professor Bernd Szyszka completed his PhD at Justus Liebig Universität Giessen. His research addressed materials and process technologies for optoelectronic thin film devices at the Fraunhofer Institute for Surface Engineering and Thin Films. Since 2012, he holds the chair thin film devices at Technische Universität Berlin.

Dr. Oliver Lux received his PhD from Technische Universität Berlin in 2013. His research focuses on laser physics and nonlinear optics for lidar applications. Since 2016, he has been affiliated with the German Aerospace Center, where he operates airborne lidar systems and supports the European Space Agency’s Doppler wind lidar space mission Aeolus and its follow-on mission, Aeolus-2.

(004)

Exploring Proxima Centauri b

C. Phipps
Photonic Associates, LLC, 1556 Escondida Ct., Santa Fe NM 875007, USA
Tel.: + 01 2153584360
E-mail: crphipps@aol.com

Summary: In papers published in 2024 and 2025, we discussed travel at significant fractions of the speed of light. Now that Breakthrough Statshot is dead or dying, it makes sense to reconsider what can reasonably still be done. We conclude that an instrument flight to Prox.Centauri b makes the best sense. The purpose of this paper is to revive the production of MW class CW lasers required for space exploration.

Keywords: Photon pressure propulsion, Proxima Centauri b

1. Summary

Although the Breakthrough Starshot project has been suspended for lack of funds, a project using photon pressure propulsion can be used to explore our nearest planet, Prox. Centauri b, which orbits a red dwarf. This exploration might be worthwhile, compared to setting up life on Mars, on which a station would need to be placed in a plastic bubble to maintain liveable aie pressure.

In this article, we consider a manned mission to explore the planet, assuming a preliminary unmanned mission has been conducted. Prox. Centauri b is almost the same size as Earth, and has a relatively comfortable temperature. Rather than depending on a previously placed slowing laser, we assume a loop using interstellar magnetics fields to slow the craft during the last half of its voyage, which dumps its kinetic energy by powering a large laser [see ref. 3, Fig. 5]. A novel slowing mechanism is introduced. What is new here: a PPP flight with a specific mission: to see if Proxima Centauri b shows signs of advanced life or not. It is a one-way flight. Whether Prox. Centauri b is inhabited ot not is not possible to determine from Earth, because of the distance involved. The spectra of cities lit by artificial light will be too weak to distinguish from the scattered light of Pox. Centauri. We will show relative costs of manned and unmanned flights at 47nm vs. 1060 nm wavelength.

It is a one-way flight because cost of advance placement of a slowiug laser in the neighborhood would be too large, and no gravitational object exists around whieh the probe might orbit, to return to Earth.

2. Introduction

Prox. Centauri is a red dwarf star 4.24 light years distant, one of three stars in the Alpha Centauri system, and the same star that was to be explored by Breakthrough Starshot before it lost fumding. Although Proxima has plasma flares which were thought to be strong enough to strip planets of their atmosphere, in 2016 the ESO discovered the planet Proxima b, just a bit larger than Earth. Like other red dwarves, the lifetime of Prox. Centauri can be trillions of years, leaving plenty of time for life to develop if it can. Anoxygenic photosynthesis may be possible, as on early Earth.

The interesting thing is that the verdict for life on Prox. b could go either way: flares from Prox. Centauri can decimate the atmosphere of Prox. Centauri b, but flares can also spark life.

Here is an artist's conception, for what it is worth:

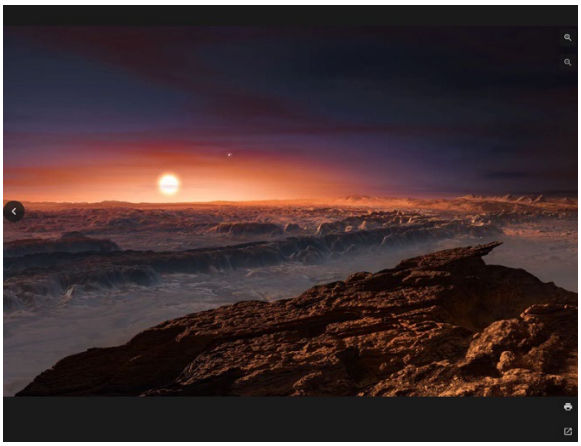

Fig. 1. Artist's conception of Prox. Centauri b (1).

This may not be a hospitable place, in particular because tidal locking has caused the same face of Prox. Centauri b to always face its star. Its year is 11 Earth days.

Yet, its temperature is probably -39C. It has a magnetic field and dramatic aurorae. [1-3]. It was discovered recently by ESO (August 24, 2016) [1] using Doppler spectroscopy of the wobbles of Prox. Centauri. It may be water-rich.

Anoxygenic photosynthesis (Fig. 2) will involve sulfur, and could lead to life on Prox. Centauri b. This process was present on the early Earth.

2.1. Modeling Manned Flight at 1060 nm and UV Wavelength

As in [3], the equations for the elapse of onboard time with travel distance are (including appropriate relativistic factors), the goal being just to reach Prox. Centauri b and explore are acceleration

$$\frac{d^2z}{dt^2} = \frac{2P}{m_o c D} \tag{1}$$

Here

$$D^2 = \frac{1+\beta}{1-\beta}, \tag{2}$$

with P received laser power, D the relativistic doppler factor of the lightsail relative to the laser, and β=v/c.

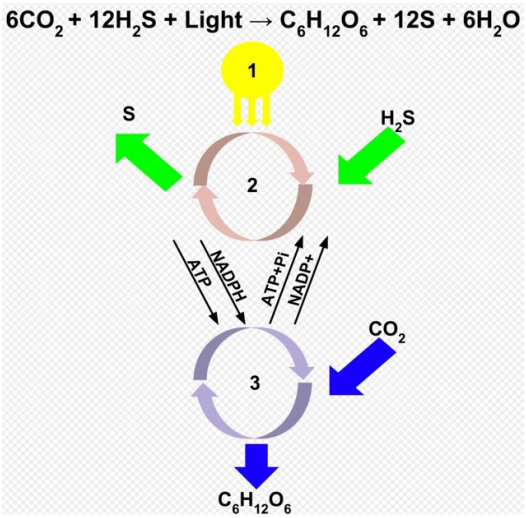

Fig. 2. Anoxygenic photosynthesis.

We do the calculations just by integrating Eq. (1) two times. The time and mass dilation parameter is

$$\gamma = \frac{1}{\sqrt{1-\beta^2}} \tag{3}$$

It's important to realize that the craft's kinetic energy is given by

$$KE = \gamma m_o c^2, \tag{4}$$

and that γ can be >>1. Beam waist is governed by

$$w^2(z) = w_o^2[1+(z/z_R)^2], \tag{5}$$

Rayleigh range

$$z_R = \pi w_o^2 / \lambda \tag{6}$$

is the distance over which at which intensity drops by a factor of two due to diffraction.

2.2. Costs

We base mission cost on the work of Parkin [5], and use total laser energy expended as the scaling factor. (Costs are extrapolated using total laser energy from Parkin, K., Ch. 03 of Laser Propusion in Space, Fundamentals, Technology and Future Missions. We consider UV and IR wavelegths to have the same cost. The UV laser will be an FEL). Previously, the laser sail mass has not been accurately calculated in all cases which have been reported. We assume its thickness is 0.5 μm.

The requirement for such powers dramatically increase the mission cost. Lasers of this power may have to wait for a fusion economy to exist.

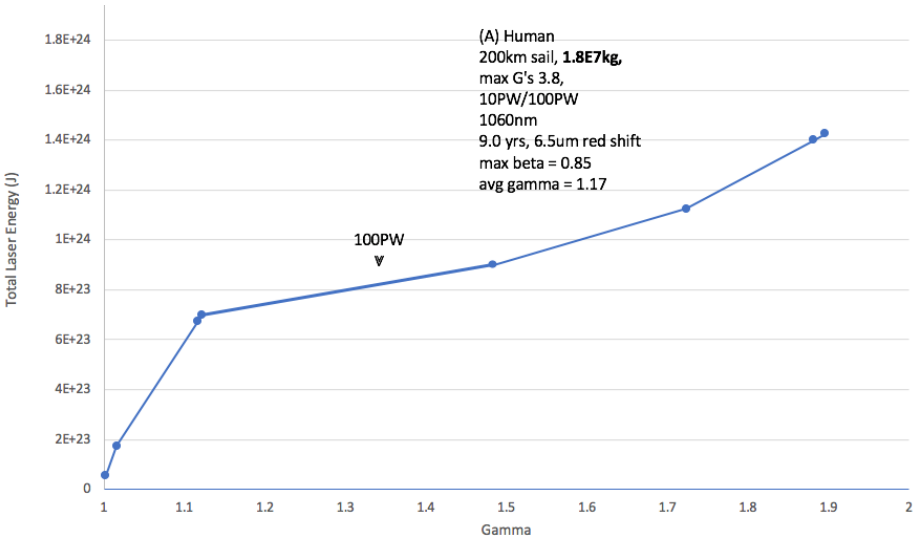

Fig. 3. Laser acceleration and magnetic field deceleration for a manned trip at 1060nm. Cost estimate: 3.2E4 T$. Compare Fig. 4 and note the 4 times larger sail mass in this case, because of the larger wavelength. The break at γ=1.7 corresponds to the transition from 10PW to 100PW at the laser station.

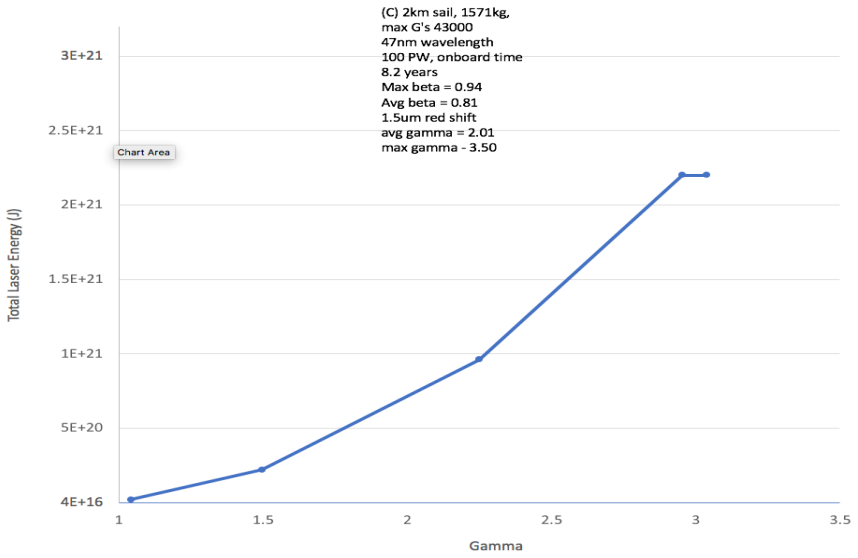

Fig. 4. The kinetic energy of the flier can be many times that of the hydrogen bomb, for which only 3% of the mass is converted to energy, because maximum $\gamma \sim 1$. See Eq. (3). Because of this, with average γ=0.96, onboard time is 4.20 yrs. The UV wavelength makes much smaller sails possible, because of Eq. (5).

2.3. Modeling Instrument Flight

We conclude that an instrument flight with a 2500m diameter sail weighing just 25,000 kg would be much more reasonable to do in the near future, because there are no constraints on acceleration, as is required for human flight, so cost can be lower. It will be necessary to create this sail within a fiber net to keep it from tearing. [4]

Deceleration is not based on a model because precise values of interstellar magnetic fields are not precisely defined. We assume B=800 pT as in ref. 3 (Fig. 5).

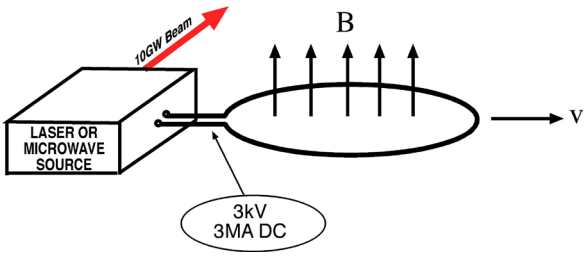

Fig. 5. Slowing in interstellear magnetic field. This device should provide 3kV at 3MA DC (3), dumped overboard to prevent heating the spacecraft.

2.4. Design Consequences

In order to obtain the reduction in payload implied by Fig. 4, it will be necessary to place the laser station in space (in orbit or on the Moon), because UV is rapidly absorbed in the atmosphere. The 47 nm laser will be a free electron laser. The precise wavelength is arbitrary because the laser is an FEL.

2.5. Benefits

Times listed in Figs. 3 and 4 and Table 1 are onboard times, so the crew will finish their trip having moved into the future. Their time dilation factor will have averaged 1.1 to 1.25 during their trip. Because of this, the people back home are, in fact, up to 2 years older than the crew. This is how you go into the future! However, the cost may make this option prohibitive.

Table 1. Comparison of Human and Instrument Flights.

Laser Wavelength	Human, 1060 nm	Human, 47 nm	Instrument, 47 nm
Total Energy	1.13e24	3.6e23	3.6E21
Laser Power	10, 100 PW	1, 10 PW	2 PW
Max Beta	0.81	0.59	0.59
Max G's	0.37	0.38	38
Sail Diameter, m	200000	100000	2500
Sail Mass, kg	1.8e7	4.5E6	2.5e4
Mission Cost (proportional to total laser energy	3.24T$	1.03T$	9.6B$
Mission Duration	7.1 years	22.8 years	1000 hrs. (onboard time)

2.6. Laser Development

It is clear that the laser technology implied in this paper remains to be developed. There hsve been many proposals for FEL oscillatotrs which would satisfy these requirements, but they have not yet been funded. Laser development needs to be emphasized soon.
A free-electron laser (FEL) is the perfect candidate for the high average power short wavelength laser discussed in this paper.

3. Questions That Will Be Answered by these Flights

Does advanced technical life exist in our immediate neighborhood? Do we need a manned probe? Is Prox. Centauri b lit up at night as our own planet is? What a discovery that would be! Unfortunately, at 4.2 light years distance, the planet is too far away to reliably show the presence of cities, when the whole planet is just a blur.

4. Conclusions

It is recsommended that devleopment of high average power PCSEL lasers at the kW level be initiated quickly for this application. Also, studies of topics suggested in this paper should be pursued.

It is recommended that plans be made very soon to launch small instrument packages using techniques outlined in this paper. Every effort should be made to develop and fund concepts for near Earth exploration using FEL arrays.

Only then will we gain a true appreciation of how critically important for the advancement of life that we have developed on Earth is.

Acknowledgments

I gratefully acknowledge conversations with K. Parkin of Parkin Research.

6. References

[1]. Proxima Centauri b, https://en.wikipedia.org/wiki/Proxima_Centauri_b
[2]. Anoxygenic photosynthesis, https://en.wikipedia.org/wiki/Anoxygenic_photosynthesis
[3]. C. R. Phipps, Parameters for photon pressure propulsion to relativistic speeds, in *Proceedings of the 8th International Conference on Optics, Photonics and Lasers (OPAL'25)*, 2025, pp. 7-11.
[4]. C. R. Phipps, Laser sails for photon pressure propulsion to relativistic speeds, in *Proceedings of the 9th Annual World Congress of Smart Materials (WCSM'25)*, 2025.
[5]. K. Parkin, Chapter 3, in Laser Propulsion in Space: Fundamentals, Technology, and Future Missions (C. Phipps, Ed.), *Elsevier*, 2024.

(006)

High-Quality 3D Visualization of Light Field Microscopy with 2D/3D Switchable Holographic Optical Element Micro Lens Array

K. C. Kwon [1], H. Y. Wu [1], N. Kim [1], S. H. Kim [2] and K. H. Yoo [2,*]
[1] School of Information and Communication Engineering, Chungbuk National University, 1 Chungdae-ro, Seowon-gu, Cheongju, Chungbuk 28644, South Korea
[2] Department of Software Engineering, Chungbuk National University, 1 Chungdae-ro, Seowon-gu, Cheongju, Chungbuk 28644, South Korea
[*] E-mail: khyoo@cbnu.ac.kr

Summary: This study presents a high-quality 3D visualization system for a light field microscopy (LFM) utilizing a peristrophically multiplexed holographic optical element – microlens array (HOE-MLA). The properties of the MLA and mirror are recorded orthogonally on a single HOE through peristrophic multiplexing. In the proposed system, Mode 1 (LF image) and Mode 2 (2D image) are sequentially acquired as the HOE-MLA rotates in synchronization with a trigger signal. This design enables the integrated acquisition of complementary depth and texture data, which are processed by a robust image-processing subsystem to generate natural-view 3D reconstructions. The proposed system is experimentally validated through a simplified optical configuration, demonstrating superior 3D visualization performance.

Keywords: Light field microscopy, Holographic optical element, Peristrophic multiplexing, 3D visualization.

1. Introduction

Light field (LF) imaging captures the 4D plenoptic function of a scene, recording both the intensity and direction of light rays via a microlens array [1]. This multifaceted data acquisition allows for the synthesis of novel views and post-capture refocusing. By decoupling the spatial and angular information, light field technology provides a robust framework for 3D perspective shifts and precise depth estimation, offering significant advantages over standard intensity-based cameras.

Light Field Microscopy (LFM) is a powerful imaging technique that applies the principles of plenoptic capture to the microscopic scale. It allows for instantaneous 3D imaging of fast-moving biological processes, such as neural activity or cardiac dynamics, which are difficult to capture using traditional point-scanning methods (like confocal microscopy) [2]. Despite these advantages, the practical application of LFM is hindered by several fundamental challenges. The most critical issue is the spatial-angular trade-off, where spatial resolution is inherently sacrificed to multiplex angular information onto the sensor.

Furthermore, LFM suffers from non-uniform axial resolution and reconstruction artifacts near the native focal plane, where angular diversity is minimal. Additionally, as imaging depth increases, optical scattering within thick biological tissues leads to signal degradation and loss of contrast [3].

Recent advancements have sought to address these limitations through wave-optics-based deconvolution and deep learning-assisted reconstruction [4]. However, achieving a balance between high spatial resolution and computational efficiency remains a key area of research.

In this study, we propose a method for high-quality 3D visualization of microscopic samples using LFM with a 2D/3D switchable holographic optical element – microlens array (HOE-MLA) to overcome the limitations of spatial resolution and image quality of existing LFM. The proposed system orthogonally records the characteristics of the MLA and mirrors onto a single HOE through peristrophic multiplexing [3]. The HOE-MLA, located at the mid-image plane of the LFM optics, rotates in response to a trigger signal, sequentially acquiring high-resolution 2D images and integral imaging (II) data containing 3D information. The acquired II data is then converted to LF format to generate a depth map. By fusing this depth information with texture data from the high-resolution 2D image, the system reconstructs a 3D model, enabling high-quality 3D visualization of the sample.

2. Light Field Microscopy Optics

Fig. 1 illustrates the peristrophically multiplexed HOE–MLA positioned at the intermediate image plane along the optical axis of the proposed LFM system.

In the recording scheme of the hologram, an interference pattern formed by the plane-wave reference beam (R) and signal beam (S) that contained properties of the optical MLA. For the experiments involving LFM, a 2D/3D switchable HOE-MLA was employed. This array was implemented using peristrophic multiplexing to function as an optical lens array with a pitch of 125 μm, a focal length of 2.4 mm, and a total aperture size of 12.5 mm².

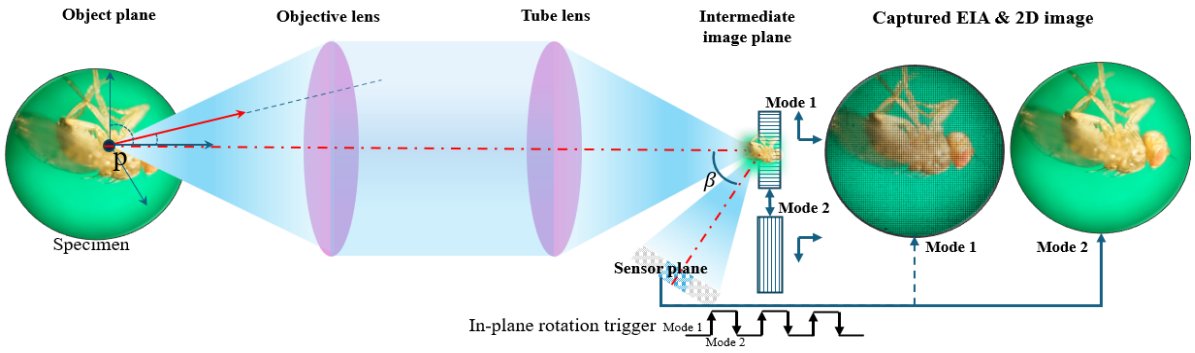

Fig. 1. Schematic diagram of proposed LFM system using a peristrophically multiplexed (2D/3D switchable) HOE-MLA.

This configuration, integrated with a single image sensor, enables the HOE-MLA to sequentially acquire II data and high-resolution 2D images of the sample as it rotates in synchronization with a trigger signal. To record the optical properties of the lens array, a photopolymer film (Bayfol® HX200) was utilized as the holographic recording medium. The HOE was recorded as a reflection-type element with a 40-degree asymmetry.

This configuration using a single image sensor allows the HOE-MLA to sequentially acquire II data and high-resolution 2D images of the sample as it rotates in response to a trigger signal.

3. 3D Visualization of LFM

Fig. 2 illustrates the 3D visualization workflow for generating a 3D model from images captured by the proposed LFM system.

First, the II data from the acquired dataset is reconstructed into an object viewpoint image (OVI) to create a light field (LF) image.

Depth information is estimated using a robust depth estimation (RDE) algorithm that uses both the LF image and a high-resolution 2D image as input [6]. The estimated depth map and the high-resolution 2D image are fused to reconstruct a 3D point cloud model that integrates color and texture information.

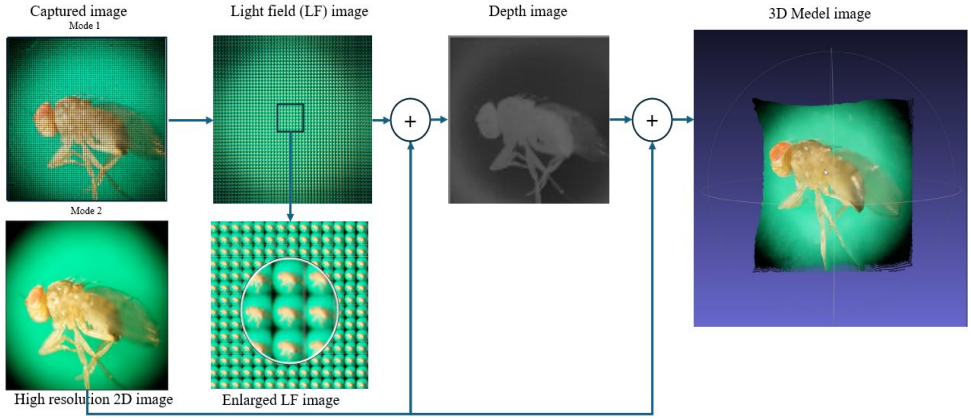

Fig. 2. Flowchart of the 3D visualization process using the proposed LFM system.

To maintain spatial resolution consistency, the depth map corresponding to the 2D image is resized to match the resolution of the reconstructed 2D image. For smoother visualization, the resized depth map is interpolated using a surface-fitting technique based on corner vertices and boundary curves to fill in any gaps.

Finally, the estimated depth map, the reconstructed 3D surface, and the high-resolution 2D image are integrated to generate a high-quality red-green-blue (RGB-D) point cloud model. The proposed system is experimentally validated using simple optical devices and demonstrates high-quality 3D visualization performance.

4. Conclusions

Conventional LFM typically requires two optical channels for image acquisition, increasing system complexity and challenging optical alignment. In this study, we propose and demonstrate a single-axis microscope system that sequentially acquires high-resolution 2D images and 3D depth information using rotationally multiplexed HOE-MLA. This system reconstructs a high-precision 3D visualization by integrating LF depth maps with high-resolution 2D images and texture data. This approach efficiently acquires and processes 3D information, generating

natural and accurate 3D reconstructions that faithfully preserve the depth, color, and texture of the sample.

Acknowledgements

Korea Government (RS-2025-02316245); Korea Government (No. P0022336); Korea Government (IITP-2025-RS-2020-II201462).

References

[1]. E. H. Adelson, J. R. Bergen, The plenoptic function and the elements of early vision, Chapter 1, in Computational Models of Visual Processing (M. S. Landy, J. A. Movshon, Eds.), *MIT Press*, Cambridge, 1991, pp. 3-20.

[2]. M. Levoy, R. Ng, A. Adams, M. Footer, et al., Light field microscopy, *ACM Transactions on Graphics*, Vol. 25, Issue 3, 2006, pp. 924-934.

[3]. K. C. Kwon, K. H. Kwon, M. U. Erdenebat, H. Y. Wu, et al., High-quality three-dimensional visualization system for light field microscopy using a robust-depth estimation algorithm and holographic optical element-microlens array, *Optics and Lasers in Engineering*, Vol. 176, 2024, 108096.

[4]. G. Wu, B. Masia, A. Jarabo, Y. Zhang, et al., Light field image processing: An overview, *IEEE Journal of Selected Topics in Signal Processing*, Vol. 11, Issue 7, 2017, pp. 926-954.

[5]. K. Curtis, A. Pu, D. Psaltis, Method for holographic storage using peristrophic multiplexing, *Optics Letters*, Vol. 19, Issue 13, 1994, pp. 993-994.

(007)

Precision-Engineered Sensing: Simulation-Driven Analysis and Design of Chirped and Apodized Fiber Bragg Gratings

Vivekanand Mishra [1] and Arnav Mishra [2]
[1] Department of Science, Alliance University, Bengaluru-562106, India
[2] VIT, Chennai-600127, India
Tel.: +7203947787
E-mail: vivekanand.mishra@alliance.edu.in

Summary: Fiber Bragg Grating (FBG) sensors are modern, very sensitive, compact, and multiplexable instruments that can monitor a wide variety of physical parameters, including strain, temperature, and pressure, and have been used for applications such as structural health monitoring, aerospace engineering, biochemical sensing, and environmental monitoring. FBG sensors are known for their capability in real-time, distributed sensing without interference by electromagnetic noise common in high-performance sensing systems. In this study, we simulate and analyse the performance of uniform, apodized, and linearly chirped FBGs using Opti Grating 4.2.3. The simulation focuses on how grating index modulation, chirp, and apodization profiles affect the reflectivity, bandwidth, and central Bragg wavelength shift. These parameters are critical for high-resolution sensing applications. The results show that apodized gratings reduce side-lobes, while chirped gratings broaden reflection bandwidth, improving sensitivity and resolution under dynamic perturbations. The outcomes lay a foundation for the optimized design of FBG-based sensors in DWDM-compatible environment.

Keywords: Fiber Bragg Gratings (FBGs), Optical sensors, Apodized and chirped gratings, Opti grating simulation, Dense Wavelength Division Multiplexing (DWDM).

1. Introduction

Fiber Bragg Gratings (FBGs) are periodic perturbations in the refractive index of the core of an optical fiber, usually through induced ultraviolet (UV) light exposure. These periodic structures are specific wavelength mirrors, meaning they reflect a specific wavelength, known as the Bragg wavelength, and allow other wavelengths through the fiber [1]. For these reasons, FBGs are well-adapted for precise, distributed sensing (multiple sensor locations) in fields and environments that difficult harsh and/or electromagnetically noisy. FBG sensors are commonly used in optical sensing systems for several reasons: their compactness, high-sensitivity, immunity from electromagnetic interference, and the ability to multiplex many sensors along one fiber. FBG sensors are suitable for applications in structural health monitoring [2], aerospace & mechanical engineering [3], biomedical diagnostics [4], and smart grid systems [5]. The Bragg wavelength, λB, is given by $\lambda B = 2n_{eff}\Lambda$, where n_{eff} is the effective refractive index of the core, and Λ is the grating period [6].

A Fiber Bragg Grating (FBG) operates as an optical filter because of its stop band, a frequency range over which a large part of the incident light is reflected. This effect results from the uniform periodic modulation of the refractive index in a single-mode optical fiber. In uniform FBGs, the grating planes are set periodically and are perpendicular to the longitudinal direction of the fiber. The uniformly structured FBG is considered the building block behind many more complex Bragg grating designs.

When an optical signal travels through a fibre with a periodic refractive index modulation, as shown in Fig. 1, there can occur efficient coupling of the forward-propagating core mode to a backward-propagating core mode (or any other related backward-propagating mode). This coupling occurs in a manner that is resonant and is governed by the Bragg condition. The Bragg condition is satisfied when the difference in propagation constants (Δβ) between the two modes equals the grating wavevector, which is the spatial frequency of the refractive index modulation. FBG sensors operate by monitoring the shift in λ_B caused by environmental perturbations like temperature and strain. The shift is defined as: $\Delta\lambda_B = \lambda(\alpha+\zeta)\,\Delta T + \lambda_B(1 - P_e)\epsilon$.

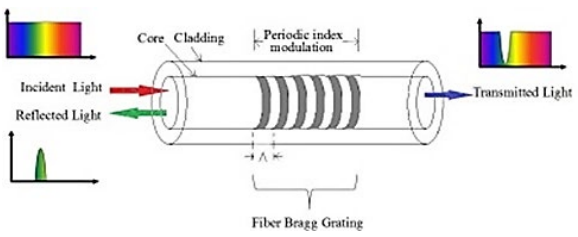

Fig. 1. Schematic Illustration of the Operating principle of FBG.

Where α denotes the thermal expansion coefficient, ζ is the thermo-optic coefficient, P_e represents the photo-elastic coefficient and ϵ corresponds to the applied strain.

2. Grating Design Variants

Fiber Bragg gratings (FBGs) show several distinct structural configurations which can be manipulated to engineer their spectral performance for specific applications including filtering, sensing, and dispersion compensation. This section describes three main configurations; uniform, apodized, and chirped grating.

2.1. Uniform Gratings

Uniform FBGs consist of a constant-period (or uniform) modulation of the refractive index, along the fiber axis. Uniform FBGs produce narrow reflection peaks as a result of their high spectral resolution, which can be used for quasi-wavelength filtering and strain sensing. Unfortunately, because of a sudden increase and decrease in the index modulation, uniform gratings have significant side lobes. The side lobes reduce signal-to-noise ratio for sensing applications and can cause crosstalk in Wavelength-Division Multiplexed (WDM) systems. While these side lobes have been suppressed to a modest spatial extent through the use of femtosecond laser inscribed and phase-mask engineered gratings, uniform gratings are inherently limited when it comes to applications that require high spectral purity.

2.2. Apodized Gratings

In order to overcome the disadvantages of uniform FBGs, engineers have sought ways to apodize the FBG so that the amplitude of index modulation gradually varies over the length of the grating. With apodized gratings, the refractive index envelope is shaped (most commonly with Gaussian, raised-cosine, or Blackman profiles) to nearly eliminate side lobes while maximizing peak reflectivity. As a result, improved spectral selectivity is made possible since there would be less interference for closely spaced channels [7]. New advances in femtosecond laser-based line-by-line inscription have allowed for the production of complex apodization profiles with high photo-spatial resolution, with further spectral tailoring available [8]. These gratings have proven useful for applications that include precision sensing, narrowband optical filtering, and tunable laser cavities.

2.3. Chirped Gratings

Chirped fibre Bragg gratings (CFBGs) allow a change in the grating period ($\Lambda(z)$) in space giving rise to a broad reflection spectrum and wavelength dependent group delay, permitting chirped grating to act as a dispersive element, correcting for chromatic dispersion in optical communications systems [9]. Although the linear chirp profile is the most commonly used; further designs such as quadratic, and exponentially chirped profiles have been developed to yield specific group-delay characteristics for ultrafast pulse shaping and delay lines. Recent attention has been paid to hybrid grating structures, which utilize combinations of chirp and apodization. The apodized-chirped FBGs that we have constructed show reduced group-delay ripples and suppressed sidelobes. This grating structure is ideal for applications where low-noise performance with broadband reflection are required [10]. Furthermore, recently developed inverse design methods based on machine learning can optimize chirped-apodized profiles to achieve desired spectral and temporal performances [11]. This approach represents an opportunity for application-specific grating engineering with unprecedented precision of spectral properties.

2.4. Chirped Simulation Setup in OptiGrating

Simulating the performance of different Fiber Bragg Grating (FBG) designs was done using Opti Grating 4.2.3. All parameters were the same for all simulations except the grating profile type. The centralized Bragg wavelength was at 1550 nm, the grating length was 10,000 μm, and the index modulation depth was set at ±0.002. The simulation was done in 1000 steps, providing a fine resolution. For the apodized grating, the Gaussian envelope was applied to the refractive index modulation, whereas for the chirped grating, a linear chirp was applied with the grating period changing from 0.532819 μm to 0.534813 μm.

Table 1. Simulation Parameters and Performance Comparison of FBG Structures.

Parameter	Uniform Grating	Apodized Grating	Chirped Grating
Central Wavelength (nm)	1550	1550	1550
Grating Length (μm)	10,000	10,000	10,000
Index Modulation Depth	± 0.002	± 0.002	± 0.002
Steps	1000	1000	1000
Apodization Profile	None	Gaussian	None
Chirp Range (μm)	N/A	N/A	0.532819 – 0.534813
Reflectivity	High	Moderate	Moderate
Side-Lobes	High	Low	Low
Spectral Bandwidth (nm)	~0.4	~0.6	~2.6
Application Suitability	Basic strain sensing	High-precision sensing	DWDM, dynamic temperature environments

The results highlighted various performance metrics for the three grating types. The uniform grating

had high reflectivity and a sharp spectral response, but a significant number of side-lobes that might negatively affect signal quality for precision detection applications.

The apodized grating had negligible side-lobes, improved spectral response, and increased stability; therefore, it can be used in high-resolution applications. The chirped grating reflected a broader reflection bandwidth (about 1.2 nm to 2.6 nm) that might allow the sensor to operate and respond under dynamically varying environmental conditions and enable applications such as dispersion compensation in optical communication.

3. Results and Discussions

The simulation data illustrates the unique benefits of apodized and chirped Fiber Bragg Gratings (FBGs) in high-resolution sensing applications. The apodization technique greatly increases the sensor stability by mitigating spectral artifacts, mainly with regard to reflected spectrum side-lobes. Thus, leading to more signal fidelity that is paramount in precision environments. Chirping, on the other hand, also increases the reflection bandwidth and spectral range by reducing the resolved wavelength range. This helped to reduce the grating dependence on environmental change, this means chirped FBGs would be supplemented in temperature compensated and dispersion managed DWDM systems along with their great capabilities in structural health monitoring applications, a summary shown in Table 2.

Table 2. Comparative Performance of Uniform, Apodized, and Chirped FBGs.

Grating Type	Reflectivity	Bandwidth (nm)	Side-Lobes	Use Case
Uniform	High	~0.4	High	Simple strain sensing
Apodized	Moderate	~0.6	Low	High-precision sensors
Chirped	Moderate	~2.4	Low	Temperature-compensated DWDM

In the middle of the grating exhibits the maximum value of refractive-index change, the tapered boundaries suppress side-lobes. As presented in Fig. 2 the apodized profile shows a smooth Gaussian ramp in the grating index. Such a profile is critical for dampening spectral side-lobe and providing cleaner, more stable signals; necessary for many sensing applications that require high-precision and high-sensitivity.

Also, apodization may slightly reduce peak reflectivity due to distributed coupling strength, the overall performance gain in terms of selectivity and noise reduction outweighs this limitation.

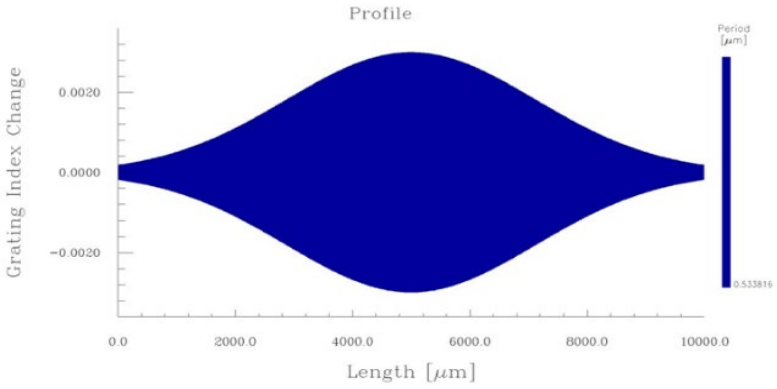

Fig. 2. Index modulation profile of an apodized Fiber Bragg Grating simulated by Opti Grating 4.2.3 program.

Fig. 3 shows the effect of the linear chirp in the grating structure, where the grating period of the Fiber Bragg Grating varies from 0.5328 μm to 0.5348 μm. The variance in the grating period allows for larger reflection bandwidths. The grating can accommodate dynamic changes in the environment and can be implemented in DWDM and dispersion-managed optical systems (Hill & Meltz, 1997). A 16-channels WDM RoF system was simulated and analyzed for optimum performance using dispersion compensation fiber (DCF) and fiber Bragg grating (FBG) with channel spacings of 100 GHz and 50 GHz, and SMF lengths of 20 km and 50 km (12). The color code indicates local grating periodic length changes and results in larger spectral reflective capacity. This linear variation in period ensures that different segments of the grating reflect different wavelengths, resulting in a broadened and continuously varying reflection spectrum. Such a chirped structure is particularly effective for applications requiring dispersion compensation and wideband filtering, as it introduces controlled group delay variations across the reflected spectrum. The smooth and monotonic change in grating period also minimizes abrupt spectral distortions, thereby improving signal integrity.

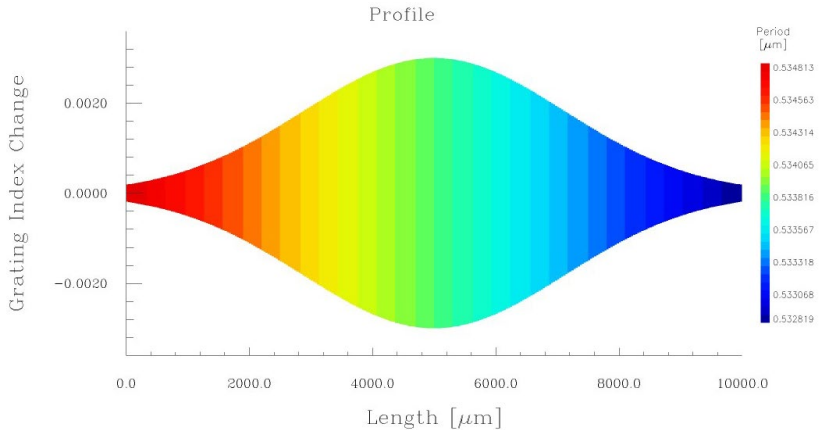

Fig. 3. Profile of a Linearly Chirped Fiber Bragg Grating showing gradual increase of grating period along the fiber length.

As seen in Fig. 4, the uniform FBG offers constant index modulation and grating period, leading to a steep reflection peak; however, the reflectivity comes with strong side-lobes. It should be noted that the uniform FBG will provide consistent index modulation and grating direction that will yield a consistent reflection peak; however strong side-lobes can be created leading to poor spectral purity. These issues are less of a concern in standard strain sensing applications as they do have enough separation from the primary peak. But if the fibre is being used in an environment with high levels of background noise, this can negatively affect overall sensor accuracy.

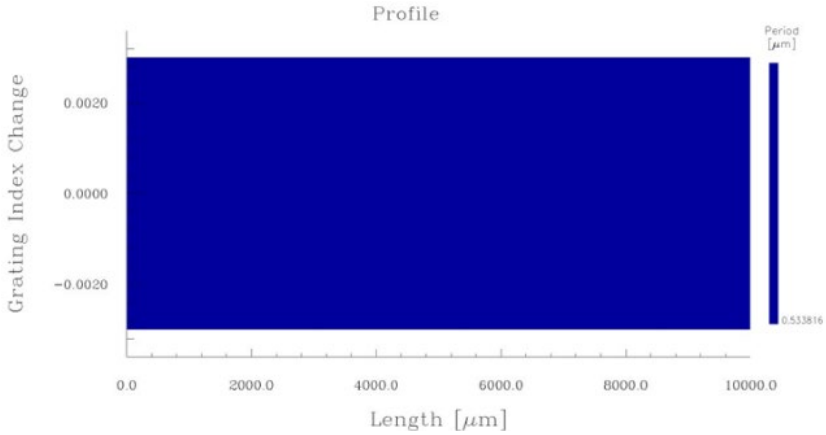

Fig. 4. Uniform Fiber Bragg Grating profile with constant index modulation and fixed grating period throughout the fiber length.

This uniformity ensures a well-defined and narrowband reflection centered at the Bragg wavelength, making it highly suitable for applications requiring precise wavelength selectivity. However, the abrupt start and end of the grating introduce spectral sidelobes, which can limit performance in high-density systems.

Despite this limitation, the simplicity, ease of fabrication, and strong peak reflectivity of uniform FBGs make them an essential baseline for understanding and designing more advanced structures such as apodized and chirped gratings.

Fig. 5 shows the reflectivity spectrum comparison reveals that anodized Fiber Bragg Gratings exhibit a narrow and well-defined spectral peak with minimal side lobes, enabling high-precision sensing. In contrast, chirping gratings produce a broadened spectral response due to spatial variation in grating period, which is advantageous for distributed sensing applications. This clearly demonstrates the trade-off between spectral resolution and sensing range, reinforcing the concept of precision-engineered sensing. Apodized Fiber Bragg Gratings exhibits a narrow bandwidth with very low sidelobes, allowing for tight channel spacing and requiring only small guard bands, which results in a low risk of crosstalk. In contrast, chirped Fiber Bragg Gratings have a broader bandwidth and moderate sidelobes, necessitating larger channel spacing and wider guard bands; if not carefully managed, this can lead to a higher risk of

inter-channel crosstalk specially in DWDM. Fig. 5: DWDM channel allocation versus wavelength.

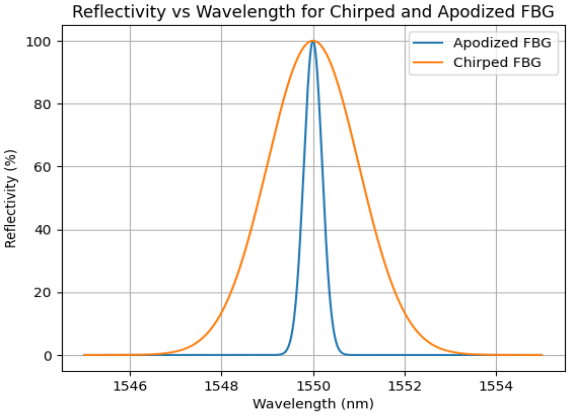

Fig. 5. Reflectivity vs. Wavelength.

It is clear from above Fig. 5 that Apodized Fiber Bragg Gratings enable tight channel spacing, efficient spectrum utilization, and minimal crosstalk, making them highly suitable for dense DWDM systems. In contrast, chirped Fiber Bragg Gratings, due to their broader spectral response, necessitate larger channel spacing, well-defined guard bands, and careful spectral management to ensure reliable and interference-free operation. Also, inter-channel crosstalk in Fiber Bragg Gratings reveals that chirped gratings, owing to their inherently broadband spectral response, are more susceptible to spectral overlap and power leakage between adjacent channels. This makes crosstalk evaluation critically dependent on bandwidth control, guard band allocation, and channel spacing optimization. In contrast, apodized gratings, with their narrow bandwidth and suppressed sidelobes, naturally limit spectral overlaps and thus exhibit significantly lower inter-channel crosstalk. Overall, this entire comparison of the uniform, apodized, and chirped FBGs provides physical changes necessary for proportional changes in sensor performance. Uniform FBGs provide simple, high reflectivity and narrow bandwidth advantages for basic strain sensing applications. However, the side-lobe levels are such that they can also be an issue for noise-sensitive applications. The advantage of the apodized grating, for an application that requires a cleaner spectrum to accentuate the primary peak, could be either a biomedical application, such as stress tests to gauge blood leaks, or in an aerospace application where extreme precision is required. While chirped FBGs provide an acceptable low side-lobe level and wider bandwidth for coupling temperature insensitive DWDM systems with minimum adverse effects. All studies have shown FBGs are effectively used in telecommunication systems. Therefore, the suitability of FBG configurations relies on the specific resolution, bandwidth, and stability for the application.

4. Conclusion

This investigation illustrates that the combination of both apodized and chirped profiles for Fiber Bragg Gratings (FBGs), albeit only in a simulated basis using Opti Grating 4.2.3, can dramatically improve performance with optical sensors (i.e., FBGs) in the areas of spectral clarity and operating bandwidth. Apodization of FBGs will reduce spectral side-lobes, which can improve both the signal-to-noise ratio and stabilized performance, both important in situations where a high level of precision is required and where any operation within the spectral region may adversely affect the result of the intended measurement. Chirped FBGs, on the other hand, can also result in broadened reflection spectra resulting in greater functional operating range and increased response to environmental variations that can occur on a time scale relevant to dynamic conditions.

This makes them applicable for use in several different areas where a high-resolution, multi-parametric measurement is required, such as in situ structural health monitoring, aerospace diagnostics, photonic communication networks, and temperature compensated Dense Wavelength Division Multiplexing (DWDM) systems. The observed simulation comparisons provided affirmation that adjusting other parameters of the grating, i.e., apodization shape and chirp rate, would offer an attractive option to modify FBG sensor performance, allowing tailoring of the digital filtering suited to its intended use in each application such as structural health monitoring. There are several potential research directions, including experimentally validating these simulation results under realistic loading and thermal conditions, exploring integrated combined apodization–chirp functions for hybrid optimization, and studying and integrating nonlinear or adaptive chirp functions for flexible sensing applications. Furthermore, embedding these optimized FBG designs into composite materials, microfluidics, and flexible substrates is likely to have significant potential for next-generation biological and wearable sensing technologies.

Advanced simulations with machine learning-based design optimization may also be a particular area of interest that can advance our knowledge of application- and contextual-specific FBG designs.

References

[1]. J. Kumar, S. Kumar, R. Mahakud, K. Kumar, et al., Studies and development of FBG based multi-point temperature sensor for vacuum chambers of synchrotron radiation source Indus-2, *Results in Optics*, Vol. 19, 2025, 100805.

[2]. C. Zhou, Z. Jia, S. Song, Z. Xu, Application of FBG sensor in health monitoring of engineering building structure: A review, *Sensor Review*, Vol. 45, Issue 1, 2025, pp. 129-145.

[3]. A. Rovera, A. Tancau, N. Boetti, M. D. L. Dalla Vedova, et al., Fiber optic sensors for harsh and high radiation environments in aerospace applications, *Sensors*, Vol. 23, Issue 5, 2023, 2512.

[4]. X. Song, Y. Fan, X. Tang, FBG-based wearable sensors and devices in the healthcare field: A review, *Optics & Laser Technology*, Vol. 181, 2025, 111920.

[5]. M. H. Yassin, M. H. Farhat, R. Soleimanpour, M. Nahas, Fiber Bragg grating (FBG)-based sensors: A review of technology and recent applications in structural health monitoring (SHM) of civil engineering structures, *Discover Civil Engineering*, Vol. 1, Issue 1, 2024, 151.

[6]. B. Ghosh, S. Mandal, Fiber Bragg grating-based optical filters for high-resolution sensing: A comprehensive analysis, *Results in Optics*, Vol. 12, 2023, 100441.

[7]. N.-H. Sun, M.-Y. Tsai, J.-J. Liau, J.-S. Chiang, Chebyshev apodized fiber Bragg gratings, *Science Progress*, Vol. 104, Issue 4, 2021, 00368504221094173.

[8]. W. Hu, C. Shao, C. Yu, L. Deng, et al., Radiation effects on pure silica and Ge-doped silica core optical fibers and fiber Bragg grating sensors, *Journal of Applied Physics*, Vol. 137, Issue 2, 2025, 0244240.

[9]. S. R. Devarajan, J. Zacharias, Performance investigation of fiber Bragg gratings with diverse chirp profiles in a multistage approach for chromatic dispersion compensation, *Journal of Optical Communications*, 2025 (in print).

[10]. H. N. Mandal, S. Sidhishwari, Ensemble learning approach for differentiating simultaneous temperature and strain impacts on apodized FBG-based sensor, in *Proceedings of the 1st IEEE International Conference on Smart and Sustainable Developments in Electrical Engineering (SSDEE'25)*, 2025, pp. 1-6.

[11]. E. Adibnia, M. Ghadrdan, M. A. Mansouri-Birjandi, Chirped apodized fiber Bragg gratings inverse design via deep learning, *Optics & Laser Technology*, Vol. 181, 2025, 111766.

[12]. M. Sliti, 16 channels WDM radio over fiber system with DCF and FBG compensators, in *Proceedings of the 27th Asia Pacific Conference on Communications (APCC'22)*, 2022, pp. 54-59.

(008)

Photonic Bandgap – Mediated Raman and SERS Enhancement in One-Dimensional Porous Silicon Photonic Crystals

M. Krajačić [1], N. Baran [2], A. Tolić [2,3], L. Mikac [2], M. Ivanda [2], O. Gamulin [1] and M. Škrabić [1]
[1] University of Zagreb, School of Medicine, Department of Physics and Biophysics,
Šalata 3, 10000 Zagreb, Croatia
[2] Ruđer Bošković Institute, Laboratory for Molecular Physics and Synthesis of New Materials,
Division of Materials Physics, Bijenička cesta 54, 10000 Zagreb, Croatia
[3] Hospira Pfizer Group, Slavonska avenija 6, 10000 Zagreb, Croatia
Tel.: + 385 1 4566 798
E-mail: maria.krajacic@mef.hr

Summary: Photonic crystals enable control of light propagation through the formation of a photonic bandgap, which strongly affects the group velocity and local density of optical states, particularly at the bandgap edges. Here, one-dimensional porous silicon photonic crystals designed as rugate filters were systematically investigated as substrates for Raman and surface-enhanced Raman scattering (SERS). By tuning the photonic bandgap position relative to the excitation wavelength, the influence of spectral alignment on signal enhancement was examined. Raman measurements were performed using crystal violet, while SERS experiments involved gold nanoparticle deposition and Rhodamine 6G as the probe molecule. Maximum Raman and SERS enhancement was observed when the excitation wavelength overlapped with the photonic bandgap edges. In contrast, alignment with the bandgap center caused strong suppression of the silicon 520 cm^{-1} band due to high reflectance, while the Raman and SERS signals of the probe molecules remained comparable to the reference rather than showing enhancement.

Keywords: Photonic crystals, Photonic bandgap, Raman scattering, Surface-enhanced Raman scattering, Signal enhancement.

1. Introduction

Photonic crystals (PhCs) are periodic dielectric structures that enable control over light propagation through the formation of a photonic bandgap (PBG), a spectral region where electromagnetic wave propagation is forbidden [1]. Beyond their strong reflectance properties, PBGs modify key optical parameters such as the group velocity of light and the local density of optical states, particularly at the bandgap edges, leading to prolonged light-matter interaction and enhanced spectroscopic response [1-3].

Raman scattering and surface-enhanced Raman scattering (SERS) are widely used analytical techniques, but their sensitivity is often limited by low scattering cross-sections or variability in enhancement mechanisms. While SERS primarily relies on plasmonic field enhancement, PhCs provide an additional and potentially more controllable route for signal enhancement.

Several studies have investigated Raman enhancement in PhCs by examining the spectral alignment between the excitation wavelength and the PBG. However, reported results remain inconsistent, with optimal enhancement conditions observed both at the bandgap edges and near the bandgap center, and enhancement factors (EFs) spanning from modest values to several orders of magnitude [4, 5]. This lack of consensus highlights the need for a systematic experimental investigation of the role of PBG positioning in both Raman and SERS enhancement. Rather than introducing a new photonic-crystal platform, the distinct contribution of this work lies in resolving these longstanding inconsistencies in the literature by systematically and quantitatively testing how alignment between the excitation wavelength and the photonic bandgap affects Raman and SERS signal intensities.

In this work, one-dimensional porous silicon (pSi) PhCs were employed as tunable platforms to investigate PBG-mediated enhancement of Raman and SERS signals by systematically tuning the PBG relative to the excitation wavelength.

2. Materials and Methods

One-dimensional PhCs were fabricated from porous silicon using electrochemical etching, enabling controlled modulation of the refractive index along the depth of the structure. The PhCs were designed as rugate filters with a sinusoidal refractive index profile, allowing precise tuning of the PBG position. A series of samples was prepared with PBGs spectrally shifted relative to the excitation wavelength to enable a systematic investigation of bandgap-mediated enhancement effects (Fig. 1).

Raman measurements were performed using a laser excitation wavelength of 785 nm. Crystal violet was employed as a probe molecule for Raman experiments. SERS measurements were conducted on selected PhC substrates after deposition of gold nanoparticles, using Rhodamine 6G as the probe molecule. In both cases, probe molecules were adsorbed on the sample surface and partially infiltrated the porous photonic structure.

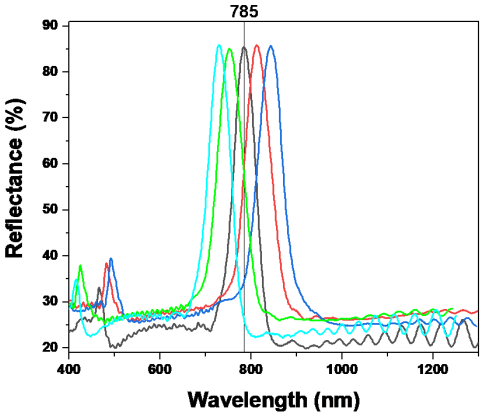

Fig. 1. Reflectance spectra of pSi PhCs with shifted PBGs. The vertical line indicates the 785 nm excitation wavelength.

All Raman spectra were acquired under identical experimental conditions to ensure comparability across samples. The Raman band of crystalline silicon (cSi) was used as an internal reference to verify the relative alignment between the excitation wavelength and the PBG and to assess sample reproducibility. All measurements were performed at room temperature.

3. Results and Discussion

The influence of PBG positioning on Raman signal intensity was investigated by varying the spectral alignment between the excitation wavelength and the PBG. Reflectance spectra (Fig. 1) confirm controlled shifting of the PBG relative to the 785 nm excitation wavelength. Enhancement factors were calculated as the ratio between the Raman intensity measured for a given PhC sample and that measured for non-photonic pSi under identical experimental conditions.

The Raman band of cSi at 520 cm^{-1} served as an internal indicator of excitation-PBG alignment, showing approximately fivefold suppression when the excitation wavelength coincided with the center of the PBG due to high reflectance. In contrast, overlapping the excitation with the PBG edges resulted in enhanced intensity of the 520 cm^{-1} band, with EFs of approximately 2.1 at the high-frequency edge and 1.4 at the low-frequency edge.

For the CV Raman bands, enhancement was likewise observed when the excitation wavelength overlapped with the PBG edges, with EFs between 2 and 3 for the most intense vibrational modes, particularly at 724, 1172, 1363, 1391, and 1618 cm^{-1}. In contrast to previous reports [4], alignment with the PBG center resulted in mean intensities within the standard deviation of the reference for 9 out of 10 observed CV Raman bands. Although enhancement varied between individual bands, the trend was reproducible across all samples.

In SERS measurements, gold nanoparticles were deposited under deliberately moderate conditions to avoid complete masking of the underlying PhC by the plasmonic response. FE-SEM showed substantial but not perfectly uniform coverage, with gaps between nanoparticles, indicating that plasmonic heterogeneity and hotspot-related variability remained important factors in the overall SERS response. Under these conditions, alignment between the excitation wavelength and the PBG edges resulted in only a weak additional enhancement of approximately 1.1-1.3 relative to ordinary pSi, showing that the photonic contribution to SERS is limited and does not compete with the dominant plasmonic enhancement, helping to clarify previous reports of strong PhC-assisted SERS effects.

4. Conclusions

This study demonstrates that Raman and SERS signal enhancement in 1D pSi PhCs is strongly governed by the relative spectral alignment between the excitation wavelength and the PBG. The strongest enhancement was observed when the excitation wavelength overlapped with the high- and low-frequency edges of the bandgap, while alignment with the bandgap center did not enhance the molecular signal relative to the reference.

The results confirm that reduced group velocity and increased local density of optical states at the bandgap edges provide a reproducible and predictable photonic contribution to Raman signal enhancement, particularly for molecules infiltrated into the PhC structure.

In SERS measurements, plasmonic effects dominate the absolute signal intensity, while the PhC provided only a weak secondary modulation under deliberately moderate nanoparticle coverage conditions.

These findings highlight the importance of precise PBG engineering for reproducible Raman enhancement and for clarifying the limited extent of photonic contributions under SERS conditions.

Acknowledgements

The authors acknowledge financial support from the European Regional Development Fund for the project 'Materials for clean energy, advanced sensors and quantum technologies' (Grant No. PK.1.1.10.0002).

References

[1]. J. D. Joannopoulos, S. G. Johnson, J. N. Winn, R. D. Meade, Photonic Crystals: Molding the Flow of Light (2nd Ed.), *Princeton University Press*, Princeton, 2008.

[2]. E. Yablonovitch, Inhibited spontaneous emission in solid-state physics and electronics, *Physical Review Letters*, Vol. 58, Issue 20, 1987, pp. 2059-2062.

[3]. J. M. Bendickson, J. P. Dowling, M. Scalora, Analytic expressions for the electromagnetic mode density in finite, one-dimensional, photonic band-gap structures, *Physical Review E*, Vol. 53, Issue 4, 1996, pp. 4107-4121.

[4] M. Fränzl, S. Moras, O. D. Gordan, D. R. T. Zahn, Interaction of one-dimensional photonic crystals and metal nanoparticle arrays and its application for surface-enhanced Raman spectroscopy, *The Journal of Physical Chemistry C*, Vol. 122, Issue 18, 2018, pp. 10153-10158.

[5]. O. Deparis, S. R. Mouchet, B. L. Su, Light harvesting in photonic crystals revisited: Why do slow photons at the blue edge enhance absorption?, *Physical Chemistry Chemical Physics*, Vol. 17, Issue 45, 2015, pp. 30525-30532.

(011)

Modeling Bifilar-Effect Excitation for Energy Enhancement in 46.9 nm Ar^{8+} Capillary Lasers

M. Kiss [1] and S. V. Kukhlevsky [2]
[1] Department of Experimental Physics, University of Pécs, Ifjuság str. 6, 7624 Pécs, Hungary
[2] Department of Theoretical Physics, University of Pécs, Ifjuság str. 6, 7624 Pécs, Hungary
E-mail: szergej@fizika.ttk.pte.hu

Summary: The 46.9 nm Ne-like argon soft X-ray laser, driven by low-voltage (35-45 kV) capillary Z-pinch discharges employing the bifilar effect, represents one of the most promising short-wavelength laser sources for a wide range of scientific and practical applications [AIP Advances, Vol. 14, p. 025048 (2024)]. The system utilizes a C-C excitation circuit, similar to that commonly used in conventional TEA XeCl excimer lasers. Owing to its relatively low operating voltage, the laser setup is compact, portable, and cost-effective compared to traditional high-voltage soft X-ray laser systems. The laser produces output pulses with energies of 3-4 μJ at 46.9 nm. In this work, we present modeling results of the bifilar-effect-based excitation scheme, demonstrating the potential for approximately twofold enhancement of the laser output energy. The simulations were carried out using a one-fluid, two-temperature, one-dimensional magnetohydrodynamic (MHD) model coupled with an atomic kinetics code.

Keywords: Soft X-ray laser modeling, 46.9 nm Ne-like argon laser, Capillary Z-pinch discharge, Bifilar effect, Magnetohydrodynamic simulation, Atomic kinetics, Laser energy enhancement,

1. Introduction

The 46.9 nm Ne-like argon soft X-ray laser, driven by low-voltage (35-45 kV) capillary Z-pinch discharges employing the bifilar effect, represents one of the most promising short-wavelength laser sources for a wide range of scientific and practical applications [1, 2]. The laser excitation system is based on a bifilar effect that reduces the transient magnetic field and thus the plasma-conductor inductance. To utilize the advantage offered by the phenomenon, the discharge circuit's impedance is matched to a pulse-forming circuit. The bifilar system produces a low-inductance (~2 nH) 35 cm-long Z-pinche discharge with a current rise time of ~15 ns and amplitude of ~17 kA. In the 46.9-nm Ar^{8+} laser, light pulses 3-4 μJ of energy were produced at a very low operating voltage of 35-45 kV. The laser utilizes a C-C excitation circuit, similar to that commonly used in conventional TEA XeCl excimer lasers. Owing to its relatively low operating voltage, the laser setup is compact, portable, and cost-effective compared to traditional high-voltage soft X-ray laser systems (for instance, see [3]). In this work, we present modeling results of the bifilar-effect-based excitation scheme, demonstrating the potential for approximately twofold enhancement of the laser output energy. The simulations were carried out using a 1-fluid, 2-temperature, 1-D MHD model coupled with an atomic kinetics code, interfaced with COMSOL-based electrical circuit model.

2. 46.9-nm Ar^{8+} laser

Fig. 1 shows the laser system that uses the bifilar reduction of plasma inductance and combines an L-C excitation circuit with a magnetic switch compressor in the laser (for details, see [1, 2]).

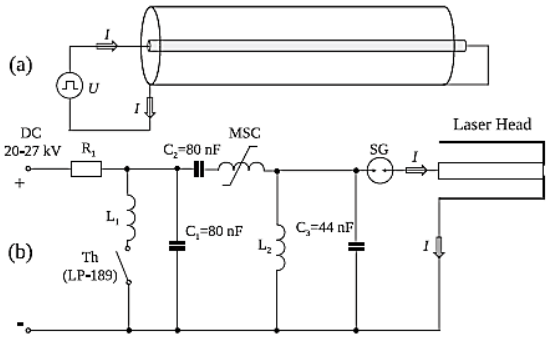

Fig. 1. (a) Bifilar configuration used to reduce the self-inductance of the Z-pinch discharge. (b) Schematic diagram of the excitation circuit employed for Z-pinch formation and laser pumping [2].

The laser excitation is studied to further increase the laser energy using the following model.

3. The Laser Model

The atomic kinetic code: The density of energy levels of Ar^{+Z} ions is found using the balance equations

$$\frac{dn_{ik}^{Z}}{dt} = \sum_{m>k} n_{im}^{Z}\left[n_e\left(C_{km}^{ex} - C_{mk}^{de}\right) + A_{mk}\right] - \\ -n_{ik}^{Z}\sum_{m<k}\left[n_e\left(C_{mk}^{ex} + C_{km}^{de}\right) + E(\tau_{km})A_{km}\right], \quad (1)$$

where C_{km}^{ex} and C_{mk}^{dx} are the excitation and de-excitation coefficients. The ion and electron

densities are denoted by n_i and n_e. The photon escape factor $E(\tau_{km})$ in the optically thick lines depends on the optical depth τ_{km}. Balance equations of the densities n_{ion}^{Z} of ion stages are given by

$$\frac{dn_{ion}^{Z}}{dt} = n_e[n_{iion}^{Z-1} I^{Z-1} + n_{ion}^{Z+1}(R_{rr}^{Z+1} + R_{dr}^{Z+1} + R_{cr}^{Z+1})] - n_e[n_{iion}^{Z} I^{Z} + n_{ion}^{Z}(R_{rr}^{Z} + R_{dr}^{Z} + R_{cr}^{Z})], \quad (2)$$

where I and R are the ionization and recombination coefficients.

The standard MHD model of capillary Z-pinch plasma is used to determine the plasma parameters for the atomic kinetic code:

$$\frac{\partial n_i}{\partial t} + \frac{1}{r}\frac{\partial}{\partial r}(r v_r n_i)_i = 0, \quad (3)$$

$$m_i n_i \left(\frac{\partial v_r}{\partial t} + v_r \frac{\partial v_r}{\partial r}\right) = J_z \frac{\partial A_z}{\partial r} - \frac{\partial p}{\partial r} - \frac{1}{r}\frac{\partial}{\partial r}(r\pi_{rr}) + \frac{\pi_{\phi\phi}}{r}, \quad (4)$$

$$\frac{3}{2} n_e \left(\frac{\partial T_e}{\partial t} + v_r \frac{\partial T_e}{\partial r}\right) = -\frac{p_r}{r}\frac{\partial}{\partial r}(r v_r) - \frac{1}{r}\frac{\partial}{\partial r}(r q_e^r) - \pi_e^{rr}\frac{\partial v_r}{\partial r} - \pi_e^{\kappa\phi}\frac{v_r}{r} - \pi_e^{rz}\frac{\partial v_r^{ez}}{\partial r} + Q_e, \quad (5)$$

$$\frac{3}{2} n_i \left(\frac{\partial T_i}{\partial t} + v_r \frac{\partial T_i}{\partial r}\right) = -\frac{p_i}{r}\frac{\partial}{\partial r}(r v_r) - \frac{1}{r}\frac{\partial}{\partial r}(r q_i^r) - \pi_i^{rr}\frac{\partial v_r}{\partial r} - \pi_i^{\kappa\phi}\frac{v_r}{r} + Q_i, \quad (6)$$

$$\frac{1}{r}\frac{\partial}{\partial r}(r A_z) = \mu_0 A_z, \quad (7)$$

$$\frac{\partial J_z}{\partial t} + \frac{1}{r}\frac{\partial}{\partial r}(r v_r J_z) = \frac{e}{r m_e}\frac{\partial}{\partial r}(r\pi_z^r), \quad (8)$$

where v_r is the plasma radial speed, the axial current density by J_z, A_z is the axial potential, p is the plasma pressure p, $\pi_{\alpha\beta}$ is the stress tensor, the radial electron and ion heat flows are denoted by $q^r{}_e$ and $q^r{}_i$, and the heating of electrons and ions by Q_e and Q_i. The energy of Ar^{+8} laser pumped by low-voltage capillary Z-pinches is determined by the gain coefficient reduced by the ray refraction in the plasma:

$$G = \frac{\lambda^4}{8\pi\Delta\lambda} A_{ul}\left(n_{iu}^{Z} - n_{il}^{Z}\frac{g_u}{g_l}\right) - \frac{F_{cyl}}{r}\sqrt{\frac{n_e}{n_e^c}}, \quad (9)$$

where F_{cyl} = 2.347 is the geometrical factor for cylindrical plasmas, n_e^c is the critical electron density, g_u and g_l are the statistical weights of upper and lower levels of energy, and A_{ul} is the radiation decay rate [1, 2]. The energy of Ar^{+8} laser pumped by low-voltage capillary Z-pinches is determined by the gain coefficient reduced by the ray refraction in the plasma.

4. The Simulation Example and Conclusion

Simulation example is shown in the Fig. 2.

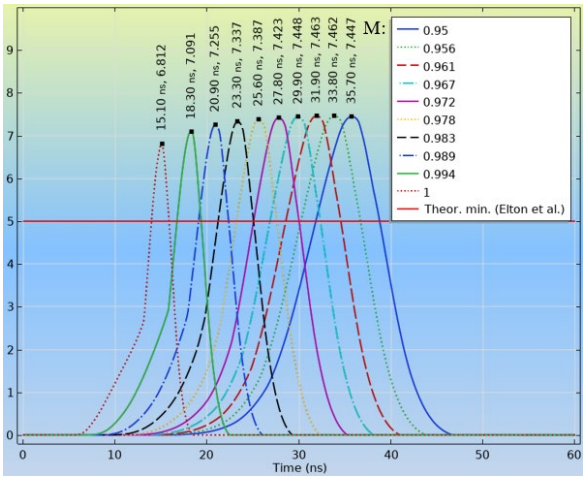

Fig. 2. Simulation example illustrating the gain–length (GL) product in laser energy ($E \sim \exp(GL)$, L is plasma length), for different values of the parameter M (M characterizes the efficiency of the bifilar configuration).

In conclusion, the presentation will demonstrate the potential for approximately twofold enhancement of the laser output energy.

Acknowledgements

This work was supported by the Research Fund of the University of Pécs (Contract No. 003_2025_PTE_RK/11 to S.V.K.).

References

[1]. B. Fekete, M. Kiss, A. A. Shapolov, S. Szatmari, et al., Soft x-ray Ar+8 laser excited by low-voltage capillary discharge, *Optics Express*, Vol. 31, Issue 21, 2023, pp. 34381-34390.

[2]. B. Fekete, M. Kiss, A. A. Shapolov, S. Szatmari, et al., Short rise- and decay-time Z-pinch currents for soft x-ray laser excitation, *AIP Advances*, Vol. 14, Issue 2, 2024, 025048.

[3]. D. Zhao, H. Cui, S. Wang, Y. Yi, et al., The study of capillary discharge Ne-like 46.9 nm laser with a 2.5 mm inner diameter capillary, *Optics Communications*, Vol. 575, 2025, 131257.

(012)

Optimization of the Structure of Spatially Multiplexed Single-Photon Sources

A. Kaszás [1], M. Mechler [2,3] and P. Adam [2,3]
[1] Institute of Engineering and Smart Technologies, Faculty of Engineering and Information Technology, University of Pécs, 7624 Pécs, Boszorkány út 2, Hungary
[2] Institute for Solid State Physics and Optics, HUN-REN Wigner Research Centre for Physics, 1121 Budapest, Konkoly-Thege Miklós út 29-33, Hungary
[3] Institute of Physics, University of Pécs, 7624 Pécs, Ifjúság útja 6, Hungary
E-mail: adam.peter@wigner.hun-ren.hu

Summary: We present a method for finding the optimal structure of general binary-tree multiplexers consisting of asymmetric binary photon routers that can be applied for any number of multiplexed units to improve the performance of spatially multiplexed single-photon sources. The overall structure optimization method introduced in [11] scales with the factorial of the number of multiplexed units, hence it can be applied only for multiplexers containing low numbers of photon routers. In contrast, the proposed method applies a hybrid source strategy that, beyond a given number of multiplexed units, is based on an extended stepwise optimization procedure. We accomplish the full optimization problem for realistic ranges of the loss parameters; hence we determine the optimal input mean photon number, the optimal number of multiplexed units, and the optimal structure of the spatial multiplexer for which the single-photon probability of a spatially multiplexed single-photon source is maximal. The results confirm that the application of such optimal multiplexers in single-photon sources increases the achievable single-photon probabilities.

Keywords: Single-photon sources, Spatial multiplexing, Structure optimization.

1. Introduction

Numerous experiments and applications of quantum optics and quantum computing require single-photon sources with high reliability.

Promising candidates for realizing such perfect sources are multiplexed single-photon sources [1-6].

Such sources are based on heralded single-photon sources that generate photon pairs in two correlated optical modes, commonly referred to as the signal and idler modes. Detection of a photon in the idler mode heralds the presence of its partner in the signal mode. The problem with heralded single-photon sources is that the number of generated photon pairs is probabilistic, hence the number of photons generated by such sources can differ from one. This issue can be addressed by multiplexing several such sources. Multiplexing involves decreasing the output single-photon probability of the individual sources, thus reducing the probability of multiphoton events, and at the same time combining the signals of several heralded sources by a multiplexer that reduces the probability of zero-photon events at the output of the multiplexed source. In the case of spatial multiplexing, several heralded sources are used in parallel, and the signal of these sources is directed to the input of a multiplexer formed by binary photon routers. Using the statistical theory of multiplexed single-photon sources, it becomes possible to optimize multiplexed single-photon sources, that is, to maximize the output single-photon probability by determining the optimal number of multiplexed units, and the optimal mean number of photon pairs generated in the multiplexed units for a given set of loss parameters [7-10].

Single-photon sources based on different types of spatial multiplexers can exhibit considerably different performances. Hence, one can conclude that the structure of the multiplexer must be also optimized, that is, one must find the structure the application of which in a single-photon source results in the highest output single-photon probability. Complete optimization of the multiplexer structure involves considering all possible different structures constructed of a given number of photon routers [11]. This covers an inconveniently large number of different structures even for relatively low numbers of photon routers; therefore, the complete structure optimization becomes increasingly difficult with increasing numbers of photon routers. Here we recommend a novel structure optimization method that combines full structure optimization with extended stepwise optimization based on elitist selection. This method can be applied for arbitrary numbers of multiplexed units. Hence, we can accomplish the full optimization task of spatially multiplexed single-photon sources for realistic values of the loss parameters.

2. Method

The multiplexer in a spatially multiplexed single-photon source containing N multiplexed units is composed of $N-1$ binary photon routers. Any binary multiplexer with N input ports can be characterized by an integer sequence S of length $N-1$. The nth number in the sequence indicates the input port of a specific multiplexer formed by $n-1$ photon routers to which

the newly inserted router is connected. This coding shows that the number of different structures that can be formed by $N-1$ photon routers is $(N-1)!$. In the case of binary multiplexers, due to the symmetries of the system, several structures characterized by different integer sequences may be physically equivalent. The repeated sequences can be filtered out by stipulating that the difference $S_n - S_{n-1}$ between consecutive elements of the sequence can be at most one. With this restriction, the number of different structures comprised of $N-1$ photon routers is reduced to the $(N-1)$st Catalan number C_{N-1}, but this number is still too high to perform a complete structure optimization for large numbers of multiplexed units.

To solve this problem, we propose the following method for optimizing the structure of the multiplexer. When $C_{N-1} < (N-1)^k$ $(k \in \mathbb{Z}^+)$ for a binary multiplexer consisting of $N-1$ photon routers, we perform complete optimization. Otherwise, we perform an extended stepwise optimization. Starting from the first N value for which $C_{N-1} > (N-1)^k$ we select the structures the application of which in a multiplexed single-photon source yields the first $(N-1)^k$ highest achievable single-photon probabilities $P_{1,N}$. Then, by placing the next router on each possible input of each selected structure, we calculate the achievable single-photon probabilities $P_{1,N+1}$ in each case for optimized input mean photon numbers λ. Then, we perform the previously described elitist selection method to find the first N^k structures with the highest single-photon probabilities and repeat the stepwise process with them. We note that the $k = 0$ case corresponds to the simple stepwise optimization method described earlier in [12].

The computational complexity of the proposed method is obviously smaller than that of the complete structure optimization. In this context computational complexity refers to the number of structures that must be analyzed in order to find the optimal structure the application of which in a single-photon source results in the highest achievable single-photon probability. We have found that the computational complexity of the proposed method can be approximated by $\sum_{n=2}^{N}(n-2)^k(n-1)$; specifically, for $k = 1$ it gives $(N^3 - 3N^2 + 2N)/3$. Hence, the complexity scales polynomially with the number N of the multiplexed units instead of the factorial scaling that characterizes complete structure optimization. We have checked that the above statement is also valid for higher values of k.

3. Results

In this communication, we consider the proposed structure optimization method for $k = 1$. We assume that the number of generated photon pairs in the multiplexed units follows Poissonian statistics.

Applying the statistical theory of multiplexed single-photon sources [7] and the proposed structure optimization method, we carry out the full optimization of spatially multiplexed single-photon sources for realistic ranges of the loss parameters, that is, of the transmission coefficients V_r and V_t characterizing the photon routers and the detection efficiency V_D describing the resolving capabilities of the detector. The optimization problem involves determining the optimal input mean photon number λ_{opt}, the optimal number of multiplexed units N_{opt}, and the optimal structure $S_{N,opt}$ of the spatial multiplexer that yields the highest single-photon probability $P_{1,max}$ of a spatially multiplexed single-photon source.

In Fig. 1 we show a correspondence plot of the optimal structures obtained for multiplexed s ingle-photon sources based on general binary-tree multiplexers and on extended stepwise optimized binary-tree multiplexers for $k = 1$ as function of the transmission coefficients V_t and V_r for the number of multiplexed units $N = 12$ and the detector efficiency $V_D = 0.95$. White (black) points indicate that the structures obtained by using complete structure optimization and the proposed extended stepwise optimization are the same (different). We note that as the method gives the same result if the roles of V_t and V_r are interchanged, the figure would be symmetric to the $V_t = V_r$ line. Therefore, we show results only for the $V_r \geq V_t$ region, and color yellow is used for all the points in the other region where $V_r < V_t$. The figure shows that for the numbers of multiplexed units as low as $N = 12$ the proposed optimization method can be used to find the globally optimal structure for a wide range of the loss parameters even for $k = 1$.

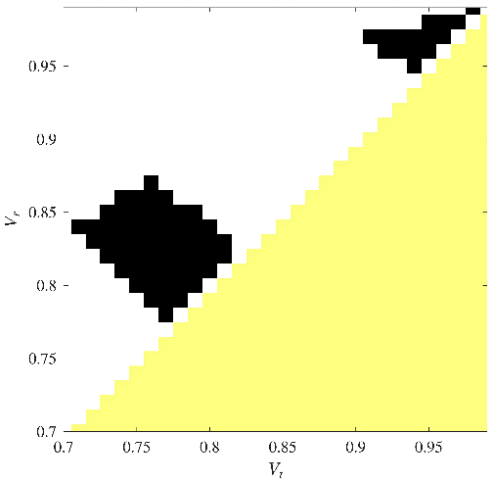

Fig. 1. Correspondence plot of the optimal structures for multiplexed single-photon sources based on general binary-tree multiplexers and on extended stepwise optimized binary-tree multiplexers for $k = 1$ as function of the transmission coefficients V_t and V_r for the number of multiplexed units $N = 12$ and the detector efficiency $V_D = 0.95$. White (black) points indicate that the structures obtained by using complete structure optimization and the proposed extended stepwise optimization are the same (different). Color yellow represents points with $V_t > V_r$.

Fig. 2 presents the difference $\Delta_{P_1}^{1,0} = P_{1,max}^{(1)} - P_{1,max}^{(0)}$ between the maximal single-photon probabilities $P_{1,max}^{(1)}$ and $P_{1,max}^{(0)}$ corresponding to SPSs based on extended stepwise optimized binary-tree multiplexers for $k = 1$ and $k = 0$, respectively, as a function of the transmission coefficients V_t and V_r for the detector efficiency $V_D = 0.95$. We have found that spatially multiplexed single-photon sources based on multiplexers optimized using the proposed method generally yield higher single-photon probabilities than multiplexed single-photon sources based on stepwise-optimized binary-tree multiplexers.

As an example, in Fig. 3 we show an optimal structure for $N = 12$ for a specific set of the loss parameters.

4. Conclusions

We have recommended a novel method for optimizing the structure of a multiplexer applied in a spatially multiplexed single-photon source.

The proposed method combines full structure optimization with extended stepwise optimization based on elitist selection, and it can be applied for arbitrary numbers of multiplexed units.

The method makes it possible to accomplish the full optimization task of spatially multiplexed single-photon sources for realistic values of the loss parameters.

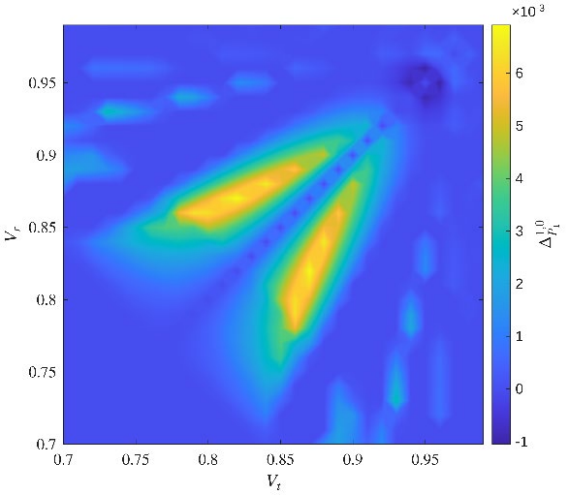

Fig. 2. The difference $\Delta_{P_1}^{1,0} = P_{1,max}^{(1)} - P_{1,max}^{(0)}$ between the maximal single-photon probabilities $P_{1,max}^{(1)}$ and $P_{1,max}^{(0)}$ corresponding to SPSs based on extended stepwise optimized binary-tree multiplexers for $k = 1$ and $k = 1$, respectively, as a function of the transmission coefficients V_t and V_r for the detector efficiency $V_D = 0.95$.

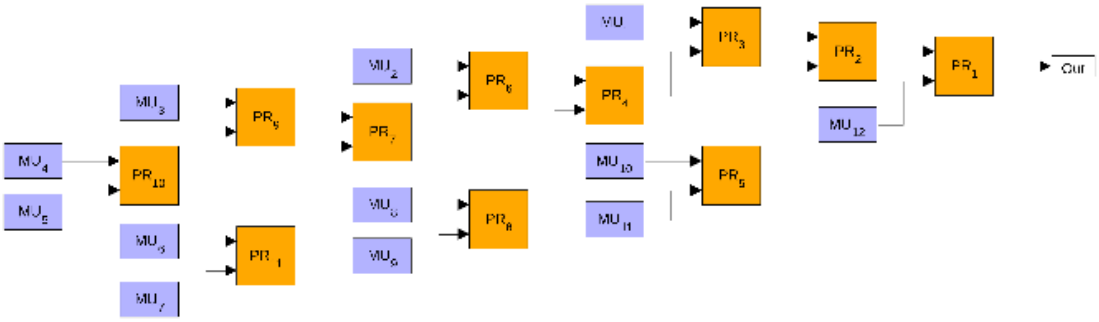

Fig. 3. Optimal structure of a single-photon source based on extended stepwise optimized binary-tree multiplexer for $k = 1$ using $N = 12$ multiplexed units for the transmission coefficients $V_r = 0.96$ and $V_t = 0.85$, and the detector efficiency $V_D = 0.95$. MUis are multiplexed units, PRks are asymmetric binary photon routers.

Acknowledgements

This research was supported by the National Research, Development and Innovation Office, Hungary ("Frontline" Research Excellence Programme Grant No. KKP133827, and Grant No. TKP2021-NVA-04), and the Smart University Program of the University of Pécs.

References

[1]. M. D. Eisaman, J. Fan, A. Migdall, S. V. Polyakov, Invited review article: Single-photon sources and detectors, *Review of Scientific Instruments*, Vol. 82, Issue 7, 2011, 071101.

[2]. X. Cao, M. Zopf, F. Ding, Telecom wavelength single photon sources, *Journal of Semiconductors*, Vol. 40, Issue 7, 2019, 071901.

[3]. E. Meyer-Scott, C. Silberhorn, A. Migdall, Single-photon sources: Approaching the ideal through multiplexing, *Review of Scientific Instruments*, Vol. 91, Issue 4, 2020, 041101.

[4]. Y. Wang, K. D. Jöns, Z. Sun, Integrated photon-pair sources with nonlinear optics, *Applied Physics Reviews*, Vol. 8, Issue 1, 2021, 011314.

[5]. A. Elefante, S. Dello Russo, F. Sgobba, L. Santamaria Amato, et al., Recent progress in short and mid-infrared single-photon generation: A review, *Optics*, Vol. 4, Issue 1, 2023, pp. 13-38.

[6]. P. Adam, M. Mechler, Recent progress in multiplexed single-photon sources, *Applied Sciences*, Vol. 14, Issue 23, 2024, 11249.
[7]. F. Bodog, M. Mechler, M. Koniorczyk, P. Adam, Optimization of multiplexed single-photon sources operated with photon-number-resolving detectors, *Physical Review A*, Vol. 102, Issue 1, 2020, 013513.
[8]. P. Adam, F. Bodog, M. Mechler, Spatially multiplexed single-photon sources based on incomplete binary-tree multiplexers, *Optics Express*, Vol. 30, Issue 5, 2022, pp. 6999-7016.
[9]. P. Adam, F. Bodog, M. Koniorczyk, M. Mechler, Single-photon sources based on asymmetric spatial multiplexing with optimized inputs, *Physical Review A*, Vol. 105, Issue 6, 2022, 063721.
[10]. P. Adam, M. Mechler, Single-photon sources based on incomplete binary-tree multiplexers with optimal structure, *Optics Express*, Vol. 31, Issue 19, 2023, pp. 30194-30211.
[11]. M. Mechler, P. Adam, Spatially multiplexed single-photon sources based on binary-tree multiplexers with optimized structure, *Scientific Reports*, Vol. 15, 2025, 1244.
[12]. P. Adam, M. Mechler, Single-photon sources based on stepwise optimized binary-tree multiplexers, *Optics Express,* Vol. 32, Issue 10, 2024, pp. 17173-17188.

(013)

A 24-Channel Optical Trigger for Use in 3D Holographic Display Systems

G. Ivanova, B. Ivanov * and D. Dimov
Institute of Optical Materials and Technologies, Laboratory "Holography", 109,
Acad. G. Bontchev Str., 1113 Sofia, Bulgaria
Tel.: + 33 601825261
* E-mail: branimirivanov@iomt.bas.bg

Summary: This work presents a 24-channel holographic optical element (HOE) engineered to function as a high-speed optical trigger incorporating eight phase states, each combined with three distinct frequency states. This configuration yields 24 independent, multiplied replicas of the incident optical signal. Such parallel replication enables simultaneous execution of diverse optical-domain processing algorithms across the channels at the intrinsic speed of light propagation, while preserving at least one unmodified copy of the primary signal for subsequent holographic reconstruction and analysis. This architecture directly addresses the performance demands of next-generation volumetric 3D holographic displays, which require extremely rapid recalculation of depth variations in RGBD holograms and fast generation of auxiliary holographic layers relative to the base frame. Performing these computations for every holographic frame is essential for achieving smooth temporal continuity and perceptual stability when transitioning from static holographic imagery to dynamic holographic video sequences, a key challenge in scalable real-time holographic display systems.

Keywords: Holographic optical elements, Multi-channel optical trigger, Phase and frequency multiplexing, 3D displays, RGBD hologram computation, Parallel optical triggering architectures, Dynamic holographic video rendering.

1. Introduction

Three-dimensional holographic display systems represent one of the most demanding frontiers in modern optical engineering. Computer-generated holography (CGH) has emerged as the dominant paradigm for digitally synthesizing holographic interference patterns capable of reconstructing volumetric scenes in free space, yet display applications must address millions of scene points simultaneously, imposing severe algorithmic and computational burdens on any holographic video pipeline [1]. Existing approaches – whether based on point cloud representations, light field models, polygon meshes, or layered red, green, blue, and depth (RGBD) images – rely on numerically intensive diffraction simulation steps that are typically time-consuming and sensitive to parameter tuning [1].

1.1. Methods for Generation of Holograms for 3D Display

Holographic stereogram approaches encode full light field information and natively support view-dependent lighting effects, yet CGH algorithms based on wavefront propagation inherently struggle to reproduce occlusions and specular reflections [2]. Reconstructing a scene as a layered point-cloud from multiple perspective projections improves reproduction of motion parallax and accommodation [3], but even these representations require significant numerical propagation for every frame [3], rendering real-time holographic video computationally intractable without parallel processing.

This fundamental limitation motivates the present work, in which we propose a 24-channel holographic optical element operating as a dedicated optical processor, capable of generating and processing multiple independent optical replicas of an incident signal in parallel, directly at optical bandwidths.

1.2. Image Quality and Optical Correction in Holographic Displays

The quality of reconstructed holographic images is further constrained by optical aberrations and blur phenomena. In full-parallax holographic displays, the spectral width of the illumination source introduces color blurring that significantly reduces image sharpness [4], while accurate modeling of off-axis diffraction for large-scale aberration-correcting optical elements remains computationally demanding even with state-of-the-art sampling schemes [5].

The present work addresses these constraints by performing aberration correction directly in the optical domain, embedding the correction within the physical structure of the HOE itself. Each of the 24 independent trigger channels carries sufficient processing bandwidth to accommodate such corrections for a given optical sub-channel, making optical aberration compensation inherently achievable within the proposed architecture.

1.3. Multichannel Interferometric and Holographic Optical Systems

Early demonstrations of multichannel holographic interferometry established that HOEs could serve as

active beam-steering and wavefront-shaping components, producing compact, light-efficient designs inherently capable of aberration compensation [6]. Trigger-based architectures employing phase-shifting have further confirmed the potential of such systems as a structural principle for parallel holographic processing [7].

Our previous work introduced a four-channel HOE for phase-stepping digital speckle pattern interferometry, demonstrating that a single compact HOE could carry substantial parallel optical processing capacity across two wavelengths and two polarization states [8]. In the present work, the HOE is recorded in a single-beam interferometer configuration with three wavelengths, following the approach established in [8], and the architecture is scaled to 24 channels by encoding eight phase states combined with three distinct frequency states, thereby multiplying the parallel processing capacity by a factor of six.

1.4. Holographic Material Platform for Multichannel Optical Element Construction

The physical realization of this architecture relies on advances in holographic material science. The demonstration of efficient coherent holographic beam combiners based on angle multiplexing of gratings in thick polymeric substrates confirms that a large number of independent beams can be independently combined within a single compact holographic element with efficiency well predicted by coupled-wave theory [9], directly underpinning the feasibility of our 24-channel design based on bisphenol-derived polymer optical elements. This material platform provides the physical foundation for scaling the present architecture toward higher channel counts in subsequent work.

2. 24-Channel Holographic Optical Trigger: Design and Architecture

The 24-channel HOE is designed as an all-optical trigger that performs fully parallel computation of holographic depth planes through physically encoded color and phase states within a single compact holographic device, generating a minimum of 49 independent focal depth planes per holographic frame for accurate volumetric reproduction of dynamic holographic scenes.

Each of the eight optical channels processes three wavelength states simultaneously, yielding 24 independent functional processing channels.

The eight-channel base unit is organized into three functional blocks (Fig. 1).

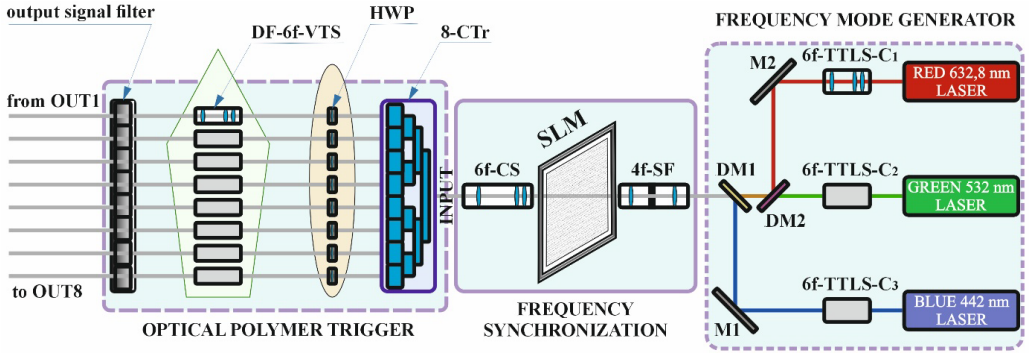

Fig. 1. Eight-channel base unit of the all-optical holographic trigger; three wavelength states per channel yield 24 independent optical processing channels.

The first block is a frequency mode generator comprising three laser sources – red, green, and blue – whose output spatial mode structures are combined by a six-focal tele-translating laser system (6f-TTLS-Cn) into a unified spatial mode, matched in shape, size, and intensity distribution. Chromatic beam combining is performed by two dichroic mirrors and two total-reflectance mirrors.

The second block handles frequency synchronization and spatial filtering. A frequency synchronization unit aligns the optical frequencies of all sources, after which a four-focal spatial filter (4f-SF) groups, conditions, and retransmits the composite signal with initialized phases across all input frequencies. The unified beam then illuminates a monochromatic SLM, which generates the holographic frames for optical processing. A six-focal collimator system (6f-CS) adapts the SLM output to the trigger input parameters.

The third block is an all-optical trigger realized within a single bisphenol-derived polymer matrix, in which the holographic recording substrate is embedded. This monolithic structure comprises eight parallel optical pipelines, each processing all three wavelength states simultaneously. Four integrated sub-blocks perform sequential operations: an eight-channel holographic multiplexer (8-CTr), half-wave plate rotators (HWP) for polarization control, a six-focal depth-focus and video translation system (DF-6f-VTS) for chromatic propagation correction, and an output

filter synchronizing the color holographic frames for volumetric display.

At outputs OUT1–OUT8, the system delivers holographic frames at eight independently regulated focal depths, each carrying the three input colors, yielding 8 × 3 = 24 RGBD holographic frames for each individual SLM-generated input frame.

The HOE is recorded on silver halide holographic plates using three simultaneous laser sources: a He-Ne laser HNA-188 (λ = 632.8 nm), a Coherent Verdi V2 (λ = 532 nm), and a He-Cd laser KIMON (λ = 442 nm). Recording imposes stringent technical requirements: a spatial resolution exceeding 6000 line/mm, a precisely controlled exposure dose of 0.5–1 mJ/cm², and a diffraction efficiency averaging 50 % of the maximum, a level found to be adequate for experimental development and characterization.

The SLM operates at 90 monochromatic frames per second, corresponding to real-time RGB video transmission at 30 color frames per second, with color processing delegated entirely to the HOE. Each frame encodes 49 depth-resolved RGBD sub-frames, requiring 4410 sub-frames per second at 30 holo-frames per second – a computational load intractable for GPU-based real-time processing at 4K resolution, which the present architecture resolves through fully parallel optical computation.

Scaling the eight-channel base unit to the full 49-focal-plane architecture requires three identical optical polymer triggers combined through a multiplexor M, with the DF-6f-VTS of each configured for a distinct depth zone: post-focal (24 planes behind the screen), on-focal (1 plane coinciding with the screen surface), and pre-focal (24 planes in front of the screen). The 24-plane capacity per trigger follows from the 8 × 3 channel decomposition (8 phase states × 3 wavelengths), yielding a total of 49 independent focal planes and satisfying the minimum depth-plane requirement for perceptually correct volumetric 3D reconstruction [1, 3]. The 23 remaining channels of the third trigger are reserved for image calibration and auxiliary processing.

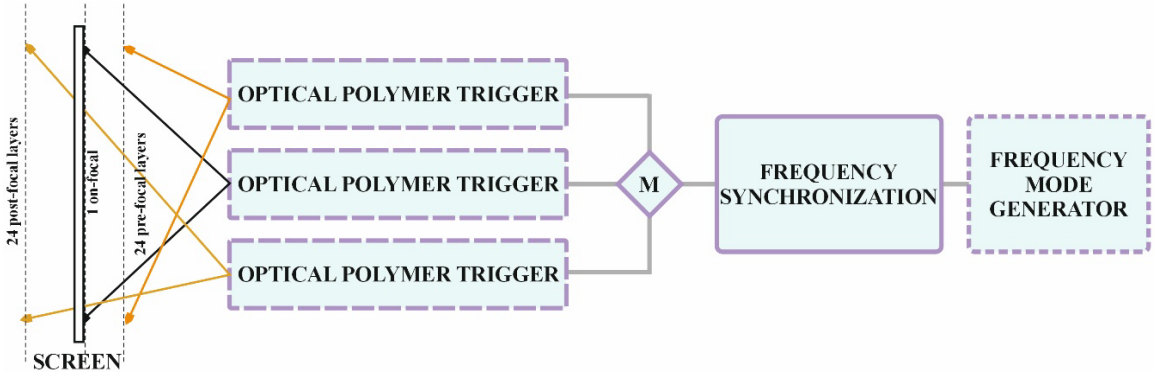

Fig. 2. Schematic of the 49-focal-plane architecture combining three optical polymer triggers through multiplexor M, yielding 24 post-focal, 1 on-focal, and 24 pre-focal image layers.

3. Experimental Implementation and Results

The present HOE is a volume reflection hologram implementing a 24-channel optical trigger system, recorded in a single-beam interferometer configuration with three wavelengths. This extends the approach established in [8].

The resulting system yields a minimum of 49 focal depth planes per holographic frame, distributed symmetrically about the nominal focal plane as 24 pre-focal layers, 1 on-focal layer, and 24 post-focal layers, collectively spanning the full volumetric depth range required for accurate reconstruction of dynamic holographic scenes.

Each channel incorporates a dedicated optical subsystem that performs an independently adjustable optical processing operation on the transmitted signal. Phase state encoding is achieved by rotating the HWP in successive steps of 10°, at angular positions of 0°, 10°, 20°, 30°, 40°, 50°, 60°, and 70°. As illustrated in Fig. 2, panels (a) through (h) show the progressive angular orientation of the HWP fast axis at each successive channel position, confirming the uniform distribution of polarization states. Combined with wavelength multiplexing, this assigns a distinct processing function to each of the 24 channels. This yields 8 × 3 = 24 independently encoded optical channels.

This wavelength parallelism multiplies the effective processing throughput threefold, with each channel carrying one independent optical function per laser color in the present three-wavelength configuration.

The HOE is recorded on Ultimate 04 (U04) silver halide holographic plates, an ultra-high sensitivity iso-panchromatic emulsion with a grain size of 4 nm, a spatial resolution of 18000 lines/mm, and a spectral sensitivity ranging from 440 nm to 700 nm [10]. The minimum recommended exposure energy is 320 µJ/cm² per laser for full-color recording, with a diffraction efficiency reaching up to 98 % for reflective HOE configurations.

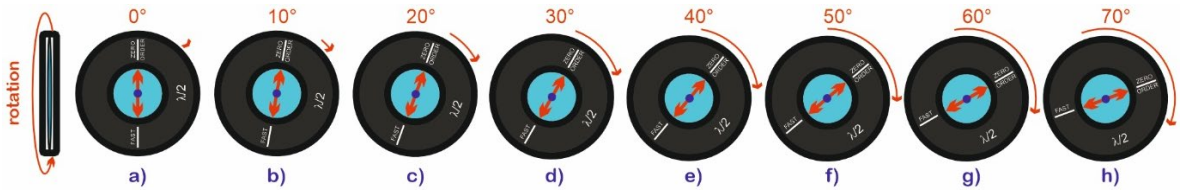

Fig. 3. Sequential HWP rotation in 10° steps for discrete phase state encoding across the 24-channel trigger; (a)–(h) denote the eight independent polarization channels from 0° to 70°.

Fig. 4 presents the measured diffraction efficiency distribution across the 8 channels of a prototype holographic optical trigger. The channel efficiencies span a range of about 20–50 %, with a mean value of approximately 35 %. This spread is consistent with the inherent non-uniformity of sequential multi-exposure recording in volume holographic media, where cumulative exposure and inter-grating coupling effects introduce channel-to-channel variation.

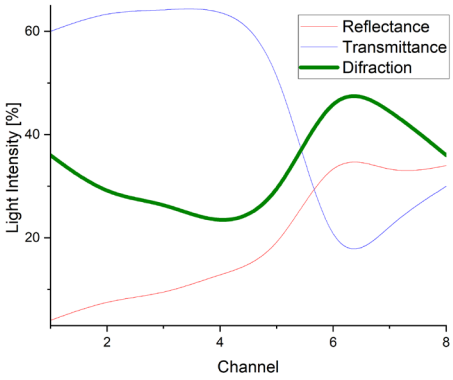

Fig. 4. Measured distributions of diffraction efficiency, transmittance, and reflectance across the 8 channels of the holographic optical trigger.

The measured mean efficiency of ~35 % is sufficient for the intended optical processing function. For channels exhibiting efficiencies at the lower bound of the observed range (~20 %), the reduction in diffracted power can be compensated by proportionally increasing the illumination intensity of the corresponding source – a correction requiring no more than a twofold increase in source power, sufficient to match the output level of the highest-efficiency channels, well within the operating range of standard diode laser drivers. This straightforward intensity-balancing scheme ensures uniform signal levels across all 8 channels without requiring re-optimization of the holographic recording process.

The observed range of approximately 20–50 % thus defines the practical operating window for this trigger architecture, and the results confirm that the fabrication protocol yields diffraction efficiencies adequate for real-time parallel optical processing in the 24-channel holographic display system.

As an example of the optical transfer function realizable within a single channel of the 24-channel trigger, we consider a 6-focal (6f) translator. In a standard 4-focal (4f) system, inserting an intermediate lens at the common focal plane leaves imaging unchanged; displacing it toward the input increases the optical power of the input stage, modifying the optical power ratio of the input and output stages and providing a continuously adjustable magnification – a real-time zoom function within the channel (Fig. 5).

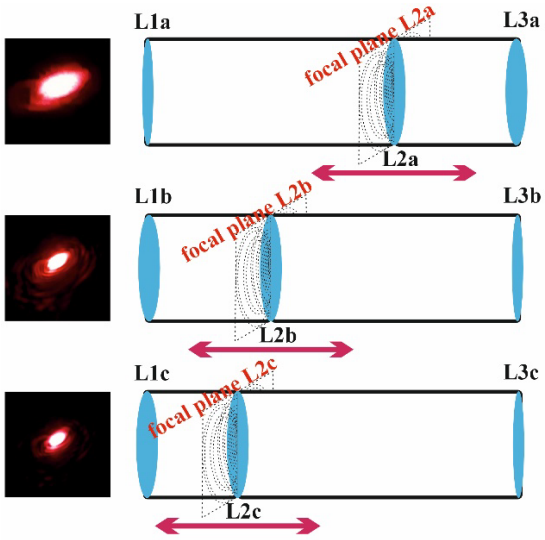

Fig. 5. Real-time zoom function within a single 6f channel: axial displacement of intermediate lens L2 (a)–(c) between L1 and L3 produces three independent focal planes, confirmed by the recorded beam profiles (left).

In the 6f configuration, replacing the intermediate lens with a tunable doublet enables real-time focal adjustment and continuous aberration correction across a range from negative to positive spherical aberration values; as an example, negative spherical aberration is compensated by introducing a positive focal shift, restoring diffraction-limited image quality without digital post-processing.

Crosstalk is suppressed when the overlap amplitude between adjacent Gaussian channel profiles remains below 12.5 % of their peak value – the condition corresponding to one inactive channel among the eight. By the Rayleigh/FWHM criterion for two identical Gaussian lines, channels are just resolved when their center separation Δ equals the FWHM

($\Delta \approx 2.3548\sigma$), corresponding to an overlap threshold of approximately 42 % of the peak. The 12.5 % overlap is well below this resolution limit, yielding 87.5 % channel purity and fully resolvable channel operation.

Polarization isolation is achieved by rotating the half-wave plate of each successive channel by 10°, distributing eight polarization states from 0° to 70°. Each channel occupies a distinct polarization subspace, preventing inter-channel interference and allowing independent processing of each assigned optical wavelength.

Within a single channel, the three wavelengths – 632.8 nm, 532 nm, and 442 nm – are propagated simultaneously without mutual interference, with a spectral spacing of about 90–100 nm sufficient to suppress beat-frequency artifacts and enable fully parallel three-wavelength processing.

4. Conclusions

The 24-channel all-optical holographic trigger presented here is realized as a volume reflection hologram within a single compact bisphenol-derived polymer device, extending our previous four-channel architecture [8] by a factor of six. By encoding eight phase states across three wavelength channels, the element generates a minimum of 49 sequential focal depth planes per holographic frame, ensuring accurate volumetric reproduction of dynamic holographic scenes entirely in the optical domain.

The fabricated prototype exhibits a diffraction efficiency of 20–50 % across all channels (mean ~35 %), with crosstalk suppression well below the Rayleigh/FWHM resolution limit – performance levels adequate for real-time parallel optical processing at computational throughputs intractable for GPU-based digital approaches.

The present architecture constitutes the foundational building block for a forthcoming 72-channel system, designed to satisfy the multilayer conditions required for full real-time volumetric holographic video display.

References

[1]. L. Shi, B. Li, W. Matusik, End-to-end learning of 3D phase-only holograms for holographic display, *Light: Science & Applications*, Vol. 11, 2022, 247.

[2]. N. Padmanaban, Y. Peng, G. Wetzstein, Holographic near-eye displays based on overlap-add stereograms, *ACM Transactions on Graphics*, Vol. 38, Issue 6, 2019, 214.

[3]. A. Gilles, P. Gioia, R. Cozot, L. Morin, Computer generated hologram from multiview-plus-depth data considering specular reflections, in *Proceedings of the IEEE International Conference on Multimedia Expo Workshops (ICMEW'16)*, 2016, pp. 1-6.

[4]. A. Klein, Dispersion compensation for reflection holography, Master's Thesis, *Massachusetts Institute of Technology*, Cambridge, 1996.

[5]. H. Wei, X. Liu, X. Hao, E. Y. Lam, et al., Modeling off-axis diffraction with the least-sampling angular spectrum method, *Optica*, Vol. 10, Issue 7, 2023, pp. 959-962.

[6]. C. M. E. Holden, S. C. J. Parker, P. J. Bryanston-Cross, Quantitative three-dimensional holographic interferometry for flow field analysis, *Optics and Lasers in Engineering*, Vol. 19, Issue 4-5, 1993, pp. 285-298.

[7]. M. Fujigaki, H. Minamino, Y. Murata, Interferometric trigger method with dual piezoelectric transducers for digital holographic interferometry, *Optical Engineering*, Vol. 57, Issue 11, 2018, 114105.

[8]. B. Ivanov, M. Shopova, A. Baldjiev, E. Stoykova, et al., Four-channel holographic infrared optical element, *Proceedings of SPIE*, Vol. 7747, 2011, 77470K.

[9]. H. N. Yum, P. R. Hemmer, A. Heifetz, J. T. Shen, et al., Demonstration of a multiwave coherent holographic beam combiner in a polymeric substrate, *Optics Letters*, Vol. 30, Issue 22, 2005, pp. 3012-3014.

[10]. P. Gentet, Y. Gentet, S.-H. Lee, The new reference for ultra-realistic color holography, in *Proceedings of the International Conference on Emerging Trends & Innovation in ICT (ICEI'17)*, 2017, pp. 162-166.

(014)

Two-Stage Hybrid Yb:YAG / Yb:LuAG Ultra-High Gain Chirped Pulse Amplifier

A. Grigaravičienė, P. Mackonis and A. M. Rodin
Center for Physical Sciences and Technology, Solid State Lasers Laboratory,
231 Savanoriu Ave, 02300 Vilnius, Lithuania
Tel.: +37067751413
E-mail: auguste.grigaraviciene@ftmc.lt

Summary: This study presents an advanced ultra-high gain chirped pulse amplifier incorporating an all-fiber seed laser, a quad-pass Yb:YAG preamplifier, and a double-pass Yb:LuAG booster-amplifier. The setup achieved a record-breaking small-signal gain of 60 dB in the first stage, delivering 0.5 mJ pulses at 100 Hz, while the second stage scaled them up to over 10 mJ, yielding a total system gain of nearly 70 dB. Precise polarization control ensured the effective suppression of parasitic oscillations, while the use of hybrid active media further improved the gain. The Pockels cell pulse divider effectively suppressed post-pulses and amplified spontaneous emission (ASE). Despite the substantial amplification, the system maintained an energy stability of 1.5 % (RMS) and excellent beam quality (M^2 = 1.07). By eliminating multiple fiber preamplifiers, this compact and cost-effective architecture enables the generation of intense ~1.3 ps pulses from a seed level of ~1 nJ.

Keywords: Yb:YAG, Yb:LuAG, Chirped pulse amplification, Picosecond pulses, Four-pass amplifier, ASE.

1. Introduction

High-energy ultrafast lasers play a vital role in industrial and scientific applications, ranging from high-precision material processing to advanced spectroscopy and high-field physics. Due to its high thermal conductivity and low quantum defect, the Yb:YAG gain medium has been widely adopted in chirped pulse amplifiers (CPAs) for the generation of high-energy pulses. However, achieving ultra-high gain in a compact and energy-efficient setup remains challenging, particularly when utilizing low-energy seed pulses directly from fiber oscillators. While Yb:YAG-based CPAs have demonstrated excellent energy scaling to the mJ-level [1, 2] in multi-pass and regenerative configurations, these approaches often suffer from gain narrowing, thermal lensing, and polarization distortions [3], which can degrade beam quality and pulse compressibility. Furthermore, fiber-based seed sources are limited by nonlinear effects in the preamplifiers as pulse energy increases.

We achieved an outstanding gain of ~10^6 by substantially redesigning the previously reported Yb:YAG CPA [4]. Precise polarization control suppressed parasitic oscillations in the quad-pass Yb:YAG CPA, enabling the amplification of nJ-level seed pulses to sub-mJ energies. This stage was followed by a double-pass Yb:LuAG booster-amplifier delivering pulses with energies exceeding 10 mJ. The integration of hybrid gain media facilitated gain scaling while maintaining a compressed pulse width of ~1.3 ps. The demonstrated approach paves the way for the development of compact, high-intensity laser systems.

2. Experiment

The redesigned CPA consists of a low-energy fiber seed laser, a quad-pass Yb:YAG preamplifier, and a booster-amplifier based on Yb:LuAG gain medium (Fig. 1). A passively mode-locked seed source delivered ~1 nJ pulses at 1030 nm, stretched to ~200 ps by an integrated fiber Bragg grating. Although eliminating the fiber preamplifiers resulted in a 6.5×10^3-fold reduction in seed energy, it enabled a simpler and lower-cost system design. The first modified Yb:YAG CPA stage incorporated two additional passes, requiring special measures to suppress parasitic lasing and mitigate induced depolarization at record gain. In the second CPA stage, the Yb:YAG rod was replaced by a Yb:LuAG crystal, offering better thermal conductivity and higher gain. The amplified pulses were compressed to ~1.3 ps in a four-pass transmission grating pulse compressor with a diffraction efficiency of ~97 %.

3. Results

Pulse amplification in a quad-pass configuration is highly sensitive to polarization, as it defines the beam path within the amplifier. Precise polarization control is therefore essential for both effective seeding and decoupling the output beam. In the previous double-pass CPA setup, two Faraday isolators were used to prevent back-reflected depolarized emission from reaching the seed laser. In the current quad-pass design, this issue is further exacerbated, since the depolarized components are rejected after two propagation passes. However, a small residual portion

(~0.1 %) of the induced depolarized component persists in the amplifier due to the finite extinction ratio of the polarizing optics. Consequently, spurious pulses were observed at the output (Fig. 2), separated by a 10.8 ns interval, which is consistent with the round-trip time of the double-pass Yb:YAG stage.

To suppress post-pulses and parasitic lasing, seed-pulse gating was implemented using a BBO Pockels cell and a polarizing cube on the last two propagation passes. The Pockels cell timing window and delay were meticulously optimized to eliminate residual pulses returning to the amplifier while reducing amplified spontaneous emission (ASE) to below 1 mW. This was achieved at a pulse repetition rates of 0.1 – 10 kHz and a pump power of ~100 W. Subsequently, the quad-pass Yb:YAG CPA demonstrated a record small-signal gain exceeding 60 dB (>0.5 × 10⁶ times), resulting in an output pulse energy of ~0.5 mJ (Fig. 3, red line).

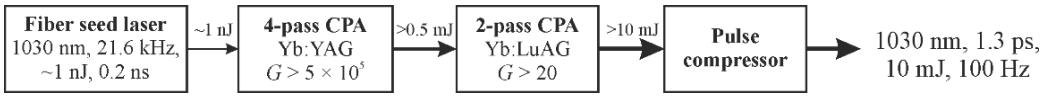

Fig. 1. Layout of high-gain chirped pulse amplifier, based on a four-pass Yb:YAG preamplifier followed by a two-pass Yb:LuAG booster-amplifier and grating pulse compressor.

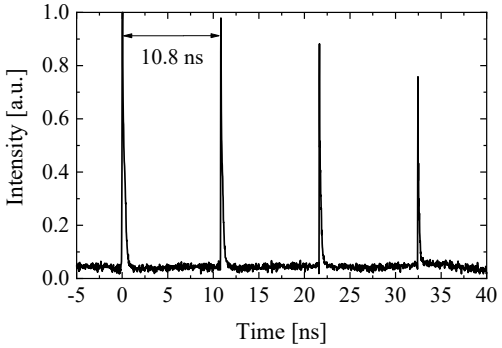

Fig. 2. Amplified pulses at the output of the quad-pass Yb:YAG CPA operated without a Pockels cell.

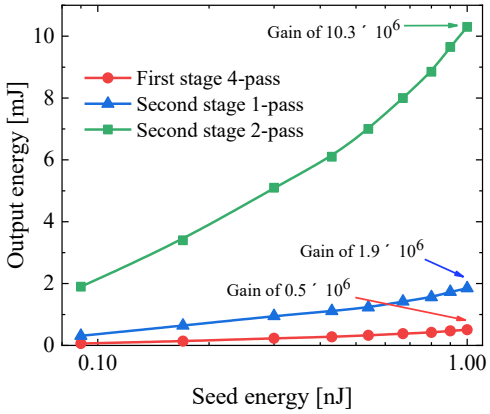

Fig. 3. Output energy as a function of seed energy after the quad-pass Yb:YAG (red line) and double-pass Yb:LuAG (blue and green lines) CPA stages.

The pulses exiting the first CPA stage were further amplified by a factor of ~20 in a second double-pass Yb:LuAG stage, yielding energies greater than 10 mJ. This enabled an overall signal gain of nearly 70 dB (>10 × 10⁶ times) when operating with the maximum input seed energy (Fig. 3, green line). Despite the substantial amplification, energy stability was well-maintained; the output pulse energy exhibited a stability of 1.54 % (RMS), representing only a marginal increase from the 1.3 % stability of the seed laser. The system also demonstrated an excellent beam quality factor of M^2 = 1.07 and a beam pointing stability of 4.1 µrad. Due to gain narrowing and the inherently narrower gain bandwidth of Yb:LuAG, the initial 3.6 nm seed spectrum was reduced to 1.3 nm. Nevertheless, pulses were compressed to ~1.3 ps, nearly reaching the close to the transform-limited duration of 1.26 ps.

4. Conclusions

An advanced ultra-high gain CPA was realized by combining a quad-pass Yb:YAG stage with a subsequent double-pass Yb:LuAG stage. This approach provides a record small-signal gain exceeding 60 dB in the first CPA stage, yielding an output energy of ~0.5 mJ at 100 Hz. The second CPA stage boosts the pulse energy to over 10 mJ, corresponding to an overall gain of ~70 dB. By comparison, our previously reported CPA system provided an overall gain of 40 dB. This performance is primarily attributed to precise polarization control using a BBO-based Pockels cell to suppress spurious pulses, and the optimized choice of gain medium in the second CPA stage. The amplified pulses were compressed to ~1.3 ps, approaching the transform limit. Future efforts will focus on achieving higher repetition rates

This research paves the way for the development of cost-effective and compact high-peak-power lasers designed for challenging applications in high-throughput material processing, high-field physics, nonlinear optics, and precision spectroscopy. In particular, the developed setup, delivering 1.3 ps pulses with an energy of ~10 mJ, has broad prospects for use in advanced table-top TW-class optical parametric chirped-pulse amplification (OPCPA) architectures in the near-IR [5] and mid-IR [6] ranges, enabling both efficient pumping and stable supercontinuum [7] generation. Furthermore, it can be

successfully applied to high-throughput direct laser interference patterning (DLIP) of metallic dies and stainless-steel rolls [8] for the subsequent embossing of polymer films imparting superhydrophobic [9] and other functional surface properties.

Acknowledgements

This research was funded by Research Council of Lithuania, grant number: S-LU-26-1.

References

[1]. I. Kuznetsov, I. Mukhin, O. Palashov, K. Ueda, Thin-rod Yb:YAG amplifiers for high average and peak power lasers, *Optics Letters*, Vol. 43, Issue 16, 2018, pp. 3941-3944.

[2]. J. Novák, J. Green, T. Metzger, T. Mazanec, et al., Thin disk amplifier-based 40 mJ, 1 kHz, picosecond laser at 515 nm, *Optics Express*, Vol. 24, Issue 6, 2016, pp. 5728-5733.

[3]. J. Lee, H. Kim, K. Um, J. Park, et al., Compensation of polarization distortion of a laser beam in a four-pass Nd:glass amplifier by using a Faraday rotator, in *Proceedings of the Advanced Solid State Lasers (ASSL'96),* 1996, HP6.

[4]. P. Mackonis, A. M. Rodin, Laser with 1.2 ps, 20 mJ pulses at 100 Hz based on CPA with a low doping level Yb:YAG rods for seeding and pumping of OPCPA, *Optics Express*, Vol. 28, Issue 2, 2020, pp. 1261-1268.

[5]. P. Mackonis, A. Rodin, OPCPA investigation with control over the temporal shape of 1.2 ps pump pulses, *Optics Express*, Vol. 28, Issue 8, 2020, pp. 12020-12027.

[6]. A. Petrulenas, P. Mackonis, A. M. Rodin, High-efficiency bismuth borate-based optical parametric chirped pulse amplifier with ~2.1 mJ, 38 fs output pulses at ~2150 nm, *High Power Laser Science and Engineering*, Vol. 11, 2023, e53.

[7]. P. Mackonis, A. Petrulenas, V. Girdauskas, A. M. Rodin, Stable 1100–2400 nm supercontinuum in YAG with picosecond pumping for simplified OPCPA, in *Proceedings of the Conference on Lasers and Electro-Optics Europe and European Quantum Electronics Conference (CLEO/Europe-EQEC'19)*, 2019, ca_p_43.

[8]. H. Sun, J. Li, M. Liu, D. Yang, et al., A review of effects of femtosecond laser parameters on metal surface properties, *Coatings*, Vol. 12, Issue 10, 2022, 1596.

[9]. S. Caragnano, et al., Femtosecond laser-engineered molds for long-term stable superhydrophobic polydimethylsiloxane (PDMS) surfaces, *Advanced Materials Interfaces*, Vol. 12, 2025, e00808.

(015)

Probing the Role of the Dangling Bonds on the Ultrafast Excited Charge Carriers' Relaxation Dynamics in Silicon Nanocrystals

Yazhou Xu [1], Anas Bokhari [1], Bernard Gelloz [2], Qingyan Han [3] and Andrey Kaplan [1]
[1] University of Birmingham, Department of Physics and Astronomy. Birmingham, B15 2TT, UK
[2] Nagoya University, Furo-cho, Chikusa-ku, Nagoya, 464-8601, Japan
[3] School of Electronic Engineering, Xi'an University of Posts & Telecommunications, Xi'an 710121, China
Tel.: + 44 7741766209
E-mail: YXX773@student.bham.ac.uk

Summary: Our investigation explores the role of surface dangling bonds within the interconnected silicon nanocrystal network of porous silicon, elucidating their pivotal impact on ultrafast carrier relaxation. Employing femtosecond pump–probe spectroscopy, Fourier-transform infrared spectroscopy (FTIR), and time-resolved photoluminescence, we establish that thermal annealing enhances the density of defect states, thereby increasing non-radiative recombination and diminishing emission. Conversely, high-pressure water-vapour annealing (HWA) effectively passivates nanocrystal surfaces, markedly restoring carrier lifetimes and photoluminescence intensity. These findings provide quantitative evidence that links surface chemistry within the nanocrystal network to carrier dynamics on femtosecond-to-picosecond timescales, offering a strategic avenue for engineering defect-controlled relaxation phenomena in silicon-based optoelectronic and photonic devices.

Keywords: Porous silicon, Photoluminescence, Ultrafast.

1. Introduction

Silicon nanostructures, particularly porous silicon composed of interconnected silicon nanocrystals, have long been regarded as promising materials for silicon-based optoelectronics. Their compatibility with standard CMOS technology and their size-dependent optical properties offer a viable pathway toward integrated light-emitting and sensing devices. However, the optical response of porous silicon is heavily influenced by its surface chemistry [1]. The large internal surface area leads to surface-related defects that significantly affect carrier recombination pathways. Among these defects, dangling bonds create localised electronic states within the bandgap, serving as efficient non-radiative recombination centres that reduce radiative efficiency and shorten carrier lifetimes.

Various surface passivation techniques have been explored; however, many studies rely primarily on steady-state photoluminescence or long-term lifetime measurements, which provide limited insight into the initial stages of carrier relaxation, where defect-assisted processes dominate [2]. Ultrafast spectroscopic methods are essential for directly investigating carrier dynamics on femtosecond to picosecond timescales and for clarifying the relationship between surface chemistry and recombination mechanisms [3].

This study thoroughly investigates the impact of oxidative surface passivation on carrier relaxation dynamics in porous silicon [3, 4]. This work builds upon our previous research, where oxidation was limited through controlled annealing, which did not yield a well-structured passivation layer. Through subsequent treatment with HWA, the quality of passivation can be substantially enhanced, allowing for a detailed examination of its effects on relaxation processes. By combining ultrafast pump–probe spectroscopy with FTIR analysis and both continuous-wave and time-resolved photoluminescence measurements, we establish a direct correlation between the density of surface dangling bonds and radiative as well as non-radiative recombination processes. Systematic comparisons involving thermal annealing and subsequent high-pressure water vapour treatments provide insights into the role of surface oxidation in modulating carrier dynamics in nanostructured silicon.

2. Experimental Methods

Porous silicon specimens were produced through electrochemical etching of crystalline silicon wafers utilising a wet chemical process. The etching parameters were selected to achieve nanoscale porous silicon layers with an approximate thickness of 80 μm and a porosity of roughly 75 %, thereby resulting in a highly developed internal surface comprised of interconnected silicon nanocrystals.

Post-fabrication annealing treatments were employed to modify the surface passivation and defect density. Thermal annealing (TA) was carried out in a tube furnace at 450 °C for 300 s under a continuous flow of 99 % pure nitrogen, limiting uncontrolled oxidation while promoting surface restructuring.

Following thermal annealing, selected samples were subjected to high-pressure water vapour annealing (HWA). The procedure was conducted at a

water vapour pressure of 2.6 atm for 4 hours. This treatment aimed to improve the oxidative passivation of the porous silicon surface and to decrease the density of dangling bonds generated during thermal annealing.

Surface bonds were analysed using Fourier-transform infrared (FTIR) spectroscopy, with particular attention given to vibrational modes associated with Si–H and Si–O–Si bonds. Photoluminescence (PL) spectra were measured using an excitation wavelength of 532 nm. Carrier recombination dynamics were examined through femtosecond pump–probe spectroscopy. The probe beam had a wavelength of 2.5 μm, while the pump beam had a wavelength of 800 nm, both with durations of approximately 80 fs.

3. Results and Discussion

Surface chemistry (FTIR). Fig. 1 compares the FTIR transmittance spectra of porous-silicon membranes following the different post-etch treatments. Thermal annealing produces a clear reduction of Si–H stretching features alongside enhanced Si–O–Si vibrational modes [4], indicating incomplete oxidation and a concomitant rise in surface defect density (dangling bonds) across the large internal area of the porous network. In contrast, high-pressure water-vapour annealing (HWA) increases the signatures associated with a high-quality oxide while suppressing residual hydride-related features, consistent with effective passivation of the internal nanocrystal surfaces. These spectral trends establish the chemical origin of the subsequent changes in recombination pathways.

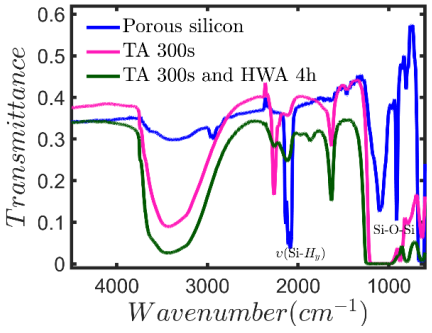

Fig. 1. FTIR transmittance spectra of porous silicon (PSi) samples under different annealing conditions: as-prepared (blue), thermally annealed for 300 s (pink), and high-pressure water vapour annealing (HWA) at 2.6 atm for 4 h following the 300 s TA (green).

Steady-state photoluminescence (PL). The FTIR-inferred increase in dangling-bond density after thermal annealing correlates with a pronounced quenching of the PL intensity (Fig. 2), providing evidence of an enhanced non-radiative channel that competes with radiative recombination in the silicon nanocrystals. Since the emitting centres are located on an interconnected network of nanocrystals that constitute the porous silicon skeleton, defect states on individual nanocrystals can influence carrier migration and capture across adjacent domains, thereby amplifying their impact on ensemble emission. Following HWA, the PL not only recovers but is significantly enhanced relative to the thermally annealed state, which is consistent with a reduction in surface-defect density and improved exciton confinement at well-passivated nanocrystal/oxide interfaces [5].

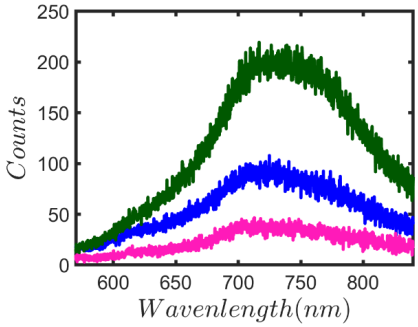

Fig. 2. PL spectra of PSi samples measured at 532 nm excitation: as-prepared (blue), thermally annealed for 300 s (pink), and subsequent HWA treatment at 2.6 atm for 4 h (green). The spectra illustrate the influence of different thermal processes on the emission properties of PSi.

Ultrafast carrier dynamics (pump–probe). Femtosecond pump–probe measurements provide a direct, time–resolved observation of the defect–mediated relaxation pathways (Fig. 3). Thermally annealed samples exhibit a markedly accelerated decay component of ~70 picoseconds in the normalised transient-transmittance traces, reflecting a substantial rise in the non-radiative recombination rate that we attribute to the increased dangling-bond density identified by FTIR and manifested by the PL quenching. Quantitatively, the non-radiative relaxation is faster by roughly a factor of ~20 compared with freshly prepared samples which have a recovery time > 1.2 nanoseconds. In samples subsequently treated with HWA, the fast defect-assisted channel is strongly suppressed: the carrier lifetime of ~220 picoseconds extends by approximately a factor of ~3–4 relative to the thermally annealed state, indicating effective passivation of the internal nanocrystal surfaces throughout the porous skeleton [6].

The combined analysis of FTIR, photoluminescence (PL), and ultrafast spectroscopy presents a coherent sequence of cause-and-effect relationships: (i) oxidation processes influence the density of surface dangling bonds as detected by FTIR; (ii) these defects introduce non-radiative pathways that suppress steady-state emission observed in PL measurements; and (iii) these identical pathways predominate the femtosecond to picosecond relaxation

processes within the interconnected silicon nanocrystal network, as evidenced by pump–probe experiments. The deliberate transition from defect-rich surfaces following thermal annealing to defect-poor interfaces after HWA exemplifies a viable methodology for engineering ultrafast carrier relaxation in nanostructured silicon. Beyond enhancing photoluminescence efficiency, this approach is highly relevant to ultrafast laser–matter interactions, where surface chemistry modulation enables precise control over sub-nanosecond recombination dynamics – a critical factor for the development of silicon-based photonic emitters, sensors, and integrated optoelectronic devices.

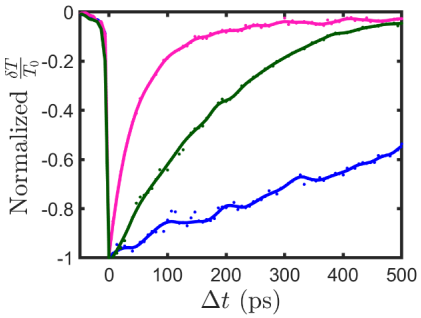

Fig. 3. Normalised transient transmittance change ($\delta T/T_0$) of PSi samples as a function of pump-probe delay time under various annealing conditions. Blue: as-prepared PSi; Pink: thermally annealed PSi (300 s); Green: PSi subjected to high-pressure water vapour annealing (HWA, 2.6 atm, 4 h) following a 300 s thermal pre-treatment.

4. Conclusions

This work demonstrates that carrier relaxation in porous silicon is strongly governed by the density of surface dangling bonds within its interconnected nanocrystal network. FTIR, photoluminescence, and ultrafast pump–probe spectroscopy jointly show that thermal annealing increases defect-mediated non-radiative recombination, while high-pressure water-vapour annealing effectively passivates these defects and restores longer carrier lifetimes. By directly correlating surface chemistry with femtosecond–picosecond relaxation dynamics, the study identifies a clear pathway for tailoring recombination processes in nanostructured silicon for optoelectronic and photonic applications.

Acknowledgements

We thank the School of Physics and Astronomy at the University of Birmingham for providing the Moreton Fund.

References

[1]. H. R. J. Simpson, N. Sadeghi, T. Chutora, R. A. Wolkow, et al., Ultrafast terahertz dynamics of dangling bonds on the Si(100)-2x1 surface, in *Proceedings of the 50th International Conference on Infrared, Millimeter, and Terahertz Waves (IRMMW-THz'25)*, 2025, pp. 1-2.

[2]. M. Rashidi, J. Burgess, M. Taucer, R. Achal, et al., Time-resolved single dopant charge dynamics in silicon, *Nature Communications*, Vol. 7, 2016, 13258.

[3]. A. Zakar, R. Wu, D. Chekulaev, V. Zerova, et al., Carrier dynamics and surface vibration-assisted Auger recombination in porous silicon, *Physical Review B*, Vol. 97, Issue 15, 2018, 155203.

[4]. R. Wu, E. Nekovic, J. Collins, C. J. Storey, et al., Taming non-radiative recombination in Si nanocrystals interlinked in a porous network, *Physical Chemistry Chemical Physics*, Vol. 24, Issue 22, 2022, pp. 13519-13526.

[5]. B. Gelloz, A. Kojima, N. Koshida, Highly efficient and stable luminescence of nanocrystalline porous silicon treated by high-pressure water vapor annealing, *Applied Physics Letters*, Vol. 87, Issue 3, 2005, 031107.

[6]. C.-L. Guo, L. Wang, Y.-R. Zhang, H.-F. Zhou, et al., High-pressure water-vapor annealing for enhancement of a-Si:H film passivation of silicon surface, *Chinese Physics Letters*, Vol. 31, Issue 10, 2014, 108501.

(016)

Au-Ag Impregnated Porous Silicon Offering Broad-Band SERS Response, Enhanced Detection Volume, and High Internal Surface Area

F. Alayed[1, 2], Q. Han[3], Y. Xu[2], A. Bokhari[2] and A. Kaplan[2]
[1] King Saud bin Abdulaziz University for Health Sciences (KSAU-HS), Riyadh, Saudi Arabia
[2] University of Birmingham, School of Physics and Astronomy,
Edgbaston, Birmingham B152TT, UK
[3] Xi'an University of Posts & Telecommunications, School of Electronic Engineering,
Xi'an 710121, China
Tel.: +447500478634, E-mail: Faisal.alayed1@gmail.com

Summary: We present a bimetallic Au–Ag plasmonic SERS substrate in which a thin, porous silicon layer is impregnated with hybrid nanoparticles to broaden the scope of plasmonic excitation. The high-porosity (~77 %) porous silicon layer offers a substantial internal surface area, while its three-dimensional impregnation with Au/Ag nanoparticles results in an extended excitation volume rich in accessible hot spots. Structural and optical properties were examined using SEM, EDX, and reflectance spectroscopy, and the SERS performance was evaluated under 532 nm and 633 nm excitation wavelengths. The combined Au–Ag system provides a broadened and efficient plasmonic response, enabling strong, wavelength-flexible SERS enhancement. Raman signatures of Rhodamine 6G remain detectable at picomolar concentrations, demonstrating stable and reliable trace-level detection. An enhancement factor of approximately 4.7×10^9 substantiates the platform's potential for high-sensitivity chemical and bioanalytical sensing, aligning with emerging applications in photonic sensors.

Keywords: SERS, Thin porous silicon, Bimetallic Au/Ag nanoparticles, Immersion plating, Rhodamine 6G.

1. Introduction

Surface-Enhanced Raman Spectroscopy (SERS) offers a pathway for highly sensitive molecular detection by amplifying Raman scattering through localised surface plasmon resonance (LSPR) in metallic nanostructures [1]. The most substantial enhancement is typically observed in nanoscale regions such as tips and interparticle gaps that support intense electromagnetic fields, commonly referred to as hot spots. The integration of silver (Ag) and gold (Au) within a single SERS substrate enhances the density and spectral diversity of plasmonic hot spots by leveraging the complementary optical properties of both metals. This strategy concurrently addresses their individual limitations: while Ag provides a more robust electromagnetic enhancement, it is vulnerable to oxidation and chemical instability. Conversely, Au exhibits chemical resilience and biocompatibility but offers a weaker and narrower plasmonic response. The hybrid Au–Ag arrangement thus facilitates broader excitation ranges and more diverse hot-spot environments, resulting in more reliable and wavelength-flexible SERS performance [1–3].

Achieving high sensitivity alongside uniformity and reproducibility necessitates precise control over nanostructure morphology and analyte access to plasmonic sites. Porous silicon, characterised by a three-dimensional scaffold with high surface area and tunable pore structure, can host plasmonic nanostructures throughout its depth, thereby increasing the number of accessible active sites [4–7].

This type of nanostructured silicon can also support optical localisation effects that help concentrate light within the structured silicon environment [8].

In this study, for the first time, thin, porous silicon was sequentially embedded with gold (Au) and silver (Ag) nanoparticles via a wet-chemical immersion method to form a bimetallic plasmonic composite [4, 5]. This method differs from previous approaches where gold and silver were co-deposited. By adjusting metal-ion concentrations and deposition durations, precise control of Au and Ag loadings within the porous silicon is achieved. This process results in a semi-pore-filled architecture that maintains pore openness while accommodating a high density of plasmonically active sites. The present investigation demonstrates that the sequential incorporation of gold (Au) and silver (Ag) into a thin, high-porosity porous silicon scaffold produces a bimetallic structure that broadens the detectable volume while preserving the large internal surface area of the porous layer. The resulting configuration enables efficient analyte penetration and deep-volume SERS excitation under both 532 nm and 633 nm illumination. Under these conditions, the substrate achieves picomolar detection limits for Rhodamine 6G with an enhancement factor of approximately 4.7×10^9, thereby confirming its high sensitivity and wavelength-flexible performance. Such high enhancement can be attributed to plasmonic mode localisation confined by the silicon environment. It has been demonstrated that the electric field of the plasmonic mode is highly concentrated, as it is focused within a few tens of nanometers of the surface of the embedded particles [9]. These findings exemplify an

effective approach for integrating multi-metal plasmonic functionalities within a compact porous silicon platform, offering significant advantages for broadband and ultrasensitive chemical detection.

Compared to our previous research on embedded gold nanoparticles [6], we expanded the methodology to sequentially deposit silver, thereby extending the excitation bandwidth to shorter wavelengths. Additionally, the porosity of the matrix material is increased to facilitate easier penetration of the analyte, enabling deeper infiltration to a few microns.

2. Experimental Methods

2.1. Thin Porous Silicon Fabrication

Thin porous silicon was fabricated through electrochemical anodization of heavily boron-doped silicon in an electrolyte comprising 40 % hydrofluoric acid (HF) mixed with methanol in a 1:1 volume ratio. Anodization at a current density of 100 mA for 3 minutes yielded a layer thickness of approximately 3 μm and an estimated porosity of approximately 77 %, as determined by gravimetric analysis and corroborated by cross-sectional scanning electron microscopy (SEM).

2.2. Au/Ag Nanoparticles Growth and Analyte Deposition

Gold and silver nanoparticles were synthesised within the pores via electroless immersion plating. Prior to metals deposition, porous silicon was immersed in a 2 % hydrofluoric acid (HF) solution in ethanol to remove native oxide layers and facilitate hydride termination. Gold deposition was performed from a 0.5 mM $HAuCl_4$ solution in ethanol using ultrasonic agitation for 4 min. Subsequently, silver deposition was conducted from a 1 mM $AgNO_3$ solution in ethanol under ultrasonic agitation for ten minutes. Ethanol rinsing steps were implemented to enhance liquid penetration and to facilitate the release of hydrogen gas from the pores. Rhodamine 6G was deposited by immersing the substrate in ethanol solutions with concentrations ranging from 1 μM to 1 pM, under ultrasonic agitation for 5 minutes, followed by drying under a nitrogen atmosphere.

2.3. Raman Spectroscopy, Scanning Electron Microscopy (SEM), Energy Dispersive X-ray (EDX) Analysis, and Optical Measurements and Characterisation

Raman spectra were acquired utilising a high-sensitivity confocal Raman microscope (Renishaw inVia, England), employing excitation wavelengths of 532 nm and 633 nm. A 50× objective was used to focus the laser beam and collect the Raman signal, while multiple laser power levels were tested at both wavelengths with an integration time of 10 seconds. The morphology and structural characteristics of the samples were examined through scanning electron microscopy (SEM), and the elemental composition was verified via energy-dispersive X-ray microanalysis (EDX) using an INCA PentaFETx3 X-ray spectrometer (Oxford Instruments, England). Optical reflectance spectra were obtained to assess variations in optical response following impregnation, utilizing a Bruker FTIR Hyperion microscope equipped with a 50× objective.

3. Results and Discussion

The high porosity of the thin porous silicon layer provides an extensive internal surface area for metal loading and analyte accommodation, forming the foundation for a deep-volume SERS-active scaffold. Under the selected deposition conditions, Au and Ag nanoparticles distribute throughout both the surface and within the pore network, creating a semi–pore–filled architecture rather than fully occluding the pores. This morphology is corroborated in Fig. 1, where the surface SEM (Fig. 1b) exhibits dense nanoscale features associated with plasmonic junctions, while the cross-sectional SEM (Fig. 1c) illustrates the penetration of bimetallic particles on the top of approximately 3 μm porous layer. The EDX spectrum (Fig. 1d) confirms the presence of both Au and Ag, and the reflectance variations in (Fig. 1e) suggest changes in the optical response following metallization. Collectively, these observations verify the successful formation of a bimetallic Au/Ag network within the porous architecture, establishing the structural foundation for the enhanced SERS performance discussed in subsequent sections.

The Surface-Enhanced Raman Scattering (SERS) enhancement factor was evaluated in (Fig. 2a) by comparing the Raman signal obtained from R6G adsorbed onto the Au–Ag/PSi substrate with that acquired from a non-enhancing reference sample measured under identical optical conditions. For this analysis, the 610 cm^{-1} vibrational band of R6G was selected due to its robust, well-defined intensity and consistent presence across various concentrations. The integrated peak area from the SERS spectrum was divided by the corresponding integrated area measured on the reference substrate, with appropriate scaling to account for the relative number of probed molecules in each case. Employing this methodology, the bimetallic Au–Ag/PSi system exhibited an enhancement factor of approximately 4.7×10^9, signifying a dense distribution of highly active plasmonic sites throughout the porous layer. This exceptionally large enhancement aligns with the semi–pore-filled architecture, which facilitates analyte access and excitation throughout the approximately 3 μm porous depth and supports strong electromagnetic coupling within nanoscale junctions formed by the Au/Ag nanoparticles.

The Au–Ag/PSi composite was employed to explore the apparent detection limit of analyte

concentration. Specifically, the analyte was subjected to Surface-Enhanced Raman Spectroscopy (SERS) testing over a range from an upper limit of 1 mM to the lowest detectable signal, observed at 1 pM. The corresponding SERS spectra are presented in Fig. 2b. It is evident that the SERS signal intensity diminishes with dilution; however, characteristic bands remain discernible down to picomolar concentrations, demonstrating high sensitivity facilitated by Au and Ag nanoparticles dispersed throughout the porous silicon matrix.

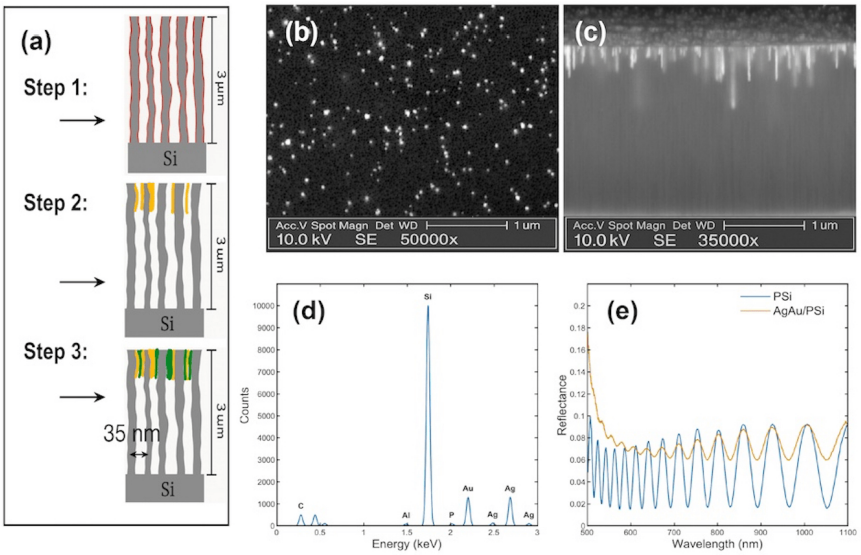

Fig. 1. Characterization of the Au/Ag/PSi composite: (a) schematic of the main preparation steps, including (1) removal of the native oxide by HF, (2) gold deposition, and (3) silver deposition; (b) surface SEM image; (c) cross-sectional SEM image; (d) EDX spectrum; and (e) reflectance spectra.

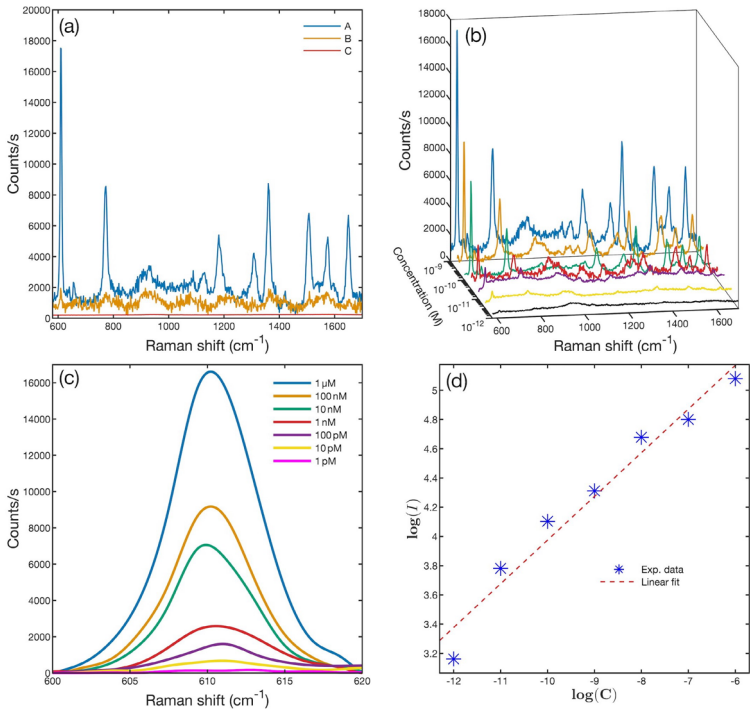

Fig. 2. (a) Raman spectra comparing 1 µM R6G on the Au–Ag/PSi substrate (blue), porous silicon exposed to 100 mM R6G (gold), and the Au–Ag/PSi substrate without R6G (red), all recorded under 532 nm excitation, (b) Raman spectra measured for R6G concentrations ranging from 1 pM to 1 mM, demonstrating the broad dynamic range of the substrate, (c) Integrated intensity of the 610 cm^{-1} Raman band as a function of R6G concentration, showing sensitivity across multiple orders of magnitude, (d) Log–log representation of Raman intensity versus R6G concentration for the 610 cm^{-1} peak, illustrating the characteristic concentration-dependent response of the substrate.

To quantify the concentration-dependent response, the 610 cm^{-1} peak (illustrated in Fig. 2c) was selected. The peak area was integrated and plotted on a log-log scale against concentration. This representation facilitates the assessment of the concentration–intensity relationship across multiple orders of magnitude and uncovers a distinct power-law dependence. Fitting the data with a linear model in log–log space yields the effective scaling exponent, which indicates the efficiency of the SERS signal's increase with analyte concentration. The near-linear trend observed herein demonstrates that the Au–Ag/PSi substrate supports proportional signal growth across the examined range, with no indication of early hotspot saturation or limited analyte access. This behaviour affirms that the semi-pore-filled architecture supports uniform hotspot distribution and consistent deep-volume excitation, thereby underpinning the composite's broad dynamic range.

4. Conclusions

We have demonstrated that thin, high-porosity porous silicon can be sequentially loaded with gold (Au) and silver (Ag) to form a unified bimetallic network, thereby confirming the reliable integration of the two metals within a three-dimensional scaffold. The resulting semi-pore-filled architecture maintains pore openness and extends the effective detection volume, facilitating analyte access and surface-enhanced Raman scattering (SERS) excitation throughout the approximately 3 μm layer. When excited at 532 nm and 633 nm, the substrate exhibits high sensitivity, achieving picomolar-level detection of R6G with an enhancement factor of approximately 4.7×10^9, thereby demonstrating wavelength-flexible performance from a compact platform. Although the study does not assess spatial uniformity across a large area, we believe the approach can be refined to achieve industrial-grade material. Collectively, these findings establish a practical approach to integrating multiple plasmonic metals within porous silicon to realize deep-volume, high-surface-area SERS sensing suitable for photonic sensor applications.

References

[1]. P. Yu, C. Shen, X. Yin, J. Cheng, et al., Au-Ag bimetallic nanoparticles for surface-enhanced Raman scattering (SERS) detection of food contaminants: A review, *Foods*, Vol. 14, Issue 12, 2025, 2109.

[2]. M. Kong, Y. Wu, D. Men, Q. Ding, et al., Preparation of hydrophobic porous Au-Ag alloy nanoparticle arrays and their SERS properties, *RSC Advances*, Vol. 13, Issue 51, 2023, pp. 36181-36187.

[3]. S. Zhao, Y. Zhang, Y. Wang, S. Yang, et al., Nanopores-coupled SERS platforms on superslippery surfaces using Au&Ag alloy pillars for biomolecules enrichment and detection, Rare Metals, Vol. 44, Issue 12, 2025, pp. 10404-10417.

[4]. F. Zhong, Z. Wu, J. Guo, D. Jia, Porous silicon photonic crystals coated with Ag nanoparticles as efficient substrates for detecting trace explosives using SERS, *Nanomaterials*, Vol. 8, Issue 11, 2018, 872.

[5]. N. D. Thien, T. H. Dang, S. C. Doanh, L. Q. Thao, et al., A study on fabrication of SERS substrates based on porous Si nanostructures and gold nanoparticles, *Journal of Materials Science: Materials in Electronics*, Vol. 34, Issue 2, 2023, 94.

[6]. R. Wu, Q. Jin, C. Storey, J. Collins, et al., Gold nanoplasmonic particles in tunable porous silicon 3D scaffolds for ultra-low concentration detection by SERS, *Nanoscale Horizons*, Vol. 6, Issue 10, 2021, pp. 781-790.

[7]. M. T. Hoang, H. Bui, T. H. C. Hoang, V. H. Pham, et al., Silver nanoparticles-decorated porous silicon microcavity as a high-performance SERS substrate for ultrasensitive detection of trace-level molecules, *Nanomaterials*, Vol. 15, Issue 13, 2025, 1007.

[8]. L. A. Osminkina, K. A. Gonchar, V. S. Marshov, K. V. Bunkov, et al., Optical properties of silicon nanowire arrays formed by metal-assisted chemical etching: Evidences for light localization effect, *Nanoscale Research Letters*, Vol. 7, Issue 1, 2012, 524.

[9]. R. Wu, T. Mathieu, C. J. Storey, Q. Jin, et al., Localized plasmon field effect of gold clusters embedded in nanoporous silicon, *Advanced Optical Materials*, Vol. 9, Issue 9, 2021, 2002119.

(017)

Orthogonal Sampling Expansions for Finite Fresnel Transform

T. Aoyagi and K. Ohtsubo
Toyo University, Faculty of Information Sciences and Arts, Kujirai 2100, Kawagoe Saitama, Japan
Tel.: + 81 080-1143-8267
E-mail: t-aoyagi@toyo.jp

Summary: Fresnel transform has been widely used in many optical application areas and formulated mathematically. In this paper, we focused mainly on spatially band-limited effect in Fresnel transform plane. By using double Fourier series in finite region, the sampling theorem for Fresnel transform pair in rectangular coordinate system is derived. In the side result, new orthogonal functional systems which are expressed by the integral equation are induced. Its orthogonal functional systems are formulated and the properties are revealed. In application of the sampling theorem, any elements in Hilbert space can be expressed by linear combination of the orthonormal or orthogonal functional systems and its inner products. In computer simulations, we consider the application of our sampling theorem to the problem of approximating any function to demonstrate its validity. We showed that if the number of orthogonal functional systems increase, a normalize mean square error for an original function decrease sufficiently.

Keywords: Fresnel transform, Double Fourier series, Orthogonal functional system, Sampling theorem, Approximation error.

1. Introduction

Fresnel diffraction patterns diffracted by a plane object have been treated as orthogonal integral transforms of amplitude transmittance of the object. The Fresnel transformation of optical image was formulated mathematically and developed with respect to functional analytic method. By solving Rayleigh integral equation approximately for small diffraction angles where wave field is source free, the Fresnel transform operator can be derived. The Fresnel transform has been shown to be a bounded additive, a one-parameter group of unitary and factor-type operators from its algebraic and topological properties in Hilbert space $H(E_2)$ which is constituted by any continuous complex-valued square-integrable functions in the two-dimensional Euclidean space [1-3]. It can be of one-parameter transformation group geometrically. These properties of Fresnel transform operator are induced by the Rayleigh diffraction operator. In recently, it is used in image processing, optical information processing, optical waveguides, computer-generated holograms, Fresnel hologram, phase retrieval techniques, speckle pattern interferometry and so on [4-11].

In optical signal processing, up to data, spatially band-limited effectiveness has been considered and studied with respect to Fourier transform pair. By band-limited effect in Fourier transform plane, sampling functional systems have been derived and shown its orthogonal property. From sampling theorem about the Fourier transform, orthogonal functional systems were formulated from the point of view of functional analysis [12, 13]. In generalized sampling theorem, orthogonal functional systems are an important tool in both engineering and mathematics. In the literature, there are many sampling theorems and examples about the Fourier transform. Its applications and reference therein [14, 15].

In general, an optical Fourier transform is composed of Fresnel diffraction and finite convex lens. To compute the amplitude distribution precisely and analyze the optical property, it is necessary and crucial to reveal the band-limited effect in Fresnel diffraction plane. Moreover, the property of the orthogonal function about finite Fresnel transforms which restricted by the finite area is not revealed sufficiently yet.

In our previous papers [16-18], we have sought the function that its total power in finite Fresnel transform plane is maximized, on condition that an input signal is zero outside the bounded region. This leads to the eigenvalue problems of Fredholm integral equation of the first kind. We confirmed the dual orthogonal property of the eigen functional systems of the integral equation. By discretizing the integral equation, its orthonormal functional systems and the properties have been revealed.

In this paper, the band-limited effect in Fresnel transform plane is investigated. By considering spatial band-limited effect and using a double Fourier series expansion, the sampling theorem for Fresnel transform pair in rectangular coordinate system is derived. In the side result, new orthogonal functional systems which are expressed by the integral equation are induced. Its orthogonal functional systems are formulated and the properties are revealed. In computer simulations, we consider the application of our sampling theorem to the problem of an approximating a function in Hilbert space to demonstrate its validity. By fixing the parameters, a concrete orthogonal functional system is constructed. We show that if the number of orthogonal functional systems increase for the orthogonal sampling expansions, approximating error which is

defined by the normalized mean square error decrease sufficiently.

2. Fresnel Transform

The diffracting aperture is assumed to lie in the (ξ,η) plane, and is illuminated in the positive z direction. We will calculate the wavefield across the (x,y) plane and at normal distance z from it. The z axis pierces both planes at their origins. Fig. 1 shows a general optical system and its coordinate system. If the function $f(\xi,\eta)$ represents the amplitude transmittance, the diffracted amplitude distribution $g(x,y;z)$ at a point $(x,y;z)$ for Fresnel approximation can be assumed by

$$g(x,y;z) = \frac{k\exp(ikz)}{i2\pi z}\iint_{-\infty}^{\infty} f(\xi,\eta)\times \\ \times \exp\left[\frac{ik}{2z}\{(x-\xi)^2+(y-\eta)^2\}\right]d\xi d\eta, \quad (1)$$

where $i = \sqrt{-1}$ and k is the wave number which is given by $k = 2\pi/\lambda$, λ is the wavelength. The inverse Fresnel transform is defined by

$$f(\xi,\eta) = -\frac{k\exp(-ikz)}{i2\pi z}\iint_{-\infty}^{\infty} g(x,y;z)\times \\ \times \exp\left[-\frac{ik}{2z}\{(x-\xi)^2+(y-\eta)^2\}\right]dxdy \quad (2)$$

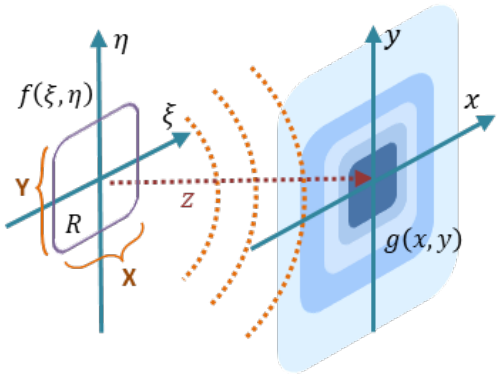

Fig. 1. Sketch of a general optical system and its coordinate system.

3. Double Fourier Series

Double Fourier series is Fourier series on a square and have been applied in various areas [19-22].

Let $f(x,y)$ be integrable in the square $|x|\le\pi, |y|\le\pi$ which represent any integrable 2π-periodic function on $\mathbb{R}$. Then, we can define the double Fourier series, that is,

$$f(x,y) = \\ = \sum_{m=-\infty}^{\infty}\sum_{n=-\infty}^{\infty} D_{mn}\exp(imx)\exp(iny) \quad (3)$$

where the coefficient D_{mn} is given by

$$D_{mn} = \frac{1}{(2\pi)^2}\int_{-\pi}^{\pi}\int_{-\pi}^{\pi} f(x,y)\times \\ \times \exp\{-i(mx+ny)\}dxdy \quad (4)$$

If $(x,y)\in L^P([-\pi,\pi]\times[-\pi,\pi])$ for some $p>1$, then $f(x,y)$ in eq. (3) converges for almost all $(x,y)\in[-\pi,\pi]\times[-\pi,\pi]$.

4. Orthogonal Functional System

Consider a spatial band-limited signal $f(\xi,\eta)$ with the Fresnel transform $g(x,y,z)$. We denote by R the rhombus region in object plane, and denote by $C_R(\xi,\eta)$ its characteristic function,

$$C_R(\xi,\eta) = \begin{cases} 1 & (\xi,\eta)\in R \\ 0 & (\xi,\eta)\notin R \end{cases} \quad (5)$$

Since the given function multiplied by $\exp\{ik(\xi^2+\eta^2)/2z\}$ is limited within the rectangular region R, it can be expanded in a double Fourier series within this region

$$f(\xi,\eta)\exp\left\{\frac{ik}{2z}(\xi^2+\eta^2)\right\} = C_R(\xi,\eta)\times \\ \times\sum_{m=-\infty}^{\infty}\sum_{n=-\infty}^{\infty} B_{mn}\exp\left(\frac{i2\pi m\xi}{X}+\frac{i2\pi n\eta}{Y}\right) \quad (6)$$

The Fourier coefficient B_{mn} is given by

$$B_{mn} = \frac{1}{XY}\iint_R f(\xi,\eta)\exp\left(-\frac{i2\pi m\xi}{X}-\frac{i2\pi n\eta}{Y}\right)\times \\ \times\exp\left\{\frac{ik}{2z}(\xi^2+\eta^2)\right\}d\xi d\eta = \\ = \frac{1}{XY}\exp\left[-\frac{ik}{2z}\left\{\left(\frac{2\pi mz}{kX}\right)^2+\left(\frac{2\pi nz}{kY}\right)^2\right\}\right]\times \\ \times\iint_R f(\xi,\eta)\exp\left\{\frac{ik}{2z}\left(\frac{2\pi mz}{kX}-\xi\right)^2\right\}\times \\ \times\exp\left\{\frac{ik}{2z}\left(\frac{2\pi nz}{kY}-\eta\right)^2\right\}d\xi d\eta, m,n\in\mathbb{Z} \quad (7)$$

From eq. (1) and (7), we can obtain the relation of the coefficient B_{mn} and Fresnel transform $g(.)$, that is

$$B_{mn} = \frac{i2\pi z}{kXY\exp(ikz)}\times \\ \times\exp\left[-\frac{ik}{2z}\left\{\left(\frac{2\pi mz}{kX}\right)^2+\left(\frac{2\pi nz}{kY}\right)^2\right\}\right]\times \\ \times g\left(\frac{2\pi mz}{kX},\frac{2\pi nz}{kY};z\right) \quad (8)$$

Substituting this into eq. (2), we have

$$f(\xi,\eta) = \frac{i2\pi z}{kXY\exp(ikz)}\exp\left\{-\frac{ik}{2z}(\xi^2+\eta^2)\right\}\times \\ \times C_R(\xi,\eta)\sum_{m=-\infty}^{\infty}\sum_{n=-\infty}^{\infty} g\left(\frac{2\pi mz}{kX},\frac{2\pi nz}{kY};z\right)\times \\ \times\exp\left[-\frac{ik}{2z}\left\{\left(\frac{2\pi mz}{kX}\right)^2+\left(\frac{2\pi nz}{kY}\right)^2\right\}\right]\times \\ \times\exp\left(\frac{i2\pi m\xi}{X}+\frac{i2\pi n\eta}{Y}\right) \quad (9)$$

By taking the Fresnel transforms of both sides in eq. (9), we have the following the sampling expansion.

$$\begin{aligned} g(x,y;z) &= \frac{1}{XY}\exp\left\{\frac{ik}{2z}(x^2+y^2)\right\}\times \\ &\times\sum_{m=-\infty}^{\infty}\sum_{n=-\infty}^{\infty} g\left(\frac{2\pi mz}{kX},\frac{2\pi nz}{kY};z\right)\times \\ &\times\exp\left[-\frac{ik}{2z}\left\{\left(\frac{2\pi mz}{kX}\right)^2+\left(\frac{2\pi nz}{kY}\right)^2\right\}\right]\times \\ &\times\iint_R C_R(\xi,\eta)\exp\left\{\frac{ik}{z}\left(\frac{2\pi m\xi z}{kX}+\frac{2\pi n\eta z}{kY}\right)\right\}\times \\ &\times\exp\left\{-\frac{ik}{z}(x\xi+y\eta)\right\}d\xi d\eta = \\ &= \sum_{m=-\infty}^{\infty}\sum_{n=-\infty}^{\infty} g\left(\frac{2\pi mz}{kX},\frac{2\pi nz}{kY};z\right)S_{mn}(x,y,z) \end{aligned} \tag{10}$$

where sampling functional systems S_{mn} can be of the following.

$$\begin{aligned} S_{mn}(x,y,z) &= \frac{1}{XY}\exp\left\{\frac{ik}{2z}(x^2+y^2)\right\}\times \\ &\times\exp\left[-\frac{ik}{2z}\left\{\left(\frac{2\pi mz}{kX}\right)^2+\left(\frac{2\pi nz}{kX}\right)^2\right\}\right]\times \\ &\times\iint_R C_R(\xi,\eta)\exp\left\{i\left(\frac{2\pi m\xi}{X}+\frac{2\pi n\eta}{Y}\right)\right\}\times \\ &\times\exp\left\{-i\left(\frac{kx\xi}{z}+\frac{ky\eta}{z}\right)\right\}d\xi d\eta \end{aligned} \tag{11}$$

Definition 1. Let $\{S_{mn}(x,y;z)\}_{m,n\in\mathbb{Z}}$ be sampling functional systems in an optical Fresnel transform region.

Theorem 2. If the amplitude distribution $f(\xi,\eta)$ is limited within a finite region R in an optical system, by using the discrete sampling values $\left\{g\left(\frac{2\pi mz}{kX},\frac{2\pi nz}{kY};z\right)\right\}_{m,n\in\mathbb{Z}}$, the Fresnel transform $g(x,y;z)$ can be expanded as eq. (10).

This is the sampling theorem on Fresnel transform pair in rectangular coordinate. From the symmetricalness of Fresnel transform pair, the following corollary can be derived.

Corollary 3. If the amplitude distribution $g(x,y;z)$ is limited with in a finite region S in Fresnel diffraction plane, by using discrete sampling value $\left\{f\left(\frac{2\pi mz}{kX},\frac{2\pi nz}{kY}\right)\right\}_{m,n\in\mathbb{Z}}$ and the sampling functional systems, the invers Fresnel transform $f(\xi,\eta)$ can be expanded, that is,

$$\begin{aligned} f(\xi,\eta) &= \\ &= \sum_{m=-\infty}^{\infty}\sum_{n=-\infty}^{\infty} f\left(\frac{2\pi mz}{kX},\frac{2\pi nz}{kY}\right)S_{mn}(\xi,\eta;z) \end{aligned} \tag{12}$$

The sampling functional system is defined by

$$\begin{aligned} S_{mn}(\xi,\eta;z) &= \frac{1}{XY}\exp\left\{-\frac{ik}{2z}(\xi^2+\eta^2)\right\}\times \\ &\times\exp\left[\frac{ik}{2z}\left\{\left(\frac{2\pi mz}{kX}\right)^2+\left(\frac{2\pi nz}{kX}\right)^2\right\}\right]\times \\ &\times\iint_S C_S(x,y)\exp\left\{i\left(\frac{2\pi mx}{X}+\frac{2\pi ny}{Y}\right)\right\}\times \\ &\times\exp\left\{-i\left(\frac{k\xi x}{z}+\frac{k\eta y}{z}\right)\right\}dxdy \end{aligned} \tag{13}$$

Theorem 4. Sampling functional systems $S_{mn}(x,y;z)$ form a complete orthogonal system in Hilbert space.

A set of orthogonal functions $\{S_{mn}(\xi,\eta)\}_{m,n\in\mathbb{Z}}$ is termed complete in the closed interval $(\xi,\eta)\in X\times Y$ if, for every piecewise continuous function $f(\xi,\eta)$ in the interval, the minimum square error converges to zero with respect to a weighting function $w(\xi,\eta)$, that is,

$$\begin{aligned} &\lim_{s,t\to\infty}\iint_R |f(\xi,\eta)-\sum_{m=0}^{s}\sum_{n=0}^{t} a_m b_n S_{mn}|^2\times \\ &\times\lim_{s,t\to\infty}\iint_R |f(\xi,\eta)-\sum_{m=0}^{s}\sum_{n=0}^{t} a_m b_n S_{mn}|^2 \end{aligned} \tag{14}$$

where the above integral is a Lebesgue integral.

If R is a rectangle with side $2a$ and $2b$ shown in Fig. 2, then sampling functional systems $S_{mn}(x,y,z)$ can be obtain concretely, i.e.

$$\begin{aligned} S_{mn}(x,y;z) &= \frac{1}{4ab}\exp\left\{\frac{ik}{2z}(x^2+y^2)\right\}\times \\ &\times\exp\left[-\frac{ik}{2z}\left\{\left(\frac{\pi mz}{ka}\right)^2+\left(\frac{\pi nz}{kb}\right)^2\right\}\right]\times \\ &\times\int_{-a}^{a}\int_{-b}^{b}\exp\left\{i\left(\frac{m\pi\xi}{a}+\frac{n\pi\eta}{b}\right)\right\}\times \\ &\times\exp\left\{-\frac{ik}{z}(x\xi+y\eta)\right\}d\xi d\eta\times= \\ &= \exp\left\{\frac{ik}{2z}(x^2+y^2)-\frac{i\pi^2m^2z}{2ka^2}-\frac{i\pi^2n^2z}{2kb^2}\right\}\times \\ &\times\frac{1}{m\pi-\frac{kxa}{z}}\sin\left(m\pi-\frac{kxa}{z}\right)\times \\ &\times\frac{1}{n\pi-\frac{kyb}{z}}\sin\left(n\pi-\frac{kyb}{z}\right) \end{aligned} \tag{15}$$

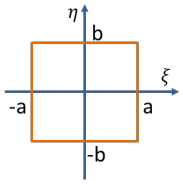

Fig. 2. A fixed finite region in rectangular coordinate.

Proof of Theorem 4: Restricted finite region in integral range of the sampling functional system, the sampling functional system are calculated concretely as eq. (15). The sampling functional systems is composed of chirp function and Sinc function [23]. By the orthogonality of Sinc function and modification of chirp function, the sampling functional system can be of orthogonal system. Moreover, by the completeness of Sinc function and the property of chirp function, the sampling functional system can be of complete. ■

5. Computer Simulations

To simplify the discussion, we consider only one-dimensional functional systems. By computer simulations, we consider the application of the above sampling theorem to the problem of approximating a function to demonstrate its validity.

5.1. Sampling Expansion in Functional Space

Let us consider the reformulation of the sampling problem from generalized functional spaces. Assume

that f is defined on a subset D and belongs to a complex Hilbert space denoted by H. For any element f in H, using orthonormal basis $\{\varphi_n\}_{n=1}^{N}$, we can write

$$f = \sum_{n=1}^{N} \langle f, \varphi_n \rangle \varphi_n, \tag{16}$$

where $\langle \cdot, \cdot \rangle$ is an inner product. The inner product can be expressed by using discrete sampling value $\{x_n\}$ and weighting factors $\{w_n\}$ as following.

$$\langle f, \varphi_n \rangle = w_n f(x_n) \tag{17}$$

Then, eq. (16) can be rewritten, that is

$$f(x) = \sum_{n=1}^{\infty} w_n f(x_n) \varphi_n(x) \tag{18}$$

$\{\varphi_n\}_{n=1}^{\infty}$ is said to be an orthonormal sampling basis [24].

By restricted only x-direction, we can obtain the following functional systems from eq. (15).

$$S_m(x) = \exp\left\{\frac{i}{2}\left(x^2 - \frac{\pi^2 m^2}{x^2}\right)\right\} \times \times \frac{\sin(ax - m\pi)}{ax - m\pi}, \tag{19}$$

where we set $y = 0, n = 0$ and $k/z = 1.0$. Fig. 3 shows one-dimensional sampling functional systems which eq. (19) is fixed parameters and discretized by 100 points at equal distance. Because of complex-valued function, it plots the both of real and imaginary part.

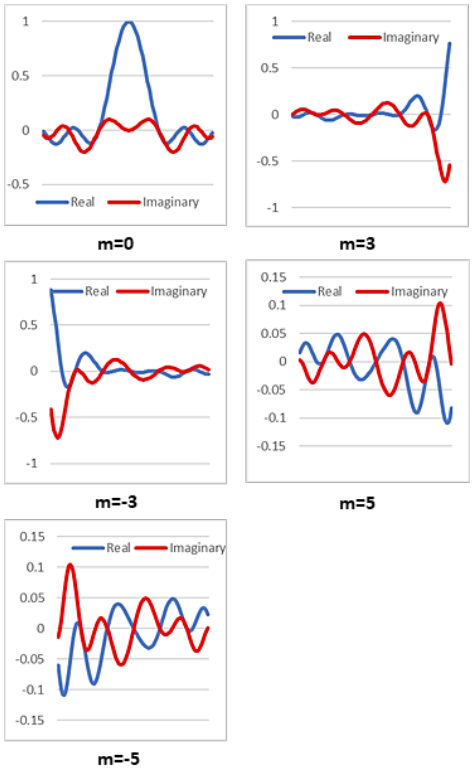

Fig. 3. Discretized version of one-dimensional sampling functional systems.

5.2. Approximation of Any Functions

It was confirmed that original test vector can be expressed by the sampling functional expansions in eq. (16) and (18). To set the concrete sampling functions, it is necessary to decide the parameters, such as k, z, a.

Let us consider a following real value test function.

$$f(x) = Sin(\mathrm{cx})\ \mathrm{x} \in [0, 2\pi[, c \in \mathbb{N} \tag{20}$$

By discretizing the test function evenly-spaced at 100 points, we created test vectors in 100-dimensional real valued vector space ($\mathbb{R}^{100}$). Fig. 4(a) shows original test vector. In this case, we set $X = 20.0$, $a = 10.0$ and other parameters were fixed a constant. Fig.4 (b) shows reconstructed vector when the number of sampling functions is 101.

Fig. 5 illustrates the mean square error versus the number of sampling functions. The normalized mean square error (NMSE) is defined by

$$\mathrm{NMSE}(n) = \frac{\|u^n - u\|_2}{\|u\|_2}, \tag{21}$$

where u^n is the sum up to n, u is the original vector and $\|\cdot\|_2$ is the ℓ^2-norm [25]. From Fig. 5, we can see that the error decreases with increasing number of sampling functions used in the expansion. Up to about 60, error decreases rapidly. But after 60 error is sufficiently small and decreases slowly. It means that the function can be sufficiently well approximated by at least about 60 sampling functions in this condition.

To confirm the effect of the parameter "a" in eq. (19), it can be changed from 2.0 to 16.0. In this case, we set the number of sampling functions is 101. Fig. 6 illustrates the mean square error versus parameter "a" of sampling functions. From Fig. 6, we can see that NMSE is increasing mainly around "a = 12". This variation depends on the original test function.

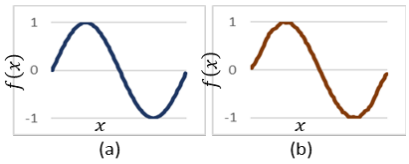

Fig. 4. (a) Original test function $f(x) = Sin(x)$, $x \in [0, 2\pi[$, (b) Reconstructed function with sampling functional systems.

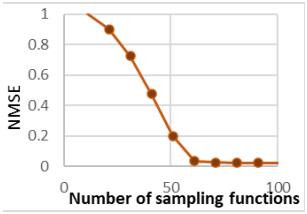

Fig. 5. Plots of normalized mean square error versus the number of sampling functions.

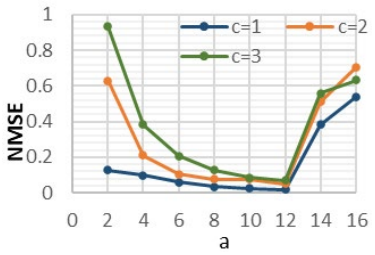

Fig. 6. Plots of normalized mean square error versus the parameter "a".

6. Conclusions

We have investigated the band-limited effect in Fresnel transform plane. By considering spatial band-limited effect and using a double Fourier series, the sampling theorem for Fresnel transform pair in rectangular coordinate system was derived. By setting the parameters, any concrete functional systems were constructed and plotted. We applied it to the problem of approximating a function and evaluated the error. We confirmed the validity of the sampling theorem for finite Fresnel transform by computer simulations.

References

[1]. N. Aoyagi, Theoretical study of optical Fresnel transformations, PhD Thesis, *Tokyo Institute of Technology*, Tokyo, 1973.

[2]. N. Aoyagi, S. Yamaguchi, Functional analytic formulation of Fresnel diffraction, *Japanese Journal of Applied Physics*, Vol. 12, Issue 3, 1973, pp. 366-370.

[3]. N. Aoyagi, S. Yamaguchi, Generalized Fresnel transformations and their properties, *Japanese Journal of Applied Physics*, Vol. 12, Issue 9, 1973, pp. 1343-1350.

[4]. D. P. Kelly, Numerical calculation of the Fresnel transform, *Journal of the Optical Society of America A*, Vol. 31, Issue 4, 2014, pp. 755-764.

[5]. Z. Zalevsky, D. Mendlovic, R. G. Dorsch, Gerchberg-Saxton algorithm applied in the fractional Fourier or Fresnel domain, *Optics Letters*, Vol. 21, Issue 12, 1996, pp. 842-844.

[6]. F. Gori, Fresnel transform and sampling theorem, *Optics Communications*, Vol. 39, Issue 5, 1981, pp. 293-297.

[7]. F. Gori, The converging prolate spheroidal functions and their use in Fresnel optics, *Optics Communications*, Vol. 45, Issue 1, 1983, pp. 5-10.

[8]. D. F. V. James, G. S. Agarwal, The generalized Fresnel transform and its application to optics, *Optics Communications*, Vol. 126, Issue 4-6, 1996, pp. 207-212.

[9]. M. Liebling, T. Blu, M. Unser, Fresnelets: New multiresolution wavelet bases for digital holography, *IEEE Transactions on Image Processing*, Vol. 12, Issue 1, 2003, pp. 29-43.

[10]. A. VanderLugt, Optimum sampling of Fresnel transform, *Applied Optics*, Vol. 29, Issue 23, 1990, pp. 3352-3361.

[11]. F. S. Roux, Complex-valued Fresnel-transform sampling, *Applied Optics*, Vol. 34, Issue 17, 1995, pp. 3128-3135.

[12]. H. Ogawa, What can we see behind sampling theorems?, *IEICE Transactions on Fundamentals*, Vol. E92-A, Issue 3, 2009, pp. 688-695.

[13]. H. Ogawa, A Theory of Pseudobiorthogonal Bases and Its Applications, *University of Tokyo Press*, Tokyo, 2020 (in Japanese).

[14]. A. J. Jerri, The Shannon sampling theorem - its various extensions and applications: A tutorial review, Proceedings of the IEEE, Vol. 65, Issue 11, 1977, pp. 1565-1596.

[15]. T. Kida, On restoration and approximation of multi-dimensional signals using sample values of transformed signals, *IEICE Transactions on Fundamentals*, Vol. E77-A, Issue 7, 1994, pp. 1095-1116.

[16]. T. Aoyagi, K. Ohtsubo, N. Aoyagi, Fredholm integral equation for finite Fresnel transform, in *Proceedings of the 6th International Conference on Photonics, Optics and Laser Technology (PHOTOPTICS'18)*, 2018, pp. 286-291.

[17]. T. Aoyagi, K. Ohtsubo, N. Aoyagi, Band-limited orthogonal functional systems for optical Fresnel transform, in *Proceedings of the 7th International Conference on Photonics, Optics and Laser Technology (PHOTOPTICS'19)*, 2019, pp. 147-153.

[18]. T. Aoyagi, K. Ohtsubo, Numerical analysis of orthogonal functional systems for finite Fresnel transform, *Optical Review*, Vol. 30, Issue 3, 2023, pp. 376-386.

[19]. M. Razzaghi, A. Arabshahi, S. D. Lin, Analysis of linear distributed parameter systems via double Fourier series, *Applied Mathematics and Computation*, Vol. 87, Issue 2-3, 1997, pp. 205-215.

[20]. H. Watanabe, Summability of double Fourier series, *Tohoku Mathematical Journal*, Vol. 17, 1965, pp. 150-160.

[21]. S. Mildenberger, M. Quellmalz, Approximation properties of the double Fourier sphere method, *Journal of Fourier Analysis and Applications*, Vol. 28, Issue 2, 2022, 31.

[22]. H.-B. Cheong, Double Fourier series on a sphere: Applications to elliptic and vorticity equations, *Journal of Computational Physics*, Vol. 157, Issue 1, 2000, pp. 327-349.

[23]. J. W. Goodman, Introduction to Fourier Optics (3rd Ed.), *Roberts & Company*, Englewood, 2005.

[24]. H. Ogawa, Functional Analysis, *Morikita Publishing Company Limited*, Tokyo, 2010 (in Japanese).

[25]. M. Reed, B. Simon, Methods of Modern Mathematical Physics, Vol. 1, *Academic Press*, New York, 1972.

(018)

Generation of Multiphoton States by Multiplexing Heralded Photon Sources with Optimized Input

B. M. Szilasi, M. Mechler and P. Adam
Institute of Physics, University of Pécs, Ifjúság útja 6, H-7624 Pécs, Hungary
Institute for Solid State Physics and Optics, Wigner Research Centre for Physics, P.O. Box 49, H-1525 Budapest, Hungary
E-mail: adam.peter@wigner.hun-ren.hu

Summary: We show that the multiphoton probabilities of spatially multiplexed multiphoton sources can be increased by optimizing the input mean photon numbers for each input of the multiplexer separately. We determine the achievable multiphoton probabilities for multiphoton states up to five photons against the number of multiplexed units for various set of the loss parameters. We analyze the performance spatially multiplexed two-photon sources in more detail. We discuss the dependence of the advantage of using optimized input mean photon numbers for each input of the multiplexer on the loss parameters of the system. We determine the optimal number of multiplexed units corresponding to maximal values of the output two-photon probabilities for a range of the transmission coefficients characterizing the photon routers.

Keywords: Fock-state generation, Multiphoton source, Spatial multiplexing.

1. Introduction

Reliable multiphoton sources are required for several quantum optics experiments and quantum technology applications [1–3]. One technique suitable for generating multiphoton states is based on heralded photon sources, in which photon pairs are generated through some nonlinear optical process. Detecting a given number of photons in the idler mode using a photon-number-resolving detector heralds the presence of the corresponding multiphoton state in the signal mode. This technique has also been successfully applied to produce single-photon states. The probabilistic nature of heralded photon sources can be compensated by multiplexing [4–6]. In the case of spatially multiplexed single-photon sources, many heralded photon sources are used in parallel. Reducing the mean photon number of the photon pairs generated in each individual source while simultaneously operating many sources ensures a high single-photon probability and a low multiphoton contribution.

Recently, spatial multiplexing of heralded multiphoton sources for the generation of multiphoton states was proposed [7]. The statistical theory developed to describe multiplexed single-photon sources [6, 8–11] can be extended to multiplexed multiphoton sources as well. Using this theory, it becomes possible to determine the optimal input mean photon number and the optimal number of multiplexed units for which the output i-photon probability is maximal. In [7] it has been shown that optimized spatially multiplexed multiphoton sources can be used to generate multiphoton states with considerably higher multiphoton probabilities than those that can be achieved with a single heralded multiphoton source. In that paper, minimum-based, maximum-logic, output-extended incomplete binary-tree multiplexers (OMAXV) comprised of asymmetric binary photon routers were applied, and identical input mean photon numbers were assumed in the multiplexed units.

In this communication we show that the output i-photon probability of spatially multiplexed multiphoton sources can be further increased by optimizing the input mean photon number separately for each input of the OMAXV multiplexer.

2. Statistical Framework

For spatially multiplexed multiphoton sources containing photon-number-resolving detectors and assuming different input mean photon numbers in the multiplexed units, the probability that j photons appear at the output is

$$P_j = \prod_{k=1}^{N}\left[1-P_k^{(D)}(i)\right]\delta_{i,0} + \sum_{n=1}^{N}\left\{\prod_{k=1}^{n-1}\left[1-P_k^{(D)}(i)\right]^{(1-\delta_{1,n})} \times \sum_{l=i}^{\infty} P^{(D)}(i|l)P_n^{(\lambda_n)}(l)V_n(j|l)\right\} \quad (1)$$

Here we assumed that the detectors produce a signal only if i photons were detected. In the above equation $P_n^{\lambda_n}(l)$ denotes the probability that l photons were produced in the nth multiplexed unit when the input mean photon number is λ_n. For $P_n^{\lambda_n}(l)$ we assume thermal probability distribution. $P^{(D)}(i|l)$ is the probability that the detector registered i photons out of l incoming photons, while $P_n^{(D)}(i)$ represents the probability of any event where i photons were detected. These quantities read as

$$P^{(D)}(i|l) = \binom{l}{i} V_D^i (1-V_D)^{(l-i)}, \quad (2)$$

and

$$P_n^{(D)}(i) = \sum_{l=i}^{\infty} P^{(D)}(i|l) P_n^{(\lambda_n)}(l), \quad (3)$$

where V_D is the detector efficiency. The quantity $V_n(j|l)$ is the conditional probability that out of the l photons generated in the nth multiplexed unit j photons reached the output, which can be calculated as

$$V_n(j|l) = \binom{l}{j} V_n^j (1-V_n)^{l-j}, \quad (4)$$

where V_n is called the total transmission probability of the nth arm of the multiplexer and characteristic of each multiplexer type. For the OMAXV type multiplexers it is defined in [11], and it is the function of the V_b, V_r and V_t parameters. V_b is the general transmission coefficient which we fix at $V_b = 0.98$. The V_r and V_t transmission coefficients describe the loss assigned to the two inputs of the asymmetric photon routers. Using the described statistical theory, the optimal input mean photon numbers $\lambda_{n,\mathrm{opt}}$ in the multiplexed units and the optimal number of multiplexed units N_{opt} can be determined.

3. Results

First, we calculated the highest achievable multiphoton probabilities $P_{i,N}^{\lambda_n}$ up to an overall number of multiplexed units N, by finding the optimal input mean photon numbers $\lambda_{n,\mathrm{opt}}$ for each multiplexed unit, for various sets of the loss parameters. The values of the different input mean photon numbers λ_n were optimized by using sequential quadratic programming. The optimization procedure scales practically linearly with the number of inputs of the multiplexer; hence it can be performed even on standard computers.

As an example, in Fig. 1 we present results for multiphoton states up to five output photons for the detector efficiency $V_D = 0.9$ and the transmission coefficients $V_r = V_t = 0.95$ which set can be realized experimentally. It can be seen that local maxima are present where low-loss arms appear in the multiplexer. Comparing these results with our previous calculations where we assumed identical input mean photon numbers λ_{opt} at each multiplexed unit, we found that using different input mean photon numbers results in higher multiphoton probabilities for all values of N and for every multiphoton state i.

In Fig. 2 we show the difference $\Delta P_{2,N} = P_{2,N}^{\lambda_n} - P_{2,N}^{\lambda}$ between the achievable two-photon probabilities $P_{2,N}^{\lambda_n}$ and $P_{2,N}^{\lambda}$ of multiplexed multiphoton sources based on OMAXV multiplexers assuming different and identical input mean photon numbers λ_n and λ, respectively. The figure shows that the magnitude of the advantage is considerably different for various sets of the loss parameters and for various values of the number of multiplexed units. In all cases, the highest advantage can be observed close to the local minima of the multiphoton probabilities found in Fig. 1. In general, we have found that for lower detector efficiencies the advantage is higher for a fixed set of transmission coefficients.

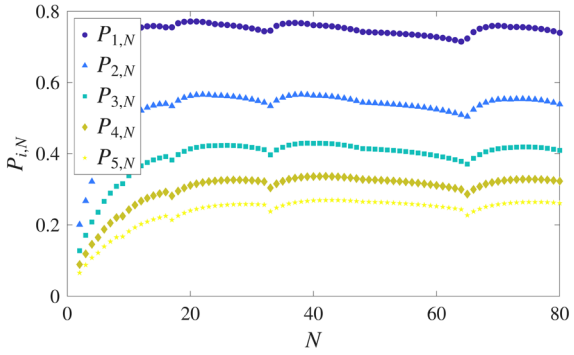

Fig. 1. The achievable i-photon probabilities $P_{i,N}$ of multiplexed single- and multiphoton sources based on OMAXV multiplexers as functions of the number of multiplexed units N for $V_r = V_t = 0.95$ and $V_D = 0.9$.

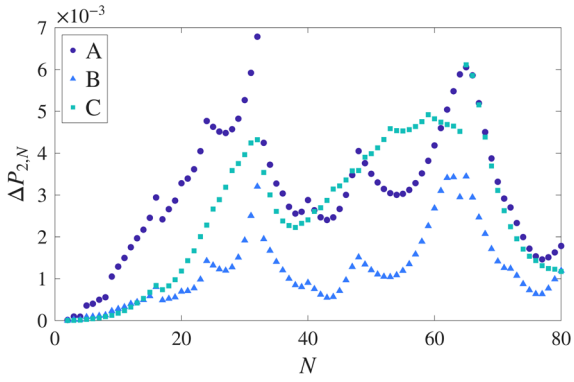

Fig. 2. The difference $\Delta P_{2,N} = P_{2,N}^{\lambda_n} - P_{2,N}^{\lambda}$ between the achievable two-photon probabilities $P_{2,N}^{\lambda_n}$ and $P_{2,N}^{\lambda}$ of multiplexed multiphoton sources based on OMAXV multiplexers assuming different and identical input mean photon numbers λ_n and λ, respectively, as functions of the number of multiplexed units N. The parameters of the curves are as follows: A: $V_D = 0.8$, $V_r = 0.95$, $V_t = 0.95$; B: $V_D = 0.9$, $V_r = 0.95$, $V_t = 0.95$; C: $V_D = 0.95$, $V_r = 0.99$, $V_t = 0.985$.

Fig. 1 shows that the discrete function $P_{i,N}(N)$ describing the achievable output photon probabilities has an absolute maximum. The optimal values of the number of multiplexed units N_{opt} corresponding to these global maxima are presented in Fig. 3 for multiplexed two-photon sources based on OMAXV multiplexers as a function of the transmission coefficients V_t and V_r for the detector efficiency $V_D = 0.95$. The figure shows that the optimal number of multiplexed units N_{opt} is low for low values of the transmission coefficients V_t and V_r, while for simultaneously high values and for highly asymmetric values of V_r and V_t the corresponding values of N_{opt} are high.

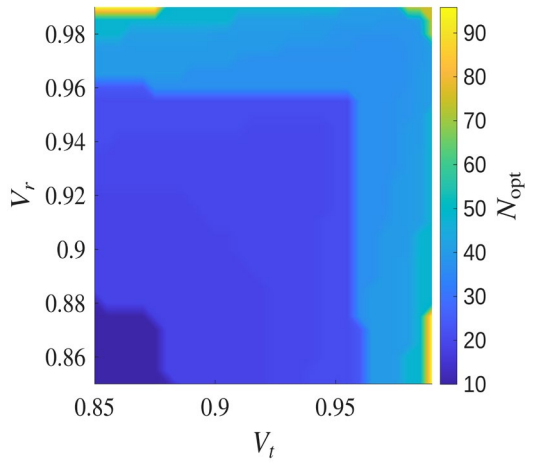

Fig. 3. The optimal number of multiplexed units N_{opt} for multiplexed two-photon sources based on OMAXV multiplexers as functions of the transmission coefficients V_r and V_t for the detector efficiency $V_D = 0.95$.

4. Conclusions

We have shown that the multiphoton probabilities of spatially multiplexed multiphoton sources can be increased by optimizing the input mean photon numbers for each input of the multiplexer separately instead of using identical inputs.

Acknowledgements

This research was supported by the National Research, Development and Innovation Office, Hungary ("Frontline" Research Excellence Programme Grant No. KKP133827, and Grant No. TKP2021-NVA-04), and the Smart University Program of the University of Pécs.

References

[1]. G. Y. Xiang, H. F. Hofmann, G. J. Pryde, Optimal multi-photon phase sensing with a single interference fringe, *Scientific Reports*, Vol. 3, 2013, 2684.
[2]. A. Ourjoumtsev, H. Jeong, R. Tualle-Brouri, P. Grangier, Generation of optical 'Schrödinger cats' from photon number states, *Nature*, Vol. 448, 2007, pp. 784-786.
[3]. L. Zhang, K. W. C. Chan, Scalable generation of multi-mode NOON states for quantum multiple-phase estimation, *Scientific Reports*, Vol. 8, Issue 1, 2018, 11440.
[4]. M. D. Eisaman, J. Fan, A. Migdall, S. V. Polyakov, Invited review article: Single-photon sources and detectors, *Review of Scientific Instruments*, Vol. 82, Issue 7, 2011, 071101.
[5]. E. Meyer-Scott, C. Silberhorn, A. Migdall, Single-photon sources: Approaching the ideal through multiplexing, *Review of Scientific Instruments*, Vol. 91, Issue 4, 2020, 041101.
[6]. P. Adam, M. Mechler, Recent progress in multiplexed single-photon sources, *Applied Sciences*, Vol. 14, Issue 23, 2024, 11249.
[7]. B. M. Szilasi, M. Mechler, P. Adam, Generation of multiphoton Fock states by multiplexing heralded photon sources, *Optics Express*, Vol. 33, Issue 25, 2025, pp. 53483-53500.
[8]. P. Adam, M. Mechler, I. Santa, M. Koniorczyk, Optimization of periodic single-photon sources, *Physical Review A*, Vol. 90, Issue 5, 2014, 053834.
[9]. F. Bodog, M. Mechler, M. Koniorczyk, P. Adam, Optimization of multiplexed single-photon sources operated with photon-number-resolving detectors, *Physical Review A*, Vol. 102, Issue 1, 2020, 013513.
[10]. P. Adam, F. Bodog, M. Koniorczyk, M. Mechler, Single-photon sources based on asymmetric spatial multiplexing with optimized inputs, *Physical Review A*, Vol. 105, Issue 6, 2022, 063721.
[11]. P. Adam, M. Mechler, Single-photon sources based on incomplete binary-tree multiplexers with optimal structure, *Optics Express*, Vol. 31, Issue 19, 2023, pp. 30194-30211.

(019)

A Self-Compression Approach for Generating ~150 fs Laser Pulses in the SWIR Range Based on Transient SRS

P. Mackonis, A. Grigaravičienė, A. M. Rodin and R. Pečiulytė
Center for Physical Sciences and Technology, Solid State Lasers Laboratory,
231 Savanoriu Ave, 02300 Vilnius, Lithuania
Tel.: +37067025050
E-mail: paulius.mackonis@ftmc.lt

Summary: Our recent findings demonstrate that transient stimulated vibrational Raman amplification of supercontinuum pulses provides an unexplored route toward the efficient generation of femtosecond laser pulses in the SWIR spectral range. This approach eliminates the need for optical parametric chirped pulse amplification and its inherent compression layouts based on chirped mirrors or prisms. The experimental setup was driven by ~1.3 ps pump pulses at 1030 nm from a Yb:YAG laser. Although transient SRS initiated from quantum noise was inefficient, stimulated Raman amplification seeded with a supercontinuum pulse exhibited a sixfold lower threshold and achieved a conversion efficiency above 30 %. By tuning the temporal delay between the pump and seed pulses in a hydrogen cell, we compressed 575 fs transform-limited, steep-fronted Stokes pulses with energies up to 0.36 mJ at 1.8 μm to 145 fs transform-limited pulses with energies up to 0.25 mJ. Overall, the initial experimental results highlight the potential of this self-compression approach for highly efficient femtosecond pulse generation, while simultaneously extending spectral coverage from the widely used near-infrared (NIR) into the hard-to-reach short and mid-infrared ranges (SWIR and mid-IR).

Keywords: Self-compression, SWIR, Mid-IR, Stimulated Raman scattering, Femtosecond pulses, Compressed hydrogen.

1. Introduction

The generation of high-energy femtosecond pulses in the short- and mid-infrared (SWIR/mid-IR) spectral range remains a significant technological challenge. Ho- and Tm-based lasers operating near 2 μm typically rely on multi-stage or regenerative chirped pulse amplifiers (CPA) for energy scaling [1, 2], often requiring additional nonlinear compression stages to reach sub-ps pulse durations [3]. Similarly, while optical parametric chirped pulse amplification (OPCPA) offers wavelength flexibility, it relies on complex multi-stage architectures and dispersion compensation using chirped mirrors or prisms [4].

In this work, we demonstrate that transient stimulated vibrational Raman scattering (SRS) in compressed hydrogen provides an alternative and simplified route for generating SWIR femtosecond pulses. Driven by ~1.3 ps pump pulses at 1030 nm, the white light supercontinuum (WLC) seeded transient SRS achieves conversion efficiencies exceeding 30 %. After optimization, near-transform-limited 575 fs Stokes pulses at 1.8 μm with energies up to 0.36 mJ were obtained. Furthermore, by tuning the temporal delay between the pump and seed pulses, we demonstrate a self-compression effect that shortens the pulses below 150 fs.

2. Experiment

The experimental setup for SRS amplification is shown in Fig. 1. The pump source for both the WLC seed and the SRS converter was a home-built two-stage hybrid Yb:YAG/Yb:LuAG chirped-pulse amplifier with a grating compressor, providing transform limited 1.3 ps pulses with energies up to 10 mJ at a 100 Hz repetition rate. A small portion of the pump energy (~10 μJ) was used to generate the WLC in an undoped YAG rod. After spectral selection via acousto-optic programmable dispersive filter (AOPDF), the seed beam was collimated using a lens L2. Collinear propagation of the seed and pump beams was achieved using a dichroic mirror (DM), while precise temporal overlap was adjusted using a delay line (DL). The WLC seed and pump beams were focused into the center of a 1 m long cell filled with hydrogen at pressures up to 3.5 MPa using lenses L3 and L4, both with a focal length of 750 mm.

3. Results

When initiated from quantum noise, transient vibrational SRS in hydrogen exhibits a high excitation threshold and low conversion efficiency. At a hydrogen pressure of 3.5 MPa, the first-order Stokes component appears at a pump energy of ~0.9 mJ, but reaching a maximum conversion efficiency of only ~1.5 % (Fig. 2, triangles). As the pump energy exceeds 1.7 mJ, WLC generation and other competing nonlinear processes in hydrogen begin to dominate, effectively suppressing the SRS.

In contrast, injecting a WLC seed spectrally matched to the first-order vibrational Stokes (at 4155 cm^{-1}) reduces the effective SRS threshold by approximately a factor of six. The WLC seed was spectrally filtered to 50 nm (FWHM) at a center wavelength of 1.8 μm (Fig. 3) to prevent unintended seeding of rotational Stokes (at 587 cm^{-1}), which could otherwise be driven by the Stokes pulse at 1.8 μm.

At a pump energy of 1.2 mJ (corresponding to a peak intensity of 1.1 TW/cm^2 at the beam waist), a maximum conversion efficiency of 30 % was achieved (Fig. 2, circles), yielding a quantum efficiency of ~53 %. The Stokes pulse energy reached ~0.36 mJ while maintaining a Gaussian beam intensity profile (Fig. 2, inset), measured via two-photon excitation using a Si CMOS camera placed at the focus of a 750 mm CaF_2 lens.

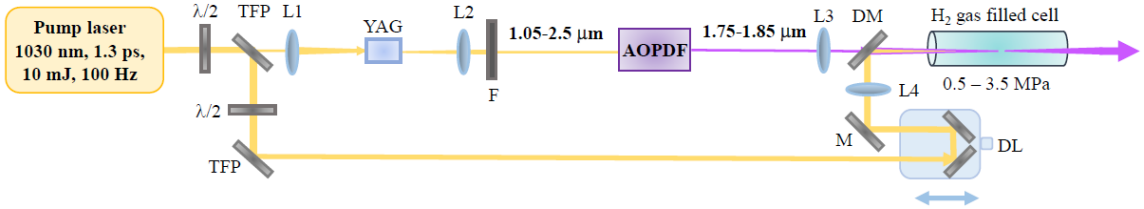

Fig. 1. Experimental setup for the investigation of transient SRS amplification in a hydrogen-filled cell.

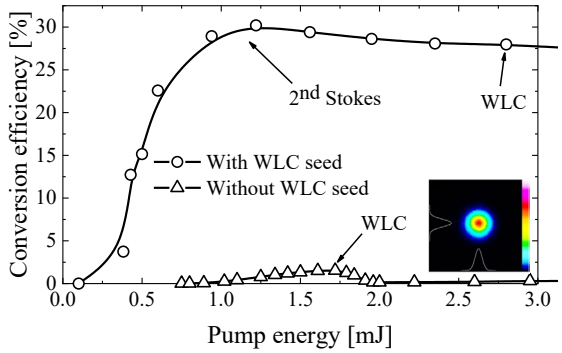

Fig. 2. Conversion efficiency to the first-order Stokes without (triangles) and with (circles) WLC seeding. Inset: normalized far-field Stokes beam profile at maximum conversion efficiency.

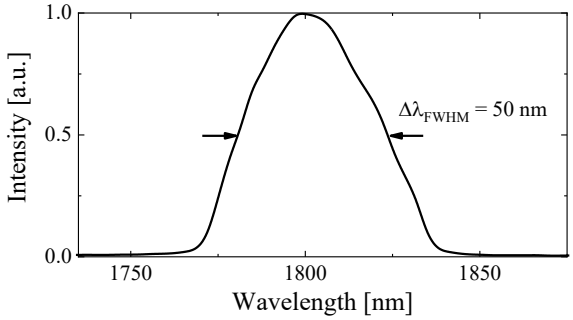

Fig. 3. Spectrum of the spectrally filtered WLC seed centered at 1.8 μm with a 50 nm (FWHM) bandwidth.

At higher pump energies, the second-order Stokes component emerges, leading to a decrease in conversion efficiency. Still, owing to the dominance of the pump-to-Stokes energy-transfer process, competing WLC generation in the hydrogen cell appears only at pump energies above 2.8 mJ. The incident 1.3 ps pump pulses were converted into 575 fs first-order Stokes pulses with a nearly flat temporal phase (Fig. 4a). The obtained spectral bandwidth supports transform-limited pulses of 573 fs at a central wavelength of 1.8 μm (Fig. 4b). These Stokes pulse exhibit a steep trailing edge, typical of transient scattering phenomena.

Further spectral broadening requires maintaining an optimal balance between self-phase modulation (SPM) and SRS. By increasing the pump energy to 1.7 mJ (2.1 TW/cm²) and detuning the seed-pump delay, the SRS conversion efficiency was reduced to ~15 %, which in turn favored spectral broadening and temporal steepening (Fig. 4c, d). Here, the insets in (Fig. 4a) and (Fig. 4c) show the measured and retrieved FROG traces, obtained with ~1 % error using a 512×512 grid, while the insets in (Fig. 4b) and (Fig. 4d) present the FTL temporal shapes calculated from the measured spectra of the Stokes pulses. As a result, the delayed WLC seed enabled the generation of Stokes pulses with a spectral bandwidth supporting transform-limited pulses of 145 fs (Fig. 4d, inset). Owing to the negligible group velocity dispersion (GVD) of hydrogen (0.16 fs²/mm), only a small residual group delay dispersion (GDD) of <100 fs² was accumulated over the 1 m interaction length and the CaF_2 windows. This dispersion is negligible for the achieved spectral bandwidth, enabling nearly transform-limit Stokes pulses of 145 fs and eliminating the need for additional pulse compression stages.

4. Conclusions

We have demonstrated the efficient generation of femtosecond pulses in the SWIR spectral range by utilizing WLC-seeded transient vibrational SRS in compressed hydrogen. Near-transform-limited 575 fs Stokes pulses at 1.8 μm with energies up to ~0.36 mJ were achieved, reaching a conversion efficiency of 30 %. By adjusting the temporal overlap between the seed and pump pulses, we exploited the interplay between nonlinear spectral broadening via SPM and transient SRS to achieve self-compressed Stokes pulses of ~150 fs, with an anergy of 0.25 mJ, corresponding to a conversion efficiency of 15 %. Due to the negligible dispersion of hydrogen in this spectral range, the obtained broadband pulses remain transform-limited, eliminating the need for external pulse-compression stages.

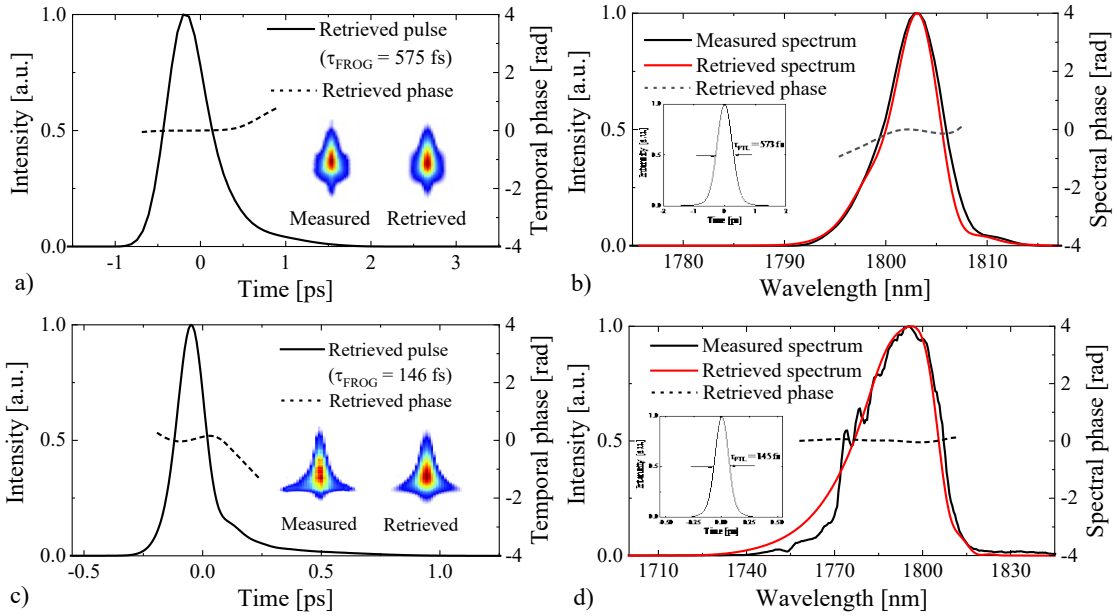

Fig. 4. a) Temporal profile (solid) and phase (dashed); b) measured (black), retrieved (red) spectral profiles and phase (dashed) of the Stokes pulse obtained from SHG-FROG measurements with a temporally overlapped WLC seed; c) Temporal profile (solid) and phase (dashed); d) measured (black), retrieved (red) spectral profiles and phase (dashed) of the Stokes pulse obtained from SHG-FROG measurements with a delayed WLC seed.

These results demonstrate WLC-seeded transient SRS as a viable alternative to Ho-/Tm-based CPA and OPCPA systems, offering a practical pathway toward high-energy femtosecond pulse generation while simultaneously enabling spectral conversion from the NIR to the SWIR and mid-IR ranges.

Acknowledgements

This research was funded by Research Council of Lithuania, grant number S-MIP-25-17.

References

[1]. S. A. Rezvani, M. Suzuki, P. Malevich, C. Livache, et al., Millijoule femtosecond pulses at 1937 nm from a diode-pumped ring cavity Tm:YAP regenerative amplifier, *Optics Express*, Vol. 26, Issue 22, 2018, pp. 29460-29470.

[2]. P. Malevich, G. Andriukaitis, T. Flöry, A. J. Verhoef, et al., High energy and average power femtosecond laser for driving mid-infrared optical parametric amplifiers, *Optics Letters*, Vol. 38, Issue 15, 2013, pp. 2746-2749.

[3]. K. Murari, G. Cirmi, H. Cankaya, G. J. Stein, et al., Sub-50 fs pulses at 2050 nm from a picosecond Ho:YLF laser using a two-stage Kagome-fiber-based compressor, *Photonics Research*, Vol. 10, Issue 3, 2022, pp. 637-645.

[4]. A. Petrulenas, P. Mackonis, A. M. Rodin, High-efficiency bismuth borate-based optical parametric chirped pulse amplifier with ~2.1 mJ, 38 fs output pulses at ~2150 nm, *High Power Laser Science and Engineering*, Vol. 11, 2023, e53.

(020)

Non-Gaussianity as an Indicator for Security of Entanglement-Based Quantum Key Distribution

M. Gumberidze and V. Usenko
Palacky University, 17. Listopadu 12 7146 Olomouc, Czech Republic
Tel.: + 420 585634723
E-mail: usenko@optics.upol.cz

Summary: We theoretically analyse the relation between non-Gaussianity of entangled quantum states and security of entanglement-based quantum key distribution (QKD) protocols, namely device-independent and conventional BB84. Considering imperfect detection with dark counts and limited efficiency, we study entangled Bell states as produced by quantum-dot type sources, shared over quantum channels with signal depolarization and linear coupling to noise having either thermal or Poisson statistics. We consider single-photon avalanche photodiodes and photon number resolving detectors and use respective criteria for non-Gaussianity of the detected states. We show cross-regions for both security and non-Gaussianity, hence, the possibility to conclude about the suitability of a given channel for QKD based on non-Gaussianity criteria, in a major range of noise coupling ratios. Our results can be used as a pre-check for the implementation of entanglement-based QKD protocols.

Keywords: Quantum communication, Quantum key distribution, Discrete variables, Quantum entanglement, Non-Gaussian quantum states.

1. Introduction

QKD is well known to develop and implement protocols for information-theoretically provably secure key distribution between two remote trusted parties. Research in QKD is stimulated by the rapid development of quantum computing, posing the threat to broadly used asymmetrical classical encryption methods. Being based on information encoding into quantum states with discrete energy spectra, discrete-variable QKD is well suited for long-distance key distribution due to its robustness against channel losses [1]. Particularly, entanglement-based QKD offers key distribution from a typically photonic source, which produces entangled pairs of photons, each measured by a remote trusted party. This approach enables advanced device-independent security as well as scalability by means of entanglement swapping. Being robust against losses in the quantum channel, such protocols are still susceptible to noise, which can be present in the channel e.g. due to imperfect mode isolation or separation [2].

Non-Gaussianity is an essential quantum property for a state to be unrepresentable as a mixture of Gaussian states (hence, the states with the Gaussian Wigner function). This property can be confirmed using certain criteria developed for major quantum detection types [3], such as single-photon avalanche photodiodes (SPADs) and photon number resolving detectors (PNRDs). It was shown that non-Gaussianity of the quantum states can be used as an indicator of security of QKD realizations in case of the conventional prepare-and-measure protocols, where the sender (Alice) prepares the signal states, while the receiver (Bob) performs the measurement [4]. In the current work we extend this analysis to entanglement-based protocols considering perfect entangled Bell-type states, which can be produced by the quantum dot sources [5], and are shared over quantum channels, inclined to depolarization and noise.

2. Methods

We consider entanglement-based QKD scheme as shown in Fig. 1(a), where Alice and Bob measure polarization entangled states to establish correlated raw keys using their respective analyzers, based on polarizing beamsplitters and photodetectors. Alternatively, Alice and Bob can decide to identify non-Gaussianity and either detect coincidences on the outputs of a balanced beamsplitter measured by on/off SPADs, as shown in Fig. 1(b), or directly measure the incoming light by PNRDs, as shown in Fig 1(c).

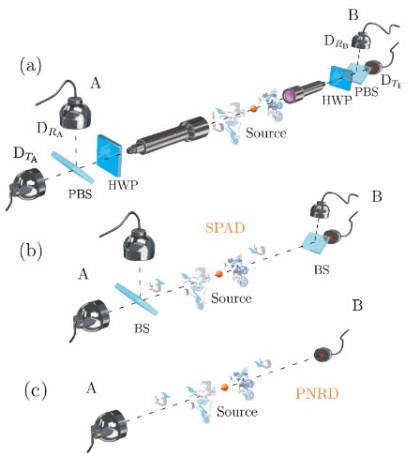

Fig. 1. Entanglement-based QKD (a), non-Gaussianity measurements using SPADs (b) and PNRDs (c).

The secret key rates for DI and BB84 protocols are bounded by the Devetak-Winter rates [6], which read, respectively

$$r_{DW}^{DI} = 1 - h(Q) - h\left(\frac{1+\sqrt{(S/2)^2-1}}{2}\right), \quad (1)$$

and

$$r_{DW}^{BB84} = 1 - h(Q) - h\left(Q + \frac{S}{2\sqrt{2}}\right), \quad (2)$$

where $h(Q) = -Q\log_2 Q - (1-Q)\log_2(1-Q)$ is the binary entropic function, Q is the quantum bit error rate (QBER), and S is the CHSH Bell parameter. We assume that Alice and Bob optimally measure the Bell parameter obtaining $S = 2\sqrt{2}(1-2Q)$ for a depolarized version $\hat{\rho}_{AB} = p|\Phi^+\rangle\langle\Phi^+| + \frac{1-p}{4}\hat{\mathbb{I}}\otimes\hat{\mathbb{I}}$ of the Bell state $|\Phi^+\rangle = \frac{1}{\sqrt{2}}(|00\rangle + |11\rangle)$.

We apply photodetection theory to characterize the measurement statistics by employing positive operator-valued measures for SPADs and PNRDs, depending on the detection efficiency η and dark count rate ν. From these we obtain QBER needed for evaluation of the Devetak-Winter rates and the event probabilities required for non-Gaussianity criteria. For SPADs this is based on "successful" events with probabilities P_s, when only one detector clicks on Alice's side and one clicks on Bob's side, and "error" events with P_e, when both detectors click on either side. The criteria then reads $P_s > \frac{1}{2}\sqrt{\frac{P_e}{8+P_e}}\left(2 + P_e + \sqrt{P_e(8+P_e)}\right)$. For the PNRDs the successful events are the detection of exactly one photon simultaneously on both sides, while all multi-photon detections are erroneous, the criteria then reads $P_s > \sqrt{P_e} - P_e$ [3]. Finally, we add thermal or Poisson noise with mean photon number $\bar{n}$ by coupling the noise mode to a signal mode with linear coupling ratio T, and calculate the resulting detection probabilities, QBER and key rates (see [7] for details).

3. Results

We present the results in Fig. 2 as the plots of the maximum tolerable thermal noise $\bar{n}$ for security of DI and BB84 protocols and for non-Gaussianity versus coupling ratio T for a PNRD detector (left). For SPAD we incorporate Poisson (multi-mode thermal) noise in the detector and plot, respectively, maximum tolerable dark count rate ν versus efficiency η (right). It is evident from the plots, that for these cases the security region lies within the non-Gaussianity area for most of the coupling/efficiency ratios (above 0.25), which suggests that observing non-Gaussianity in these regimes indicates possibility to establish QKD over the given channels. This is particularly pronounced for DI QKD protocols, where security region is well below the non-Gaussianity threshold. For the PNRD and thermal noise, however, situation is inconclusive, as upon low or high efficiencies non-Gaussianity is broken by the lower noise levels and can be used as an indicator for QKD only in the middle range of efficiencies.

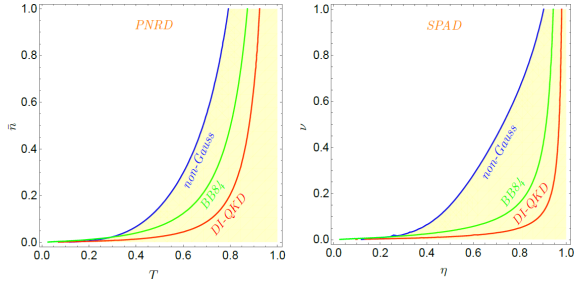

Fig. 2. Non-Gaussianity and security regions for PNRD and thermal (left) and SPAD and Poisson noise (right).

4. Conclusions

In conclusion, we have analyzed non-Gaussianity of entangled Bell states produced by a perfect quantum-dot type source in relation to security of entanglement-based QKD in DI and conventional BB84 implementations over depolarizing and noisy channels. By employing photodetection theory, we obtained the bounds on non-Gaussianity and security in terms of the maximum tolerable noise levels. Our results show that non-Gaussianity can indicate the security of QKD in the case of PNRD detectors with thermal channel noise and in the case of SPAD detectors and Poisson noise as its region covers the security region in the broad range of noise coupling ratios. For PNRD and Poisson noise the result is inconclusive for low and high coupling ratios in the sense of non-Guassitnity wanishing faster than security of QKD. These qualitative results can be used to benchmark and pre-check set-ups for entanglement-based QKD. In our study we omit discussion of state preparation or detection imperfections, which will be incorporated in further research.

Acknowledgements

Authors acknowledge support from the project no. 21-44815L of the Czech Science Foundation, the project 8C22003 (QD-E-QKD) of MEYS of Czech Republic, and "Quantum Secure Networks Partnership" (QSNP, grant agreement No. 101114043) project funded from the European Union's Horizon Europe research and innovation programme.

References

[1]. M. Lasota, R. Filip, V. C. Usenko, Robustness of quantum key distribution with discrete and continuous

variables to channel noise, *Physical Review A*, Vol. 95, Issue 6, 2017, 062312.

[2]. M. Lasota, O. Kovalenko, V. C. Usenko, Robustness of entanglement-based discrete- and continuous-variable quantum key distribution against channel noise, *New Journal of Physics*, Vol. 25, Issue 12, 2023, 123003.

[3]. L. Lachman, R. Filip, Quantum non-Gaussian photon coincidences, *Physical Review Letters*, Vol. 126, Issue 21, 2021, 213604.

[4]. M. Lasota, R. Filip, V. C. Usenko, Sufficiency of quantum non-Gaussianity for discrete-variable quantum key distribution over noisy channels, *Physical Review A*, Vol. 96, Issue 1, 2017, 012301.

[5]. C. Schimpf, M. Reindl, F. Basso Basset, K. D. Jöns, et al., Quantum dots as potential sources of strongly entangled photons: Perspectives and challenges for applications in quantum networks, *Applied Physics Letters*, Vol. 118, Issue 10, 2021, 100502.

[6]. A. Acín, N. Brunner, N. Gisin, S. Massar, et al., Device-independent security of quantum cryptography against collective attacks, *Physical Review Letters*, Vol. 98, Issue 23, 2007, 230501.

[7]. M. Gumberidze, V. C. Usenko, Non-Gaussianity and security of entanglement-based QKD, *arXiv*, 2025, arXiv:2511.01761.

(021)

Linear Stokes Polarimeter for THz Frequencies

R. Tudor
IMT-Bucharest, 126A, Erou Iancu Nicolae Street, Voluntari, RO-077190, Romania
Tel.: + 40 21 269 0770
E-mail: rebeca.tudor@imt.ro

Summary: The paper investigates a linear Stokes polarimeter (LSP) operating at THz frequencies. This polarimeter is designed as an array of wire-grid polarizers at different angles (0°, 45°, 90°, 135°) which are characterised by the same period, height and fill factor. This LSP is designed as a phased array on high-resistivity silicon with area of 5 cm x 5 cm. The Stokes polarimeters have a variety of applications including medical imaging, communications, remote sensing and interferometry.

Keywords: Array of polarizer, Full Stokes imaging, Polarimetry, Wire-grid polarizer, High-speed applications.

1. Introduction

The 4D characterization of THz optical fields includes amplitude, phase, time, polarisation. One can estimate polarisation states with focal plane Stokes imaging polarimeter.

In this paper it is presented a linear Stokes polarimeter (LSP) generated as an array of wire-grid polarizers characterized by the same period, height and fill factor. This LSP is designed as a phased array on high-resistivity silicon.

The imaging polarimeters have a variety of applications including medical imaging, communications, remote sensing and interferometry [1-8].

A Stokes imaging polarimeter can estimate the incident polarisation state quantified as Stokes vector, $\vec{S}$,

$$\vec{S} = \begin{bmatrix} S_0(x,y) \\ S_1(x,y) \\ S_2(x,y) \\ S_3(x,y) \end{bmatrix} = \begin{bmatrix} I_{0^\circ}(x,y) + I_{90^\circ}(x,y) \\ I_{0^\circ}(x,y) - I_{90^\circ}(x,y) \\ I_{45^\circ}(x,y) - I_{135^\circ}(x,y) \\ I_{\mathrm{RH}}(x,y) - I_{\mathrm{LV}}(x,y) \end{bmatrix} \quad (1)$$

Important metrics can be extracted from the Stokes vector as degree of polarisation (DOP), the angle of linear polarisation, degree of linear polarisation (DOLP), by using the Eqs. (2)-(5) respectively [1].

$$\theta_{linear} = \frac{1}{2}\theta^{-1}\frac{S_2}{S_1}, \quad (2)$$

$$DOP = \frac{\sqrt{S_1^2+S_2^2+S_3^2}}{S_0}, \quad (3)$$

$$DOPL = \frac{\sqrt{S_1^2+S_2^2}}{S_0}, \quad (4)$$

$$DOCP = \frac{S_3}{S_0} \quad (5)$$

2. Design and Simulation of Linear Stokes Polarimeter

We present a linear Stokes polarimeter (LSP) generated as an array of wire-grid polarizers characterized by the same period, T = 24 μm, same height H = 130 μm, same fill factor, η = 50 %. This LSP is designed as a phased array on a silicon substrate with area of 5 cm x 5 cm in order to operate at a central wavelength 300 μm, as it is illustrated in Fig. 1: upper corner left 0°, lower corner left 45°, lower corner right 90°, upper corner right 135°. With this configuration, one can estimate the incident polarization only with four measurements of intensities I_{0°, I_{90°, I_{45°, I_{135° which allows the determination of which allows to generate S_0, S_1 and S_2.

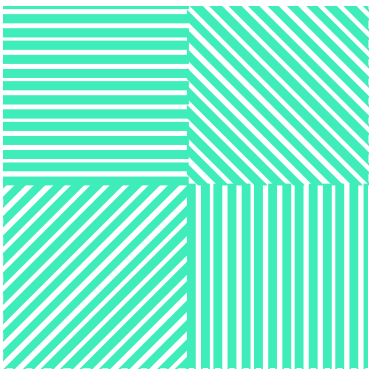

Fig. 1. Array of wire-grid polarizer: upper corner left 0°, lower corner left 45°, lower corner right 90°, upper corner right 135°, T = 24 μm, η = 50 %.

The proposed LSP is simulated in OptiFDTD software with the input ultra-short Gaussian pulse with a Full Width at Half Maximum FWMH of 0.5 ps suitable for high-speed optical measurements which is illustrated in Fig. 2.

In Fig. 3 shows the Power spectrum of bandwidth B = 1,765 THz corresponding to the transverse

electric-field component *Ex* of THz incident pulse on the array of wire-grid polarizer.

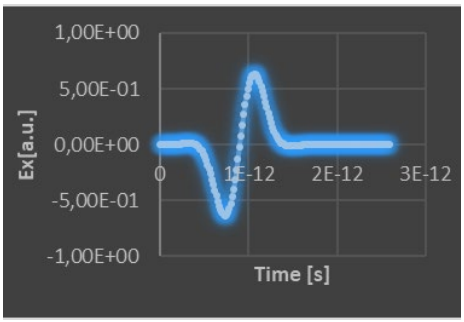

Fig. 2. Transverse electric-field component *Ex* of THz pulse incident on the array of wire-grid polarizer.

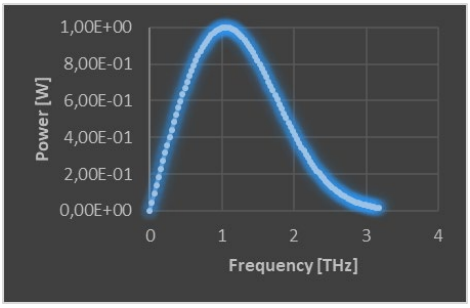

Fig. 3. Power spectrum for the transverse electric-field component *Ex* of THz pulse incident on the array of wire-grid polarizer.

3. Discussion

The paper investigated the efficiency of a linear Stokes polarimeter, operating at central THz frequency, f = 1 THz. The polarimeter was designed as an array of wire-grid polarizers on silicon, at different angles (0°, 45°, 90°, 135°) with period T = 24 μm, height H = 130 μm and fill factor, η = 50 %. The OptiFDTD simulations were investigated with a Gaussian pulse of 0.5 ps (FWMH), and bandwidth B = 1,765 THz (FWMH) while LSP has an operating bandwidth approximately of 0.4 THz, extinction ratio ER~30 dB at normal incidence. The presented focal plane array allows the simultaneous measurement of linear Stokes parameters S_0, S_1 and S_2 without any rotation of it. Moreover, the fabrication feasibility of the proposed LSP rely on standard fabrication techniques (lithography and deep ion reactive etching which brings great potential in a variety of applications including suitable for high-speed optical measurements in advanced laser technology, transient spectroscopy experiments, remote sensing, medical imaging, communications, remote sensing and interferometry.

Acknowledgements

This research was funded by the European Commission, under Horizon Europe Programme, grant agreement No. 101046651 – ”4D Microscopy of biological materials by short pulse terahertz sources (MIMOSA).

References

[1]. D. H. Goldstein, Polarized Light, 3rd Ed., *CRC Press*, Boca Raton, 2011.
[2]. J. S. Tyo, D. L. Goldstein, D. B. Chenault, J. A. Shaw, Review of passive imaging polarimetry for remote sensing applications, *Applied Optics*, Vol. 45, Issue 22, 2006, pp. 5453-5469.
[3]. G. Myhre, W. L. Hsu, A. Peinado, C. laCasse, et al., Liquid crystal polymer full-Stokes division of focal plane polarimeter, *Optics Express*, Vol. 20, Issue 25, 2012, pp. 27393-27409.
[4]. V. Pavelyev, S. Khonina, S. Degtyarev, K. Tukmakov, et al., Subwavelength diffractive optical elements for generation of terahertz coherent beams with pre-given polarization state, *Sensors*, Vol. 23, Issue 3, 2023, 1579.
[5]. S. S. Stafeev, A. G. Nalimov, M. V. Kotlyar, L. O'Faolain, et al., Subwavelength gratings for polarization control, *Journal of Physics: Conference Series*, Vol. 1096, Issue 1, 2018, 012020.
[6]. X. Dong, J. Cheng, F. Fan, S. Chang, Sub-terahertz wideband vector beam generator based on superwavelength lattice dielectric grating, *Optik*, Vol. 193, 2019, 162991.
[7]. J. Lafrenière-Greig, R. Tudor, G. Gandubert, J. E. Nkeck, et al., Spatial-temporal shaping of THz pulse with segmented metasurface, in *Proceedings of the 50th International Conference on Infrared, Millimeter, and Terahertz Waves (IRMMW-THz'25)*, 2025.
[8]. R. Tudor, S. Hmidi, X. Ropagnol, O.-G. Simionescu, et al., Polarization control of broadband THz pulses with hybrid metadevice, in *Proceedings of the Frontiers in Optics + Laser Science (FiO/LS'25)*, 2025, JTu4A.46.

(022)

40 ps Pulses at 1064 nm from SBS-Compressor with Trailing-Edge Reshaping by Transient Forward SRS

A. M. Rodin, A. Grigaravičienė, P. Mackonis and R. Pečiulytė
Center for Physical Sciences and Technology, Solid State Laser Laboratory, 231 Savanoriu Ave,
02300 Vilnius, Lithuania
Tel.: +370642 09935
E-mail: aleksej.rodin@ftmc.lt

Summary: We present results on record-level compression of ~1-ns incident laser pulses down to ~40 ps using stimulated Brillouin scattering (SBS) in HT-230 within a phase-conjugated Nd:YAG amplifier configuration, with a trailing-edge reshaping provided by transient forward stimulated Raman scattering (SRS) in a KGW crystal. In contrast to widely used cascaded SBS and SRS-compressors, the output pulse wavelength after ~22-fold compression remains within the gain bandwidth of Nd:YAG amplifiers. Thus, the newly developed high-efficiency picosecond-pulse generation method not only eliminates the need for bulky and costly mode-locking architectures with regenerative amplifiers, but also delivers superior beam quality and high temporal coherence. Lasers employing this method are particularly advantageous for DLIP-based surface texturing of functional materials, enabling the fabrication of water-repellent patterns.

Keywords: SBS-compression, Stimulated Raman scattering, SRS-compression, Picosecond pulses, Perfluorooctane, KGW.

1. Introduction

SBS-compression makes it possible to achieve pulse width of ~110 ps in perfluorooctane [1], ~70 ps in carbon tetrachloride [2] and ~175 ps in fused quartz [3]. As our experiments have shown [4], with an appropriate choice of SBS-active medium, self-seeded SBS-compressors coupled with a double-pass phase-conjugated amplifier can serve as an effective source of ~90 ps pulses with energies of ~10 mJ and superior beam quality. Long before that, counter-propagating SRS-amplification of ~20 ps Stokes pulses to energies of ~30 mJ was demonstrated in compressed methane [5] at a wavelength of 630 nm, which lies outside the gain bandwidth of available solid-state laser materials.

The results of record-level SBS-compression with trailing-edge depletion of the generated pulse via transient forward SRS in a KGW crystal are presented in this work, achieved without the wavelength shift and thus enabling further amplification in Nd:YAG amplifiers.

2. Experiment

The experimental setup is shown in Fig. 1. The pump source was a passively Q-switched Nd:YAG laser delivering ~0.9 ns pulses at 1064 nm. A Faraday isolator (FI) protected the laser from backscattered radiation, while the beam diameter was adjusted using a beam-expansion telescope (L1, L2). A half-wave plate (λ/2) together with a thin-film polarizer (TFP) was used to control the incident pulse energy. The beam was directed into the side-pumped Nd:YAG gain modules (AMP1, AMP2), where the pulse energy was increased to 8 mJ before entering the SBS stage. In contrast to the previous configuration [4], linear σ-polarization was used instead of circular in order to improve the interaction efficiency and spatial overlap of the counter-propagating waves. The linearly polarized, collimated beam passed through the SBS-cell filled with HT-230 without reaching SBS threshold during the forward pass. After exiting the cell, the beam passed through a quarter-wave plate (λ/4), was converted to circular polarization, and was reflected by a spherical mirror (SM, R = 500 mm). After the second pass through the λ/4 plate, the polarization was rotated to the orthogonal π-polarization. The beam was then redirected into the SBS-cell in a counter-propagating geometry relative to the incident pulse. This configuration ensured collinear interaction and improved spatial overlap compared to the slightly tilted beam trajectory used previously [4]. The unused pump radiation was diverted by TFP3 to a beam dump (BD). Meanwhile, the phase-conjugated Stokes beam propagated backward along the same path and, after double pass through the λ/4 plate, its polarization was rotated back to the initial σ-state. Passing through the Faraday rotator (FR), the π-polarized Stokes beam was directed for a second pass through the gain modules and subsequently extracted through TFP2. The amplified SBS-compressed pulse was then directed to the SRS stage based on a c-cut, 15-mm-long $KGd(WO_4)_2$ crystal, where a λ/2-TFP4 pair was used to adjust the incident pulse energy. A beam-reducing telescope (L3, L4) was used to reach the SRS threshold.

Transient forward SRS in the KGW crystal resulted in preferential depletion of the trailing edge of the pulse. The Raman-shifted Stokes component was separated using a dichroic mirror (DM) that was reflective above 1100 nm.

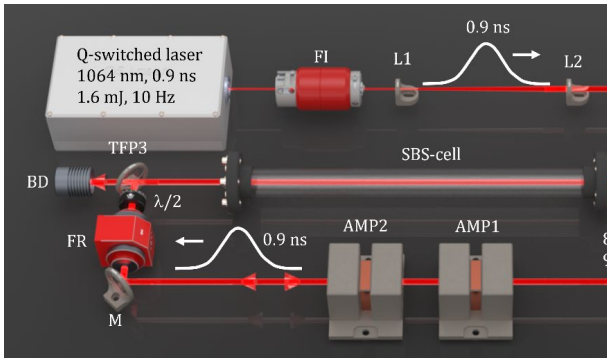

Fig. 1. Experimental setup for the investigation of SBS-compression with trailing-edge reshaping by transient forward SRS: FI – Faraday isolator, FR – Faraday rotator, L1, L2 – beam expanding telescope, TFP – thin film polarizers, λ/2 and λ/4 – half- and quarter-wave retardation plates, AMP – side diode-pumped Nd:YAG gain modules, SM – spherical mirror, L3, L4 – beam reducing telescope, DM – dichroic mirror (HT@1064 nm, HR@>1100 nm), KGW – $KGd(WO_4)_2$ crystal.

3. Results

The modified layout provides markedly improved performance of the SBS-compression stage, as the use of linear polarization enables a fully collinear geometry for the counter-propagating pump and Stokes waves, thereby ensuring superior spatial overlap within the SBS-cell. This leads to a lower SBS threshold and a consistently higher reflectivity across the entire range of pump energies (Fig. 2). As a result, shorter compressed pulses were obtained – down to ~80 ps (red solid line) compared to ~90 ps (red dashed line) in the previous configuration. In this case, the output energy after amplification reached up to ~9 mJ (black solid line). The slight reduction compared to ~10 mJ (black dashed line) is attributed to the lower optimal pump energy, which decreased from ~6.5 mJ to ~5.5 mJ in this configuration. It was also found that the collinear interaction geometry enhances both the temporal and energy stability of the SBS-compressed pulses. In particular, the sensitivity to slow drifts, such as those induced by ambient conditions (e.g., temperature fluctuations and air flows), was reduced, resulting in more stable overall operation.

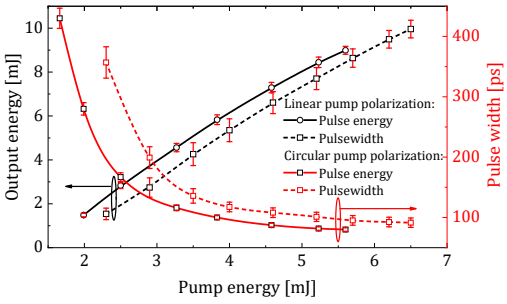

Fig. 2. Output energy (black lines) and pulse with (red lines) of SBS-compressed pulses as a function of pump energy for linear (solid lines) and circular (dashed lines) pump polarizations.

The amplified SBS-compressed pulses were directed to the SRS reshaping stage based on a KGW crystal oriented for a Raman shift of 901 cm^{-1}. The threshold for efficient SRS (defined here at >1 % conversion efficiency) was observed at a pump pulse energy of 3.8 mJ (Fig. 3, black line), corresponding to a peak intensity of 14 GW/cm^2. With increasing pump energy, the pump depletion grows and approaches saturation at ~8 mJ (33 GW/cm^2).

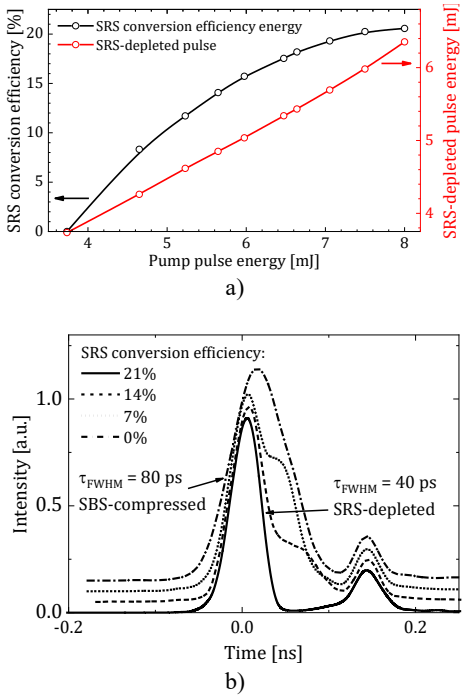

Fig. 3. a) Dependance of SRS conversion efficiency on pump pulse energy, b) Temporal waveforms evolution of the 1064 nm pulse depleted by transient forward SRS in KGW at various SRS-conversion efficiencies.

In this regime, the conversion to the first Stokes component at 1177 nm reaches ~21 %. At the same time, the residual 1064 nm pulse retains an energy of 6.3 mJ (Fig. 3, red line).

The pulse reshaping is governed by the transient nature of forward SRS. Since the Stokes wave builds up over the duration of the pulse, the interaction is strongly time-dependent. The leading edge of the pulse is only weakly affected, whereas the trailing edge undergoes pronounced depletion. As a result, the pulse acquires an asymmetric temporal profile, and effective shortening is achieved through selective removal of the trailing part. The strength of this effect increases with pump energy, reflecting the growth of the Raman gain and the associated rise in conversion efficiency (Fig. 3b). Under optimal conditions at a pump energy of ~8 mJ (corresponding to a 21 % SRS conversion efficiency), efficient temporal reshaping was achieved without noticeable distortion of the main pulse peak (Fig. 3b, solid line). In this regime, the SRS interaction provides strong trailing-edge depletion while avoiding the onset of additional temporal structures associated

with overdriven interaction. As a result, the SBS-compressed ~80 ps pulse is further shortened to ~40 ps. The pulse duration was measured using a Hamamatsu streak camera with a temporal resolution of 3 ps.

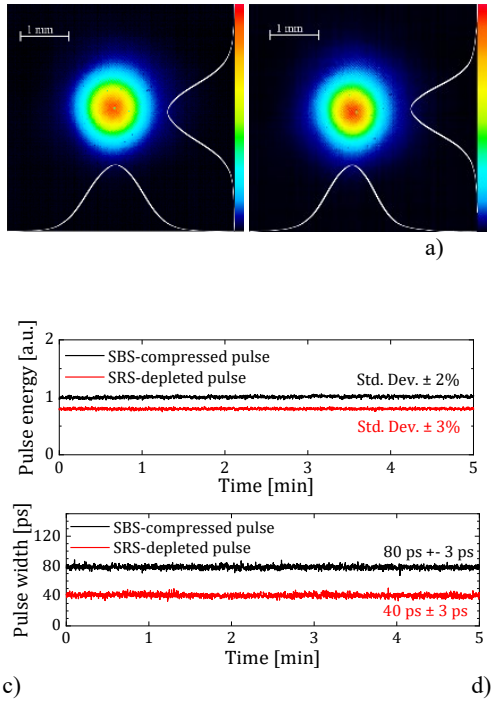

Fig. 4. Spatial beam profiles of a) SBS-compressed and b) SRS-depleted pulses under optimal operating conditions, c) Pulse energy stability and d) pulse width stability of SBS-compressed (black) and SRS-depleted (red) pulses measured over 5 min of operation. The spatial beam profile remains unchanged after the SRS stage (Fig. 4, a, b), indicating that the reshaping process does not introduce noticeable spatial distortions and preserves a Gaussian beam distribution. The energy fluctuations measured over 5 min were ±2 % for the SBS-compressed pulses and ±3 % for the SRS-depleted pulses (Fig. 4, c). At the same time, the pulse width remains stable, with variations within ±3 ps for both stages (Fig. 4, d). These results indicate that the SRS-based reshaping does not degrade temporal stability, despite the strong nonlinear interaction. Thus, the combined SBS / SRS setup ensures efficient pulse shortening while maintaining good beam quality and stable operation.

4. Conclusions

We have demonstrated, to the best of our knowledge, record-level SBS-compression of a nanosecond pulse, using transient forward SRS to efficiently deplete the trailing edge of the pump pulse. For the first time, this approach enabled achieving a ~40 ps pulse width and an output pulse energy of 6.3 mJ at 1064 nm without resorting to mode-locking, while preserving compatibility with subsequent amplification in standard Nd:YAG gain modules. The developed approach may pave the way toward a significant reduction in the cost of Direct Laser Interference Patterning (DLIP) used to impart water-repellent properties to functional surfaces.

Acknowledgements

This research was funded by Research Council of Lithuania, grant number S-MIP-25-17.

References

[1]. N. F. Andreev, E. A. Grishin, O. Kulagin, A. Rodin, Picosecond lasers with Brillouin and Raman pulse compression, in *Proceedings of the International Conference on High Power Laser Beams (HPLB'06)*, 2006.

[2]. A. S. Dement'ev, I. Demin, et al., Compression of pulses during their amplification in the field of a focused counterpropagating pump pulse of the same frequency and width in media with electrostriction nonlinearity, *Quantum Electronics*, Vol. 41, Issue 2, 2011, pp. 153-159.

[3]. G. Marcus, S. Pearl, G. Pasmanik, Stimulated Brillouin scattering pulse compression to 175 ps in a fused quartz at 1064 nm, *Journal of Applied Physics*, Vol. 103, Issue 5, 2008, 053105.

[4]. A. M. Rodin, A. Černeckytė, et al., Optimizing self-seeded perfluorooctane SBS-compressor configurations to achieve 90 ps high-energy pulses, *Photonics*, Vol. 10, Issue 9, 2023, 1060.

[5]. V. Girdauskas, A. S. Dement'ev, et al., SRS-amplification of picosecond Stokes pulses in the field of counterpropagating pump pulses, *Journal of Applied Spectroscopy*, Vol. 60, Issue 3-4, 1994, pp. 207-212.

(023)

Statistical Properties of the Displaced Fock and Squeezed States

J. C. Vega [1] and D. Ojeda-Guillén [2]
[1] Escuela Superior de Física y Matemáticas, Instituto Politécnico Nacional, Ed. 9, U. P. Adolfo López Mateos, Alc. Gustavo A. Madero, C.P. 07738, Ciudad de México, México
[2] Escuela Superior de Cómputo, Instituto Politécnico Nacional, Av. Juan de Dios Bátiz esq. Av. Miguel Othón de Mendizábal, Col. Lindavista, Alc. Gustavo A. Madero, C.P. 07738, Ciudad de México, México
E-mail: jvegap1601@alumno.ipn.mx

Summary: We investigate the statistical properties of displaced Fock states and squeezed displaced states to identify the parameter regimes that lead to sub- and super-Poissonian photon-number distributions. Furthermore, we explicitly determine the parameter values for which bunching and antibunching effects dominate, thereby distinguishing classical and non-classical behavior. To this end, we calculate the Mandel Q-parameter and the second-order correlation function $g^{(2)}(0)$ for each state. As an application in quantum optics, we explain how these parameters can be used to describe the statistical behavior of the parametric amplifier.

Keywords: Displaced Fock states, Squeezed displaced states, Mandel Q-parameter, Second-order correlation function, Photon-number distribution, Bunching and antibunching effects.

1. Introduction

1.1. Fock Space and Fock States

In quantum optics, the electromagnetic field is quantized to describe each oscillation mode as a harmonic oscillator. Therefore, it is necessary to specify the appropriate state space, known as the Fock space and the basis states are the Fock states [1]. Considering a single-mode of radiation as in ref. [1], we can use the annihilation and creation operators from the harmonic oscillator, which satisfy $[\hat{a}, \hat{a}^\dagger] = 1$, to define the number operator as $\hat{n} = \hat{a}^\dagger \hat{a}$, and the action of this operator on the states of the number operator is

$$\hat{a}^\dagger \hat{a}|n\rangle = n|n\rangle, \tag{1}$$

where the states $|n\rangle$ are the Fock states and $n = 0,1,2,....$ For $n = 0$, we can obtain the state $|0\rangle$ which is the vacuum state as it contains no quanta of the radiation field. Applying the creation operator to this state, we get the single-photon state $\hat{a}^\dagger|0\rangle = |1\rangle$ [1]. If we continue this process, we obtain the n photon state defined as

$$|n\rangle = \frac{(\hat{a}^\dagger)^n}{\sqrt{n!}}|0\rangle, \tag{2}$$

with a factor that leads to the correct normalization of the state [1].

1.2. Coherent and Squeezed States

A particular class of harmonic oscillator states plays a significant role in the quantum theory of radiation and in quantum optics which minimizes the Heisenberg uncertainty relation, $\Delta p \Delta q \geq \hbar/2$, where the standard deviation of one observable can be squeezed and the conjugate observable has to be stretched [2]. These states are known as squeezed states. Furthermore, there is a subclass of states which simultaneously minimizes the variance in both the position and momentum operators, called coherent states [2]. In [3], there are three equivalent ways to define the coherent states, but the main one is the action of the displacement operator on the vacuum state

$$|\alpha\rangle = \hat{D}(\alpha)|0\rangle, \tag{3}$$

where $\hat{D}(\alpha) = e^{\alpha\hat{a}^\dagger - \alpha^*\hat{a}}$. Analogously, while there are multiple equivalent ways to define the squeezed states, in this work, we focus on the combined action of the displacement and squeezing operators on the vacuum state

$$|\alpha, \xi\rangle = \hat{D}(\alpha)\hat{S}(\xi)|0\rangle, \tag{4}$$

where $\hat{D}(\alpha) = e^{\alpha\hat{a}^\dagger - \alpha^*\hat{a}}$ and $\hat{S}(\xi) = e^{\frac{1}{2}\left(\xi^*\hat{a}^2 - \xi\hat{a}^{\dagger 2}\right)}$ with $\xi = re^{i\theta}$ [3-6]. Moreover, the squeeze parameter r satisfies $0 \leq r < \infty$ and $0 \leq \theta \leq 2\pi$ [2]. These quantum states exhibit properties that closely resemble those of a classical harmonic oscillator [3].

1.3. Statistical Properties

The quantum states of light can be classified as classical and nonclassical states depending on the presence of some quantum features related to the discrete nature of the photons [1]. To identify this behavior, we could use some statistical properties, such as the relative fluctuation in photon number or intensity (correlation functions), which allow us to characterize classical and nonclassical radiation fields [7].

A very useful statistical tool is the Mandel Q-parameter, which allows us to measure the deviation from the Poisson distribution to distinguish quantum processes from classical ones because the photon number distribution for a coherent field is Poissonian, so, any distribution which is narrower than Poissonian must correspond to a nonclassical field [1, 7]. This parameter is defined as

$$Q = \frac{\langle \hat{n}^2 \rangle - \langle \hat{n} \rangle^2}{\langle \hat{n} \rangle} - 1, \tag{5}$$

where it describes a super-Poissonian distribution for $Q > 0$, a Poissonian distribution for $Q = 0$, and a sub-Poissonian distribution for $Q < 0$ [1, 5, 7].

Another useful parameter is the second-order correlation function $g^2(0)$ which quantifies the intensity fluctuations and is closely related to the Mandel parameter [7, 8]. This parameter provides information on the bunching or the anti-bunching effects and is defined as

$$g^2(0) = \frac{\langle \hat{n}^2 \rangle - \langle \hat{n} \rangle}{\langle \hat{n} \rangle^2} = \frac{Q}{\langle \hat{n} \rangle} + 1, \tag{6}$$

where the bunching effect appears when $g^2(0) > 1$ and the anti-bunching effect when $g^2(0) < 1$ [1,5,7].

2. Results

2.1. The Displaced Fock State

Using the Hadamard identity [3] defined as

$$e^A B e^{-A} = B + [A,B] + \frac{1}{2!}\big[A,[A,B]\big] + \\ + \frac{1}{3!}\Big[A,\big[A,[A,B]\big]\Big] + \cdots, \tag{7}$$

we obtain the following translation properties of the annihilation and creation operators as follows [3-5]

$$\hat{D}^\dagger(\alpha)\hat{a}\hat{D}(\alpha) = \hat{a} + \alpha, \tag{8}$$

$$\hat{D}^\dagger(\alpha)\hat{a}^\dagger\hat{D}(\alpha) = \hat{a}^\dagger + \alpha^* \tag{9}$$

Now, we can obtain the expected values to calculate the Mandel Q-parameter, considering [3]

$$\hat{a}|n\rangle = \sqrt{n}|n-1\rangle, \tag{10}$$

$$\hat{a}^\dagger|n\rangle = \sqrt{n+1}|n+1\rangle \tag{11}$$

Therefore, the expectation values are

$$\langle \hat{a}^\dagger\hat{a} \rangle = n + |\alpha|^2, \tag{12}$$

$$\langle (\hat{a}^\dagger\hat{a})^2 \rangle = n(n-1) + 4|\alpha|^2 n + |\alpha|^4, \tag{13}$$

and the Mandel Q-parameter is

$$Q = \frac{n(2|\alpha|^2-1)}{n+|\alpha|^2}, \tag{14}$$

where we obtain a sub-Poissonian distribution for $|\alpha|^2 < 1/2$ while for larger values, a super-Poissonian distribution as shown in Fig. 1. In addition, when $|\alpha|^2 = 1/2$, the Mandel Q-parameter is $Q = 0$, indicating a Poissonian distribution which means it has photon statistics similar to the coherent states. In Fig. 2, we show the Mandel Q-parameter as a function of the quantum number n and the displaced parameter α.

Then, we can obtain the other statistical parameter, the second-order correlation function $g^2(0)$ where we get the following result

$$g^2(0) = \frac{n(2|\alpha|^2-1)}{(n+|\alpha|^2)^2} + 1, \tag{15}$$

where antibunching effects appear for $|\alpha|^2 < 1/2$, which means that for small displacements, the Fock state character dominates (antibunching) but for large displacements, the state behaves more classically. In Fig. 3, we can see the plot of this parameter, and we can establish the transition of this behavior at $|\alpha|^2 = 1/2$ where it behaves as a coherent state.

2.2. The Squeezed Displaced State

Similarly, using Eqs. (7)-(9) some properties of the annihilation and creation operators can be obtained [3-6]

$$\hat{S}^\dagger(\xi)\hat{D}^\dagger(\alpha)\hat{a}\hat{D}(\alpha)\hat{S}(\xi) = \mu\hat{a} - \nu\hat{a}^\dagger, \tag{16}$$

$$\hat{S}^\dagger(\xi)\hat{D}^\dagger(\alpha)\hat{a}^\dagger\hat{D}(\alpha)\hat{S}(\xi) = \mu\hat{a}^\dagger - \nu^*\hat{a}, \tag{17}$$

where $\mu = \cosh(r)$ and $\upsilon = e^{i\theta}\sinh(r)$. Therefore, the expectation values for the Mandel Q-parameter are

$$\langle \hat{a}^\dagger\hat{a} \rangle = |\alpha|^2 + sinh^2(r), \tag{18}$$

$$\langle (\hat{a}^\dagger\hat{a})^2 \rangle = |\alpha|^2 \Big(e^{-2r}cos^2\Big(\phi - \frac{\theta}{2}\Big) + \\ e^{2r}sin^2\Big(\phi - \frac{\theta}{2}\Big)\Big) + +2sinh^2(r)(sinh^2(r)+1), \tag{19}$$

we define $\alpha = |\alpha|e^{i\phi}$ and the Mandel Q-parameter is

$$Q = \frac{|\alpha|^2(e^{-2r}-1)+2sinh^4(r)+sinh^2(r)}{|\alpha|^2+sinh^2(r)}, \tag{20}$$

where we choose $\phi = \theta/2$ to align the displacement along the squeezed quadrature which means we minimize the photon number fluctuations [5]. In this case, it is possible to obtain both sub- and super-Poissonian distribution depending on the values of r and α as shown in Fig. 4 and in Fig. 5 [4, 5]. For larger values of r, the super-Poissonian regime

dominates. In contrast, the sub-Poissonian distribution appears for small values of r and $|\alpha|^2 \neq 0$.
Then, we can obtain the second-order correlation function $g^2(0)$

$$g^2(0) = \frac{|\alpha|^2(e^{-2r}-1)+2sinh^4(r)+sinh^2(r)}{(|\alpha|^2+sinh^2(r))^2} + 1, \quad (21)$$

where we can obtain both bunching and anti-bunching effects depending on the values of r and α as shown in Fig. 6 [4]. For larger values of r, only bunching effects appear. On the other hand, antibunching effects are obtained for small values of r and for $|\alpha|^2 \neq 0$. This indicates that a small contribution of the squeezed parameter r leads to non-classical effects.

The squeezed vacuum states are generated by techniques of nonlinear optics, such the degenerate parametric amplifier [8]. In [7] appears an algebraic approach to find the eigenfunctions and eigenvalues of the problem which it is possible since the symmetry group of the squeezed states is $SO(2,1)$ [3]. This group is isomorphic to $SU(1,1)$, so we can define the compression operator with the $su(1,1)$ lie algebra.

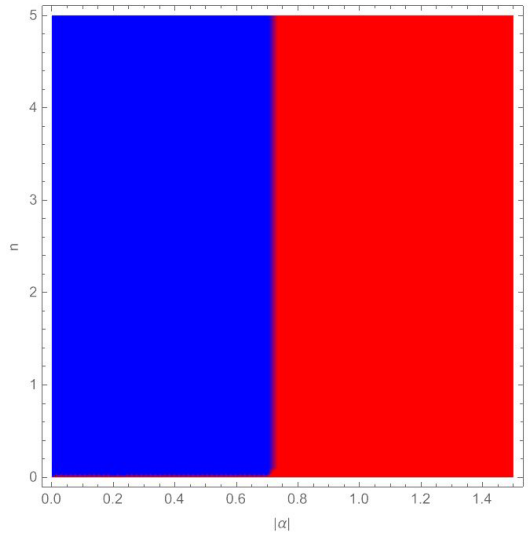

Fig. 1. Phase diagram of the Mandel Q-parameter for the displaced Fock state. Blue region: $Q < 0$. Red region: $Q > 0$.

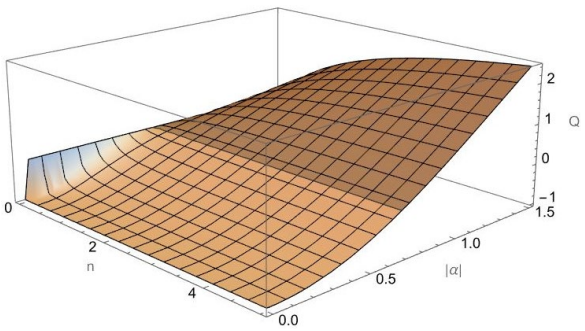

Fig. 2. Mandel Q-parameter for the displaced Fock state.

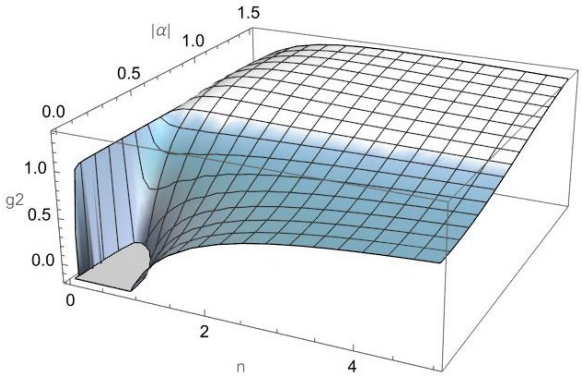

Fig. 3. Second-order correlation function $g^2(0)$ for the displaced Fock state.

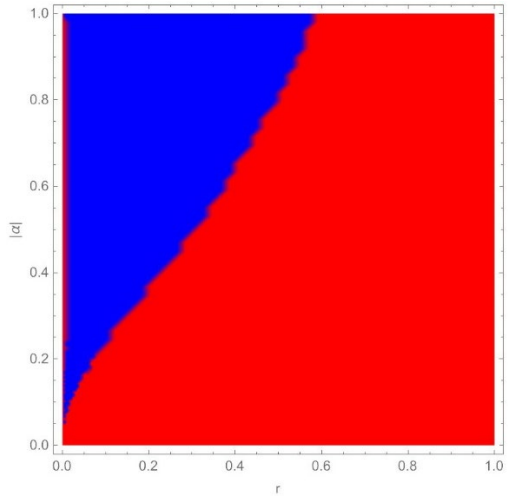

Fig. 4. Phase diagram of the Mandel Q-parameter for the squeezed displaced state. Blue region: $Q < 0$. Red region: $Q > 0$.

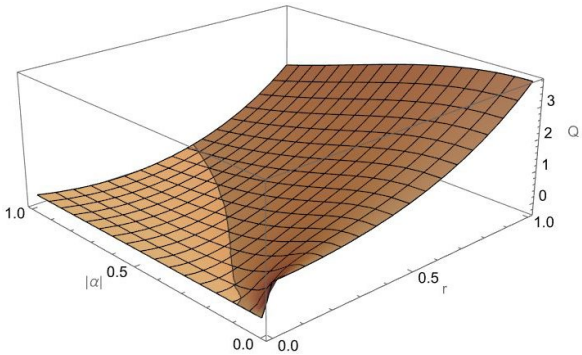

Fig. 5. Mandel Q-parameter for the squeezed displaced state.

3. Conclusions

In this work, we have studied the statistical properties of the displaced Fock states and the squeezed displaced states. Using the Mandel Q-parameter, we find a sub-Poissonian distribution for

$|\alpha|^2 < 1/2$ in the displaced Fock state, and for larger values we obtain a super-Poissonian distribution. Moreover, it exhibits coherent state behavior when $|\alpha|^2 = 1/2$. In addition, we can identify antibunching effects when $|\alpha|^2 < 1/2$, which means that for small displacements, the Fock state character dominates (antibunching) but for large displacements, the state behaves more classically, that means the coherent part dominates. In addition, we establish the transition of this behavior at $|\alpha|^2 = 1/2$ where it behaves as a coherent state.

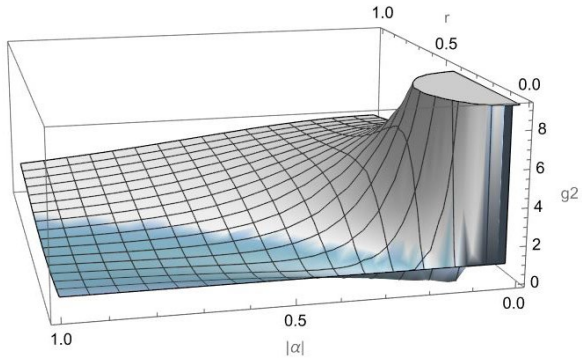

Fig. 6. Second-order correlation function $g^2(0)$ for the squeezed displaced state.

For the squeezed displaced state, we suppose $\phi = \theta/2$ to align the displacement along the squeezed quadrature so that the photon number fluctuations have been minimized (less noise deviation), so we obtain not only sub-Poissonian and super-Poissonian distributions but also bunching and antibunching effects depending on the values of r and α. For larger values of r, only bunching effects appear. On the other hand, antibunching effects are obtained for small values of r and for $|\alpha|^2 \neq 0$. This indicates that a small contribution of the squeezed parameter r lead to non-classical effects.

One application of these states can be seen in the degenerate parametric amplifier. To study these amplifiers, it is possible to use an algebraic method taking advantage of the symmetry group of the squeezed states, $SO(2,1)$, which is isomorphic to $SU(1,1)$, so the compression operator can be defined with the $su(1,1)$ lie algebra.

References

[1]. G. S. Agarwal, Quantum Optics, *Cambridge University Press*, Cambridge, 2013.
[2]. P. Meystre, Quantum Optics: Taming the Quantum, *Springer*, Cham, 2021.
[3]. D. Ojeda-Guillén, Mecánica cuántica de los estados coherentes y comprimidos, Master's Thesis, *Instituto Politécnico Nacional*, Mexico City, 2011 (in Spanish).
[4]. M. Orszag, Quantum Optics, *Springer*, Berlin, 2008.
[5]. L. Mandel, E. Wolf, Optical Coherence and Quantum Optics, Cambridge University Press, Cambridge, 1995.[6]. C. Gerry, P. Knight, Introductory Quantum Optics, *Cambridge University Press*, Cambridge, 2005.
[7]. J. C. Vega, D. Ojeda-Guillén, R. D. Mota, SU(1,1)×SU(2) approach and the Mandel parameter to the Hamiltonian of two oscillators with weak coupling, *Journal of the Optical Society of America B*, Vol. 42, Issue 3, 2025, pp. 683-692.
[8]. M. Fox, Quantum Optics: An Introduction, *Oxford University Press*, Oxford, 2006.

(025)

Picowell Arrays for Microfluorescence, Written Directly by Ion Microbeam in a Cyclic Olefin Copolymer: Quality Dependence on Fabrication Parameters

I. Bányász [1], I. Rajta [2], V. Havránek [3], A. J. Laki [4], Á. Nagyné Szokol [5], M. Kellermayer [6], Z. Szittner [7], S. Novák [7] and G. U. L. Nagy [8]

[1] Széchenyi István University, Egyetem tér 1, H-9026 Győr, Hungary
[2] HUN-REN Institute for Nuclear Research, P.O.B. 51, 4001 Debrecen, Hungary
[3] Nuclear Physics Institute AV CR, 250 68 Řež near Prague, Czech Republic
[4] Faculty of Information Technology and Bionics, Pázmány Péter Catholic University, Práter u. 50a, H-1083 Budapest, Hungary
[5] HUN-REN Wigner Research Centre for Physics, P.O. Box 49, H-1525 Budapest, Hungary
[6] Department of Biophysics and Radiation Biology, Semmelweis University, Tűzoltó u. 37-47, H-1094 Budapest, Hungary
[7] Nanobiosensorics Laboratory, Centre for Energy Research, P:O.B. 49, H-1525 Budapest, Hungary
[8] TU Wien, Institute of Applied Physics, 1040 Vienna, Austria
Tel.: + 00 36308847750
E-mail: banyasz.istvan@sze.hu

Summary: Picowell arrays, intended for microfluorescence studies of individual cells, were fabricated in cyclic olefin copolymer substrates by direct writing with microbeams of swift heavy ions. Since ion beam implantation caused swelling of the polymer, toroidal structures were written in the samples by implanting annuli of adequate diameter with the ion microbeams.

Four experiments were carried out at two tandem particle accelerators.

The target materials were two types of ZEONOR copolymer. Microbeams of 10.5 MeV N^{4+} and 9 and 10.5 MeV C4+ ions were used in the experiments. Microbeam sizes were between 2 and 3 microns. Beam current was in the 16–800 pA range, and fluence was between 10^{12}–10^{13} ion/cm^2. Picowells of various internal and external diameters were written form 14/16 to 40/42 microns.

In general, picowell depth was proportional to the implanted fluence in the fluence range used, although in some experiments saturation was observed. Very similar results were obtained by carbon and nitrogen ions.

It was found that the most important fabrication parameter was the current density or flux of the implanted ions. At the same energy and fluence (and similar beam size), much higher picowell depth was obtained at a current density of 90 A/m^2 (800 pA) than at 20 A/m^2 (125 pA).

One of the most important findings of the experiments was that -besides of the parameters of the ion beam implantation- the resulting picowell depth strongly depended on the elastic properties of the ZEONOR sample.

The best results were obtained by a 10.5 MeV N^{4+} microbeam, in the form of a 9 x 9 picowell array in one of the ZEONOR types, labelled as "OLD". Diameters of the individual picowells were 20/22 microns, their depth was 4.8 micron, and they comprised a volume of 820 femtoliter. Although absorption of the ion beam implanted torus increased at the highest ion fluences, the unimplanted bottom of the picowell preserved the high transparency of ZEONOR. So, such picowell arrays are good for microfluerescence studies. When picowell arrays were written in another type of ZEONOR samples, labelled as "NEW", the maximum depth of the picowells was below 1.0 micron. AFM measurements of the Young moduli of the pristine and as-implanted samples of the two types of ZEONOR revealed a significant difference between the elasticity of the two samples. The large differences in the maximum picowell depth could be attributed to this fact.

Keywords: Microfluorescence, Picowell array, Cyclic olefin copolymer, Ion beam implantation, Swift heavy ion, Ion microbeam.

1. Introduction

Microplate consist of a two-dimensional array of wells. They are standard tools in analytical research and clinical diagnostic testing [1]. The volume of an individual well on a microplate range between tens of nanoliters to several milliliters. Nanowells are already routinely fabricated [2, 3].

It is a difficult task to fabricate very small microrecipients of a volume of picoliter or even femtoliter [4-6].

We proposed and accomplished a completely new method for fabrication of picowell arrays in a polymer by direct writing with microbeams of swift heavy ions. [7]. To our best knowledge, direct ion microbeam writing of microstructures in Cyclic Olefin Copolymers (COC) had not been previously proposed. A thorough review of the applications of such materials in microfluidics and microdevices was recently published by Agha *et al.* [8].

2. Experimental

2.1. Fabrication Method

Based on our previous results in ion beam implantation of optical and mechanical elements in polymers, we designed two types of implanted patterns: a homogeneously implanted disk, and a homogeneously implanted annulus We used microbeams of a high-energy medium-mass ion for the fabrication of the picowell arrays. Due to the chain scissoring and cross-linking processes either compaction or swelling of polymer sample could be expected.

The target material was a cyclic olefin copolymer (COC), commercialized under the name of ZEONOR.

It turned out that ion beam implantation of ZEONOR resulted in the swelling of the implanted parts of the polymer surface, so that only the implanted annuli could produce picowell recipients. The implantation of disk resulted in the fabrication of microlenses.

2.2. Implantations

Four campaigns of implantation of picowell arrays in ZEONOR samples were carried out: Three of them performed at the Tandetron Laboratory of the institute UJF of the Czech Academy of Sciences in Řež near Prague, Czech Republic, and the fourth one at the Tandetron of the HUN-REN Atomki institute in Debrecen, Hungary.

Parameters of the implantations of the picowell arrays are presented in Table 1.

2.2. Results

Atomic Force Microscopic (AFM) image of a part of the picowell array fabricated in the first UJF experiment is shown in the left side of Fig, 1. Three cross sections of a picowell along its diameter are also shown in the right side of Fig. 1. Depth of the picowell is 4.8 μm. Average volume of the picowells of the 9 × 9 array was 820 ± 65 fl.

Table 1. Parameters of the implanted picowell arrays.

Exp. No. Tandetron	Ion species and charge	Ion energy [MeV]	Beam current [pA]	Beam size [μm]	Fluence [10^{12} ion/cm^2]	Zeonor type	Inner/outer radii [μm]
1. UJF	N^{4+}	10.5	800	3 × 3	7.8	Old	3/4, 22/12
2. UJF	C^{4+}	10.5	16	2.7 × 2.7	5.0-20	New	7/8, 10/11, 14/15, 20/21
3. UJF	N^{4+}	10.5	125	2.5 × 2.5	5.0-80	New	7/8, 10/11, 14/15, 20/21
4. Atomki	C^{4+}	9.0	2-4	3 × 5	2-16	New, Old	10/11, 14/15

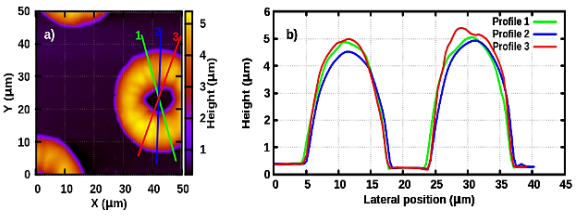

Fig. 1. Height-contrast AFM image (**left**) of part of a picowell array, and topographical height profiles of a picowell (**right**) in it. Sections of the picowell where profiles were extracted are indicated on the left panel. 1. UJF Experiment. OLD ZEONOR. Figure taken from [7].

It can be seen in Fig. 1 that well defined regular picowell were fabricated in the first UJF Experiment. Mechanical stability of the picowells was checked by microhardness measurements of both the implanted toroidal walls of the picowells and the unimplanted bottom of the picowells. Results are shown in Fig. 2.

No difference in the microhardness of the implanted and unimplanted areas was found.

Functionality of the picowell array was demonstrated by a micofluorescence experiment, in which HeLa Fucci cells were placed in individual picowells, and their microfluorescence was observed, as it can be seen in Fig. 3.

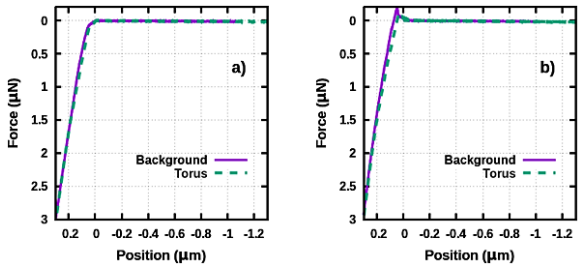

Fig. 2. Microhardness measurements of a picowell. 1. UJF Experiment. (**a**) Indentation of the sample surface and the toroidal wall. Continuous line: background, dashed line: torus (**b**) Retraction traces for the sample surface and the toroidal wall. Continuous line: background, dashed line: torus. Figure taken from [7].

To further study the possibilities of the fabrication of picowell arrays in ZEONOR samples by ion microbeam writing, further experiments were performed, see Table 1.

However, in spite of reproducing the main parameters of the first experiment (1. UJF), and extending the range of the implanted fluence, and using two ion species, maximum depth of the picowells was much smaller in the experiments 2. UJF, 3. UJF and 4. Atomki, then in first experiment of 1. UJF.

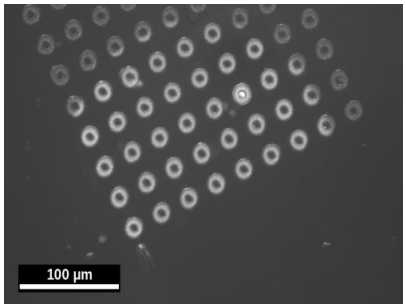

Fig. 3. A Fucci cell emitting strong fluorescent signal is seen in a picowell**.** Figure taken from [7].

Some results are presented in Figs. 4 and 5.

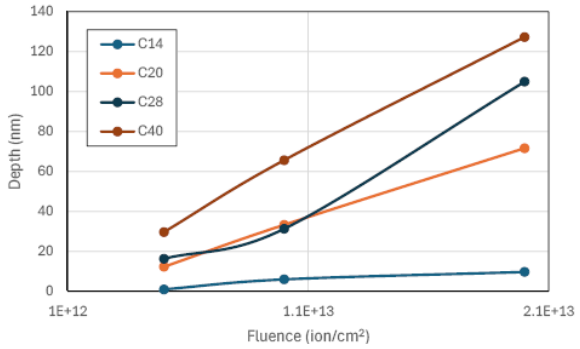

Fig. 4. Depths of the picowells in NEW ZEONOR *vs.* the implanted fluence. 2. UJF Experiment. 10.5 MeV C^{4+} ion microbeam, Inner diameter of the picowells is 14, 20, 28 and 40 µm. Connecting lines only serve as visual guides.

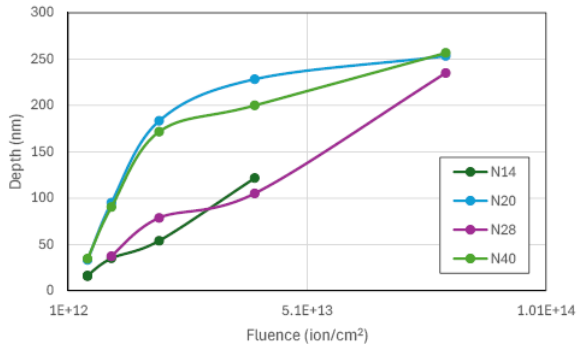

Fig. 5. Depths of the picowells in NEW ZEONOR *vs.* the implanted fluence. 3. UJF Experiment. 10.5 MeV N^{4+} ion microbeam, Inner diameter of the picowells is 14, 20, 28 and 40 µm. Connecting lines only serve as visual guides.

3. Conclusions

Fabrication of microstructures in optical materials, especially in soft ones, like the ZEONOR copolymer, is an intricate process, and the quality of the microstructures depends on various parameters.

Our first results on direct ion microbeam writing of picowell arrays on ZEONOR cyclic olefin copolymer proved that the proposed method could produce such arrays that were usable for the study of single cells, thanks to the subpicoliter volume of the individual picowells.

Besides of briefly resuming the results of our first experiments, published earlier [7], here we presented the results of our more recent experiments, aimed at the reproduction of the first results, and to study the applicability of the method by significantly extending the range of the implanted fluence, and, besides of the nitrogen ion, also using carbon ions.

According to the results of these experiments, one of the most important parameters is the ion beam current, or rather the current density, which is equal to the ion flux. Since in the four experiments presented here the differences in the cross section of the microbeams were small, one could attribute the large depth of the picowells (or rather the large height of the toruses) in 1. UJF Experiment to the fact that beam current was very high, 800 pA, while the second highest value of beam current was only 125 pA (3. UJF), only 16 % of the former one. Apparently, higher ion flux maintains the large swelling of the implanted sample surface, and thus hinders its relaxation due to the elasticity of the sample.

Another key parameter can be the microhardness (or elasticity) of the unimplanted sample. It is supposed that the "Old" and "New" ZEONOR samples (provided by different companies) have different microhardness. So, it is possible that the difference in the depth of the picowells written in the two types of ZEONOR could be increased by the difference in their microhardness.

Study of the picowell arrays fabricated in the last experiment in both "Old" and "New" ZEONOR is under way. The results would hopefully shed light on the mechanism of microstructure formation in this polymer. Besides of systematically measuring microelasticity of the walls of the ion microbeam implanted picowells, micro Raman experiments are also planned. It is hoped that ion beam induced structural changes in the ZEONOR polymer could be identified by changes in the Raman spectra.

References

[1]. Q. Zhou, K. Son, Y. Liu, A. Revzin, Biosensors for cell analysis, *Annual Review of Biomedical Engineering*, Vol. 17, 2015, pp. 165-190.

[2]. S. Lindstrom, M. Eriksson, T. Vazin, et al., High-density microwell chip for culture and analysis of stem cells, *PLoS ONE*, Vol. 4, Issue 9, 2009, e6997.

[3]. H. Antypas, M. Veses-Garcia, E. Weibull, et al., A universal platform for selection and high-resolution phenotypic screening of bacterial mutants using the nanowell slide, *Lab on a Chip*, Vol. 18, Issue 12, 2018, pp. 1767-1777.

[4]. D. Bernhard, S. Mall, P. Pantano, Fabrication and characterization of microwell array chemical sensors, *Analytical Chemistry*, Vol. 73, Issue 11, 2001, pp. 2484-2490.

[5]. J. R. Rettig, A. Folch, Large-scale single-cell trapping and imaging using microwell arrays, *Analytical Chemistry*, Vol. 77, Issue 17, 2005, pp. 5628-5634.

[6]. T. Molter, S. McQuaide, M. Suchorolski, et al., A microwell array device capable of measuring single-cell oxygen consumption rates, *Sensors and Actuators B: Chemical*, Vol. 135, Issue 2, 2009, pp. 678-686.

[7]. I. Bányász, I. Rajta, V. Havránek, et al., Design, fabrication, and characterization of picowell arrays on cyclic olefin copolymer surfaces generated with a 10.5 MeV N4+ ion microbeam, *Applied Physics Letters*, Vol. 123, Issue 5, 2023, 053701.

[8]. A. Agha, W. Waheed, N. Alamoodi, et al., A review of cyclic olefin copolymer applications in microfluidics and microdevices, *Macromolecular Materials and Engineering*, Vol. 307, Issue 10, 2022, 2200053.

(028)

Design of a Porous Polydimethylsiloxane Metamaterial for Passive Daytime Radiative Cooling

N. Namazzade [1] and A. Baron [1,2]
[1] University of Bordeaux, CNRS, CRPP, UMR 5031, 33600 Pessac, France
[2] Institut Universitaire de France, 75231 Paris Cedex 05, France
E-mail: alexandre.baron@u-bordeaux.fr

Summary: Passive daytime radiative cooling (PDRC) is investigated using porous polydimethylsiloxane (PDMS) with spherical air voids. We combine dependent scattering Monte Carlo simulations in the solar spectral band (0.3–2.5 μm) with full-wave finite element simulations and Nicholson-Ross-Weir effective parameter retrieval in the atmospheric transparency window (8–14 μm) to quantify solar reflectance and thermal emissivity. At high porosity (fv ≈ 0.5), an optimal void radius near 1.4 μm minimizes absorbed solar power while maintaining high thermal emissivity, maximizing net cooling. Extended Maxwell Garnett theory fails for micrometer-scale voids due to multipolar contributions, producing emissivity errors of 0.1–0.15, while retrieval-based effective parameters faithfully reproduce full-wave angular emissivity. The predicted steady-state temperature reduction reaches approximately 6 K at 300 K ambient and 12 K at 315 K. The optimal radius remains stable across ambient temperatures, providing robustness to fabrication variability.

Keywords: Passive daytime radiative cooling, Porous metamaterials, Dependent scattering, Effective parameter retrieval, Maxwell Garnett.

1. Introduction

Passive daytime radiative cooling (PDRC) enables a surface under sunlight to reject heat to the cold sky without any external energy input. Net cooling requires simultaneously (i) high reflectance across the solar spectral band (SSB, $0.3-2.5\,\mu m$) and (ii) high emissivity in the atmospheric transparency window (ATW, $8-14\,\mu m$) [1, 2]. Porous polymer films are important candidates for PDRC because of their ability to scatter light in the solar band. In particular, polydimethylsiloxane (PDMS) (Fig. 1c) is intrinsically absorptive in the infrared, and therefore emissive via Kirchhoff's law, making it a promising PDRC material. Spherical air voids in the PDMS matrix can further enhance infrared absorption while being highly effective for solar scattering.

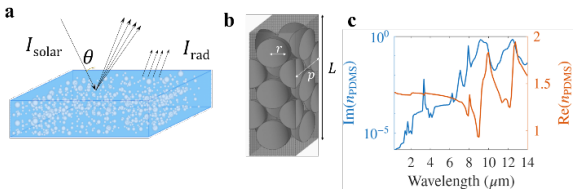

Fig. 1. a – Schematic of the porous PDMS metamaterial: spherical air voids scatter incident solar irradiance I_{solar} (angle θ) to minimize solar absorptance; I_{rad} is the emitted thermal intensity. (b) FEM unit cell: face-centered cubic void arrangement (radius r, period p) in a PDMS slab of thickness L. (c) Spectral refractive index of PDMS [12].

However, in dense porous systems, dependent scattering can bias design rules derived from simplified models. Here we systematically quantify how void radius and volume fraction affect cooling performance of a monomodal porous PDMS metamaterial. We combine Monte Carlo radiative transfer in the SSB including dependent scattering [3, 4] with full-wave finite element simulations in the ATW followed by Nicholson-Ross-Weir (NRW) effective parameter retrieval [5]. We compare predictions against extended Maxwell Garnett (EMG) theory, which is widely used in the PDRC literature but can fail for resonant or non-dipolar inclusions [6, 7].

2. Radiative Cooling Framework

The net cooling power per unit area at surface temperature T is [1]:

$$I_{net}(T, T_{atm}) = I_{rad}(T) - I_{atm}(T_{atm}) - I_{solar}, \quad (1)$$

where $I_{rad}(T)$ is the emitted thermal radiation integrated over hemisphere and spectrum, $I_{atm}(T_{atm})$ is the absorbed atmospheric irradiation, and I_{solar} is the absorbed solar contribution integrated from 0.3 to 2.5 μm. The emissivity $\varepsilon(\lambda, \theta)$ of the material and the atmospheric emissivity $\varepsilon_{atm}(\lambda)$ in the ATW enter each term. Net cooling is achieved when $I_{net} > 0$, and the steady-state temperature T_∞ satisfies $I_{net}(T_\infty, T_{atm}) = 0$.

3. Methods

The idealized metamaterial consists of spherical air voids in a PDMS matrix. We varied void radius ($r = 0.5-6\,\mu m$) and volume fraction ($f_v = 0.1-0.5$).

3.1. Solar Band: Monte Carlo

Solar reflectance was computed via Monte Carlo radiative transfer tracing 5×10^5 photon trajectories, with scattering events sampled from Mie-theory differential cross-sections [8]. To account for dense packing, we incorporate dependent scattering through the interference approximation (ITA) [3, 4], which modifies the effective scattering strength via a structure factor computed using the Percus-Yevick hard-sphere approximation [9]. Results are compared with the independent scattering approximation (ISA).

3.2. Thermal Band: Full-Wave Simulation and Parameter Retrieval

In the ATW, reflectance is computed by full-wave finite element simulations (COMSOL) of periodic void arrangements in PDMS. An NRW-type procedure retrieves effective refractive index and wave impedance from normal-incidence scattering matrix coefficients [5]. For optically thick slabs, emissivity is obtained from $\varepsilon(\lambda,\theta) = 1 - R(\lambda,\theta)$, where R is evaluated either directly from full-wave simulation or from Fresnel coefficients using the retrieved parameters. EMG theory using dipolar Mie coefficients provides a fast baseline [6, 10].

4. Results and Discussion

4.1. Model Comparison

From Fig. 2a, a we see at $f_v = 0.5$, the effect of void size on solar reflectance is pronounced and for very small particles are less visible in the solar spectrum. In the ATW, NRW retrieval reproduces full-wave angular emissivity across all investigated void radii. In contrast, EMG agrees with full-wave results only for small voids (dipolar regime, $r \leq 0.5\ \mu m$). For micrometer-scale voids, EMG fails to capture multipolar contributions and impedance effects, producing emissivity errors of 0.1–0.15 (Fig. 2, b-c).

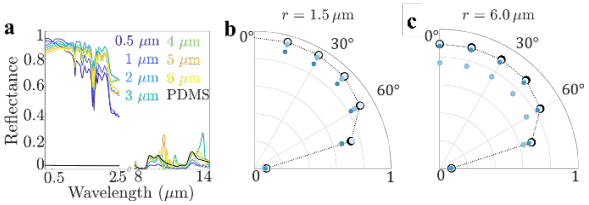

Fig. 2. Optical response of the porous PDMS metamaterial. (a) Spectral reflectance at normal incidence for varying r (f_v = 50 %): SSB via Monte Carlo-ITA, ATW via FEM. (b)–(c) Polar emittance (1 − R) at λ = 12.46 μm for r = 1.5 and 6.0 μm (f_v = 50%).

4.2. Volume Fraction Dependence

For $r = 1.4\,\mu m$ and $6\,\mu m$, increasing f_v monotonically decreases I_{solar} through enhanced solar reflectance. For $r = 50\,nm$, I_{solar} (ITA) shows an opposite trend with an optimum near $f_v \approx 0.1$, consistent with [11]. ISA systematically predicts lower I_{solar} than ITA. Net cooling ($I_{net} > 0$) is achieved at $f_v \approx 0.2$ for $r = 1.4\,\mu m$ (Fig. 3a, b), but not for $r = 50\,nm$ or $6\,\mu m$ within the explored range.

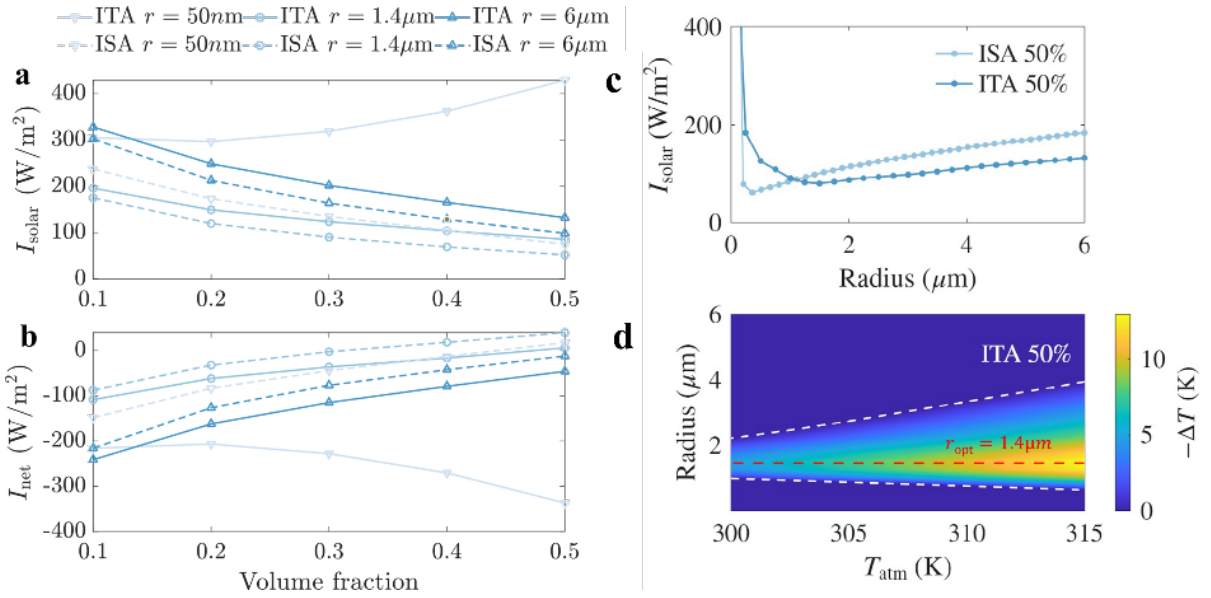

Fig. 3. Volume-fraction dependence of (a) I_{solar}, and (b) I_{net} for r = 50 nm, 1.4 μm, and 6 μm; solid (dashed) curves use ITA (ISA). Void-radius dependence at f_v = 50 %: (c) I_{solar} vs r; (d) predicted temperature drop $-\Delta T$ as a function of r and ambient temperature T_{atm}.

4.3. Optimal Void Radius

Fixing $f_v = 0.5$, both ISA and ITA predict a minimum of I_{solar} versus radius (Fig. 3c). ISA places the minimum near $r = 0.25\ \mu m$, consistent with 2D simulations by Chen et al. [6], while ITA shifts it to $r = 1.4\ \mu m$ due to dependent scattering. For larger radii, reflectance decreases weakly; for small radii, increased transparency raises solar absorption. The predicted optimal radius should be interpreted cautiously as it is not based on full-wave 3D simulations. The temperature drop $-\Delta T = T_{atm} - T_{\infty}$ versus void radius and ambient temperature confirms a cooling radius range that broadens with increasing T_{atm}, while the optimal radius remains unchanged at $1.4\ \mu m$. The maximum temperature drop reaches approximately $6\ K$ at $T_{atm} = 300\ K$ and $12\ K$ at $T_{atm} = 315\ K$ (Fig. 3d).

5. Conclusions

We studied porous PDMS metamaterials with spherical air voids for PDRC using a hybrid framework combining Monte Carlo simulations (with dependent scattering ITA) in the solar band and full-wave simulations with NRW parameter retrieval in the thermal band. Retrieval faithfully reproduces full-wave angular emissivity in the ATW, while EMG becomes unreliable beyond the dipolar regime. At high porosity ($f_v \approx 0.5$), an optimal void radius near 1.4 μm minimizes absorbed solar power while sustaining high ATW emissivity, maximizing net cooling. Predicted steady-state temperature drops reach $\approx 6\ K$ at $300\ K$ and $\approx 12\ K$ at $315\ K$ ambient. The optimum is robust across ambient temperatures, and the cooling radius interval broadens with increasing temperature. This work, recently published [7], provides practical design guidelines for porous polymer PDRC materials.

References

[1]. A. P. Raman, M. A. Anoma, L. Zhu, E. Rephaeli, et al., Passive radiative cooling below ambient air temperature under direct sunlight, *Nature*, Vol. 515, 2014, pp. 540-544.

[2]. Y. Zhai, Y. Ma, S. N. David, D. Zhao, et al., Scalable-manufactured randomized glass-polymer hybrid metamaterial for daytime radiative cooling, *Science*, Vol. 355, Issue 6329, 2017, pp. 1062-1066.

[3]. B. Wang, C. Zhao, The dependent scattering effect on radiative properties of micro/nanoscale discrete disordered media, *Annual Review of Heat Transfer*, Vol. 23, 2021, pp. 173-205.

[4]. R. A. Yalçın, E. Blandre, K. Joulain, J. Drévillon, Colored radiative cooling coatings with nanoparticles, *ACS Photonics*, Vol. 7, Issue 5, 2020, pp. 1312-1322.

[5]. D. R. Smith, S. Schultz, P. Markoš, C. M. Soukoulis, Determination of effective permittivity and permeability of metamaterials from reflection and transmission coefficients, *Physical Review B*, Vol. 65, Issue 19, 2002, 195104.

[6]. M. Chen, D. Pang, J. Mandal, X. Chen, et al., Designing mesoporous photonic structures for high-performance passive daytime radiative cooling, *Nano Letters*, Vol. 21, Issue 3, 2021, pp. 1412-1418.

[7]. N. Namazzade, A. Baron, Design of a monomodal porous metamaterial for passive daytime radiative cooling: Impact of spherical void radius and volume fraction, *APL Materials*, Vol. 14, Issue 1, 2026, 011116.

[8]. C. F. Bohren, D. R. Huffman, Absorption and Scattering of Light by Small Particles, *John Wiley & Sons*, New York, 2008.

[9]. J. K. Percus, G. J. Yevick, Analysis of classical statistical mechanics by means of collective coordinates, *Physical Review*, Vol. 110, Issue 1, 1958, pp. 1-13.

[10]. C. F. Bohren, D. P. Gilra, Extinction by a spherical particle in an absorbing medium, *Journal of Colloid and Interface Science*, Vol. 72, Issue 2, 1979, pp. 215-221.

[11]. L. Pattelli, A. Egel, U. Lemmer, D. S. Wiersma, Role of packing density and spatial correlations in strongly scattering 3D systems, *Optica*, Vol. 5, Issue 9, 2018, pp. 1037-1045.

[12]. X. Zhang, J. Qiu, X. Li, J. Zhao, et al., Complex refractive indices measurements of polymers in visible and near-infrared bands, *Applied Optics*, Vol. 59, Issue 8, 2020, pp. 2337-2344.

(032)

A Novel Technique for Simultaneous Measurements of Particles' Concentration and Velocity in a Fluid Flow

A. S. Abolhassani and B. Chebbi *
School of Engineering and Computer Science, Laurentian University, Sudbury, ON, Canada
Tel.: + 1 705 675 1151 ext. 4006
* E-mail: bchebbi@laurentian.ca

Summary: We report the development of a novel technique for the simultaneous measurements of suspended particles' concentration and velocity in a fluid flow using laser Bessel beams. An experimental setup was developed using the discharge from a closed-loop water tank system to provide the fluid flow. Fixed quantities of particles with a size less than 30 µm were added, and the scattered light from their interaction with a Bessel beam was collected and the corresponding signal was processed to measure the discharge velocity and particles' concentration. A simple numerical model was developed to simulate the interaction of particles with a Bessel beam and to determine the information that can be obtained from the light they scatter in terms of concentration and velocity. The conclusions of these simulations were validated experimentally. The numerical simulations and experimental results were successfully conducted, demonstrating the proof-of-concept for this technique. Its advantages compared to exiting techniques are discussed.

Keywords: Bessel beams, Fluid flow velocity measurement, Particles' concentration measurement.

1. Introduction

Measuring suspended particles' concentrations in fluid flows has many industrial, environmental, and biological applications. These include particle characterization in metallurgical and chemical processing plants, dust measurement in air, aerosol characterization for industrial and consumer atomizers and the use of particles in a fluid to measure the flow such as in laser Doppler velocimetry (LDV) and particle image velocimetry (PIV) techniques. Depending on the application, many techniques have been developed. In most of the applications, simultaneous measurement of the velocity of these particles, would be highly desirables as it offers important information about the flow.

These techniques range from simple gravimetric techniques, such as those used for dust measurement where particles are filtered and collected for subsequent characterization, to more sophisticated laser-based techniques. Gravimetric techniques are still considered the standard for dust and particulate matter (PM) concentration measurement, they offer accurate cumulative measurement. Their main disadvantage is that they do not allow real time monitoring [1]. The laser interferometric techniques are some of the most accurate techniques; they include the visibility technique [2], derived from LDV principles, which is used for particle concentration and size measurement, and the Phase Doppler Anemometry (PDA) technique [3], which extends LDV capabilities to measure particles' size and velocity. Doppler methods are non-intrusive techniques widely used for velocity measurement, offering significant advantages in preserving the integrity of the flow being analyzed. These advanced techniques have complicated and expensive setups, they are mostly used for research purposes, and their application in specific commercial systems is limited. Simpler existing optical techniques relate the intensity of scattered light to the concentration but do not measure the velocity of the particles. Recent assessments and comparative reviews of these techniques are reported in [4] and [5].

This motivated the research of a new technique, which has some of the advantages of interferometric techniques, such as simultaneous measurement of concentration and velocity, but is simpler in setup and more practical. Previous research has shown that Bessel beams can be used to measure solid surfaces [6]. In this article, which is part of the research accomplished by the first author's Master thesis [7], we present a new technique using a single Bessel beam for simultaneous measurement of particles' concentrations and velocity.

Bessel beams have unique characteristics such as being nearly diffraction-less and exhibiting self-healing properties, which add significant advantages to these types of measurements since the laser beam is less prone to distortions caused by diffraction or the presence of particles. It is known that employing the LDV method for measuring particle size in turbid flow has some random errors, such as underestimation of particle diameter [8].

2. Numerical Simulations

A MATLAB© program was written to simulate the passage of particles at constant velocities through a Bessel beam. By considering a two-dimensional coordinate system with its origin at the center of the Bessel beam, the particles were given random initial positions (x_0, y_0) to simulate realistic scenarios as shown in Fig. 1 The distance between the particles and the center of the Bessel beam is denoted by

$r = \sqrt{x^2 + y^2}$, where x and y are the coordinates of the particle at a time t. The intensity of the scattered light by these particles is assumed to be proportional to the light intensity in the fringes, given by the following equation:

$$I = I_0 J_0^2(k\beta r), \quad (1)$$

where, using the small angle approximation, $\beta \approx \tan^{-1}\left(\frac{k_r}{k}\right)$, k being the total magnitude of the wave vector of the Bessel beam and k_r is the magnitude of its radial component. We recognized that this is a simplified model which does not take into account the particles' size, the direction at which the scattered light would be collected or the particles' optical properties and shape. A more rigorous analysis would use the Mie scattering theory for example, but this is beyond the scope of this work. It is believed that the present model would be enough to gain an understanding of the physical problem considered. The Bessel beam parameters used in these simulations, were the same as those used in the experiments described in this work.

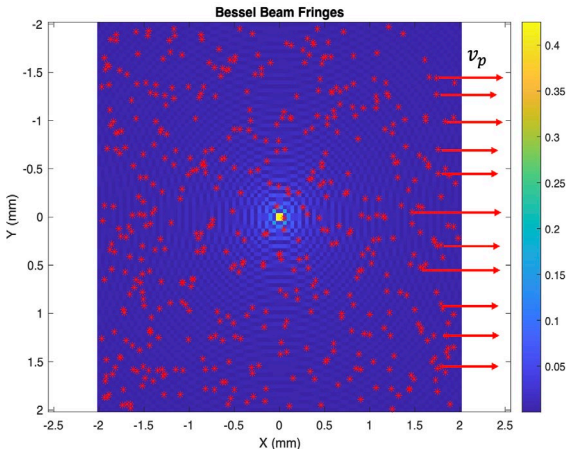

Fig, 1. Domain of numerical simulation of scattered light from particles crossing Bessel beam.

Simulations were performed with different random particles concentrations. A sample time intensity signal of the scattered light of one particle, as it crosses the fringes of the Bessel beam, obtained from these simulations is shown in Fig. 2. The total signal of the scattered light was assumed to be equal to the summation of the contributions of all particles.

The time average signal intensity for each concentration was calculated and the values are plotted in Fig. 3. This figure shows that the total intensity increases as the number of particles increases. To calculate the velocity, the spectra of the signal was obtained by using the FFT of the time signal and confirmed the distribution identifying the Bessel frequency which can be used to calculate the velocity of the particles, similar to the procedure followed in [6]. The numerical simulations results demonstrate that by using the Bessel beam to scatter light from the moving particles, the obtained signal can be used to simultaneously measure the velocity of the particles and their concentration.

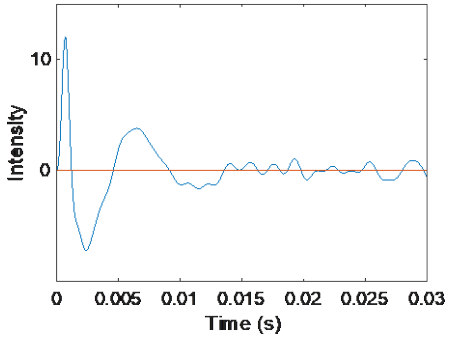

Fig. 2. Time signal of scattered light intensity.

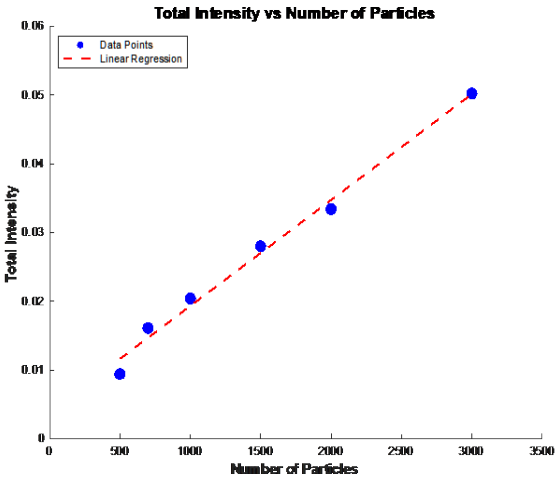

Fig. 3. Total intensity vs number of particles.

3. Experimental Procedures and Results

The experimental setup is shown in Fig. 4. Discharge from a water tank was used to provide the flow through an orifice located on the side wall near the bottom. Not shown in the figure are a container placed beneath the outlet collecting the discharged water and a pump used to continuously recirculate the collected water to the tank enabling closed loop circulation. Also, a control valve was used to adjust the height of the water in the tank and regulate the discharge velocity. Crushed ore particles (size <30 μm) were added to the distilled water circulating in the tank. The particles' concentration was varied ten times, adding a full bucket of approximately 88 mm³ internal volume, each time.

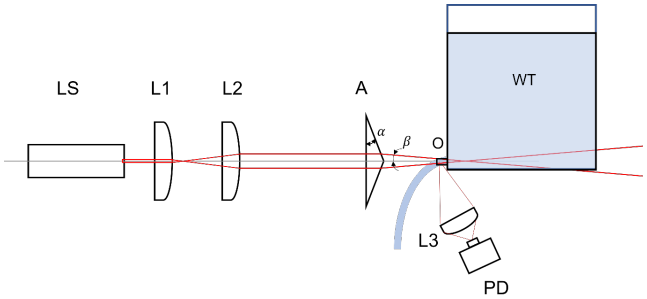

Fig. 4. Experimental setup (not to scale). LS: Laser; L1, L2 and L3: lenses; A: axicon, PD: Photodetector; WT: Water tank; O: Rectangular cross-section orifice.

A red laser diode beam was expanded using spherical lenses L1 and L2 and centered on an axicon with a base angle, $\alpha = 0.5°$, used to generate the Bessel beam. This beam was focused on the discharge flow from the tank through a rectangular plexiglass orifice. It should be noted that, initially, measurements were taken in the free discharge stream without the rectangular orifice. However, even in the absence of particles, light was scattered and velocity measurements could still be obtained. It was realized that the free surface of the water stream, when exposed to air, develops surface roughness. This roughness scatters light, similar to the seeding particles, and can be used to measure velocity in LDV systems [9]. In the present case, it was concluded that this surface roughness also scatters light at the Bessel frequency, allowing velocity measurements to be made. Since the objective is to measure particle concentration, it was decided to conduct the measurements inside an orifice.

The scattered light by the particles was collected and focused by aspheric lens L3 on a silicon photodiode detector (Thorlabs PDA10A2), which converted the optical signal into an electrical current. An Omega DAQ-3000 system was used for data acquisition. The processing of the signal consisted of filtering to remove the noise and pedestal and spectral calculations.

The spectra were used to calculate the discharge velocities and the results are reported in [7]. Time-intensity plots were used to calculate the average intensity corresponding to the different concentrations for constant velocities. The results corresponding to a discharge velocity of *0.88 m/s* of are plotted in Fig. 5 showing that by increasing the concentration the intensity increased. The variation is approximately linear and aligns well with the numerical simulations. It should be mentioned that a quantitative comparison between the numerical and experimental results is not possible because of the simplicity of the numerical model and the uncertainty in determining the exact concentration of the actual experiments. The linear trend of the variation is also consistent with similar existing techniques, which rely on scattered intensity from more common laser beams such as Gaussian or elliptic. The present technique aims to distinguish itself by simultaneous measurement of the velocity. Another significant advantage of this technique is that it makes it easier to identify the noise in the signal. Since the intensity represents the scattered light from the particles as they cross the Bessel beam fringes, the noise is mostly present at frequencies higher than the Bessel frequency.

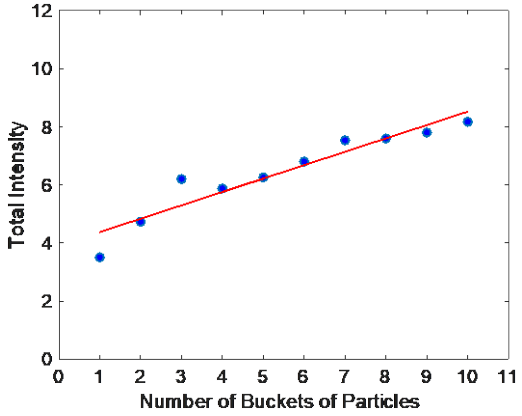

Fig. 5. Total intensity versus number of buckets of particles.

4. Conclusions

In summary, the research presented in this work successfully developed a proof of concept of a method for simultaneously measuring particles' concentration and velocity from the same signal. This technique offers cost-effective advantages due to its simplicity. In addition, it offers the advantage of better noise identification compared to similar intensity-based techniques to measure particles' concentration. The proof of concept was demonstrated for measurements in a water flow but could be tested and extended for measurements in gases and for specific applications such as in dust or particulate matter measurements.

References

[1]. V. Tasić, M. Jovašević-Stojanović, S. Vardoulakis, N. Milošević, et al., Comparative assessment of a real-time particle monitor against the reference gravimetric method for PM10 and PM2.5 in indoor air, *Atmospheric Environment*, Vol. 54, 2012, pp. 358-364.

[2]. W. M. Farmer, Measurement of particle size, number density, and velocity using a laser interferometer, *Applied Optics*, Vol. 11, Issue 11, 1972, pp. 2603-2612.

[3]. F. Durst, A. Melling, J. H. Whitelaw, Principles and Practice of Laser-Doppler Anemometry (2nd Ed.), *Academic Press*, London, 1981.

[4]. B. Alfano, L. Barretta, A. Del Giudice, S. De Vito, et al., A review of low-cost particulate matter sensors from the developers' perspectives, *Sensors*, Vol. 20, Issue 23, 2020, 6819.

[5]. D. Nicklin, H. G. Darabkhani, Techniques to measure particulate matter emissions from stationary sources: A critical technology review using Multi Criteria Decision Analysis (MCDA), *Journal of Environmental Management*, Vol. 296, 2021, 113167.

[6]. M. Sakah, B. Chebbi, Measuring solid surface velocity and detection of particle movement by laser Bessel beams, *Optical Engineering*, Vol. 55, Issue 9, 2016, 091411.

[7]. A. S. Abolhassani, Development of new particles' concentration and sizing measurement techniques, Master's Thesis, *Laurentian University*, Sudbury, 2024.

[8]. Y. Kliafas, A. M. K. P. Taylor, J. H. Whitelaw, Errors in particle sizing by LDA due to turbidity in the incident laser beams, *Experiments in Fluids*, Vol. 5, Issue 3, 1987, pp. 159-176.

[9]. D. Langevin, Light scattering by liquid surfaces, new developments, *Advances in Colloid and Interface Science*, Vol. 289, 2021, 102368.

(033)

Light-Matter Interaction: Laser Challenges Classical Laws of Diffusion

V. Freilikher, Yu. Kaganovskii and M. Rosenbluh
Dept. of Physics, Bar Ilan University, Ramat-Gan 52900, Israel
Tel.: + 972-54-651-8746
E-mail: freiliv@biu.ac.il

Summary: In this talk, an overview of recent experimental and theoretical advances in the study of the photo-induced diffusion in amorphous chalcogenide films is presented. By monitoring the evolution of surface morphology and compositional distributions under illumination, these studies provide direct insight into the kinetics of light-driven atomic motion. The results reveal that photo-induced diffusion is a light-controlled non-equilibrium transport process rather than a purely thermally activated phenomenon. The effective transport rates and spatial redistribution patterns often deviate significantly from predictions based on classical diffusion models, indicating that optical excitation modifies both the mobility of structural units and the forces responsible for their displacement.

Keywords: Chalcogenide glasses, Photo-induced diffusion, Mass transfer, Viscosity, Rough surface.

1. Introduction

The interaction of electromagnetic radiation with matter is one of the most ubiquitous phenomena in nature. Suffice it to say that our visual perception of the surrounding world relies entirely on quantum-mechanical processes that occur when light interacts with the media through which it propagates and with the objects it encounters. On the microscopic level, illumination can modify electronic states, reshape the local potential energy landscape, generate defects, and influence atomic mobility. Under certain conditions, light therefore can fundamentally alter the kinetics of atoms and drive mass transport even in the absence of conventional driving forces.

Amorphous chalcogenide films (ACF) represent a remarkable class of materials, in which effects driven by high-frequency electromagnetic field are well-pronounced and enable modifying optical and electric properties by light irradiation [1]. These semiconductors are composed of chalcogen elements such as sulfur or selenium combined with network-forming pnictides like arsenic, antimony or bismuth, and are characterized by strong optical absorption near the band edge. As a consequence, their structure is particularly sensitive to electronic excitation so that illumination with near-bandgap or above-bandgap light can induce a variety of photo-induced (PI) processes, including photo-darkening, photo-expansion, PI fluidity, PI diffusion, etc. Of a special practical interest is the light-driven mass transport, in which atoms or other structural units undergo large-scale redistribution under laser irradiation, providing a basis for the fabrication of integrated optical devices, waveguides, surface relief gratings, micro-lenses and other elements for micro-optics.

Despite decades of research, the microscopic mechanisms responsible for PI diffusion in ACF remain the subject of active investigation. To explain how optical excitation is converted into atomic motion, various models have been proposed, including defect-mediated structural rearrangements, photo-softening of the amorphous network, and effective forces associated with gradients of optical intensity or electromagnetic field polarization [2]. In many cases, optical excitation appears to modify both the mobility of structural units and the forces governing their displacement. As a result, experimentally observed phenomena, such as surface relief formation at relatively low optical powers or directed material transport in spatially modulated light fields cannot be fully described within the framework of conventional diffusion theory.

2. Photo-Induced Diffusion and Mass Transport

Unlike conventional diffusion, which is governed primarily by thermally activated formation and migration of vacancies or interstitials and described by classical relations such as Fick's law, PI diffusion in amorphous chalcogenides arises from light-induced defects and local electric fields caused by different mobilities of electrons and holes. Acceleration of the mass transport in ACFs under band gap light illumination is usually attributed to the decrease of the film viscosity [3-5]. However, direct measurements of the film viscosity at various temperatures and light intensities, made by flattening of surface relief gratings, have shown that the viscosity did not vary under illumination and the acceleration of the mass transfer was caused by the contribution of PI self-diffusion [6]. Besides, the PI diffusion coefficient is not related to the viscosity coefficient by the Stokes-Einstein relation, and PI diffusion should be considered as an additional mechanism of the overall mass transport.

In this talk, we present the atomic interpretation of PI diffusion coefficients, explain their dependence on temperature and light intensity, and compare with our

experimental data [7]. For characterization of PI acceleration of the mass transfer, we introduce the term 'diffusional viscosity', like it is used for description of diffusion creep in crystalline solids. We estimate the temperature dependence of diffusional viscosity and show that it noticeably depends on the distance over which the material is redistributed. Taking into account the diffusional viscosity allows an adequate general interpretation of many photo-induced phenomena observed in the literature.

To better understand mechanisms of photo-induced mass transfer, amplitude variations of gratings of various periods Λ (from 3 to 15 μm) on the surface of ACF $As_{20}Se_{80}$ illuminated by a band-gap diode laser (λ = 660 nm) have been analyzed using optical microscopy, atomic force microscopy, light scattering, and optical profilometry [8]. It turned out that the gratings with $\Lambda < 8$ μm exponentially flattened with time of illumination, whereas those with $\Lambda > 8$ μm exponentially grew. Similar results were obtained by analyzing the angular dependence of the intensity of light scattered from statistically rough surfaces of $As_{20}Se_{80}$ illuminated by CW laser (λ = 660 nm) [9]. Theoretical analysis shows that such rather unusual dependence of PI evolution of surface gratings on their period takes place because the profile variation occurs due to bulk diffusion of As and Se atoms, as a result of competition between capillary and electrostatic forces created by redistribution of electrons and holes generated by light. The PI diffusion coefficients estimated both from the flattening and growth kinetics of the grating amplitude are in good agreement with the theory [7].

It was also observed that the profile evolution of thin films deposited on a non-wetting substrate led to instability resulting in disintegration of a continuous ACF into isolated islands.

This phenomenon, called dewetting, has been studied on metal, polymer, and liquid thin films deposited on various substrates. Much less studied is the dewetting in ACFs, which are widely used in different photonic devices due to the unique physical properties. However, the efficiency and reliability of their performance are significantly limited by instability, the main mechanism of which at temperatures lower than the melting point of the material, is dewetting.

Recently, PI dewetting of thin amorphous $As_{20}Se_{80}$ films under CW laser illumination has been detected, and the theory of PI pore growth by volume diffusion driven by capillary forces developed [9]. When illuminated with light, the surface roughness is transformed into macroscopic ripples, which corrugate over time, and the pore nuclei are formed when the ripple amplitude reaches the film thickness. The pore radius, r, increases with time as $t^{1/2}$. The effective PI diffusion coefficients derived from this dependence for given film thickness and surface tension turned out to be in good agreement with the theoretical predictions and previous measurements.

3. Conclusions

Beyond the fundamental significance, the phenomena open promising opportunities for the optical control of matter on micro- and nanometer scales. Laser-induced mass transport in chalcogenide materials provides a versatile platform for the formation of surface relief structures, adaptive photonic elements, and reconfigurable optical components. When the optical field is spatially structured, for example through interference patterns or focused laser beams, these processes can lead to directional mass transport and the spontaneous formation of surface relief structures with characteristic length scales ranging from nanometers to micrometers. Such behavior suggests that optical fields may have significant impact on the directed diffusion mass transfer, thereby challenging the classical view of diffusion as a purely thermally-activated phenomenon.

References

[1]. K. Tanaka, K. Shimakawa, Amorphous Chalcogenide Semiconductors and Related Materials, *Springer*, New York, 2011.

[2]. K. Tanaka, Photoinduced deformations in chalcogenide glasses: What are the driving forces?, *Journal of Non-Crystalline Solids*, Vol. 500, 2018, pp. 272-281.

[3]. K. Tanaka, Photoinduced fluidity in chalcogenide glasses, *Comptes Rendus Chimie*, Vol. 5, Issue 11, 2002, pp. 805-811.

[4]. K. E. Asatryan, T. Galstian, R. Vallée, Optical polarization driven giant relief modulation in amorphous chalcogenide glasses, *Physical Review Letters*, Vol. 94, Issue 8, 2005, 087401.

[5]. H. Fritzsche, Optical anisotropies in chalcogenide glasses induced by band-gap light, *Physical Review B*, Vol. 52, Issue 22, 1995, pp. 15854-15861.

[6]. S. Molnar, R. Bohdan, V. Takáts, Y. Kaganovskii, et al., Stimulated surface relief erasing in amorphous As-Se layers: Thermal- and light-induced effects, *Physica Status Solidi A*, Vol. 215, Issue 24, 2018, 1800589.

[7]. Y. Kaganovskii, D. L. Beke, V. Freilikher, S. Kökényesi, et al., Photoinduced self-diffusion and viscosity in amorphous chalcogenide films, *Materials Research Express*, Vol. 7, Issue 1, 2020, 016204.

[8]. Y. Kaganovskii, V. Freilikher, M. Rosenbluh, Evolution of surface relief gratings in As20Se80 amorphous chalcogenide films under laser illumination, *Journal of Non-Crystalline Solids*, Vol. 588, 2022, 121611.

[9]. Y. Kaganovskii, V. Freilikher, M. Rosenbluh, Laser-induced dewetting of As20Se80 thin films, *Materials Letters*, Vol. 397, 2025, 138740.

(034)

Design and Fabrication of a 24-Channel Holographic Optical Trigger for High-Speed Optical Computation

B. Ivanov, G. Ivanova * and D. Dimov
Institute of Optical Materials and Technologies, Laboratory "Holography", 109, Acad. G. Bontchev Str., 1113 Sofia, Bulgaria
Tel.: + 33 617446640
* E-mail: givanova@iomt.bas.bg

Summary: Processing architectures that operate directly within the optical domain offer a fundamental throughput advantage over digital systems, bypassing the conversion overhead that limits the computational speed of conventional electronic processors. This paper presents the design and fabrication of a 24-channel holographic optical element engineered to function as a high-speed optical trigger similarly to an analog optical processor. The element encodes eight independent phase states – combined individually with three distinct frequency states – within a thick volume holographic substrate, generating 24 simultaneously processed, independent signal calculation channels through a reflection-geometry multichannel beam splitter architecture. All channels carry a dedicated set of optical transfer functions executing aberration correction, angular parallax correction, and focal depth positioning at the ultimate speed of light. Using three physical 24-channel holographic devices functioning as holographic optical triggers, we enable the generation of 49 sequential RGBD holograms, where every hologram corresponds to one focal depth multi-plane frame with diffraction efficiency exceeding 50 %.

Keywords: Holographic optical element, Analog optical processor, High-speed optical trigger, RGBD holographic display, Optical transfer function.

1. Introduction

Three converging research trajectories define the engineering context of the 24-channel holographic optical trigger (HOT) developed here. The first is the rapid scaling of optical computing architectures toward increasingly large information bandwidths [1–3]. The second is the established paradigm of analog co-processor design, in which dedicated hardware elements execute transfer functions directly in the analog domain, offering a processing pathway that avoids conversion overhead and operates closer to the physical limits of the medium [4–7]. The third is the demonstrated capacity of volume holographic multiplexing in polymeric media to sustain many independent optical channels within a single compact element [8–14].

The HOT element presented in this paper sits at the intersection of all three trajectories. It is a fully holographic optical transducer that encodes 24 independent processing channels entirely within the recorded volume structure of a thick holographic substrate, operating without moving parts, active switching elements, or analog-to-digital conversion at any stage.

1.1. Optical Computing as a High-Bandwidth Processing Paradigm

The sustained growth of data-intensive workloads has placed unprecedented demands on the throughput capacity of conventional processing architectures [1–3]. Optical platforms offer a complementary processing pathway well suited to high-bandwidth, parallel operation.

Wavelength-multiplexed diffractive optical networks have demonstrated that a single compact diffractive element can perform massively parallel linear transformations simultaneously across many independent wavelength channels [1]. This principle is the conceptual basis of the frequency-state multiplexing architecture of the holographic optical element (HOE). At the system interconnect level, silicon photonic transmitters operating at 10 Gbps per wavelength channel have demonstrated terabit-scale aggregate bandwidths in practical chip-scale implementations [2]. The scalability of wavelength-multiplexed optical architectures to over 100 simultaneous independent channels within a single compact photonic device has been experimentally confirmed [3], providing a performance reference for parallel optical processing against which the 24-channel HOT is contextualized.

A critical structural requirement for all such architectures is a large information bandwidth distributed across many simultaneously active independent channels. Volume holographic multichannel beam splitters have demonstrated 12 or more spectrally resolved independent channels, achieving diffraction efficiency exceeding 75 % and negligible inter-channel cross-talk [8].

1.2. Analog Co-Processor Architectures and Their Optical Counterparts

Programmable analog co-processor architectures have established that dedicated hardware executing transfer functions directly in the analog domain can avoid the conversion overhead associated with

high-speed digital processing [4]. The HOT implements this principle at the scale of a multichannel volume holographic element. Analog optical computing exploits the intrinsic physical properties of light – propagation speed, spatial parallelism, and wavelength-division capacity – to execute mathematical operations at bandwidths that are difficult to achieve with electronic hardware alone [5]. Holographic techniques and Fourier-domain optical filtering have been identified as primary implementation strategies for analog optical processing functions [5].

The realization of analog optical computing primitives in silicon photonic waveguides through engineered nonlinear optical interactions confirms that transfer functions can be encoded directly in the physical structure of a compact optical element, operating at full optical bandwidth with no conversion overhead [6]. Each HOT channel applies this principle at the volume holographic scale – the transfer function is encoded in the recorded grating structure and applied to the optical field during a single pass through the element.

In-memory analog computing architectures have demonstrated execution times up to four orders of magnitude below those of equivalent software-based implementations, with energy savings exceeding 10 % and accuracy losses below 1 % [7]. This performance profile, which scales favorably with parallelism degree, motivates the multichannel architecture of the HOT.

1.3. Multichannel Holographic Architectures within Polymeric Substrates

Realizing a multichannel optical processing element requires both a high-performance diffractive architecture and a recording medium capable of sustaining many independently multiplexed channels within a single compact volume. Among available diffractive element fabrication methods [9], holographic interferometric recording is adopted here for large aperture scales, providing full-volume simultaneous exposure free of stitching errors. Precision photolithographic pipelines for diffractive beam splitter fabrication, combining iterative Fourier transform algorithm design with controlled refractive index and layer thickness, have demonstrated close simulation-to-fabrication agreement [10].

Six-channel coherent holographic beam combining via angle multiplexing in a thick polymeric substrate established the F = N finesse scaling law – where F is the optical finesse and N is the number of multiplexed channels – with two-dimensional angle multiplexing proposed as a pathway to large channel densities [11]. Azopolymer-based nanocomposite recording media doped with metallic and non-metallic nanoparticles define the current frontier of photoanisotropic thick substrate development, with significant birefringence enhancement and concurrent improvements in diffraction efficiency and surface relief grating formation [12]. Nanoparticle morphology further governs this enhancement – elongated goethite nanorods in PAZO matrices produce a double-peak birefringence dependence on concentration [13], confirming that recording properties can be systematically engineered through morphology control.

The broader principle underlying these photoanisotropic material platforms is that a polymeric layer can function as an active optical management element, governing optical boundary conditions governed entirely by its intrinsic material structure [14]. The HOT substrate operates on the same principle: the recorded holographic volume structure manages multiple independent optical channels – encoding phase states and frequency states – entirely through its material structure.

1.4. Optical Trigger Architectures and the HOT Design Lineage

Dual piezoelectric transducer architectures have demonstrated phase-stepping optical triggers for digital holographic interferometry [15]. In that configuration, phase states are accessed through mechanical actuation, which constrains operating speed and introduces sensitivity to vibration. The HOT addresses these constraints by encoding all phase states passively within the recorded grating structure, with no moving parts, no actuators, and no feedback loop [16].

The present HOT extends the four-channel architecture of [16], in which two near-infrared laser sources – each producing two orthogonal polarization states – yielded 2 wavelengths × 2 polarization states = 4 independent channels. The present work introduces wavelength multiplexing as a second, orthogonal degree of freedom alongside polarization multiplexing, and expands the polarization basis from 2 to 8 states. Employing three laser sources in the visible spectral range, the resulting dual-axis scheme yields 3 wavelengths × 8 polarization states = 24 independent processing channels, a sixfold increase over the predecessor. The reflection-geometry recording configuration and recording parameters are retained from the prior implementation [16]. The holographic substrate used in the present work is a silver halide emulsion with lithium and molybdenum additives (LiMo) – a distinct formulation selected for its higher photoresponse rate relative to the emulsion used in [16], enabling faster modulation of the recorded light signal within the same recording geometry and channel architecture. A full characterization of the LiMo material system will be the subject of a subsequent publication.

2. Optical Design of the Multichannel Trigger

The 24-channel HOT constitutes a compact all-holographic transducer that executes dedicated transfer functions on the optical signal during a single

propagation pass through the element, with no conversion overhead and inherently parallel channel execution.

Two operational modes are available for multichannel optical switching in the trigger architecture. In parallel switching mode, the optical signal is distributed simultaneously across all channels, each assigned equal computational weight by design, enabling concurrent execution of multiple independent mathematical operations. In serial switching mode, a single information unit is processed sequentially across successive channels, applying multiple transformations to the same signal. Parallel switching is adopted here, as the architecture must process 24 independent RGBD information units simultaneously within a single holographic frame, implemented using 8-channel HOT device.

An alternative transmission-mode architecture could be implemented by replacing the holographic channel structure with a dedicated spatial light modulator (SLM) per channel. SLMs offer high dynamic reconfiguration capacity, enabling dynamic wavefront modulation within each channel independently, and their integration across 24 channels within a single holographic frame would constitute a flexible solution for real-time volumetric 3D holographic display. However, the high acquisition cost of a single high-resolution SLM renders a fully SLM-based multichannel implementation economically prohibitive at the channel density required. The present architecture addresses this limitation by employing a single SLM within a parallel-channel optical structure, dedicated to encoding and real-time correction of computational functions, while the holographic multichannel structure of the HOT sustains the full parallel analog-optical processing load.

The choice of holographic substrate material is central to achieving the photoresponse rate required by the present architecture. The silver halide emulsion used in the predecessor work [16] required wet chemical development processing. The present work employs the LiMo emulsion – a high-photoresponse-rate photoanisotropic silver halide formulation that operates in the dry state, eliminating chemical processing, and supports real-time light-to-light modulation across the visible spectral range from 400 nm to 800 nm.

The measured reflectance and transmittance spectra of the LiMo constituent layers as a function of layer thickness are presented in Fig. 1. For the thinnest active layer configuration (red lines), the reflectance curve R1 and transmittance curve T1 share no common operating point, indicating that incident optical energy is redirected outside the combined transmission-reflection window – confirming efficient energy transfer into the diffracted channel output across the full spectral range.

The absorption and diffraction efficiency characterization across all layer thicknesses, shown in Fig. 2, reveals that the thickest layer, d5, exhibits the highest diffraction efficiency, the lowest absorption, and the fastest photoresponse rate among the measured configurations. These properties identify d5 as the preferred active recording layer for the present HOT fabrication.

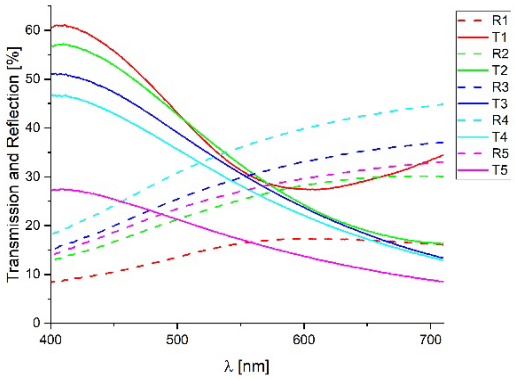

Fig. 1. Reflectance (R) and transmittance (T) spectra of the LiMo constituent layers.

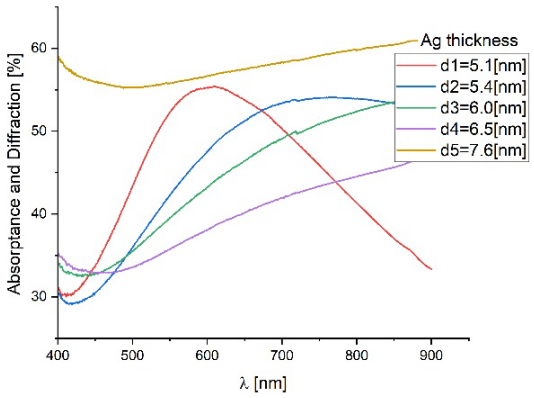

Fig. 2. Diffraction efficiency and absorption characterization of the LiMo.

3. Fabrication of Optical Component Systems for Analog-Optical Computation

One physical HOT device generates 24 RGBD focal depth planes arranged sequentially along the optical axis. The resulting volumetric depth stack of 24 planes constitute the full holographic frame set recorded within the HOT device. The trigger comprises eight phase-encoded channels with predefined optical functions, together with one supplementary channel reserved for characterization, all arranged within a single linear structure (Fig. 3).

The right side of Fig. 3 shows the controllable diffraction patterns generated for analog-optical computation. Each of the nine trigger sub-structures is characterized by three optical parameters expressed as percentages of the incident energy: the reflectance R, representing the fraction returned by the sub-structure; the transmittance T, the fraction transmitted through it; and D+A, combining the diffracted energy and absorption losses. Together these parameters sum to

100 % and fully describe the optical energy distribution across each sub-structure.

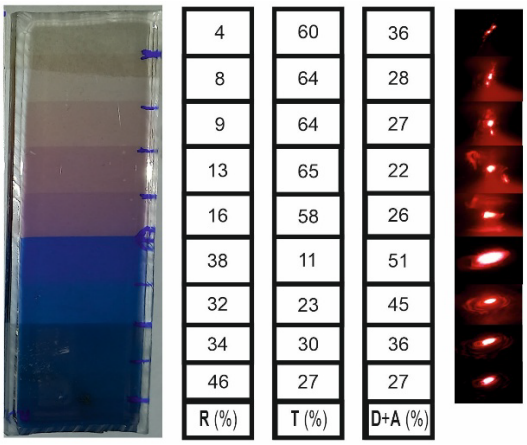

Fig. 3. Transmissive-reflective structure of the holographic optical trigger.

Independent adjustment of R, T, and A in each trigger channel enables direct manipulation of the diffracted energy D during analog-optical computation.

The optical setup consists of field lenses L1 and L3, a two-element field lens L2 adjustable along the optical axis of the 6-focal tele-transmission system for depth-focused collimation across each HOT state, a half-wave plate HW for channel phase encoding, and a combined spatial light modulator, diffractive element, and spatial filter assembly (SLM–DE–SP) functioning as the analog-optical computation elements, as illustrated in Fig. 4.

The SLM enables dynamic variation of the processor optical instructions, while the diffractive element provides static configuration. The spatial filter aperture profile independently defines the mathematical functions assigned to each processor channel for execution and correction.

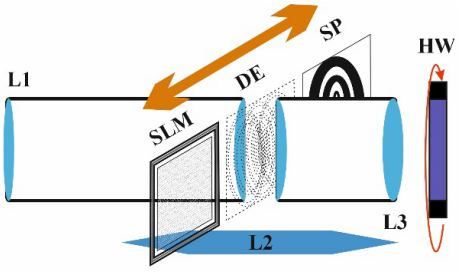

Fig. 4. Optical layout of the 6-f tele-transmission system for phase and frequency channel configuration.

Cross-talk analysis between the trigger channels reveals that the 10° polarization angular separation between adjacent channels provides adequate channel discrimination exclusively under strictly linear input polarization. The presence of any circular polarization component in the illuminating beam introduces inter-channel cross-talk, manifesting as holographic image mixing in the reconstructed volumetric 3D display. This result establishes strict linear polarization of the illumination source as a critical operating condition for the HOT architecture.

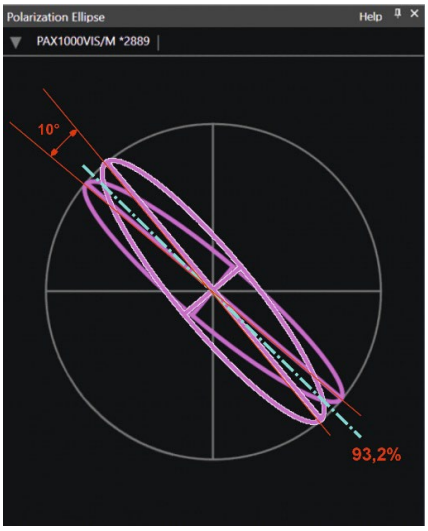

Fig. 5. Inter-channel cross-talk as a function of polarization angular separation: 10° channel spacing under mixed polarization input (cross-talk: 93.2 %).

Where inter-channel cross-talk is detected, it can be reduced by increasing the angular separation between the polarization states of the affected channels. As shown in Fig. 6, increasing the polarization angle from 10° to 37° reduces cross-talk from 93.2 % to 25.6 %, demonstrating that fine angular tuning of the polarization basis provides an effective means of cross-talk suppression in the HOT architecture.

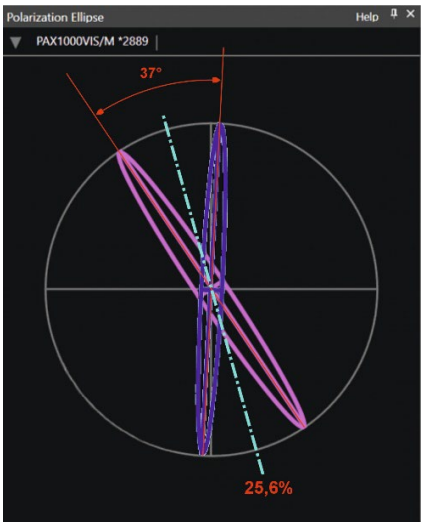

Fig. 6. Inter-channel cross-talk reduction by increased polarization angular separation: 37° channel spacing under mixed polarization input (cross-talk: 25.6 %).

Under strictly linear input polarization, the inter-channel cross-talk reduces to 21.5 % at a polarization angular separation of 10° between adjacent channels (Fig. 7).

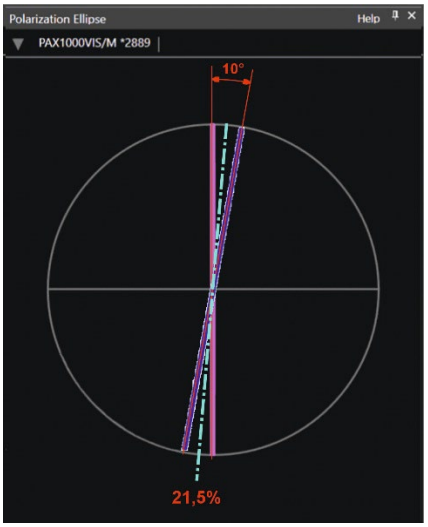

Fig. 7. Inter-channel cross-talk under strictly linear input polarization: 10° channel spacing (cross-talk: 21.5 %).

This result confirms that the 10° polarization basis adopted in the present HOT architecture is viable under the linear polarization operating condition established in the preceding analysis. The low cross-talk level at this angular separation directly supports high channel density implementation, enabling a larger number of independent polarization-encoded channels to be accommodated within a single HOT device. This scalability has direct implications for the computational capacity of the architecture: a higher channel count translates to a greater number of simultaneously executable independent optical transfer functions, expanding the range of analog-optical processing tasks addressable by a single compact holographic element – including volumetric 3D display rendering, multi-plane wavefront correction, and parallel spatial frequency filtering.

4. Conclusions

A 24-channel holographic optical trigger has been designed, fabricated, and characterized for application in high-speed analog-optical processing and volumetric RGBD holographic display. The device encodes 24 independent processing channels within a single compact reflection-geometry holographic substrate through a dual-axis multiplexing scheme combining three visible-range laser wavelengths with eight polarization states per wavelength, representing a sixfold increase in channel count over the four-channel predecessor architecture reported in [16]. By integrating active and passive diffractive elements within each trigger channel, parallel analog-optical computation is executed independently across all channels simultaneously, with no moving parts, no actuators, and no analog-to-digital conversion at any stage.

The adoption of the LiMo silver halide emulsion as the active recording medium eliminates wet chemical development processing and provides a high photoresponse rate commensurate with the frequency of the throughput optical signal. Spectral and diffraction efficiency characterization of the constituent layers identifies the thinnest layer configuration as the optimal active recording layer, establishing the material basis for the fabrication of ultra-fast holographic optical devices.

Cross-talk analysis across the polarization-encoded channel basis confirms that strictly linear input polarization is a critical operating condition for the architecture, and that fine angular tuning of the polarization basis provides an effective mechanism for cross-talk suppression without structural modification of the HOT device.

The scalability of the dual-axis polarization–wavelength multiplexing architecture supports implementation of higher channel densities within a single holographic element, with direct implications for the range of simultaneously executable analog-optical transfer functions. A full material characterization of the LiMo emulsion system and an extended experimental evaluation of the HOT computational capacity across the full channel basis will be the subject of subsequent publications.

References

[1]. J. Li, T. Gan, B. Bai, Y. Luo, et al., Massively parallel universal linear transformations using a wavelength-multiplexed diffractive optical network, *Advanced Photonics*, Vol. 5, Issue 1, 2023, 016003.

[2]. Fujitsu Laboratories, Integrated silicon optical transmitter to carry large volumes of data between CPUs, in *Proceedings of the 9th International Conference on Group IV Photonics (GFP'12)*, 2012.

[3]. X. Yu, Z. Wei, F. Sha, et al., Parallel optical computing capable of 100-wavelength multiplexing, *eLight*, Vol. 5, Issue 1, 2025, 10.

[4]. J. P. Heid, A programmable analog coprocessor, in *Proceedings of the First ISA/IEEE Sensors for Industry Conference (Sicon'01)*, 2001, pp. 29-33.

[5]. D. R. Solli, B. Jalali, Analog optical computing, *Nature Photonics*, Vol. 9, Issue 11, 2015, pp. 704-706.

[6]. Y. Jiang, P. T. S. DeVore, B. Jalali, Analog optical computing primitives in silicon photonics, *Optics Letters*, Vol. 41, Issue 6, 2016, pp. 1273-1276.

[7]. M. Elbtity, A. Singh, B. Reidy, X. Guo, et al., An in-memory analog computing co-processor for energy-efficient CNN inference on mobile devices, in *Proceedings of the IEEE Computer Society Annual Symposium on VLSI Systems (ISVLSI'21)*, 2021, pp. 188-193.

[8]. J. D. Matchett, R. I. Billmers, E. J. Billmers, M. E. Ludwig, Volume holographic beam splitter for hyperspectral imaging applications, *Proceedings of SPIE*, Vol. 6668, 2007, 66680K.

[9]. C. Shi, W. Zhao, S. Chen, W. Li, Multilevel diffractive lenses: Recent advances and applications, *Symmetry*, Vol. 16, Issue 10, 2024, 1377.

[10]. X. Dai, Y. Hu, B. Niu, Q. Dai, et al., A microfabrication technique for high-performance diffractive optical elements tailored for numerical simulation, *Nanomaterials*, Vol. 15, Issue 2, 2025, 138.
[11]. H. N. Yum, P. R. Hemmer, A. Heifetz, J. T. Shen, et al., Demonstration of a multiwave coherent holographic beam combiner in a polymeric substrate, *Optics Letters*, Vol. 30, Issue 22, 2005, pp. 3012-3014.
[12]. D. Nazarova, L. Nedelchev, N. Berberova-Buhova, G. Mateev, Nanocomposite photoanisotropic materials for applications in polarization holography and photonics, *Nanomaterials*, Vol. 13, Issue 22, 2023, 2946.
[13]. L. Nedelchev, D. Nazarova, N. Berberova, et al., Enhanced photoanisotropic response in azopolymer doped with elongated goethite nanoparticles, *Journal of Physics: Conference Series*, Vol. 700, 2016, 012031.
[14]. P. K. Petrova, R. L. Tomova, R. T. Stoycheva-Topalova, S. M. Miloshev, Influence of p-isopropenylcalixarenestyrene copolymer buffer layer over Alq_3-based OLEDs, *The European Physical Journal Applied Physics*, Vol. 51, Issue 3, 2010, 33210.
[15]. M. Fujigaki, H. Minamino, Y. Murata, Interferometric trigger method with dual piezoelectric transducers for digital holographic interferometry, *Optical Engineering*, Vol. 57, Issue 11, 2018, 114105.
[16]. B. Ivanov, M. Shopova, A. Baldjiev, E. Stoykova, et al., Four-channel holographic infrared optical element, *Proceedings of SPIE*, Vol. 7747, 2011, 77470K.

(035)

Reducing Spectral Dispersion in Athermal 20-Cannel, 100 GHz Cyclic AWG via Linear-and-Quadratic Angle-Mapping Corrections

J. Chovan [1], D. Seyringer [2], A. Kuzma [1,3], M. Tomáška [1] and I. Bugár [1]
[1] International Laser Centre, Slovak Centre of Scientific and Technical Information, Ilkovičova 3, 841 04 Bratislava, Slovakia
[2] Research Centre for Microtechnology, Vorarlberg University of Applied Sciences, Hochschulstraße 1, 6850 Dornbirn, Austria
[3] Institute of Electronics and Photonics, Slovak University of Technology, Ilkovičova 3, 812 19 Bratislava, Slovakia
Tel.: + 421 2 654 21 5757
E-mail: jozef.chovan@cvtisr.sk

Summary: Cyclic arrayed waveguide gratings (CAWGs) are key wavelength-routing elements for Super-PON, yet aligning all cyclic bands to the DWDM ITU-grid is hindered by thermal drift and the intrinsic wavelength dependence of the free spectral range. We report a fabrication-friendly optimisation of a 20-channel, 100 GHz athermal CAWG on a SiON/PMMA platform that acts solely at the equation level by correcting the output-plane angle mapping in the star coupler. The intervention separates three physically meaningful controls: a linear term that restores the 100 GHz channel spacing, a quadratic term that compensates the S-shaped curvature arising from material and waveguide dispersion, and a small global angular offset that recentres the band without altering its slope or curvature. A four-stage calibration brings the C1 band from a baseline linear offset to near-ITU conformity with single-digit-picometre residuals, while the remaining cyclic bands (C2, L2, L1) show significantly reduced, though fundamentally unavoidable, dispersion-driven offsets. Because the method leaves the photonic layout unchanged and leverages a quadratic model of the effective-index dispersion for deterministic control, it offers a practical path to production-ready athermal CAWGs for Super-PON and a robust basis for future co-design of waveguide dispersion and angle mapping.

Keywords: Cyclic AWG, Super-PON, Athermal waveguide, Chromatic dispersion, SiON/PMMA, DWDM.

1. Introduction

Cyclic arrayed waveguide gratings (CAWGs) are increasingly adopted as compact, wavelength-selective routing elements in emerging Super-PON access architectures, where multiple cyclic spectral bands across the C and L telecommunications regions must be routed with high accuracy [1]. Although athermal waveguide design can effectively suppress temperature-induced shifts of the channel centre wavelengths, achieving and maintaining alignment with the DWDM ITU frequency grid is complicated by the intrinsic wavelength dependence of the CAWG free spectral range (FSR). Consequently, even an athermal device cannot exhibit perfect agreement with the ITU grid simultaneously across all four cyclic bands of a Super-PON.

Conventional AWGs are highly sensitive to ambient temperature, which produces central-wavelength drift and limits deployment in outdoor environments where active thermal stabilisation is impractical. To address this, athermal CAWG concepts embed athermal waveguides within the phased-array section so that thermo-optic (TO) effects are intrinsically compensated. A particularly effective material combination is a silicon oxynitride (SiO_xN_y) as a core and cladding with polymethyl methacrylate (PMMA). SiO_xN_y provides a modest positive thermo-optic coefficient, whereas PMMA exhibits a relatively large negative thermo-optic coefficient (TOC) while maintaining favourable optical properties. When appropriately configured, the opposing TO responses cancel to first order, stabilising the spectral response of the CAWG without active control [2].

The transverse refractive-index profile (contour map) of the athermal waveguide used in the CAWG phased array is shown in Fig. 1. In our previous work we reported the athermal waveguide optimisation, in which we jointly tuned the SiO_xN_y core refractive index, the waveguide width W_w, height W_h, and the slab thickness S_h [2]. One of the principal outcomes is reproduced in Fig. 2, demonstrating that for a suitable geometric design, the normalised temperature dependent central wavelength shift (TD-CWS, per unit temperature change) exhibits a local minimum at a specific SiON refractive index. Crucially, this index can be set during fabrication by adjusting the process parameters, thus enabling material-level control of athermal behaviour. Balancing single-mode operation, polarisation dependence at the athermal minimum, and bend losses, the waveguide dimensions adopted in the present CAWG design are: W_w=W_h=2.5 μm, S_h=0.8 μm and refractive index of SiON core n_c=1.5611. These dimensions realise an athermal platform for the CAWG phased array while preserving low-loss and manufacturability. The value of the refractive index of the SiON layer can be controlled by the technological conditions during its deposition in

the range from 1.447 to 1.651 at the 1.55 µm wavelength [3].

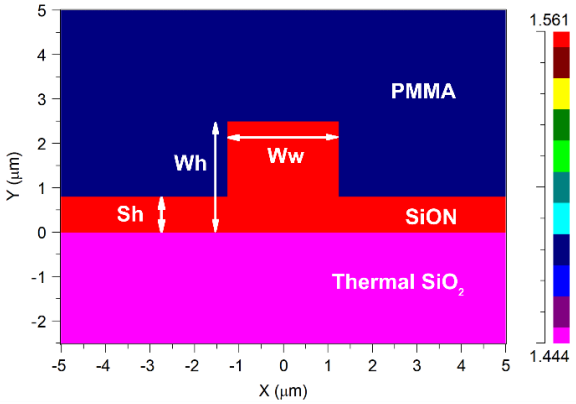

Fig. 1. Contour map of transverse refractive index profile of used athermal waveguide structure [2].

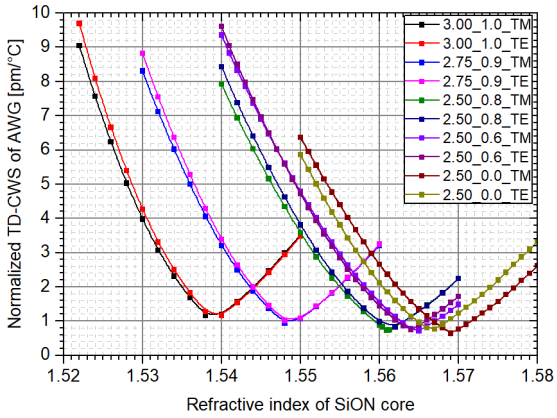

Fig. 2. Normalized TD-CWS on SiON core refractive index [2].

2. Dispersion Properties of Athermal Waveguide

The material dispersions of all constituent layers over the 420 nm – 2000 nm range are shown in Fig. 3 [3–5]. Within the telecommunication C and L bands, the refractive indices of all layers decrease monotonically with increasing wavelength. To characterise the guided mode under practical operating conditions, the effective refractive index $n_{\mathrm{eff}}(\lambda, T)$ of the athermal waveguide was computed using a beam propagation method that incorporates: (i) the thermo-optic response of each material and (ii) waveguide dispersion. Simulations were carried out for three different temperatures (−40 °C, 20 °C, and +80 °C) across the 1525 nm – 1610 nm spectral window. The resulting $n_{\mathrm{eff}}(\lambda)$ of the fundamental guided mode, plotted in Fig. 4, exhibits a weak yet systematic wavelength dependence due to the combined material and waveguide dispersion. The TOC of the individual layers are treated as constant over the evaluation spectral window. We note an *asymmetric* thermal response: for a negative temperature swing (−60 °C), the change in the effective index is larger than for a positive swing (+60 °C). Physically, this arises from waveguide dispersion induced by a temperature dependent index contrast between the SiON core and the PMMA cladding. With decreasing temperature, the PMMA refractive index increases while the SiON refractive index decreases, thereby reducing the index contrast at the core–cladding boundary. This weakens the modal confinement and the waveguide contribution to dispersion, leading to the observed asymmetry.

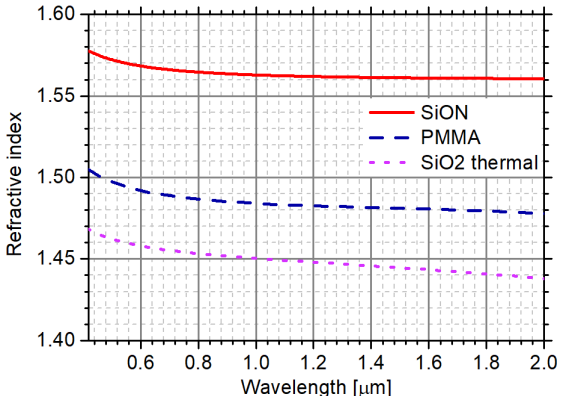

Fig. 3. Material dispersion of athermal waveguide structure materials [2].

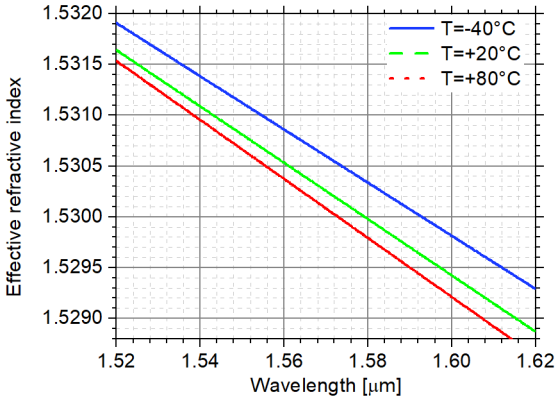

Fig. 4. Effective index dispersion of the athermal waveguide structure materials, incorporating both material and waveguide effects at different temperatures [2].

The group index is defined by

$$n_g(\lambda) = n_{\mathrm{eff}}(\lambda) - \lambda \frac{dn_{\mathrm{eff}}}{d\lambda} \quad (1)$$

If the simulated dependence of the effective index is approximated quadratically

$$n_{\mathrm{eff}}(\lambda) \approx a\lambda^2 + b\lambda + c, \quad (2)$$

then $n_g(\lambda)$ follows in closed form from the fit coefficients:

$$n_g(\lambda) = (a\lambda^2 + b\lambda + c) - \lambda\,(2a\lambda + b) = \\ = c - a\lambda^2 \quad (3)$$

This analytic relation is particularly convenient for downstream AWG modelling, as it provides a noise-free evaluation of n_g and its curvature directly from *(a, b, c)*. The group-index dispersion of the athermal waveguide for three temperatures within the ±60 °C excursion is shown in Fig. 5. The absolute value of n_g increases with temperature; over a 120 °C span the change is modest (third decimal place), yet non-negligible for precise CAWG design. Since CAWG operates via interference orders formed at the output of free-propagation region (FPR), each cyclic band corresponds to a different interference order, and the free spectral range (FSR) is governed by the group index and the phased-array path-length step ΔL:

$$FSR_f \approx \frac{c}{n_g \Delta L}\,[Hz],\ FSR_\lambda \approx \frac{\lambda^2}{n_g \Delta L}\,[m], \quad (4)$$

where ΔL denotes the incremental optical path length difference between successive arrayed waveguides. Equation (4) highlights why accurate $n_g(\lambda, T)$ is essential for predicting the FSR and, in turn, for aligning each cyclic band of the CAWG close to the DWDM ITU-grid.

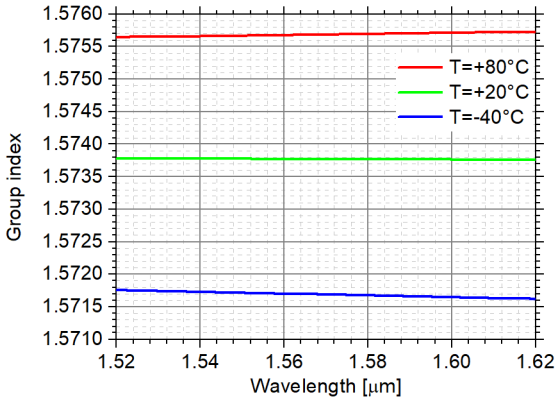

Fig. 5. Group index of the athermal waveguide structure.

3. Dispersion Properties of Athermal 20-channel, 100 GHz Cyclic AWG

3.1. Device Overview and Simulation Setup

We designed a 20-channel, 100 GHz athermal CAWG with an FSR ≈ 2.2 THz, with central wavelength λc=1 555.35 nm, for Super-PON operation across the C and L bands [1]. The top-level topology (array geometry, star-coupler radiuses, order, and port counts) was synthesised in Keysight Optical Solutions AWG Utility, using as inputs: (i) number of input/output ports, (ii) channel spacing, (iii) central wavelength, (iv) target FSR, and (v) athermal waveguide stack parameters. The on-chip footprint of the CAWG core is <36 mm². The simulated transmission over the four cyclic bands (labelled C2, C1, L2, L1 from shorter to longer wavelengths) appears in Fig. 6. Unless otherwise stated, the "central wavelength" (CW) of the device is defined as the mid-point between the CWs of channels 10 and 11 in the C1 band. To quantify absolute CW positions and temperature shifts, we post-processed the simulated spectra with in-house Python tools. For each channel in all four bands and for three temperatures (−40 °C, 20 °C, +80 °C), CW channel was taken as the mean of two wavelengths at which the transmission is 3 dB below the peak (left and right sides). The native spectral resolution of the simulation was 48 points per channel (~17 pm), after which the spectra were resampled to increase the granularity of the CW extraction. The resulting CW offsets relative to the DWDM ITU-grid [6], both for original and corrected angle mappings, are shown in Fig. 7. Although the corrected C1 band exhibits residuals in the single-digit-picometre range, these values should be interpreted within the limits of the numerical procedure. The native simulation sampling (~17 pm) was refined by resampling, which improves CW localisation but does not create metrological accuracy beyond the underlying model. In fabricated devices, deviations in refractive index, sidewall roughness, path-length errors and output-port placement would introduce additional shifts of several tens of picometres. The present results therefore quantify the intrinsic correction capability of the mapping model, rather than the absolute post-fabrication performance.

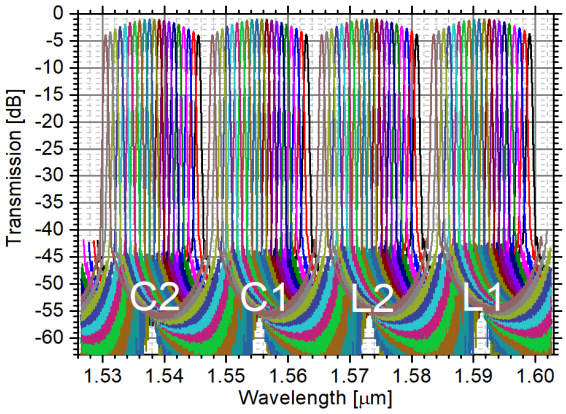

Fig. 6. Simulated transmission characteristics of four CAWG bands at 20 °C.

3.2. Output-Plane Angle Mapping and Its Correction

Let X denote the output-waveguide index ($X \in \{1, \ldots, 20\}$). In the original mapping used by the layout tool, the angular position of port X at the output of FPR is

$$zAo_X = 180^\circ - A_i(X - A_{so}), \quad (5)$$

where A_i is a geometry-dependent constant and A_{so} is the half-sum of the first and last port indices (for 20 channels, $A_{so} = 10.5$). Fig. 8 shows the positions and indices of the output CAWG waveguides on the FPR output and the position of the 180° angle. Equation (5) enforces a strictly linear channel-to-angle mapping. In practice, however, residual dispersion of the phased-array waveguides produces a small S-shaped deviation of the CWs from the ITU-grid, which a purely linear mapping cannot remove. We therefore apply a physically anchored correction that allows the linear scale, a quadratic curvature, and a global rotation to act with respect to the array centre:

$$zAo_X = 180^\circ - \begin{bmatrix} A_i(X - A_{so}) * S \\ +c_2(X - A_{so})^2 \end{bmatrix} + Z_{corr} \quad (6)$$

S tunes the linear channel spacing (i.e., the effective slope in angle versus channel index), c_2 applies a quadratic curvature (compensating the S-shape from $1/\lambda$ mapping and waveguide dispersion), Z_{corr} is a global angular offset that recentres the band without affecting slope or curvature.

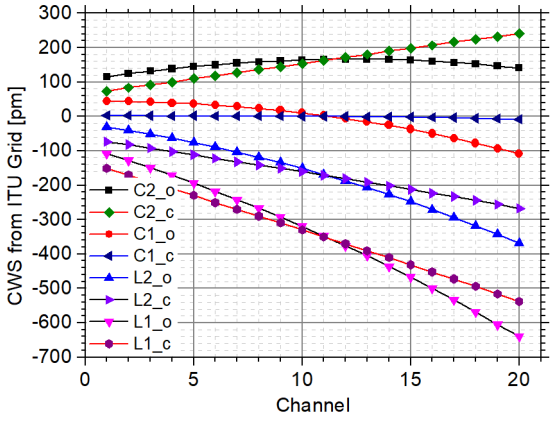

Fig. 7. CW offset from ITU GRID for all four investigated bands of the output transmission characteristics of 20 CAWG at 20 °C.

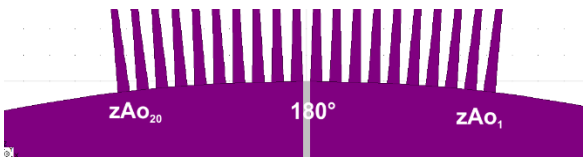

Fig. 8. Output waveguides of output FPR of AWG.

This correction acts only at the equation level; no change to the fabricated photonic layout is required. As shown in Fig. 7, it aligns the C1 band with the ITU-grid to within approximately 6–8 pm and reduces (but cannot fully eliminate) the residual offsets in the other cyclic bands that is a fundamental limitation imposed by the wavelength dependence of the FSR in cyclic AWGs. Note that the mapping correction acts on the angular placement of channels at the output FPR; the underlying spectral periodicity is still governed by the phased-array FSR via $n_g(\lambda)$ and ΔL, hence different cyclic bands may require different residual offsets even after the C1 calibration.

3.3. Four-Stage Calibration in C1 Band

We follow a compact calibration workflow to isolate and correct the three dominant components of the CW error in C1: (i) Baseline behaviour. With all corrections disabled ($S = 1, c_2 = 0$), the CAWG shows an approximately linear CW offset: +51 pm at channel 1 down to −114 pm at channel 20, with channels 10–11 near zero. This indicates a slope error corresponding to an effective spacing of about 108.5 GHz instead of 100 GHz (see the "_o" curves per band in Fig. 7). (ii) Slope correction (S). Sweeping S reveals the value that restores 100 GHz channel spacing; we obtain $S \approx 1.0047$. Physically, this slightly increases the phase gradient across the array. (iii) Curvature correction (c_2). The residual S-shape is countered by a negative quadratic term. A short sweep yields $c_2 \approx -3.5 \times 10^{-4}$, which flattens the profile without over-correcting the edges (see "_c" curves in Fig. 7). (iv) Absolute centring (Z_{corr}). After slope and curvature correction, a small residual bias of +6.4 pm at the C1 centre converts – using the local angular sensitivity (~1133 pm/°) to $Z_{corr} \approx -0.0057°$,which uniformly translates all channels, placing C1 on the ITU-grid. After the angle-mapping correction (linear scale S, quadratic term $c2$, and absolute rotation $Zcorr$), the C1 band can be brought to near-ITU alignment, while the other cyclic bands retain a small, almost purely linear residual across channels. The reason is chiefly geometric: the output star coupler places ports with an (almost) constant angular pitch, yet the angle-to-wavelength sensitivity of the FPR, $d\lambda/d\theta$, is not strictly constant with angle and interference order. A uniform pitch therefore maps into a nearly uniform wavelength spacing per cycle, which cannot exactly reproduce a frequency-defined ITU-grid. Our c_2 term removes the S-shape (second-order curvature), revealing this underlying linear mismatch; the remaining fine ripple is a secondary effect caused by the weak dispersion of the athermal waveguide and minor imaging aberrations. In practice, only one cycle (C1) can be aligned with low residuals; extending this to all cycles would require mapping beyond the linear-quadratic form, such as non-uniform port spacing or multi-band optimisation, because a single layout-level mapping cannot enforce constant Δf across all orders. For the non-design cyclic bands (C2, L2 and L1), the corrected channel positions show residual offsets that increase with interference order, reaching values on the order of 150 pm in C2, 450 pm in L2 and about 650 pm in L1. These correspond to frequency shifts ranging from several tens of gigahertz to approximately 80 GHz, reflecting the intrinsic

order-dependent behaviour of cyclic AWGs. While the proposed mapping correction significantly suppresses curvature-related deviations, the remaining offsets cannot be removed simultaneously across all cycles because each band experiences a different spectral magnification and a different FSR. This behaviour is therefore a fundamental property of cyclic AWGs rather than a limitation of the correction method.

4. Conclusions

We have presented a fabrication-friendly optimisation of a 20-channel, 100 GHz athermal cyclic AWG that operates purely at the equation level, without any modification of the underlying photonic layout. By restoring the correct channel-indexed dependence in the output-plane angle mapping and tuning three physically meaningful parameters, i.e., linear scale (*S*), quadratic curvature (c_2), and global angular offset (*Zcorr*) the C1 cycle can be aligned to the DWDM ITU-grid with residual deviations reduced to approximately 6–8 pm, as obtained using refined CW localisation. A key outcome of this work is that such precise alignment is fundamentally achievable only for a single spectral cycle. In cyclic AWGs, each band (C2, C1, L2, L1) corresponds to a different interference order, and the combination of angle-dependent spectral magnification in the output FPR and the wavelength dependence of the FSR prevents all cycles from simultaneously matching a frequency-defined ITU-grid. Consequently, while the proposed mapping correction significantly suppresses residual errors in C2, L2 and L1, complete ITU-grid alignment across all four cyclic bands cannot be realised by any linear-quadratic mapping applied to a fixed-geometry CAWG. This behaviour reflects an inherent physical property of cyclic AWGs rather than a limitation of the correction strategy.

Acknowledgements

This work was funded by the EU NextGenerationEU through the Recovery and Resilience Plan for Slovakia under the project No. 09I03-03-V04-00684.

References

[1]. C. DeSanti, L. Du, J. Guarin, J. Bone, et al., Super-PON: An evolution for access networks, *Journal of Optical Communications and Networking*, Vol. 12, Issue 10, 2020, pp. D66-D77.

[2]. J. Chovan, A. Kuzma, M. Tomáška, F. Uherek, Optimization of rib, single-mode SiOxNy optical waveguide structure for athermal AWG using PMMA cover layer, *Proceedings of SPIE*, Vol. 13698, 2025, 1369802.

[3]. L. Yin, M. Lu, L. Wielunski, W. Song, et al., Fabrication and characterization of compact silicon oxynitride waveguides on silicon chips, *Journal of Optics*, Vol. 14, Issue 8, 2012, 085501.

[4]. A. Trenti, M. Borghi, S. Biasi, M. Ghulinyan, et al., Thermo-optic coefficient and nonlinear refractive index of silicon oxynitride waveguides, *AIP Advances*, Vol. 8, Issue 2, 2018, 025311.

[5]. G. Beadie, M. Brindza, R. A. Flynn, A. Rosenberg, et al., Refractive index measurements of poly(methyl methacrylate) (PMMA) from 0.4-1.6 μm, *Applied Optics*, Vol. 54, Issue 31, 2015, pp. F139-F143.

[6]. ITU-T Recommendation G.694.1: Spectral grids for WDM applications: DWDM frequency grid, International Telecommunication Union, 2020, https://www.itu.int/rec/T-REC-G.694.1-202010-I/en

(036)

Ultra-Sensitive Plasmonic Sensor Based on MgF_2 –Al-Graphene Structure for Chemical Entity Identification

Imed Sassi
University of Monastir, IPEIM, Laboratory Study of ionized and reactive environments EMIR- LR20ES08,
Street Ibn Jazzar, Monastir, 5019, Tunisia
Tel.: 0021697537899
E-mail: imed.sassi@ipein.rnu.tn

Summary: This paper presents the design of a sensor composed of a glass prism, aluminum, and graphene for the detection of chemical entities. The sensor is modeled using the matrix method in the visible and near-infrared regions. The proposed device consists of two functional layers-aluminum and graphene-deposited on an MgF_2 glass prism substrate. The design exhibits distinctive reflectance characteristics across the studied wavelength range, making it suitable for detecting: heavy metal ions and other chemical substances for example. Multiple reflectance curves are compared to evaluate the sensor's performance. Geometrical parameters, such as the aluminum layer thickness and the number of graphene layers, are optimized for a fixed incident light angle (= 85°). A comparison of wavelength sensitivity between the present design and previously reported sensors is also conducted. After optimization, the MgF_2–Al–graphene–sensing medium demonstrates a sensitivity and a figure of merit exceeding 26600 nm/RIU, and 30.05 RIU^{-1}, respectively. The proposed plasmonic structure thus shows strong potential for detecting various chemical entities with refractive indices between 1.33 and 1.35.

Keywords: Wavelength interrogation, SPR sensor, Graphene-based structure, MgF_2 glass prism, Reflectance response.

1. Introduction

Optical sensors rely on various materials such as noble metals, dielectrics, polymers, two-dimensional materials, and glass substrates to enhance light–matter interactions. When light interacts with metal–dielectric interfaces under specific conditions, it excites surface plasmons, generating strong localized electromagnetic fields. These plasmonic effects are highly sensitive to changes in the refractive index of the surrounding medium, making them suitable for biochemical and environmental sensing applications. Several plasmonic configurations have been developed, including prism-based systems, gratings, photonic crystals, fiber optics, resonators, and waveguides. Among them, the Kretschmann prism configuration is widely used due to its simple design and high sensitivity in refractive index sensing. Numerous studies have demonstrated its efficiency for detecting pathogens, malaria infection, chemical compounds, glucose in urine, and bacterial cells in water [1–3]. Grating structures enable direct excitation of surface plasmons without a prism, while photonic crystals offer high sensitivity through shifts in their photonic band gap [4]. Hybrid plasmonic–photonic sensors combining photonic crystal fibers, waveguides, resonators, and gratings have also achieved remarkable sensitivities for refractive index detection [5-8]. Monitoring chemical contaminants is essential for environmental protection and public health. Compared with conventional analytical methods, SPR-based optical biosensors provide rapid, label-free, and highly sensitive detection. We limit our study in this work to investigate the detection of various chemical entities by using a prism configuration SPR sensor, based on MgF_2 prism, Aluminum layer, and Graphene layer.

2. Theory

A refractive index sensor based on MgF_2 prism, aluminum layer, graphene layer, and sensing medium is reported. On the top of the prism, an aluminum layer is deposited, followed by a Graphene layer, and an analyte medium is employed.

The MgF_2glass prism's RI is expressed as: [9]

$$n_{MgF_2} = \sqrt{\frac{a\lambda^2}{\lambda^2-d^2} + \frac{b\lambda^2}{\lambda^2-e^2} + \frac{c\lambda^2}{\lambda^2-f^2} + 1}, \qquad (1)$$

where, a = 0.48755108, b = 0.39875031, c = 3.8484723, d = 0.04338408, e = 0.09461442, and f = 23.793604.

Using the Drude–Lorentz model, the refractive index of aluminum is given by [41]:

$$n_{Al} = \sqrt{\left(1 - \frac{\lambda^2\lambda_c}{\lambda_p^2(\lambda_c + i\lambda)}\right)}, \qquad (2)$$

$\lambda_c(\mu m) = 24.511,\ \lambda_p(\mu m) = 0.10675.$

The refractive index of the graphene layer for a broad spectral range, can be deduced by using the results published recently by K. K. Tikuišis et al. [10]

To compute the reflectance of our sensor device, we use the transfer matrix method [1].

The wavelength sensitivity (WS) is defined as the ratio between the variation in the resonance wavelength (RW) and the corresponding change in the refractive index (Δn) of the analyte.

$$WS = \frac{\Delta(RW)}{\Delta n}, \qquad (3)$$

The Figure of Merit (FoM) in wavelength interrogation is a key parameter used to evaluate the overall performance of a sensor, as it takes into account both the sensitivity and the spectral linewidth. It indicates the ability of the sensor to detect very small variations in the measured parameter, such as refractive index changes, through shifts in the resonance wavelength. The FoM can be expressed as follows:

$$FoM = \frac{WS}{FWHM}. \quad (4)$$

Another performance parameter is the reflectance at resonance, corresponding to the minimum reflection: RR (%).

3. Results

To enhance the performance parameters of our sensor: wavelength sensitivity (WS) and the reflectance at resonance (RR (%)), we must optimize the geometrical parameters: the number of graphene layers (G=1, 2) and the thickness of the aluminum layer (T(Al)), at fixed incident light, $\theta = 85°$. Firstly, we calculate the wavelength at resonance (WR) for each refractive index value, and its corresponded RR (%), at fixed number of graphene layer (G = 2), for different values of the T(Al) (nm). To determine the optimum value of the T(Al), we investigate simultaneously both the WS and the RR (%). For different values of the T(Al), the investigation of the WS demonstrate any distinction. For all considered values the WS is ranged between 8400 to 26250 nm/RIU (see Table 1).

Table 1. Different values of the sensitivity for various values of T(Al) = 28, 30, 32, 34, and 36 nm, for G = 2.

T(Al) (nm)	28	30	32	34	36
RI	**WS (nm/RIU)**				
1.330	-	-	-	-	-
1.332	08400	08400	08400	08400	08400
1334	08750	09100	09450	09100	09450
1.336	10500	10150	09800	10150	10150
1.338	10500	10850	11200	11200	11200
1.340	12250	12600	12600	12600	12600
1.342	14000	14000	14000	14350	14000
1.344	15750	16100	16100	15750	16100
1.346	18550	18200	18550	18900	18900
1.348	21700	22050	21700	21700	21700
1.350	26250	26250	26600	26250	26250

However, the analysis of the variation of RR (%)) for different values of the T(Al), varying from 28 to 36 nm, demonstrate a distinction for T(Al) = 32 nm, which is characterised by a reflectance at resonance (RR (%)) ranged from 0.004 to 1.19 % (see Fig. 1). Consequently, the optimum value for this case is T(Al) = 32 nm.

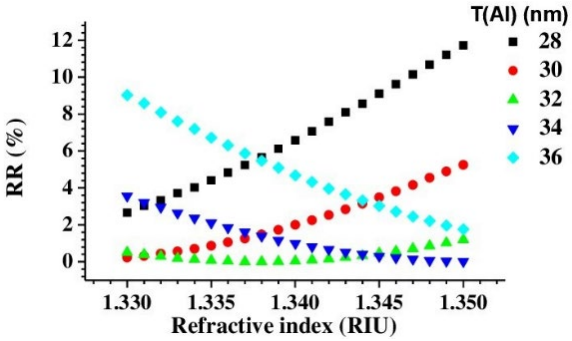

Fig. 1. Variation of the RR (%) as a function of refractive index for different values of Aluminum thickness layer.

Secondly, to demonstrate the effect of the number of graphene layers on the performance of our sensor, we compare the WS and the RR (%) values for G = 1, 2, for the same value of T(Al) (=32 nm), at fixed incident angle (= 85°). Table 2 shows , the best values of the WS and RR (%) are obtained for G = 2, for the most values of the RI ranges. Consequently, we consider the optimal parameters: T(Al) = 32 nm, and G =2 are the best values for the sensor's performance.

Table 2. Comparison of RR (%) and WS for two values of G = 1,2, at fixed T(Al) = 32 nm, and $\theta = 85°$.

RI	RR (%)		WS (nm/RIU	
	G=1	G=2	G=1	G=2
1.330	1.06	**0.508**	-	-
1.332	1.39	**0.297**	08400	**08400**
1.334	1.73	**0.131**	08750	**09450**
1.336	2.13	**0.032**	9800	**09800**
1.338	2.53	**0.004**	11200	**11200**
1.340	2.97	**0.043**	11900	**12600**
1.342	3.44	**0.161**	13650	**14000**
1.344	3.90	**0.329**	15750	**16100**
1.346	4.32	**0.572**	19700	**18550**
1.348	4.73	**0.870**	19500	**21700**
1.350	5.10	**1.195**	25550	**26600**

We present in Fig. 2 the variation of the reflectance as versus wavelength, for different values of refractive index of the sensing medium, varying from 1.33 to 1.35, with an increment of 0.002 (RIU). One can be seen, the displacement of the reflectance curves for left to right is very significant and clearer, when the RI increase for 1.33 to 1.35. That causes an increase of the wavelength sensitivity, for 8400 to 26600 nm/RIU.

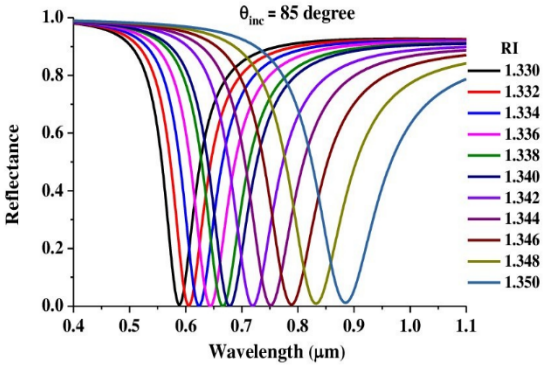

Fig. 2. Variation of the reflectance as a function of the wavelength, at fixed incident light ($\theta_{inc} = 85°$), Aluminum (Al) thickness layer = 32 nm, and number graphene layer (G=2).

At fixed incident angle $\theta = 85°$, for the optimal parameters: T(Al) (= 32 nm, and G = 2, we compute the FWHM, and the FoM. In the Table 3, we present the different values of the WS, FWHM, and FoM, for the RIs: 1.33, 1.332, 1.334, 1.336, 1.338, 1.34, 1.342, 1.346, 1.348, and 1.350.

Table 3. The parameters: FWHM, WS, and FoM, for T(Al) (= 32 nm), and G = 2.

RI	FWHM	WR	WS	FoM
1.330	063.9	588.3	-	
1.332	066.6	605.1	8400	13.88
1.334	070.0	624.0	9450	15.14
1.336	073.4	643.6	9800	15.22
1.338	077.5	666.0	11200	16.81
1.340	082.1	691.2	12600	18.23
1.342	087.4	719.2	14000	19.46
1.344	093.8	751.4	16100	21.42
1.346	099.6	788.5	18550	23.52
1.348	111.2	831.9	21700	26.08
1.350	123.5	885.1	26600	30.05

Compared to earlier studies, the current results show a notable improvement in both sensitivity and figure of merit (FoM) across all considered sensors (see Table 4).

Table 4. Comparison with existing works.

Ref./Year	Structure	WS	FoM
Thi work	Prism (MgF_2)-Al-Graphene	2660	30
[11] 2024	Prism config.	~1384	0.92
[12] 2022	Grating structure	~706	-
[13] 2025	Optical fiber	~439	21.99
[14] 2025	PCF	5450	
[15] 2024	PCF	8000	-
[16] 2024	MIM Grating	781	-
[17] 2022	MIM WG	~825	13.14

4. Conclusions

We conduct a systematic analysis of a Plasmonic RI sensor with a prism configuration, consisting of an MgF_2 prism, an aluminum layer, and a graphene coating, designed for the identification of various chemical entities in aqueous solution. The device performance was analysed using the transfer matrix method, achieving an optimal WS and FoM of 26600 nm/RIU and 30.05 RIU^{-1}, respectively. The results are characterized by a resonant wavelength varied from visible range to near infrared band across the range of analyte RIs from1.33 to 1.35, in increments of 0.002. For the MgF_2–Al–graphene–analyte configuration, the wavelength sensitivity varies between 8400 and 26000 nm/RIU, when the aluminum thickness layer is varied from 28 to 36 nm at fixed incident light (= 85°), and a number of graphene layer equal to 2.

5. Future Work

In this work, the optimization of the aluminum layer thickness has already been addressed and shown to significantly enhance the sensor performance. Future research will therefore focus on further improving the device by exploring additional parameters, such as varying the incident angle and increasing the number of graphene layers. In addition, we aim to investigate the performance of our device in detecting heavy metal ions such as Hg^{2+}, Pb^{2+}, Zn^{2+}, and Cu^{2+} in water. Furthermore, experimental validation and practical implementation will be carried out to evaluate the reliability and real-world applicability of the proposed sensor.

Acknowledgements

The author would like to thank: Laboratory Study of ionized and reactive environments EMIR-LR20ES08, IPEIM, for providing the facilities and support required to carry out this research.

References

[1]. I. Sassi, M. Ben El Hadj Rhouma, M. Zbidi, J. W. Simatupang, A highly sensitive structure based on prism, silver, and titanium dioxide for biochemical sensing applications, *Plasmonics*, Vol. 20, 2025, pp. 363–372.

[2]. A. Uniyal, M. Kumar, R. Kumar, G. Dhiman, et al., Silver, silicon, and selenium-based surface plasmon resonance sensor for pathogen bacteria detection in visible region, *Optical and Quantum Electronics*, Vol. 57, 2025, Article 196.

[3]. R. Kumar, L. Garia, T. S. Yun, M. Sain, Highly sensitive surface plasmon resonance biosensor for the detection of urine glucose concentration, *Photonics*, Vol. 13, Issue 1, 2026, Article 20.

[4]. M. G. Daher, O. Alsalman, N. M. Ahmed, I. Sassi, et al., Modeling of a novel chikungunya virus detector

based on silicon and titanium nitride multilayer thin films, *Optik*, Vol. 287, 2023, Article 171136.

[5]. L. Hajshahvaladi, H. Kaatuzian, M. Moghaddasi, M. Danaie, Hybridization of surface plasmons and photonic crystal resonators for high-sensitivity and high-resolution sensing applications, *Scientific Reports*, Vol. 12, 2022, Article 21292.

[6]. I. Sassi, A. Dhibi, M. Oumezzine, Resonances in reflection, transmission and absorption of 1-D triangular-relief metallic gratings, *Indian Journal of Physics*, Vol. 91, Issue 2, 2017, pp. 149–155.

[7]. I. Sassi, M. Ben El Hadj Rhouma, S. A. Taya, M. H. Gazzah, The effects of the geometric and optical parameters on the performance of a grating perfect absorber sensor in near-infrared band, *Optical and Quantum Electronics*, Vol. 56, 2024, Article 992.

[8]. U. Farooq, H. A. Khan, M. Asif, N. Liu, A wide-angle and polarization-insensitive graphene-based optically transparent terahertz metasurface absorber for biosensing applications, *Photonics*, Vol. 13, Issue 2, 2026, Article 181.

[9]. M. J. Dodge, Refractive properties of magnesium fluoride, *Applied Optics*, Vol. 23, Issue 12, 1984, pp. 1980–1985.

[10]. K. K. Tikuišis, A. Dubroka, K. Uhlířová, F. Speck, et al., Dielectric function of epitaxial quasi-freestanding monolayer graphene on Si-face 6H-SiC in a broad spectral range, *Physical Review Materials*, Vol. 7, 2023, Article 044201.

[11]. M. Uwais, A. Bijalwan, V. Rastogi, SPR-based sensor for colorectal cancer detection using Al–Cu and graphene, *Plasmonics*, Vol. 19, 2024, pp. 1857–1866.

[12]. M. Uwais, A. Bijalwan, V. Rastogi, Surface phonon resonance assisted refractive index sensing in mid-infrared wavelength range, *Plasmonics*, Vol. 17, Issue 3, 2022, pp. 1331–1338.

[13]. Y. Huang, Y. Chen, P. Yuan, B. Luo, et al., Ultra-sensitive SPR fiber-optic biosensor based on MNM structure with Ti_3C_2 MXene/PDA modification for placental growth factor detection, *Sensors and Actuators B: Chemical*, Vol. 443, 2025, Article 138214.

[14]. X. Gao, H. Pan, Q. You, Y. Zhu, et al., A highly sensitive slot PCF-SPR sensor for temperature and refractive index detection, *Plasmonics*, Vol. 20, Issue 11, 2025, pp. 10589–10599.

[15]. Z. S. Alshaikhli, M. T. Mahdi, Numerical analysis of high sensitivity refractive index sensor based on quad-core PCF-SPR, *Plasmonics*, Vol. 20, 2025, pp. 4553–4564.

[16]. L. B. Akcher, A. S. M. Mohsin, M. A. Haque, Study and simulation of MIM grating-based refractive index sensor for the detection of haemoglobin (Hb) in blood samples, *Plasmonics*, Vol. 20, Issue 7, 2024, pp. 4911–4918.

[17]. M. A. Butt, Plasmonic sensor realized on metal-insulator-metal waveguide configuration for refractive index detection, *Photonics Letters of Poland*, Vol. 14, Issue 1, 2022, pp. 1–3.

(038)

Replication of Microstructure Artifacts in Polymers Cast and Embossed by Femtosecond-Laser-Textured Metal Dies

A. M. Rodin [1], O. Myronyuk [2], D. Baklan [2] and A. Bilousova [2]
[1] Center for Physical Sciences and Technology, Solid State Laser Laboratory, 231 Savanoriu Ave, 02300 Vilnius, Lithuania
[2] National Technical University of Ukraine "Igor Sikorsky Kyiv Polytechnic Institute" 37, Prospect Beresteisky 21, 03056 Kyiv, Ukraine
Tel.: +370 64209935
E-mail: aleksej.rodin@ftmc.lt

Summary: The replication behavior and the influence of artifacts originating from femtosecond-laser-textured dies on polymer substrates were investigated. Micro- and nanotextures were fabricated on AISI 304 stainless steel dies using femtosecond-laser machining and then replicated onto polycarbonate and polyethylene through solvent casting and thermopressing, respectively. This study introduces a new approach to the identification and interpretation of artifacts formed after the replication process using metal molds. The findings further indicate that these artifacts constitute a reliable pathway to hierarchical microstructure fabrication. The low viscosity and superior wetting behavior of the polycarbonate solution allowed solvent casting to achieve sub-micron replication accuracy. In contrast, the thermopressed polyethylene surface exhibited coarse hollow features caused by air entrapment and the rupture of locally thinned polymer areas. These effects stem from the interplay among polymer viscosity, interfacial adhesion, and cooling dynamics. Even with reduced mold replication fidelity, the resulting artifacts offer a route to unique and reproducible microstructures. These findings underscore the dual role of laser-texture artifacts in replication: serving as both a constraint and an opportunity for new surface-engineering strategies.

Keywords: Femtosecond laser processing, Laser texturing, Functional surfaces, Polymer, Solvent-casting, Thermopressing.

1. Introduction

Femtosecond-laser processing is a highly precise technique for fabricating templates featuring reproducible, well-defined microstructures on the micrometer scale. Laser-textured metallic dies offer a reliable platform for transferring surface patterns onto polymer substrates [1]. When replicated onto polymer films [2], these textures enable scalable fabrication of functional surfaces.

However, replication does not always guarantee a faithful texture transfer. Deviations from the original template may arise under thermopressing or solvent casting [3], driven by polymer viscosity, wetting behavior, shrinkage, and relaxation during solidification [4]. Although fidelity loss is undesirable, certain artifacts may still give rise to unique and reproducible morphological features.

In this study, thermopressed polyethylene and solvent-cast polycarbonate replicas, both derived from femtosecond-laser-textured metal dies, are compared to elucidate the origin and nature of the observed artifacts and to determine their influence. This work extends our earlier investigation of polymer replication from metal templates by examining replication-induced artifacts in thermopressed polyethylene [5, 6].

2. Sample Preparation

Micro- and nanotextures were machined on AISI 304 stainless steel dies using a Light Conversion "Carbide" laser (up to 6 W at 1030 nm, ~360 fs, 60 kHz) and subsequently replicated onto polymer substrates by solvent casting or thermopressing. Grooves with a 100 μm pitch and 20 μm width (sample "*I*") and with a 60 μm pitch and 30 μm width (sample "*K*") are shown in Fig. 1.

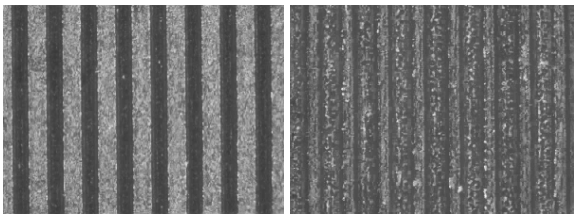

Fig. 1. Optical microscope images of the die textures for sample "*I*" (left) and sample "*K*" (right).

For solvent-casting replication, a ~5 wt % polycarbonate solution (Marlon FSX, Plastics Ukraine) in methylene chloride was deposited onto the laser-textured die and allowed to evaporate in a fume hood without heating. The solidified polymer film was then mechanically peeled off the die. For thermopressing, a 200 μm polyethylene film (HDPE, Plastics Ukraine) was used. The holding time at 110 °C was 20 s. The samples were removed from the mold at a controlled speed of approximately 0.5 cm/s to minimize mechanically induced defects. The samples were then cooled to ambient temperature. Each sample underwent three thermoforming cycles, and the

textured die was cleaned with compressed air prior to each cycle.

3. Results and Discussion

The study was conceived as a comparative analysis of artifact formation across two different laser-textured dies using two polymer replication methods (polycarbonate solvent casting and polyethylene thermoforming), rather than as a comprehensive optimization of processing parameters. Therefore, variables such as holding time, mold-ejection speed (0.5 cm/s), mold-surface treatment, and cooling conditions were selected based on preliminary optimization to ensure reproducible replica fabrication.

The laser-textured die surface exhibits a heterogeneous morphology (Fig. 2), comprising unaffected areas alongside laser-machined grooves containing sub-micron artifacts. Solvent casting ensures highly faithful negative replicas of the original die patterns (Fig. 3). This behavior stems from the low viscosity of the polycarbonate solution, allowing it to penetrate sub-micron-scale surface features. Compared to melt- or oligomer-based approaches, low-viscosity solutions provide superior wetting and more effectively infiltrate textured surface while maintaining fine structural details.

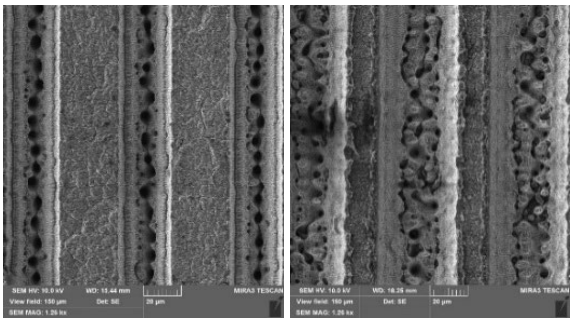

Fig. 2. SEM images of femtosecond-laser-textured die surfaces for sample "*I*" (left) and sample "*K*" (right).

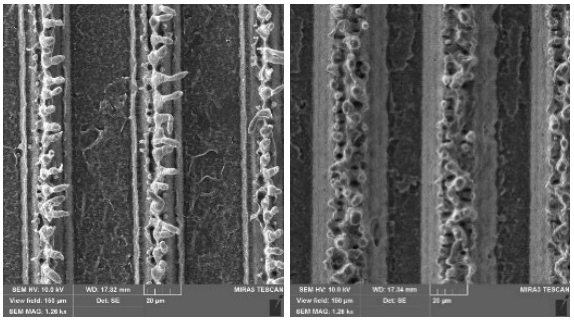

Fig. 3. SEM images of solvent-cast polycarbonate films for sample "*I*" (left) and sample "*K*" (right).

Thermopressing results in a much coarser replication (Fig. 4), characterized by hollow structures formed when air bubbles become trapped within surface irregularities at the polymer–die interface. Upon cooling, these bubbles cause local thinning of the polymer walls, with the thinned regions rupturing after demolding.

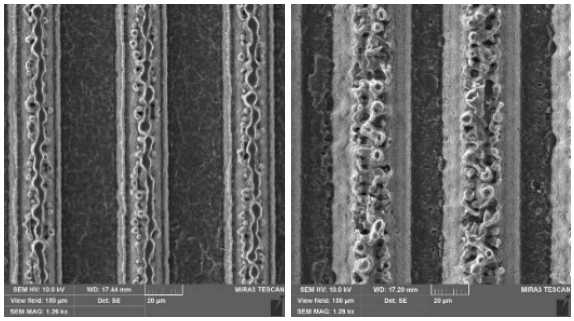

Fig. 4. SEM images of thermopressed polyethylene films for sample "*I*" (left) and sample "*K*" (right).

Dimensional analysis indicated that the groove depth on the laser-textured metal die was approximately 40 μm, whereas in the polyethylene replicas the groove depth ranged from 36 to 38 μm. The rupture of these thin polymer films occurs when their mechanical strength in locally thinned regions becomes lower than the adhesion forces binding the film to the metal die. Despite hydrophobizing treatment of the laser-textured dies, interfacial adhesion remains sufficiently strong, leading to replication-induced artifacts (Fig. 5). The resulting microstructures were not tailored for applications including superhydrophobic coatings, liquid-impregnated surfaces, microfluidic systems, or surfaces with tunable friction coefficients. The water contact angles values were 130° for sample "I" and 138° for sample "K".

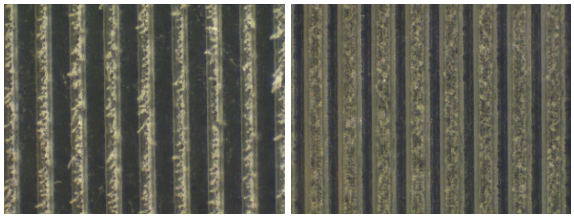

Fig. 5. Surface of thermopressed and rapidly pulled-off polyethylene films for samples "*I*" (left) and "*K*" (right).

4. Conclusions

The conducted research introduces a new approach to identifying and interpreting artifacts formed during the replication process using metal dies. Furthermore, the results show that such artifacts can be exploited as a reliable route to hierarchical microstructure fabrication. Femtosecond-laser-textured metal dies provide an efficient tool for transferring micro- and nanotextures onto polymers by solvent casting and

thermopressing, while the replication fidelity is determined by both the physicochemical properties of the polymer and the processing conditions.

Low-viscosity polymer solutions ensure superior texture filling, whereas thermopressing is constrained by limitations associated with high melt viscosity, air entrapment, and cooling-induced deformation. The formation of replication-induced artifacts is governed by interfacial adhesion, the mechanical integrity of locally thinned polymer regions, and phase-transition dynamics. Under thermopressing, the formation of hollow or ruptured structures highlights the influence of trapped air and localized stress, whereas solvent casting eliminates these issues by ensuring superior wetting and flow behavior. Although replication-induced artifacts impede the engineering of superhydrophobic or liquid-infused functional surfaces, the resulting irregular hierarchical morphologies can be exploited to develop new polymer surface functionalities.

Acknowledgements

This research was funded by Research Council of Lithuania, grant number S-LU-26-1 and Ministry of Education and Science of Ukraine, contract number M/88-2026 dated 20.02.2026.

References

[1]. H. Sun, J. Li, M. Liu, D. Yang, et al., A review of effects of femtosecond laser parameters on metal surface properties, *Coatings*, Vol. 12, Issue 10, 2022, 1596.

[2]. S. Caragnano, et al., Femtosecond laser-engineered molds for long-term stable superhydrophobic polydimethylsiloxane (PDMS) surfaces, *Advanced Materials Interfaces*, Vol. 12, 2025, e00808.

[3]. L. Piccolo, K. Puleo, M. Sorgato, G. Lucchetta, et al., Modeling the replication of submicron-structured surfaces by micro injection molding, *Materials & Design*, Vol. 198, 2021, 109272.

[4]. A. Brulez, C. Boschard, M. Larochette, S. Benayoun, Injection of a microtextured polymer part surface: Influence of experimental parameters on the replication rate, *Polymer Engineering and Science*, Vol. 60, Issue 9, 2020, pp. 2235-2247.

[5]. V. Strashenko, O. Myronyuk, Getting textured surfaces of polymer materials using metal templates, *Technologies and Engineering*, Vol. 25, Issue 2, 2024, pp. 125-131.

[6]. O. Myronyuk, D. Baklan, A. Bilousova, V. Strashenko, Development of microtextures on polymer surfaces using the transfer method from metal templates, *Technologies and Engineering*, Vol. 26, Issue 4, 2026, pp. 44-53.

(039)

Physical-Mathematical Model of Opto-Mechanical Processes in a Distributed Fiber-Optic Sensor

R. Aimagambetova [1] and A. Mekhtiyev [2]
[1] Satbayev University, Branch of the University, 52 Respublika Av., 010000 Astana, Kazakhstan
[2] Saginov University, Energy Institute, 56 Ave. Nursultan Nazarbayev, 100027, Karaganda, Kazakhstan
Tel.: + 77757688418
E-mail: rauwan2012 @mail.ru

Summary: This paper presents a physical-mathematical model describing the variation of optical power in a distributed fiber-optic sensor (DFOS) under mechanical loading, positioned explicitly as a TRL 2 theory contribution. The guiding principles of light propagation in optical fiber are reviewed, including total internal reflection and the V-number criterion for single-mode operation. The loss mechanisms under macro- and micro-bending are analyzed using an exponential attenuation model parameterized by bend radius and fiber design constants. The influence of the refractive index of the surrounding medium (air vs. concrete embedding) on the threshold curvature for optical leakage is examined. A novel curvature-loss integral model is derived, establishing a functional relationship between the spatial curvature distribution κ(x) along the fiber and the total power loss in decibels. Phase-shift and frequency-shift response channels are additionally formulated. The model provides the theoretical foundation for subsequent numerical simulation and experiment within the framework of structural health monitoring of reinforced-concrete infrastructure. The specific novelty relative to the authors' prior experimental and system-level publications [6-10] lies in the unified closed-form integral formulation and its explicit dependence on embedding medium properties.

Keywords: Distributed fiber-optic sensor, Optical losses, Fiber bending, Curvature, Structural health monitoring, TRL 2.

1. Introduction

Structural health monitoring (SHM) of civil infrastructure is a critical challenge in modern engineering [1]. Distributed fiber-optic sensors (DFOS) offer a compelling solution for continuous strain and deformation measurements, combining high sensitivity, immunity to electromagnetic interference, and the ability to perform measurements along extended objects. [4, 5]

This paper reports the results of the first project stage, corresponding to Technology Readiness Level TRL 2, consisting in the development of a physical-mathematical model that formalizes the relationship between mechanical loading of a structure and the measurable change in the optical signal of a DFOS. The central scientific hypothesis is that deformations of the fiber embedded in reinforced concrete structures produce a measurable increase in optical losses that can serve as a diagnostic indicator of structural condition [3].

The objective of this work is to establish the theoretical foundation for subsequent numerical simulation by deriving the dependence of power loss in decibels on the geometrical parameters of fiber deformation and on the properties of the surrounding medium. The present contribution is framed as a narrowly defined TRL 2 theory paper; its specific novelty consists of (i) the curvature-loss integral model formalized in equation (9) and (ii) the explicit analytical treatment of surrounding-medium refractive index as a control parameter for loss threshold. Earlier stages of the same research program – covering laboratory-sample experiments on fiber-optic sensors embedded in reinforced-concrete structures [8], fiber-optic power supply for mine-working sensor systems [9], radiation-source characterization for automatic optical parameter control [10], and full system-level monitoring of load-bearing building structures [11] – are cited here as prior stages rather than as part of the present contribution. The paper by Yurchenko et al. [6] investigated additional losses under mechanical action experimentally, and Mekhtiyev et al. [7] reported mechanical stress measurements on quartz optical fiber; the present work builds on those experimental findings by providing the unified theoretical integral model that was absent in those publications.

1.1. Optical Fiber as a Guiding Structure

A DFOS consists of an optical fiber comprising a core and a cladding made of silica glass with different refractive indices $n_1 > n_2$. The index difference confines light propagation along the fiber through total internal reflection (TIR) at the core–cladding interface [4].

Electromagnetic field propagation in a homogeneous dielectric medium is governed by the wave equation:

$$\nabla^2 E - \mu_0 \varepsilon \, \partial^2 E / \partial t^2 = 0$$

For a time-harmonic field this reduces to the Helmholtz equation:

$$\nabla^2 E + k^2 E = 0, \; k = 2\pi n / \lambda_0 \qquad (1)$$

TIR is maintained for angles of incidence exceeding the critical angle $\theta_a = \arcsin(n_2/n_1)$. The numerical aperture is $NA = \sqrt{(n_1^2 - n_2^2)}$. The modal regime is characterized by the normalized frequency (V-number):

$$V = (2\pi a/\lambda_0) \cdot NA, \quad (2)$$

where a is the core radius. Single-mode operation is obtained for $V < 2.405$. The V-number governs the field distribution between core and cladding and, consequently, the sensitivity of the fiber to bending losses.

1.2. Macro-Bending and Loss Mechanism

When the fiber is bent, the outer side of the core is stretched while the inner side is compressed. This geometrical change alters the effective angle of incidence of the guided modes at the core–cladding interface: a fraction of the modes no longer satisfies the TIR condition and becomes leaky, thereby reducing the transmitted optical power. Fig. 1 illustrates the ray propagation in a bent fiber.

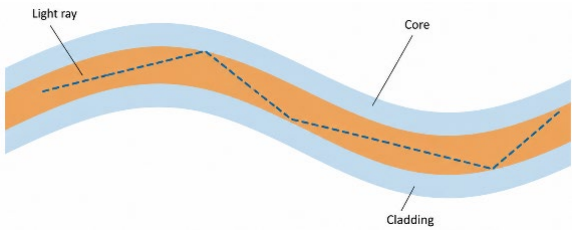

Fig. 1. Ray propagation in a bent optical fiber: at small bend radius R a fraction of rays escapes the core into the cladding (Core – orange; Cladding – blue).

The bending loss coefficient follows a phenomenological exponential dependence on the bend radius:

$$\alpha_{MM}(R) = A \cdot \exp(-B \cdot R), \quad (3)$$

where R is the bend radius; A and B are parameters depending on the operating wavelength, the V-number, and the fiber design. Smaller R (larger curvature $\kappa = 1/R$) produces higher losses. The V-number indirectly affects the magnitude of the bending loss coefficient: fibers with smaller V have a larger evanescent field fraction in the cladding and are therefore more sensitive to bending [2].

1.3. Logarithmic Loss Representation

Optical power loss is expressed on a logarithmic (dB) scale: losses along different fiber sections add algebraically, and most measurement systems register the signal directly in dB. The power at distance x from the input follows:

$$P(x) = P_0 \cdot \exp(-2\alpha x) \quad (4)$$

Power loss in dB over length L:

$$\Delta P = -10 \log_{10}[P(L)/P_0] = 8.686\ \alpha\ L\ (dB) \quad (5)$$

The total attenuation coefficient including bending losses:

$$\alpha_t^o{}_t = \alpha_0 + \alpha_{MM}(R) + \alpha_{OH}, \quad (6)$$

where α_0 is the intrinsic loss of the straight fiber, α_{MM} is the macro-bending contribution, and α_{OH} is the micro-bending contribution. Integrating over the sensitive length yields the total loss functional:

$$\Delta P_t^o{}_t = \int_0^L 8.686\ \alpha_t^o{}_t(\kappa(x))\ dx \quad (7)$$

1.4. Influence of the Surrounding Medium

The refractive index of the medium surrounding the fiber cladding significantly affects the threshold conditions for optical losses. In air ($n_{av\varphi} \approx 1.0$) the large index contrast at the cladding–air interface limits mode leakage [3]. When the fiber is embedded in concrete ($n_{av\varphi} \approx 1.4$–$1.6$), the index contrast decreases, TIR conditions are violated at larger bend radii, and losses increase even under moderate curvatures:

$$\alpha_{MM} = f(R, n_{av\varphi}) \quad (8)$$

Fig. 2 illustrates this effect: the orange curve (high $n_{av\varphi}$, concrete) lies consistently above the blue curve (air), demonstrating that an embedded fiber exhibits higher sensitivity to mechanical loading than a freely suspended fiber.

Furthermore, when rigidly bonded to concrete, the fiber directly follows the deformation of the host structure: localized deflections, micro-cracks, and non-uniform stresses create zones of elevated curvature and concentrated loss growth.

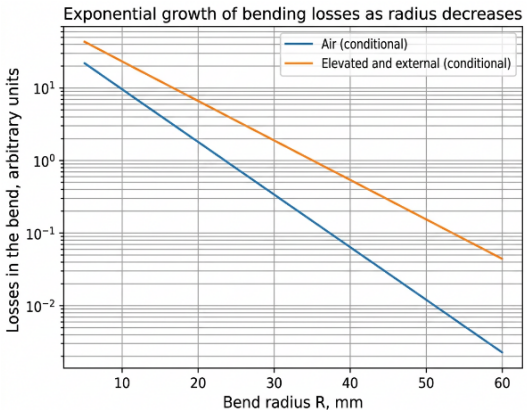

Fig. 2. Bending loss vs. bend radius R for two surrounding media (air – blue; high-index medium / concrete – orange). Log scale. Exponential growth at decreasing R.

2. Micro-Bending as a Source of Distributed Losses

Micro-bending refers to small-amplitude but spatially frequent deviations of the fiber axis caused by medium inhomogeneities, localized contact stresses, and attachment-related factors [5]. Unlike macro-bending, micro-bending does not produce a sharp loss onset at a critical radius; instead, it manifests as a gradual increase in the baseline attenuation level along the fiber.

When a developed network of micro-defects is present, the contribution $\alpha_{ои}$ becomes significant and enhances the sensor sensitivity to early-stage structural damage. The overall attenuation is determined by the superposition of both mechanisms according to equation (6).

3. Generalized Physical-Mathematical Model

Based on the foregoing analysis, a generalized model is formulated establishing a causal relationship between mechanical loading of a structure and the measurable optical response of the DFOS.

Mechanical sub-problem: an external load produces a deformed configuration of the fiber axis characterized by the curvature distribution $\kappa(x) = 1/R(x)$. The peak sensor sensitivity is determined by the maximum curvature κ_{ma}^{x}.

Optical sub-problem: the total power loss (dB) is a functional of $\kappa(x)$:

$$\Delta P = \int_0^L 8.686\,[A\cdot exp(-B/\kappa(x)) + \alpha_0 + \alpha_{ои}(\kappa(x))]\,dx \quad (9)$$

In the simplified TRL 2 formulation:

$$\Delta P \approx f(\kappa_{ma}^{x}), \quad (10)$$

which allows the results of mechanical simulation to be directly linked to predicted optical losses.

In addition, a phase (frequency) detection channel is considered. The phase shift produced by longitudinal strain ε over fiber length L is:

$$\Delta\phi = (2\pi n/\lambda_0)\cdot\varepsilon\cdot L \quad (11)$$

Fig. 3 confirms the linear character of the phase response for two representative fiber lengths (L = 1 m and L = 10 m). The slope scales proportionally with L, demonstrating the enhanced sensitivity of longer gauge lengths.

In the general case the sensor response is a linear superposition of mechanical and thermal contributions:

$$\Delta f = C\varepsilon\cdot\varepsilon + C^{T}\cdot\Delta T, \quad (12)$$

where $C\varepsilon$ and C^{T} are the strain and temperature sensitivity coefficients, respectively. Fig. 4 illustrates the two contributions: the strain sensitivity (ΔT = 0, blue) exhibits a gradual linear slope, while the temperature sensitivity (ε = 0, orange) shows a steeper response over a narrower range. Separate identification of the two contributions is required in practical applications.

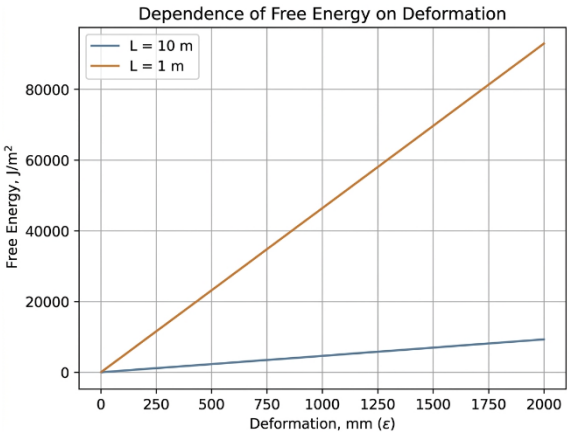

Fig. 3. Linear dependence of phase shift Δφ (rad) on longitudinal strain ε (μm/m) for L = 1 m (blue) and L = 10 m (orange). (Note: the embedded chart title should read "Dependence of Phase Shift on Strain"; any reference to free energy in the chart area is an artefact of the figure source and does not reflect the plotted quantity).

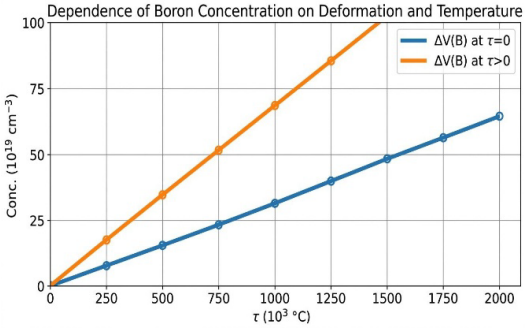

Fig. 4. Frequency shift $\Delta\nu^{O}$ (MHz) vs. strain ε (μm/m) at ΔT = 0 (blue) and vs. temperature ΔT (°C) at ε = 0 (orange), illustrating independent linear sensitivities. (Note: the embedded chart title should read "Dependence of Frequency Shift on Strain and Temperature"; any reference to boron concentration in the chart area is an artefact of the figure source and does not reflect the plotted quantities).

4. Conclusions

A physical-mathematical model of opto-mechanical processes acting on a DFOS has been developed to demonstrate the proof of concept at TRL 2. The key findings are as follows:

1) The mechanisms governing optical signal propagation in the fiber have been theoretically established. It is shown that under mechanical loading – primarily bending – the guiding conditions are

violated and part of the optical energy is transferred to leaky modes, increasing optical losses.

2) A relationship between power loss (dB) and fiber curvature has been derived (Figs. 1–2). The attenuation exhibits exponential growth with decreasing bend radius, and the surrounding medium (air vs. concrete) significantly affects the threshold curvature.

3) A generalized integral model linking the curvature distribution $\kappa(x)$ along the fiber to the total power loss has been developed, along with a simplified representation in terms of the maximum curvature as the governing parameter.

4) Phase and frequency response channels have been analyzed (Figs. 3–4), confirming the linear strain and temperature sensitivities of the DFOS and providing the basis for multi-parameter measurement.

The results form the theoretical basis for the next project stage – numerical simulation of mechanical loading and computation of the resulting optical signal variation – confirming the feasibility of the core scientific hypothesis and ensuring readiness for transition to TRL 3.

Acknowledgements

This work was supported by the grant funding project of the Ministry of Science and Higher Education of the Republic of Kazakhstan, IRN AP26194499 “System for monitoring the technical condition of extended objects and monolithic building structures using intelligent fiber-optic sensors.”

References

[1]. B. Glisic, D. Inaudi, Fibre Optic Methods for Structural Health Monitoring, *Wiley*, Chichester, 2007.

[2]. D. Marcuse, Curvature loss formula for optical fibers, *Journal of the Optical Society of America*, Vol. 66, Issue 3, 1976, pp. 216-220.

[3]. X. Bao, L. Chen, Recent progress in distributed fiber optic sensors, *Sensors*, Vol. 12, Issue 7, 2012, pp. 8601-8639.

[4]. A. H. Hartog, An Introduction to Distributed Optical Fibre Sensors, *CRC Press*, Boca Raton, 2017.

[5]. C. A. Galindez-Jamioy, J. M. López-Higuera, Brillouin distributed fiber sensors: An overview and applications, *Journal of Sensors*, Vol. 2012, 2012, 204121.

[6]. A. V. Yurchenko, A. D. Mekhtiyev, F. N. Bulatbaev, A. D. Alkina, et al., Investigation of additional losses in optical fibers under mechanical action, *IOP Conference Series: Materials Science and Engineering*, Vol. 516, Issue 1, 2019, 012004.

[7]. A. D. Mekhtiyev, A. A. Kovtun, V. V. Yugay, R. Z. Aimagambetova, et al., Research of mechanical stress at tension of quartz optical fiber (QOF), *Metalurgija*, Vol. 60, Issue 1-2, 2021, pp. 121-124.

[8]. A. D. Mekhtiyev, A. V. Yurchenko, F. N. Bulatbaev, et al., Fiber-optic converter for measuring mechanical quantities, *Russian Journal of Nondestructive Testing*, Vol. 54, Issue 7, 2018, pp. 471-477.

[9]. A. Mekhtiyev, P. Dunayev, Y. Neshina, A. Alkina, et al., Power supply via fiber-optical conductor for sensors of mine working monitoring system, *Eastern-European Journal of Enterprise Technologies*, Vol. 5, Issue 5, 2023, pp. 15-23.

[10]. A. Mekhtiyev, A. Seraly, R. Aimagambetova, A. Alkina, et al., Study of radiation sources of automatic control system of optical parameters of fiber-optic sensors, Periodicals of Engineering and *Natural Sciences*, Vol. 13, Issue 3, 2025, pp. 741-756.

[11]. A. D. Mekhtiyev, M. Y. Narkevich, Y. G. Neshina, A. K. Kozhas, et al., Fiber optics based system of monitoring load-bearing building structures, *Magazine of Civil Engineering*, Vol. 123, Issue 7, 2023, 12301.

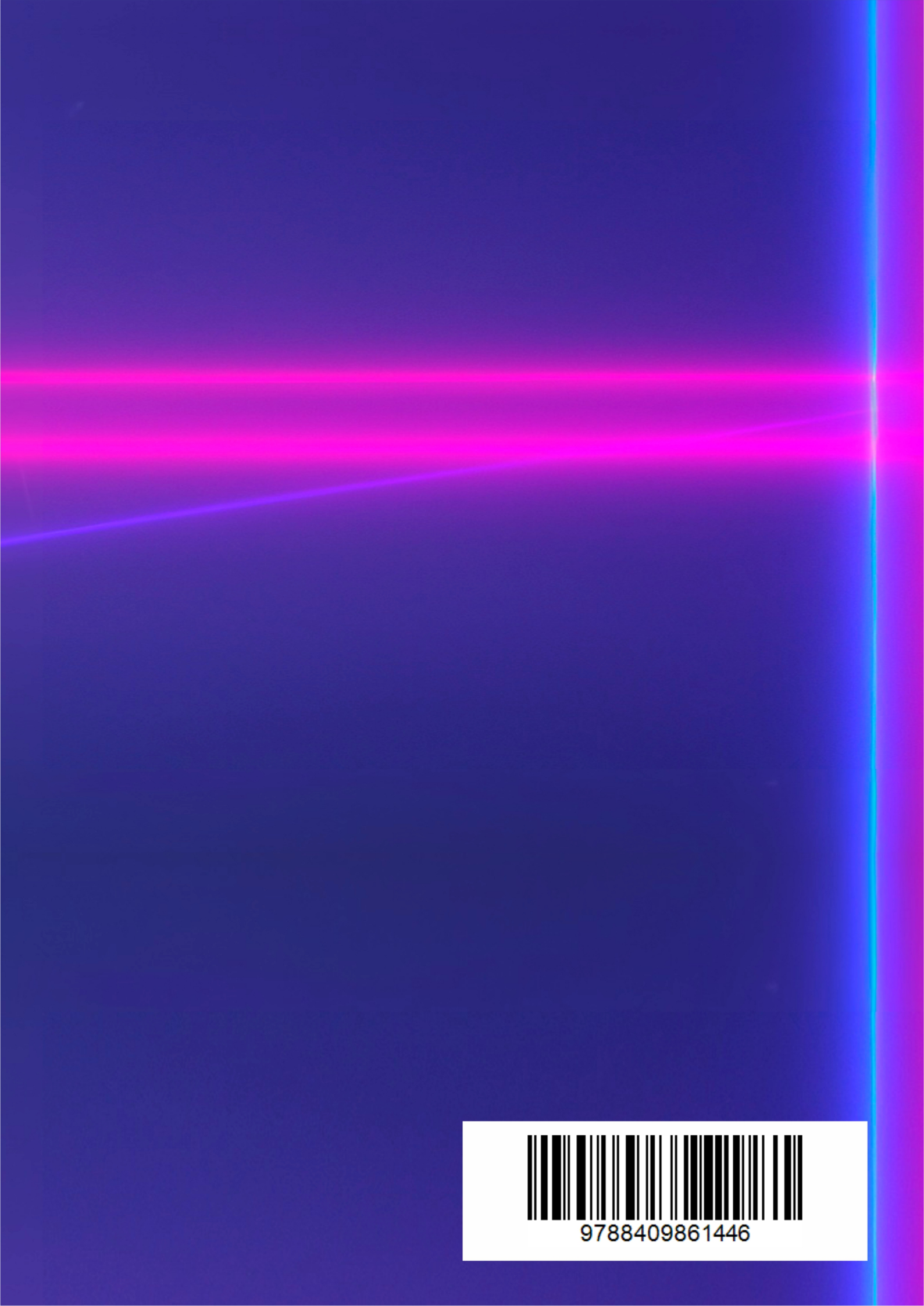
9788409861446